"L'uomo comprende tutto, salvo
cio che e' perfettamente semplice"

Hugo von Hofmannsthal

Photoelectron Spectroscopy of Radicals using Synchrotron Radiation, within the EC "Reactive Intermediates" Network

A THESIS SUBMITTED TO THE UNIVERSITY OF SOUTHAMPTON
FOR THE DEGREE OF
DOCTOR OF PHILOSOPHY

LUCIA ZUIN

SCHOOL OF CHEMISTRY
UNIVERSITY OF SOUTHAMPTON

JANUARY 2004

UNIVERSITY OF SOUTHAMPTON

ABSTRACT

FACULTY OF SCIENCE
SCHOOL OF CHEMISTRY

Doctor of Philosophy

PHOTOELECTRON SPECTROSCOPY OF RADICALS USING SYNCHROTRON RADIATION, WITHIN THE EC “REACTIVE INTERMEDIATES” NETWORK

by Lucia Zuin

The work described in this thesis is a study of unstable species in the gas phase using electron spectroscopy. The overall aim of this work was to study the photoionization behaviour of reactive species using photoelectron spectroscopy with Synchrotron Radiation. UV photoelectron spectroscopy studies of the O, N and S atoms and the OH, OD and SH radicals and a study of photodissociation of ethylene have been performed using Synchrotron Radiation. Constant ionic state (CIS) angular resolved experiments have been made. In these experiments, autoionizing resonances have been observed and assigned to members of series of Rydberg states converging towards higher ionic limits. Vibrational and rotational resolution has been obtained in OH and OD CIS spectra. For each reactive atom and molecule studied, measurement of angular distributions of photoelectrons allowed insight into the photoionization dynamics to be obtained.

The photodissociation mechanisms of ethylene have been probed through the detection of visible fluorescence emitted by the fragments, using an optical device designed in Orsay. Based on the results obtained, mechanisms of photodissociation of ethylene at the photon energies used have been proposed.

MEMORANDUM

This thesis is an account of original research performed by the author in the School of Chemistry of the University of Southampton, between October 2000 and December 2003. Where findings of other work have been used, due reference has been given.

Acknowledgments

There are an incredible number of people without which this thesis would not have been possible. First of all I will always be grateful to my supervisor, Professor John M. Dyke, for the big opportunity, help, support and trust during these three years. Thanks also to Dr. Alan Morris for having provided invaluable experimental and technical help and … a lot of fun during his stay in Trieste.
In addition to John and Alan I wish to acknowledge Professor John B. West for the interesting discussions and unique suggestions.

I thank the rest of the research group, in particular Fabrizio, Ed, Giacomino, Inma, Karinne, Levi and Santy. Thanks for the laughs, the jokes, the company, the tea-break, the pubs and the Chinese restaurants.

A huge thank goes to Professor Dolores Gauyacq and her group in France, especially Séverine, Stephane and Niloufar, for making me feel at home every time I went to Orsay and feeding me with champagne, crêpe and quiche lorraine.

Last but not least I thank Fabrice and Loredana, it is nice to have around somebody always kind and nice and somebody else more … like me!
Hey guys soon I will join you in the "One-shared-neuron Club" ☺

Lucia

Photoelectron Spectroscopy of Radicals using Synchrotron Radiation, within the EC "Reactive Intermediates" Network

3 SYNCHROTRON RADIATION 58

Acronyms Used in this Thesis

PES	Photoelectron Spectroscopy
PE	Photoelectron
PIMS	Photoionization Mass Spectroscopy
VUV	Vacuum Ultraviolet
UV	Ultraviolet
XUV	Extreme Ultraviolet
CIS	Constant Ionic State
FCF	Franck-Condon Factor
AIE	Adiabatic Ionization Energy
VIE	Vertical Ionization Energy
GE	General Electric
SURF	Synchrotron Ultraviolet Radiation Facility
INS-SOR	Institute for Nuclear Studies-Synchrotron Orbital Radiation
DESY	Deutsches Elektronen Synchrotron
SRS	Synchrotron Radiation Source
ESRF	European Synchrotron Radiation Facility
FEL	Free Electron Laser
RF	Radio Frequency
LINAC	Linear Accelerator
EEW	Electromagnetic Elliptical Wiggler
NIM	Normal Incidence Monochromator
RLS	Rotational Line Strengths
TPES	Threshold Photoelectron Spectroscopy
PFI	Pulsed Field Ionization
PEPICO	Photoelectron Photoion Coincidence
DMS	Dimethylsulphide

List of Figures

Chapter 1

1 INTRODUCTION

The work described in this thesis is a study of unstable species in the gas phase using spectroscopic techniques. Unstable species, including complexes and radicals are currently receiving a great deal of attention from the chemistry community as a result of recent developments in experimental and theoretical methods. Many of the chemical properties of molecules are a consequence of their electronic structure. Chemical reactions proceed by movement of electrons, hence to understand the properties of molecules knowledge of their electronic structure is important. Such knowledge has been gained through a variety of spectroscopic methods.

The techniques for performing vacuum ultraviolet studies of photoionization in the gas phase were introduced about four decades ago[1]. Two general methods have been employed:

- ✓ analysing the kinetic energy spectrum of photoelectrons (Photoelectron Spectroscopy, PES), and
- ✓ measuring the intensities of mass-selected ions as functions of incident photon energy (Photoionization Mass Spectroscopy, PIMS).

The results included in this thesis have been obtained by the use of the PES technique.

1.1 Photoelectron Spectroscopy (PES)

Photoionization is the term used to describe the process whereby radiation ejects one or more electrons from an atom or molecule. The origin of the subject may be traced back to the end of the last century when Hertz[2], in 1887, made the first observation of ionization of matter through the interaction of ultraviolet radiation with a solid. This discovery led Einstein[3] to describe, in 1905, the photoelectric effect from a theoretical point of view.

1.1.1 Basic principles

Photoelectron spectroscopy (PES) is a technique for investigating the electronic structure of atoms and molecules[4]. This involves photoionization of the species and subsequent measurement of the kinetic energy of the ejected electron. If a sufficiently energetic photon interacts with an atom to produce a photoelectron and a corresponding photoion, the basic process can be written as:

$$A + h\nu \rightarrow A^{+} + e^{-} \qquad \text{Eq. 1.1}$$

From the laws of energy and momentum conservation, it is easily seen that the kinetic energy of the photoelectron ejected from level i, $E_{e,kin,i}$, is given by the difference between the photon energy $h\nu$ and the binding energy of level i, $E_{bind,i}$:

$$E_{e,kin,i} = h\nu - E_{bind,i} \qquad \text{Eq. 1.2}$$

In principle this is a simple technique, it requires a source of monochromatic and sufficiently energetic radiation, a sample, an electron kinetic energy analyser and an electron detector. Hence, in a photoelectron spectroscopy experiment a target is irradiated by a monochromatic photon beam and the released photoelectrons are analysed according to their kinetic energies. Obviously, this technique is capable of providing information about the binding energies for all levels i that can be ionised. Radiation of tens of eV of energy, in the region called vacuum ultraviolet (VUV), is sufficiently energetic to ionise electrons from valence orbitals. With radiation in the region called the extreme ultraviolet (XUV), whose energy is between tens and hundreds of eV, electrons from more tightly bound orbitals can also be ionized.

Photoelectron spectroscopy has been evolving during the last thirty years, when Synchrotron Radiation has been used as the photon source[5]. Synchrotron Radiation is emitted by electrons moving at relativistic velocities, tangentially to the electron flight path. Synchrotron Radiation can be monochromatized and tuned continuously in the range of energy from the far-infrared to the hard X-ray region, in contrast to radiation at fixed wavelength emitted by most rare-gas discharge lamps.

Synchrotron Radiation is also naturally polarized and angle resolved experiments can be carried out with greater sensitivity than with an unpolarized source.

The study of a reactive intermediate with photoelectron spectroscopy using monochromatized Synchrotron Radiation[6,7] should allow more information to be obtained on the molecular ionic states produced and the associated photoionization processes than a PES study with a low pressure discharge of an inert gas as the photon source[8-10], in particular:

- a study of the relative band intensities in the valence photoelectron spectrum of a small molecule as a function of the ionizing photon energy can provide valuable information to assist band assignment
- measurement of photoelectron angular distributions at fixed photon energy allows information on photoionization dynamics to be obtained
- an autoionization resonance, once identified, can give rise to extra structure over that observed in a photoelectron spectrum recorded off resonance[11-14]. This effect was first observed by Price[15] for the oxygen molecule where one of the neon discharge resonance lines coincided with a resonance in O_2; the resulting photoelectron spectrum showed considerably more vibrational structure than one taken using the helium discharge line.

It was this last point which initially attracted the Southampton PES group to use Synchrotron Radiation because in a number of previous investigations some of the valence photoelectron bands of the reactive species studied, when recorded with a HeI (21.22 eV) photon source, showed an intense adiabatic component with very little intensity in other vibrational components. Such an observation for the first photoelectron band of a short-lived molecule is particularly disappointing, since measurement of the vibrational level separations in the ground ionic state is usually one of the main objectives of the experiment[16,17].

For the second point, the polarization properties of the Synchrotron Radiation Source are utilized to measure angular distribution parameters[18]. This facility can be important in identifying the ionic symmetries associated with new structure observed in the photoelectron spectrum, as well as being a powerful method of showing the presence of weak underlying structure in the photoionization continuum.

In order to achieve the aim of the first point, the constant ionic state (CIS) technique is used, in which the photoelectron spectrometer is set on a particular ionic vibrational level known to belong to the species of interest, and the exciting wavelength is then scanned in synchronism with the kinetic energy of the electrons that are detected. In this way a relative partial ionization cross section of the molecule is obtained, and new structure in the continuum is observed. In fact, very little is known about the ionization continua of short-lived molecules and this method is an ideal way of obtaining such information.

1.1.2 Angle resolved experiments

In the angle resolved experiments the photoelectrons are selected according to their kinetic energy and the angle θ with respect to the polarization vector of the ionizing radiation at which they are emitted. The relative photoionization cross section σ_i and the asymmetry parameter β_i may be calculated as well. These parameters are related to the experimentally observed intensity of level $I_i(\theta)$ by[6]:

$$I_i(\theta) \propto \frac{d\sigma_i}{d\Omega} = \frac{\sigma_i}{4\pi}\left[1 + \frac{\beta_i}{4}(1 + 3P\cos 2\theta)\right] \qquad \text{Eq. 1.3}$$

where $d\sigma_i/d\Omega$ is the differential cross section and P is the degree of linear polarization of the incoming radiation.

The photoelectrons are not emitted isotropically; their angular distribution is determined by β_i. By measuring the intensity $I_i(\theta)$ at two different angles, θ, the relative cross section and the asymmetry parameter can be easily calculated.

1.1.3 Constant Ionic State spectra

In addition to photoelectron spectra, constant ionic state (CIS) spectra can also be recorded with a Synchrotron Radiation Source. A CIS spectrum is the measurement of the cross section for photoionization to a specific ionic state as a function of the photon energy. A resonance in a CIS spectrum can occur when the energy of the incident radiation is equal to an excitation energy to a neutral state above the ionization limit to produce an excited state that autoionizes and modifies the process in Eq. 1.1 to the following:

$$A + h\nu \rightarrow A^* \qquad \text{Eq. 1.4}$$

$$A^* \rightarrow A^+ + e^- \qquad \text{Eq. 1.5}$$

For this kind of spectrum the evaluation of the photoionization parameters σ_i and β_i as a function of the photon energy can reveal information on of the excited state and free electron wavefunctions and can lead to a better understanding of the dynamics of the photoionization process.

1.2 Molecular photoelectron spectroscopy

Most of the chemical properties of molecules are principally determined by their electronic structure, in particular by the character of their valence electrons.

When the species investigated is a molecule there are additional possibilities of vibrational and rotational excitation on ionization; Eq. 1.2 then became:

$$E_{e,kin,i} = h\nu - E_{bind,i} - \Delta E_{vib,rot} \qquad \text{Eq. 1.6}$$

where $\Delta E_{vib,rot}$ is the change in vibrational and rotational energy on ionization.

The resolution normally achievable in VUV photoelectron spectroscopy allows vibrational structure to be resolved in most light molecules. In contrast resolution of rotational structure is beyond the capabilities of conventional PES, with some small exceptional cases[19,20].

In the case of fixed photon energy, the direct photoionization of molecules can be written schematically as:

$$M(v'') + h\nu \rightarrow M^{+}(v^{+}) + e^{-} \qquad \text{Eq. 1.7}$$

and the distribution of intensity with the v^{+} vibrational components of a photoelectron band can be approximated by the *Franck-Condon Factors* (FCFs), as described in the later theoretical section (Chapter 2.3), the square of the overlap integral between the vibrational wavefunctions of the initial ($\Psi_{M,v''}$) and ionic ($\Psi_{M^{+},v^{+}}$) states:

$$I_{v^{+}\leftarrow v''} \propto \left| \int_{0}^{+\infty} \Psi_{M^{+},v^{+}}(R)\Psi_{M,v''}(R)dR \right|^{2} \qquad \text{Eq. 1.8}$$

In the case of resonant photoionization, when the cross section for photoionization to a specific ionic state is measured as function of the photon energy:

$$M(v'') + h\nu \rightarrow M^{*}(v') \qquad \text{Eq. 1.9}$$

$$M^{*}(v') \rightarrow M^{+}(v^{+}) + e^{-} \qquad \text{Eq. 1.10}$$

the distribution of intensity of the v^+ vibrational components of a photoelectron band can be expressed by the following expression:

$$I_{v^+ \leftarrow v' \leftarrow v''} \propto \left| \int_0^{+\infty} \Psi_{M^+,v^+}(R)\Psi_{M^*,v'}(R)dR \right|^2 \times \left| \int_0^{+\infty} \Psi_{M^*,v'}(R)\Psi_{M,v''}(R)dR \right|^2 \qquad \text{Eq. 1.11}$$

which is a product of the FCFs for the two steps involved.

Any molecular system possesses a wealth of highly excited neutral states that may be accessed by resonant absorption of radiation. In particular there exist Rydberg states[21] that are grouped into series converging to ionic limits.

1.2.1 Resonant effect and Rydberg states

Rydberg electronic states are hydrogen-like states resulting from promotion of an electron to an orbital in which its average distance from the centre of the molecule is much larger than that of the other electrons. This state can be described by electronic configurations where one orbital has a principal quantum number greater than those of the other occupied orbitals. From the point of view of the distant electron, the molecule is little different from an ion with a +1 charge, since the net nuclear charge is screened by all the other electrons. The electronic configuration of the unexcited electrons corresponds to a state of the positively charged ion, and for this reason it is conventionally called the ionic core.

The energies of Rydberg states follow the formula[21]:

$$E_n = I - \frac{R}{(n-\delta)^2} \qquad \text{Eq. 1.12}$$

where I is the ionization energy for complete removal of the excited electron, R is the Rydberg constant, δ is the quantum defect and n is the principal quantum number.

The quantum defect, δ, allows for the deviation of the Rydberg energy levels from that expected for a 1-electron system. Its magnitude reflects the penetration of the Rydberg orbital into the ionic core and it is related to the radial distribution of the excited orbital.

Many of these discrete states are situated above the first ionization limit, and thus lie within an ionization continuum. When the energy of an incident photon matches that of a transition to one of these Rydberg states, two processes become viable: direct photoionization and resonant photoabsorption to the neutral state M^*.

At these resonant wavelengths there is a significant probability of an excited neutral state M^* being generated as an alternative to direct ionization to M^+. The production of the excited state can be quite large, as cross sections for resonant one-photon absorption are larger than those for photoionization at a given wavelength.

The excited neutral state can then decay by autoionization. This is a common decay route for Rydberg states although fluorescence and non-radiative processes are also possible.

1.3 Reactive Intermediates

The exact nature of short-lived reactive species is very varied. One class of species which are commonly short-lived in the gas-phase are radicals. Radicals are usually defined as neutral molecules with one or more unpaired electrons. They are frequently found to play important roles in areas such as combustion, atmospheric chemistry and energy transfer in chemical laser systems. The method of study of short-lived molecules depends upon the molecule, and the system in which it is to be studied. For *in situ* study of molecules prepared by a rapid gas phase reaction, it is necessary to study the molecules immediately after production otherwise their partial pressure will be reduced by reaction. Short-lived species, both neutral and ionized, are of great importance in atmospheric and astrophysical chemistry. Reaction intermediates, despite being present in low partial pressure, can have a major influence on the gas phase chemistry. Due to experimental difficulties, short-lived molecules of fundamental importance in these areas have not been thoroughly studied, and their electronic structure, which may be complex, not fully investigated.

The Southampton PES group has concentrated on the study of reactive intermediates as its main research topic. Initial work was performed on short-lived molecules, formed in the gas phase in discharges[22-24] or by chemical reaction[25]. A review of PES investigations performed in Southampton using HeI (21.22 eV) and HeII (40.81 eV) radiation from discharge lamps can be found in reference (17) and a review of the work performed to date with Synchrotron Radiation is contained in reference (26).

The study of the electronic structure of short-lived radical species in the gas-phase forms the major part of this work.

1.4 Aims of the Project and Structure of the Thesis

The overall aim of this thesis was to further the study of the photoinozation behaviour of reactive species using photoelectron spectroscopy with Synchrotron Radiation. This would allow information to be obtained on neutral as well as ionic states of the reactive species investigated. All the measurements would be made at the ELETTRA Synchrotron Radiation Source in Trieste[27], Italy. In this thesis the theory and the fundamental principles behind photoionization and resonant states is presented in Chapter 2, while Chapter 3 outlines a brief introduction of the characteristics of Synchrotron Radiation. Chapter 4 describes the experimental apparatus used for the study of PES of reactive intermediates. The results of angular distribution studies on oxygen atoms, OH and OD radicals, nitrogen atoms, S atoms and SH radicals are presented in Chapter 5 to Chapter 8 respectively. In Chapter 9 the results obtain during collaborations with the French group of the EC *"Reactive Intermediates"* Network are presented. Finally, Chapter 10 concludes the thesis with a summary of the project, and outlines some possibilities for further work. A short Appendix describes the results of the asymmetry parameter investigation on dimethylsulphide (DMS) performed as support to recent experiments performed at the Southampton University with HeI photoelectron spectroscopy radiation on the mechanisms and pathways of DMS reactions of atmospheric importance.

1.5 References

[1] J. Berkowitz and B. Ruscic
Vacuum Ultraviolet Photoionization and Photodissociation of Molecules and Clusters
edited by C.Y. Ng, World Scientific, London, 1991, Chapter 1

[2] H. Hertz
Annalen der Physik **31**, 983 (1887)

[3] A. Einstein
Annalen der Physik **17**, 132 (1905)

[4] J. H. D. Eland
Photoelectron Spectroscopy
Butterworths & Co, Oxford, 1984

[5] V. Schmidt
Electron Spectrometry of Atoms using Synchrotron Radiation
Cambridge University Press, New York, 1997

[6] J. B. West
Vacuum Ultraviolet Photoionization and Photodissociation of Molecules and Clusters
edited by C.Y. Ng, World Scientific, London, 1991, Chapter 8

[7] I. Nenner and J. A. Beswick
Handbook on Synchrotron Radiation
edited by G.V. Marr, Elsevier, Amsterdam, 1987, Vol. II

[8] J. M. Dyke, L. Golob, N. Jonathan, A. Morris and M. Okuda
Journal of The Chemical Society Faraday Transactions 2 **70**, 1828 (1974)

[9] J. M. Dyke, N. Jonathan and A. Morris
Internal Review of Physical Chemistry **2**, 3 (1982)

[10] J. Baker, M. Barnes, M. C. R. Cockett, J. M. Dyke, A. M. Ellis, M. Feher, E. P. F. Lee, A. Morris and H. Zamanpour
Journal of Electron Spectroscopy and Related Phenomena **51**, 487 (1990)

[11] D. M. P. Holland, J. B. West and M. A. Hayes
Journal of Chemical Physics **148**, 241 (1990)

[12] K. Codling, A. C. Parr, D. L. Ederer, R. Stockbauer, J. B. West, B. E. Cole and J. L. Dehmer
Journal of Physic B - Atomic and Molecular Physics **14**, 657 (1981)

[13] P. Natalis, J. E. Collin, J. Delwiche, G. Caprace and M. J. Hubin
Journal of Electron Spectroscopy and Related Phenomena **17**, 205 (1979)

[14] J. A. R. Samson
Physical Review **28 c**, 303 (1976)

[15] W. C. Price
Molecular Spectroscopy
edited by P. Hepple, Institute of Petroleum, London, 1968

[16] J. M. Dyke
Journal of The Chemical Society Faraday Transactions 2 **83**, 67 (1987)

[17] M. C. R. Cockett, J. M. Dyke and H. Zamanpour
Vacuum Ultraviolet Photoionization and Photodissociation of Molecules and Clusters
edited by C.Y. Ng, World Scientific, London, 1991, Chapter 2

[18] J. B. West, J. M. Dyke, A. Morris, T. G. Wright and S. D. Gamblin
Journal of Physic B - Atomic and Molecular Physics **32**, 2763 (1999)

[19] L. Asbrink and J. W. Rabalais
Chemical Physics **12**, 1821 (1971)

[20] J. W. Rabalais, T. Bergmark, L. O. Werme, L. Karlsson and K. Siegbahn
Physica Scripta **3**, 13 (1971)

[21] A. B. F. Duncan
Rydberg series in atoms and molecules
Academic Press, New York, 1971

[22] N. Jonathan, D. J. Smith and K. J. Ross
Chemical Physics Letters **9**, 217 (1971)

[23] N. Jonathan, A. Morris, K. J. Ross and D. J. Smith
Journal of Chemical Physics **54**, 4954 (1971)

[24] N. Jonathan, A. Morris, M. Okuda, K. J. Ross and D. J. Smith
Faraday Discussion Chemical Society **54**, 1 (1972)

[25] L. Andrews, J. M. Dyke, N. Keddar, N. Jonathan and A. Morris
Journal of American Chemistry Society **106**, 229 (1984)

[26] J. D. Barr, L. J. Beeching, A. DeFanis, J. M. Dyke, S. D. Gamblin, N. Hooper, A. Morris, S. Stranges, J. B. West, A. E. Wright and T. G. Wright
Journal of Electron Spectroscopy and Related Phenomena **108**, 47 (2000)

[27] http://www.elettra.trieste.it

Chapter 2

2 FUNDAMENTAL PRINCIPLES

Experimental investigations of the photoionization process began in 1887 when Hertz discovered the photoelectric effect[1]. However the understanding of the process had to wait until the crucial theory proposed by Einstein[2] in 1905, that electromagnetic radiation could be considered to be quantised in the form of photons, each with energy $h\nu$. In this Chapter the basic relations governing the photoionization process will be presented. Photoelectron spectroscopy with a fixed wavelength radiation source and photoelectron spectroscopy with a tuneable wavelength radiation source are considered from a fundamental point of view.

2.1 Photoelectron spectroscopy with a fixed wavelength radiation source

The aim of photoelectron spectroscopy (PES) is to provide information on the ionic states of atoms and molecules. Irradiation of a sample with sufficiently energetic photons causes direct ionization of that sample. Typically, photons of several tens of eV in energy are required, and suitable photon sources are those emitting vacuum ultraviolet radiation. A particular ionic state M_i^+ may be formed in this manner provided that the energy of ionization to that state, IE_i is less than the photon energy $h\nu$. The kinetic energy of the photoelectron, E_{kin}, is given by:

$$E_{kin} = h\nu - IE_i - \Delta E_{vib} - \Delta E_{rot} \qquad \text{Eq. 2.1}$$

where ΔE_{vib} and ΔE_{rot} are the differences in vibrational and rotational energy between the molecule and the ion. Typically rotational resolution is not achieved in a photoelectron spectrum, so the ΔE_{rot} term is averaged into IE_i to give IE_i'.

The resolution for this kind of experiment is typically in the region of 200 cm^{-1} (0.025 eV), hence only vibrational structure can usually be resolved. This allows an estimation of the vibrational constant ω_e^+ in an ionic state from analysis of a vibrationally resolved photoelectron band. It is assumed, to a first approximation, that all excess energy over $(IE_i'+\Delta E_{vib})$ is released as electron kinetic energy, since the electron is much lighter than any molecular or atomic ion and the law of conservation of momentum ensures that the change in kinetic energy of the ion is negligible.

A photoelectron spectrum is recorded by counting photoelectrons produced per unit time over a range of kinetic energies, with the photon energy fixed, and it thus provides a map of ionic states of a molecule. In a photoelectron spectrum, one band will be observed for ionization to each ionic state accessed.

The direct ionization processes that are allowed in photoelectron spectroscopy are governed by selection rules for the electronic and vibrational changes that may occur on ionization. In general the probability that a direct transition between the molecule ground state characterized by the eigenfunction Ψ'' and the final (ion plus free electron) state characterized by Ψ' is determined by the square of the transition moment integral[3,4]:

$$\overline{M} = \langle \Psi'' | \Sigma \overline{p} | \Psi' \rangle \qquad \text{Eq. 2.2}$$

where $\overline{p}$ is the electric dipole moment operator and the sum extends over all electrons i and nuclei j; Ψ'' and Ψ' are functions of the electron, r, and nuclear, R, coordinates.

Using the Born-Oppenheimer approximation, the initial and final eigenfunctions can be separated into the product of electronic and nuclear wavefunctions:

$$\Psi(r;R) = \Psi_{es}(r;R)\Psi_n(R) \qquad \text{Eq. 2.3}$$

The nuclear wavefunction, $\Psi_n(R)$, is treated simply as a vibrational function, $\Psi_n \equiv \Psi_v$, as by reference to a rotating molecule coordinate system the rotation may be neglected here.

The dipole operator can also be separated into an electronic and a nuclear dependent part $\Sigma_{i,j}\overline{p} = \Sigma_i \overline{p}_e + \Sigma_j \overline{p}_n$. Substituting these results into Eq. 2.2 the square of the transition moment integral becomes:

$$\overline{M} = \iint \Psi_{es}^{*}{}''(r;R)\Psi_v^{*}{}''(R) \left| \Sigma_i \overline{p}_e + \Sigma_j \overline{p}_n \right| \Psi_{es}{}'(r;R)\Psi_v{}'(R) d\tau_e d\tau_n \qquad \text{Eq. 2.4}$$

This integral can be separated according to the electronic and nuclear dipole operators:

$$\begin{aligned} \overline{M} &= \int \Psi_v^{*}{}''(R)\Psi_v{}'(R) d\tau_n \int \Psi_{es}^{*}{}''(r;R) \left| \Sigma_i \overline{p}_e \right| \Psi_{es}{}'(r;R) d\tau_e \\ &\quad + \int \Psi_v^{*}{}''(R) \left| \Sigma_j \overline{p}_n \right| \Psi_v{}'(R) d\tau_n \int \Psi_{es}^{*}{}''(r;R)\Psi_{es}{}'(r;R) d\tau_e \qquad \text{Eq. 2.5} \end{aligned}$$

Since electronic eigenfunctions belonging to different states are orthogonal to one another, the second term in Eq. 2.5 vanishes for electronic transitions. If then the dependence of Ψ_{es} on the nuclear coordinates is neglected, assuming that the variation of $\overline{p}_e$ with R is negligible, Eq. 2.5 becomes:

$$\overline{M} = \int \Psi_v^{*}{}''(R)\Psi_v{}'(R) d\tau_n \int \Psi_{es}^{*}{}''(r;R_0) \left| \Sigma_i \overline{p}_e \right| \Psi_{es}{}'(r;R_0) d\tau_e \qquad \text{Eq. 2.6}$$

This equation consists of a factor which depends on the nuclear motion alone and a factor depending on the electronic motion alone.

From the above considerations, the photoionization transition probability may be written as:

$$P \propto \left| \int \Psi_v^{*}{}''(R) \Psi_v{}'(R) d\tau_n \right|^2 \left| \int \Psi_{es}^{*}{}''(r;R_0) \middle| \Sigma_i \bar{p}_e \middle| \Psi_{es}{}'(r;R_0) d\tau_e \right|^2$$

$$\propto \left|\overline{M}_v\right|^2 \left|\overline{M}_{es}\right|^2 \qquad \text{Eq. 2.7}$$

The first term is called the *Franck-Condon Factor* and the second term is the electronic transition moment squared.

2.1.1 *Electronic selection rules*

Photoelectron transitions are allowed whenever the integral, $\overline{M}_{es}$, of Eq. 2.7 is different from zero. Only single-electron transitions are permitted in photoionization because the operator in $\overline{M}_{es}$ is a one-electron operator. If the wavefunctions for the neutral and ionized states are constructed from the same set of molecular orbitals and a one-electron operator is used, only states characterized by an electronic configuration differing from that of the neutral molecule by one molecular orbital will be allowed in PES.

For systems in which spin-orbit interaction is small, the electronic eigenfunctions including spin Ψ_{es} can be treated as a product of an orbital and a spin function:

$$\Psi_{es} = \Psi_e \times \Psi_s \qquad \text{Eq. 2.8}$$

Since the dipole operator does not operate on spin coordinates, the transition moment may be factorized as:

$$\left\langle \Psi_e^{*}{}'' \middle| \bar{p}_e \middle| \Psi_e{}' \right\rangle \left\langle \Psi_s{}'' \middle| \Psi_s{}' \right\rangle \qquad \text{Eq. 2.9}$$

The spin wavefunctions corresponding to different spin values are orthogonal to another; therefore the second integral in Eq. 2.9 vanishes for states of different spin. Photoelectron transitions are thus allowed only between initial and final states of the same total spin, that is, $\Delta S = 0$. In determining the spin of the final state, it is necessary to consider the spin of the positive ion and the photoelectron. This combined spin must be equal to that of the initial molecular state if the transition is to be allowed. Since the photoelectron has half-integral spin, the spins of the molecule and ion must differ after ionization by ±1/2. Hence, for closed-shell molecules with singlet neutral ground states, only doublet ionic states may be accessed, one for each orbital ionized. Many short-lived molecules have only partially filled outer shells, so that ionization from each orbital may yield more than one cationic state.

2.1.2 Vibrational selection rules

The probability of a vibrational transition during the ionization process is proportional to[3]:

$$\left|\overline{M}_v\right|^2 = \left|\left\langle \Psi_v^{*}{''} \middle| \Psi_v{'} \right\rangle\right|^2 \equiv \left|\left\langle \Psi_v^{*}{''} \middle| \Psi_v{}^{+} \right\rangle\right|^2 \qquad \text{Eq. 2.10}$$

where, for the ionization process, $\Psi_v{'} \equiv \Psi_v^{+}$.

This quantity corresponds to the square of the vibrational overlap integral; as mentioned before (Chapter 2.1) it is called the *Franck-Condon Factor* and is largely responsible for the relative intensities of the vibrational bands in photoelectron band. This overlap integral does not vanish by orthogonality because $\Psi_v{}^{+}$ and $\Psi_v{''}$ are vibrational functions belonging to different electronic states. Moreover the intensity of a vibrational band in an electronically allowed transition is proportional to the absolute square of the overlap integral of the vibrational wavefunctions of the initial and final states; hence the transitions are favoured when there is a large overlap between the vibrational wavefunctions.

Potential energy curves are shown in Figure 2.1 for a hypothetical molecule *AB* in its ground state and the corresponding molecular ion AB^+ in two possible ionic states, and the corresponding photoelectron band envelops.

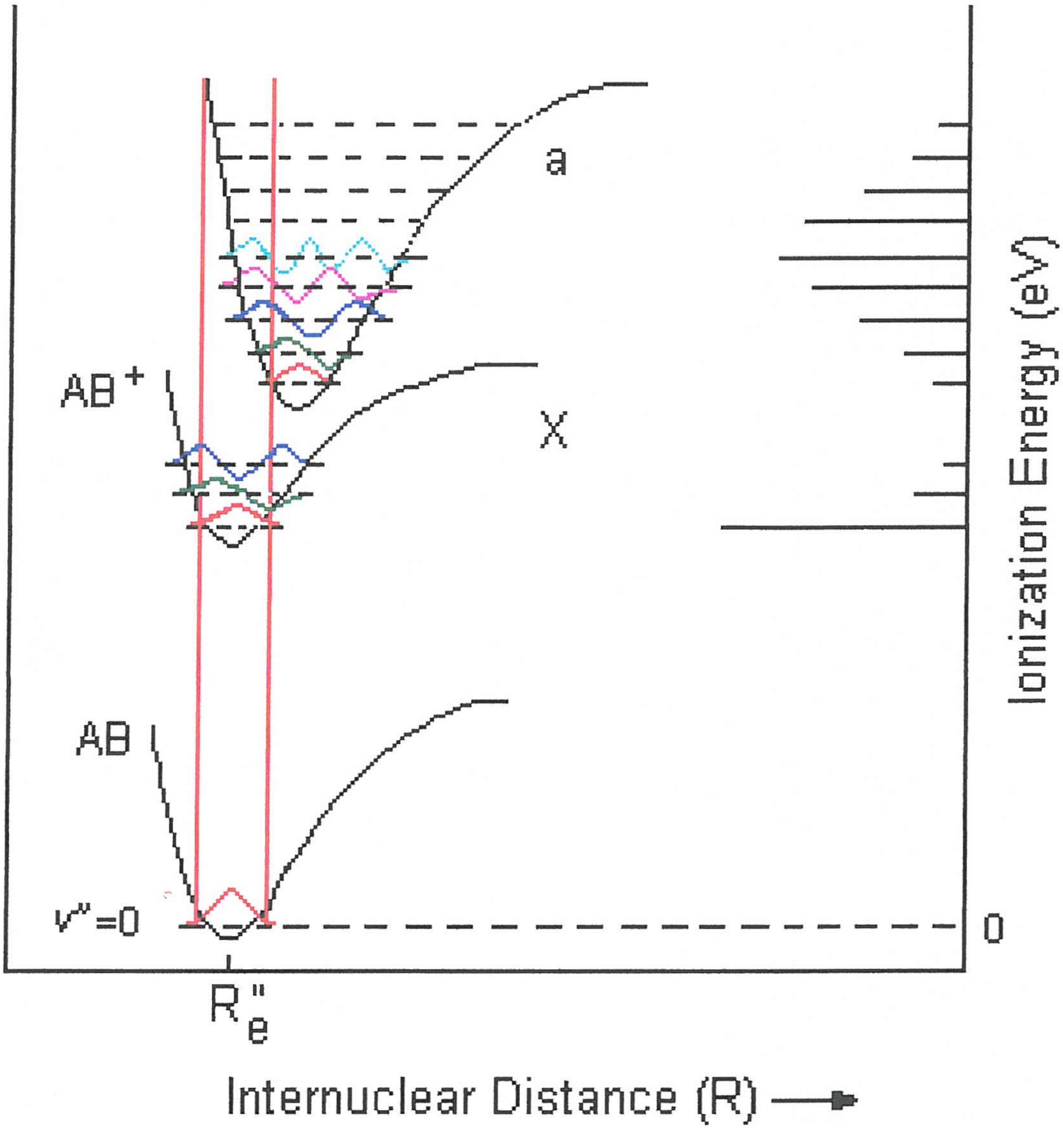

Figure 2.1: Potential energy curves for a molecule AB in its ground state and the corresponding molecular ion AB^+ state in two different ionic states

Both narrow and broad bands are frequently observed in photoelectron spectra, which have led to the definition of two different ionization energies (adiabatic and vertical ionization energies).

The Adiabatic Ionization Energy (AIE)[5] is the energy required to ionize from the lowest vibrational level of a molecule to the lowest vibrational level of an ionic state, as in the process AB^+, $v^+=0 \leftarrow AB$, $v''=0$.

The vertical ionization energy (VIE)[5] is the energy required to ionize from the lowest vibrational level of a molecule to an ionic state vibrational level that gives a maximum value for the overlap integral in Eq. 2.10. In practice, the VIE is measured as the most intense component of a photoelectron band.

The vibrational eigenfunctions drawn in Figure 2.1 are intended to approximate those of an anharmonic oscillator.

The wavefunctions for the v=0 levels are bell-shaped curves whose maxima lie between the classical turning points of the vibrational level. The eigenfunctions of the higher vibrational levels have broad maxima or minima near the classical turning points of the motion. The contributions to the overlap integral from these intermediate maxima and minima will roughly cancel one another.

Considering the $v^+=0 \leftarrow v''=0$ band, the product of the two eigenfunctions for $v''=0$ and $v^+=0$ at each R value, and, therefore, the integral of this product over all R values, is usually greatest when the minima of the two potential curves lie exactly one above the other. As the minima become separated, the overlap between the $v''=0$ and $v^+=0$ eigenfunctions decreases and the intensity of the $v^+=0 \leftarrow v''=0$ band is reduced. When the minima of the two potential curves lie at equal internuclear distances, the overlap integral for the $v^+=0 \leftarrow v''=0$ band is large, but it is obviously small for the $v^+=1 \leftarrow v''=0$ or higher levels since the positive and negative contributions to the integral effectively cancel each other.

The shapes of photoelectron bands can provide useful information concerning the type of electron ejected. Referring to Figure 2.1, the ion has the same nuclear configuration in the ground ionic state, X, as in the molecular ground state. Such a configuration is produced by ejection of a nonbonding electron. The resulting spectrum exhibits a very intense $v^+=0 \leftarrow v''=0$ band followed by a relatively short progression.

Curve *a* represents a potential surface in which R_e is increased from its ground state value. In the corresponding photoelectron band, the *Franck-Condon* maximum appears near the middle of a long vibrational progression.

The energies of vibrational levels in a diatomic molecule may be represented by the anharmonic oscillator expression[5]:

$$\varepsilon_v = \frac{E}{hc} = \left(v + \frac{1}{2}\right)\omega_e - \left(v + \frac{1}{2}\right)^2 \omega_e x_e \qquad \text{Eq. 2.11}$$

where v is the vibrational quantum number of the vibrational levels in the ionic state, ω_e is a vibrational constant (normally it has units of cm^{-1}) and x_e is an anharmonicity constant.

If the vibrational structure in a PE band is resolved, this can yield further information on the associated ionic state. The spacings, ΔG, between successive vibrational components can be expressed as[5]:

$$\Delta G = \omega_e - 2\omega_e x_e (v+1) \qquad \text{Eq. 2.12}$$

If an electron is ejected from a nonbonding orbital, the bond strengths of the molecule and ion will be altered very little. Hence, ionization from a nonbonding molecular orbital tends to leave the internuclear separation in the ion, R_e^+, essentially the same as that in the initial neutral state; similarly ω_e^+ should be similar to ω_e''. For such a case a narrow PE band would be expected with the $v^+=0 \leftarrow v''=0$ band as the most intense transition, as shown in Figure 2.1, case X.

When an electron is ejected from a bonding orbital, the bond strength is weakened and the internuclear separation in the corresponding ion is larger than in the neutral parent. Since $R_e^+ > R_e''$ a broad vibrational progression should be observed in the photoelectron band, as shown in Figure 2.1, case *a* with $\omega_e^+ < \omega_e''$.

If the electron ejected is antibonding, R_e^+ will be less than R_e'' and the bond in the ion will be stronger i.e. $\omega_e^+ > \omega_e''$.

Thus, for a diatomic molecule, comparison of measured values of ω_e^+ with the, usually well known, ω_e'' of the ground state, along with a consideration of the shape of the photoelectron band, may allow the bonding nature of the orbital from which ionization occurred to be determined.

2.2 Photoelectron Spectroscopy with a tuneable wavelength radiation source

Above the first ionization threshold there exists a profusion of neutral states, to which photoabsorption may occur when the photon energy coincides with the transition energy from the ground state. Such resonant absorption processes may compete with direct photoionization, and the decay mechanisms of these super-excited states can have a strong effect on the photoionization cross section at resonant photon energies.

Excited neutral states may be classified into two categories, valence and Rydberg state, although the distinctions between the two are often difficult to make (and states of each type may mix with each other).

2.2.1 Valence and Rydberg states

In atomic systems, the valence shell consists of the set of atomic orbitals with the same principal quantum number as that of the highest occupied orbital in the ground state[6]. Therefore in atoms a valence state is one which has an electronic configuration in which no electron is excited to an orbital outside the valence shell. An atomic Rydberg state is obtained when an electron is promoted outside the valence shell. In molecules composed of elements of the same period, such as CO, a molecular valence shell may be defined in the same way, as having an electronic configuration made up of molecular orbitals which are expressed as linear combination of atomic orbitals with principal quantum numbers, corresponding to the valence shell of the atoms. A Rydberg state may also be defined as one whose excitation energy, E_n, obeys the Rydberg formula[6]:

$$E_n = I - \frac{R}{(n-\delta)^2} \qquad \text{Eq. 2.13}$$

where I is the ionization energy of the orbital from which the Rydberg electron was promoted, R is the Rydberg constant, δ is the quantum defect and n is the principal quantum number. Each Rydberg state is a member of a series converging to a particular ionization limit of energy I. This definition is suitable for both atomic and molecular systems. In a molecule, a Rydberg state is considered to be pseudo-atomic, since to an electron in a spatially extensive Rydberg orbital, the molecular core will appear as a point charge, leading to near hydrogenic behaviour. The extent of the departure from hydrogenic (one-electron) behaviour is described by the effective quantum number, n-δ; for δ =0 the Rydberg orbital is exactly described by a hydrogenic atomic orbital, whereas a non-zero value of δ is used to fit the energy levels of a system with more than one electron. The magnitude of the quantum defect reflects the degree of penetration of the Rydberg orbital into the molecular ionic core, which is strongly dependent on the radial distribution function of that orbital, and on the nuclear charges of the atoms from which the molecule is constructed. The radial probability distribution functions of atomic *s* orbitals tend to have fairly large amplitudes close to the nucleus, while those of *p* orbitals have less amplitude at short radius, and *d* orbitals even less[7]. Thus the *s* orbitals experience the highest effective nuclear charge, so the quantum defect for an *ns* Rydberg orbital is high. Quantum defects for *np* and *nd* orbitals are progressively lower as the degree of penetration of those orbitals into the core decreases. In a heavy atom or molecule, the greater nuclear charge tends to make quantum defects larger than in a light system, where the electron-core interactions are weaker.

Typical values of δ for first row atoms (e.g. C, N, O) and second row atoms (e.g. Si, P, S) are[8]:

Table 2.1: Typical values of quantum defect δ for first row and second row atoms

	$\delta(ns)$	$\delta(np)$	$\delta(nd)$
1st Row	1.0	0.5	0.1
2nd Row	2.0	1.5	0.3

Molecular Rydberg orbitals will normally be characteristic of a particular atom in the molecule, so in a diatomic molecule AB, where A and B are from rows 1 and 2 respectively, some Rydberg states may exhibit quantum defects typical of A, and others may have δ values closer to those expected for B.

Every ionic state in an atom or molecule will have Rydberg series converging to it. Since the ionic core interacts only weakly with the Rydberg electron, the core will closely resemble the ionic state that lies at the series limit, and so the spectroscopic constants for a member of the Rydberg series will be similar to those of the ion. The similarity of the Rydberg state core to the ion at the series limit grows as the principal quantum number of the Rydberg orbital increases, so that as the ionization limit is reached there is a seamless transition into the continuum[9]. The quantum defect, δ, in a series also tends towards an asymptotic limit with increasing n. This convergence is a consequence of the nature of high n Rydberg orbitals: as n increases, the average radius of the Rydberg orbital grows rapidly. An electron in a spatially extensive orbital spends much more time at a distance from the core than close to it, and so it interacts less strongly with the core, and the Rydberg state resembles more closely the ion. The average radius of a Rydberg orbital is proportional to $(n-\delta)^2$ [10]: for high values of n the Rydberg molecule can extend over more than 100 Å. Such large molecules have high collisional cross sections and the reactions (mainly charge-transfer) of highly excited Rydberg states have generated considerable interest[11]. Rydberg series are regularly observed in absorption and ionization spectra, and the extrapolation of series limits is an effective way of determining accurate ionization energies.

Transitions to Rydberg states are subject to the electric dipole selection rules for optical absorption. Many of these rules depend upon the particular coupling cases that apply to the states in question; for example most commonly for diatomic molecules the states may be considered under *Hund's case a* or *Hund's case b*, for which the following selection rules are relevant[4]:

I. $\Delta\Lambda=0, \pm 1$
II. $\Delta S=0$
III. $\Sigma^{+} \leftrightarrow \Sigma^{+}$ $\Sigma^{-} \leftrightarrow \Sigma^{-}$ $\Sigma^{+} \nleftrightarrow \Sigma^{-}$
IV. $g \leftrightarrow u$ $g \nleftrightarrow g$ $u \nleftrightarrow u$

It should, however, be noted that Rydberg states are more appropriately described by *Hund's case d* since the shape of the molecule is not transmitted to the excited electron and its rotation is barely noticed.

The overall symmetry of a Rydberg state is determined by the coupling of the angular momenta of the excited electron and the ionic core. In a diatomic molecule the Rydberg orbital may be assigned a principal quantum number n and an azimuthal quantum number l, so that as in an atomic system there are ns, np, nd ... series. The cylindrical form of a diatomic molecule requires that another label, λ, be attached to each orbital, depending on the projection of the orbital angular momentum along the internuclear axis, and this is denoted as σ, π, δ ... symmetry[6] for λ =0, 1, 2 .... Thus examples of Rydberg orbitals are $3s\sigma$, $5p\sigma$, $5p\pi$, $4d\sigma$, $4d\pi$, $4d\delta$ ..., or $nl\lambda$ in general. These subdivisions of the p and d (and higher) orbitals each have a slightly different quantum defect as they do not interact with the cylindrical core in exactly the same manner.

A Rydberg state may thus be described by the ionic core around which it is built, that is the limiting state to which it converges, and the symmetry of the Rydberg orbital. The orbital angular momentum of the Rydberg electron may be determined experimentally, by determination of the quantum defect for a state. This may be used in conjunction with the symmetry of the ionic core to determine the symmetry of the Rydberg state.

In cases where a band is sufficiently well resolved to obtain rotational structure in the upper state, and thus derive the symmetry of that state, it is possible to determine the symmetry of the ion at the series limit, which may also be unknown.

In the present study such a potential case was found for the OH and OD work (see Chapter 6).

2.2.2 Decay mechanisms

The interaction of a vacuum ultraviolet photon with a molecule may lead to the direct production of continuum states (dissociation or ionization), or absorption to a discrete state, often a Rydberg state. Once an electron has been promoted to a Rydberg orbital, the excited neutral state will decay by one of several mechanisms[12].

For a diatomic molecule *AB*, in the absence of any collisions, these mechanisms are:

I. Re-radiation: $AB+h\nu \rightarrow AB^{*} \rightarrow AB+h\nu$
II. Predissociation $AB+h\nu \rightarrow AB^{*} \rightarrow A+B$
III. Ion pair formation $AB+h\nu \rightarrow AB^{*} \rightarrow A^{+}+B^{-}$
IV. Autoionization $AB+h\nu \rightarrow AB^{*} \rightarrow AB^{+}+e^{-}$

Fluorescent re-radiation is known to occur from Rydberg states, but will normally only take place if the other decay channels are unavailable. The radiative lifetime of an excited state of a diatomic molecule is typically of the order of 10^{-8} sec [4], while autoionization and predisssociation are frequently observed to be more rapid than one vibrational period, which is of the order of 10^{-13} sec. Hence, fluorescent decay is not usually competitive with the other decay processes.

Mechanisms II., III. and IV. are only viable if the excited state lies above the threshold for formation of their respective products.

Predissociation arises from the interaction of the bound state AB^{*} with an unbound one, resulting in a radiationless transition to the repulsive state and the fragmentation of the molecule. This tends to take place over a fairly narrow energy range, in the region where the two potential curves intersect[4], and need not affect all levels of AB^{*}.

Ion pair formation is a special case of predissociation, in which two ionic products are formed[13]. No photoelectron is emitted in this mechanism, so that PE spectra should be unaffected by ion pair formation.

Autoionization is another radiationless transition, one that occurs when the excited neutral state interacts with an ionization continuum that exists at the same energy. The transition occurs by the loss of an electron, and this can have a profound effect on the overall ionization process. There are four possible types of autoionization mechanism: rotational, vibrational, spin-orbit and electronic[14]. When a Rydberg state lies above the threshold for ionization to the particular ionic state due to rotational or vibrational excitation in the core, rotational and vibrational autoionization may occur. The Rydberg state may autoionize by transfer of vibrational energy from the core to the excited electron, which then leaves. This vibrational autoionization requires a strong interaction between the core and the Rydberg electron, and also involves a breakdown of the Born-Oppenheimer approximation, since nuclear and electronic motions are correlated in this mechanism. Studies of vibrational autoionization have revealed that the process favours the minimum possible change in vibrational quantum number, usually $\Delta v = -1$ [14,15]. Since the separation between consecutive vibrational levels in the ion is relatively small, only Rydberg states of high n that converge to the upper v^+ level will lie above the lower v^+ level. Since the probability of absorption to Rydberg states is approximately a function of $(n-\delta)^{-3}$, excitation to, and thus autoionization from these states is weak; hence vibrational autoionization is not considered to be an important process in most molecules. The same applies to rotational autoionization. Spin-orbit autoionization is only observable where the spin orbit coupling constant in the limiting ionic core is large. Electronic autoionization involves a transition from a Rydberg state built upon one (excited) ionic state interacting with a continuum corresponding to a lower one[16]. Rydberg states based upon the ground ionic state cannot autoionize electronically. Electronic autoionization is a result of interactions between the Rydberg state and the continuum, and may be visualised in one of two ways. Either the excited core relaxes to a lower energy configuration, and the energy so released is transferred to the Rydberg electron, or the Rydberg electron returns to its original orbital and the excess energy is used to eject another electron, again leaving the ion in the less excited state. Either way, it is a two electron process, requiring the close approach of the Rydberg electron to the core; only electronic motions are involved, so the Born-Oppenheimer approximation still holds. Electronic autoionization is found to be the dominant autoionization process in most diatomic molecules, where there are sufficient excited ionic states to yield fairly high densities of Rydberg states for several eV above the first ionization threshold.

A photoionization efficiency spectrum, recorded by measuring the total ion yield as a function of the photon energy, will show structure arising from the two competing processes: direct and resonant ionization. The background level in such a spectrum depends mainly on the cross section for direct photoionization, which normally varies slowly and smoothly with photon energy. Superimposed upon this continuous background are discrete structures that correspond to resonant absorption to electronically autoionizing Rydberg states, where the total ionization yield is usually enhanced by decay from these super excited neutral states.

2.2.3 Autoionization resonances

The mixing between discrete states above the first ionization energy and continuum states gives rise to autoionization phenomena. In the photoelectron spectrum they manifest themselves as excursions in the partial and total cross section as well as in the asymmetry parameter. The shape of the line of an autoionizing resonance can be a sharp feature and it can be observed as a decrease, an increase or an asymmetric profile in the cross section. The reason for this is the interference between the amplitudes of the direct and indirect processes resulting in a characteristic Fano profile[9,17] where the cross section can be expressed as:

$$\sigma(E) = \sigma_a \frac{(q+\varepsilon)^2}{1+\varepsilon^2} + \sigma_b \qquad \text{Eq. 2.14}$$

where σ_a and σ_b represent two portions of the cross section which correspond respectively to transitions to states of the continuum that do and do not interact with the discrete autoionizing state. In Eq. 2.14, the reduced energy ε is defined as:

$$\varepsilon = \frac{E - E_r}{\Gamma/2} \qquad \text{Eq. 2.15}$$

where E_r is the resonance energy and Γ is the natural width of the autoionizing state which represents the interaction between the discrete state and the continuum.
The Fano line profile index q may be defined as:

$$q = \sqrt{\frac{2}{\pi \cdot \Gamma}} \frac{\langle \gamma_d | D | \Phi \rangle}{\langle \gamma_i | D | \Phi \rangle} \qquad \text{Eq. 2.16}$$

where γ_d and γ_i are respectively the final state wavefunctions for the direct and indirect ionization process, D is the electric dipole moment operator and Φ is the wavefunction of the initial state. The q parameter characterizes the line profile: neglecting the background cross section, the resonance has a maximum at $\varepsilon_{max}=1/q$ and is zero at $\varepsilon_0=-q$. The sign of q thus determines whether the maximum occurs before or after the minimum. In Figure 2.2 typical Fano profiles are shown as a function of ε for five different values of q. The magnitude of q indicates the relative probabilities of the transition to the Rydberg state and direct ionization.

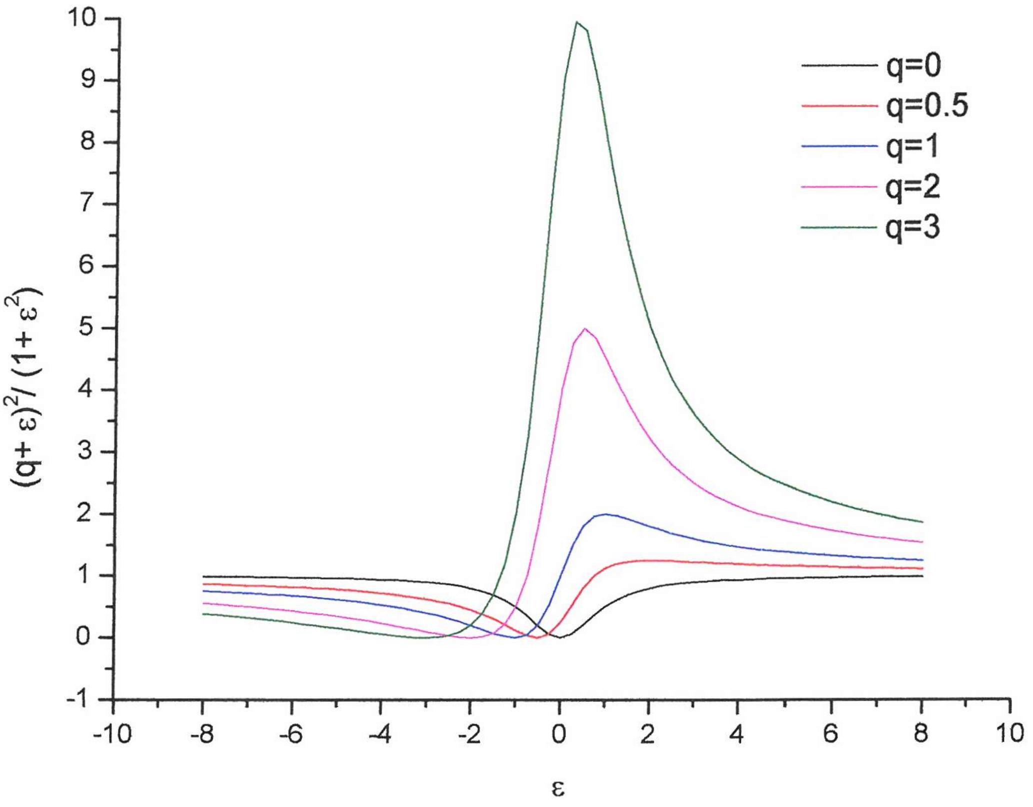

Figure 2.2: Typical Fano profiles as function of ε for five different values of q

Another parameterization of Eq. 2.14 is frequently used by defining a correlation index ρ^2 and a cross section for photon energies outside of the resonance region $\sigma_c=\sigma_a+\sigma_b$ as:

$$\rho^2 = \frac{\sigma_a}{\sigma_a+\sigma_b} \qquad \text{Eq. 2.17}$$

Eq. 2.14 can then be rewritten as:

$$\sigma(E)=\sigma_c\left[\frac{(q+\varepsilon)^2}{1+\varepsilon^2}\rho^2+\left(1-\rho^2\right)\right] \qquad \text{Eq. 2.18}$$

An autoionizing resonant state may have a strong effect on a spectrum, with positive or negative features observed. These features may be observed in photoionization, photoabsorption or photodissociation spectra, and in measurements of the angular distribution parameter. It has been shown that it is possible to use Fano's theory to fit experimental line shapes and determine values of q, ρ^2 and Γ for single resonant states[17] and entire Rydberg series[9]. In the present thesis such a study was performed for the N atom work (see Chapter 7).

2.2.4 The Franck-Condon Factor in autoionization

The radiation used in PES is of sufficiently high energy to excite electrons to discrete neutral states which are above the ionization threshold. If an atom or molecule is excited to such a state, autoionizing transitions can take place from the discrete state to the ionization continuum. This process is observed in PES as irregularities in the intensities of members of a vibrational progression and broadening of vibrational bands due to the relatively short lifetimes of the autoionizing states (~10^{-14} sec)[4].

Autoionization accompanying photoexcitation can be represented by:

$$AB+h\nu \rightarrow AB^* \rightarrow AB^+ + e^- \qquad \text{Eq. 2.19}$$

where AB^* is the molecule, or atom, in a highly excited state. Highly excited states (Rydberg states) converge to second, third or higher ionization energies. When a molecule is excited by photons whose energy coincides with that of an autoionizing resonance, there is a high probability of exciting the molecule to this autoionizing state with a well defined vibrational quantum number. If the lifetime of this autoionizing state is greater than one vibrational period, then the photoelectron spectrum can be expected to be dependent on the *Franck-Condon Factor* for transitions from the autoionizing state of the neutral molecule to the final state of the ion. In Figure 2.3 the *Franck-Condon Factors* in autoionization are illustrated.

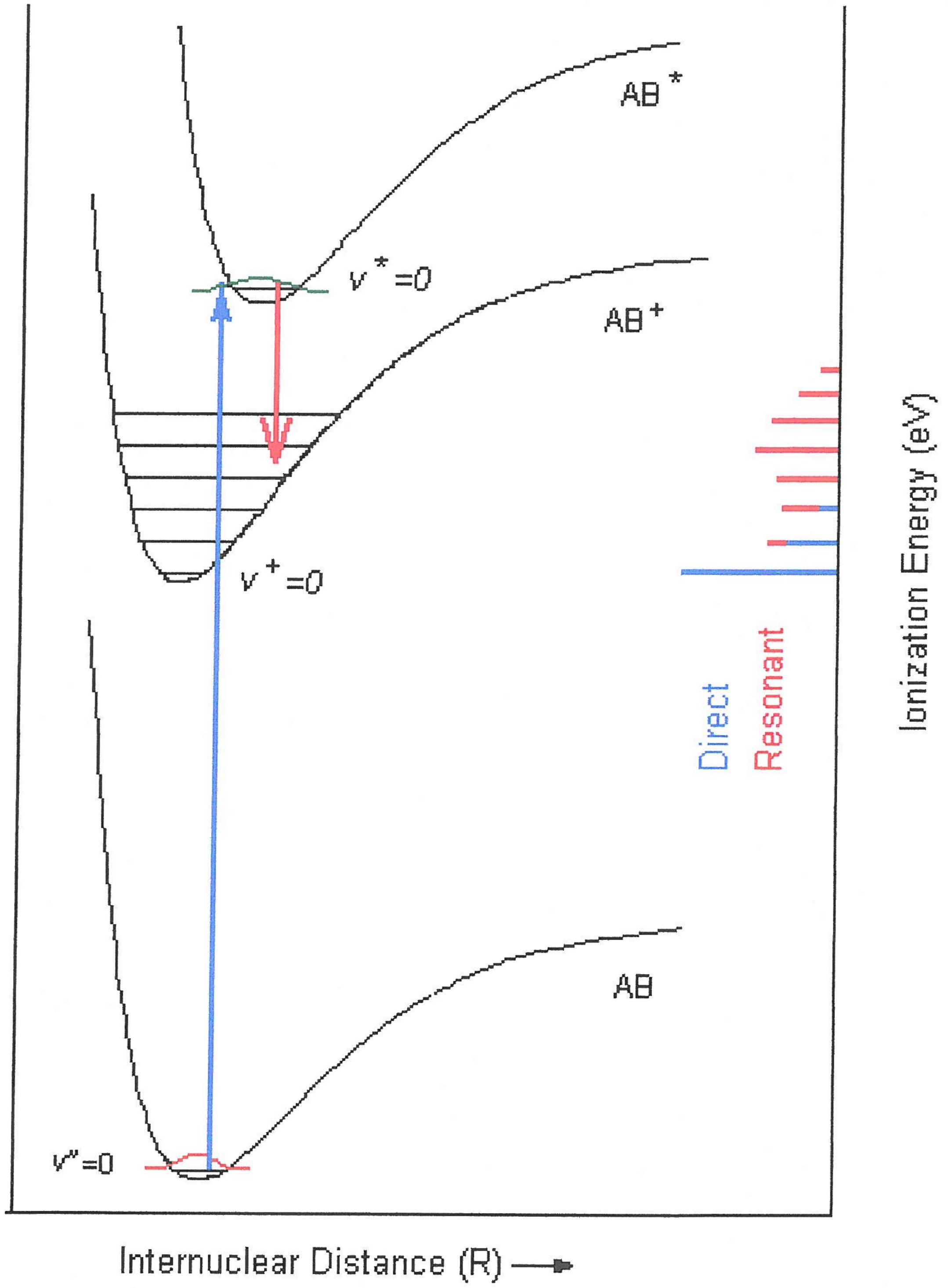

Figure 2.3: The Franck-Condon Factors in autoionization

Direct ionization to AB^+ from AB leads to a narrow photoelectron band, while the autoionizing state AB^* gives a broad contribution to the overall photoelectron spectrum. The selection rules for autoionization[3] are derived from the expression for the radiationless transition probability γ from the autoionizing level Ψ_a to the final state Ψ_f:

$$\gamma = \frac{4\pi^2}{h}\left|\left\langle \Psi_f \middle| \overline{W} \middle| \Psi_a \right\rangle\right|^2 \qquad \text{Eq. 2.20}$$

where $\overline{W}$ is a perturbation function representing certain terms in the Hamiltonian. Since $\overline{W}$ is totally symmetric, it follows that the states Ψ_f and Ψ_a must have common symmetry species in order for the radiationless transition probability to be non zero, that is:

$$\Gamma(\Psi_f) = \Gamma(\Psi_a) \qquad \text{Eq. 2.21}$$

or if the overall wavefunction is separated in the electronic, vibrational and rotational motion the selection rule in Eq. 2.21 becomes:

$$\Gamma(\Psi_e \Psi_v \Psi_\tau)_f = \Gamma(\Psi_e \Psi_v \Psi_\tau)_a \qquad \text{Eq. 2.22}$$

Information about the electronic states responsible for autoionizing resonances can be obtained from a study of photoelectron spectra. The calculation of vibrational intensities in photoelectron spectra perturbed by autoionization has received considerable attention[9,16-18]. When the source line-width $\delta(h\nu)$ is larger than the width of the autoionization line Γ_n, the relative intensities of the vibrational levels in a PE spectrum is given by:

$$I \propto F_{if} + F_{ia} \cdot F_{af} \cdot \frac{\pi \cdot q^2 \Gamma_n}{2 \cdot \delta(h\nu)} \qquad \text{Eq. 2.23}$$

where F_{if} is the *Franck-Condon Factor* for direct ionization from the initial ground molecular state i to the final ionic state f, F_{ia} is the *Franck-Condon Factor* for the transition to the autoionizing level a, F_{af} is the *Franck-Condon Factor* for the transition from the autoionizing level to the final ionic state and q is the Fano line profile index. The assumptions are made that the excited states have the same vibrational constant as the ionic state on which it is built, only one electronic state is populated by the decay of the autoionizing level and only one autoionizing state is involved in the ionizing process[3].

In the work presented in this thesis, excited states are probed by recording constant ionic state (CIS) spectra using Synchrotron Radiation. A CIS spectrum monitors the intensity of a single photoelectron feature as the photon energy is scanned. When the photon energy is coincident with a transition to an autoionizing state, discrete structure can be observed in the CIS spectrum.

2.2.5 Selection rules for autoionization of atoms

For Russell-Saunders coupling[19,20] the selection rules allow only the following transitions:

$\Delta L=0, \pm 1$ ($L=0 \leftarrow / \rightarrow L=0$), $\Delta S=0$, $\Delta J=0, \pm 1$ ($J=0 \leftarrow / \rightarrow J=0$),

$\Delta l = \pm 1$ for the electron moved

In addition to the above selection rules, in the case of an atomic autoionizing state the following rule has to be considered[21]:

no change of parity (Laporte rule)

where *parity* is determined for an atom by summing the l value for all electrons ($\Sigma_i l_i$) and determining whether the value (*parity*) is even or odd.

The complete lack of restriction on the value of l of the free electron often allows finding a continuum state for which the selection rules for L, for S and for J are fulfilled, but the rule for parity cannot always be fulfilled simultaneously. A study in which perturbation occurs, for which the Russell-Saunders coupling scheme is not valid, is presented in Chapter 5 where a comprehensive study of atomic oxygen is presented.

2.2.6 *Photoelectron angular distribution*

Yang[22] has shown that when a photon interacts with an unpolarized atomic or molecular target in the electric dipole approximation, then the angular correlation between the incident photon and any ejected particle is proportional to a linear combination of 1 and $\cos^2\theta$, where θ measures the ejection angle of the outgoing particle, typically an electron, with respect to the polarization vector of the incident photon. The upper limit of two on the powers of $\cos\theta$ that determine the angular distribution is fixed by the orbital angular momentum of unity imparted to the target by the absorbed photon in the electric dipole approximation. The angular distribution has no term linear in $\cos\theta$ since parity is conserved in a photoabsorption process.

In general the differential cross section for photoionization of an unpolarized target by incident linearly polarized radiation in the electric dipole approximation may be written as[23]:

$$\left[\frac{d\sigma}{d\Omega}\right]_{lin.pol.} = \frac{\sigma}{4\pi}\left[1+\beta P_2(\cos\theta)\right] \qquad \text{Eq. 2.24}$$

where σ is the total photoionization cross section, β is the asymmetry parameter,

$$P_2(\cos\theta) \equiv \frac{1}{2}\left(3\cos^2\theta - 1\right) \qquad \text{Eq. 2.25}$$

and θ is measured with respect to the polarization vector of the incident radiation. It is possible to see from Eq. 2.24 that the angular distribution is determined completely by the asymmetry parameter β, which comprises all of the dynamical information relevant to the angular distribution. The total cross section σ determines the overall intensity of the process; the requirement that $d\sigma/d\Omega$ be positive for all values of θ limits the magnitude of β to the range $-1 \le \beta \le 2$.

Angular momentum and parity conservation laws are then used to deduce those cases in which the β parameter assumes an analytically known constant value in the electric dipole, Russell-Saunders coupling approximation[19].

If an atom A is considered initially in a state defined in the Russell-Saunders coupling approximation, the orbital angular momentum, spin angular momentum, total angular momentum, and parity quantum numbers will be $\bar{L}_0$, $\bar{S}_0$, $\bar{J}_0$ and π_0 respectively. Consider a low-energy photoionization process ($h\nu < 100$ eV) for which the electric dipole approximation is good and the incident photon, $h\nu$, can be considered to impart an angular momentum $j_{h\nu} = 1$ and parity $\pi_{h\nu}$=-1 to the atom. The final state of the ion A^+ is specified by $\bar{L}_c$, $\bar{S}_c$, $\bar{J}_c$ and π_c and the photoelectron is specified by $\bar{l}$, $\bar{s}$, $\bar{j}$, π_e=$(-1)^l$. This general process can be written schematically as[24]:

$$A(\bar{L}_0,\bar{S}_0,\bar{J}_0,\pi_0)+h\nu(j_{h\nu}=1,\pi_{h\nu}=-1)\rightarrow A^+(\bar{L}_c,\bar{S}_c,\bar{J}_c,\pi_c)+e^-(\bar{l},\bar{s},\bar{j},\pi_e=(-1)^l) \qquad \text{Eq. 2.26}$$

The differential cross section for this photoionization process can be separated into contributions characterized by alternative magnitudes of the angular momentum transfer, defined by[24]:

$$\bar{j}_t \equiv \bar{j}_{h\nu} - \bar{l} = \bar{J}_c + \bar{s} - \bar{J}_0 \qquad \text{Eq. 2.27}$$

provided no measurement is made of either the photoelectron spin or the orientation of the residual ion. In Russell-Saunders coupling, spin angular momentum and orbital angular momentum are separately conserved. The angular momentum imparted by the photon affects only the orbital angular momentum of the system, thus: $\bar{S}_0 = \bar{S}_c + \bar{s}$ and $\bar{L}_0 + \bar{j}_{h\nu} = \bar{L}_c + \bar{l}$

These equations restrict the general Eq. 2.27 to the following Russell-Saunders coupling expression:

$$\bar{j}_t \equiv \bar{j}_{h\nu} - \bar{l} = \bar{L}_c - \bar{L}_0 \qquad \text{Eq. 2.28}$$

The constraints of parity conservation must also be considered:

$$\pi_0 \times \pi_{h\nu} = \pi_c \times \pi_e \qquad \text{Eq. 2.29}$$

which in the electric dipole approximation reduces to:

$$\pi_0 \pi_c = (-1)^{l+1} \qquad \text{Eq. 2.30}$$

In the electric dipole approximation, then, the allowed values of the angular momentum transfer $\bar{j}_t$ are determined in general by Eq. 2.27 and Eq. 2.30 and are determined in the Russell-Saunders coupling approximation by Eq. 2.28 and Eq. 2.30. In either case, once the allowed values of $\bar{j}_t$ have been determined, the asymmetry parameter β may be represented as the following weighted average[25-27]:

$$\beta = \frac{\Sigma_{j_t}\sigma(j_t)\beta(j_t)}{\Sigma_{j_t}\sigma(j_t)} \qquad \text{Eq. 2.31}$$

where the sum extends over all allowed values of j_t, and $\beta(j_t)$ and $\sigma(j_t)$ are the asymmetry parameter and the partial photoionization cross section characteristic of a given value of $\bar{j}_t$. When $\bar{j}_t$ is "parity favoured", $\pi_0\pi_c = (-1)^{j_t}$ and $\beta(j_t)$ and $\sigma(j_t)$ may be written in terms of certain scattering amplitudes $S_l(j_t)$ as follows[25-27]:

$$\beta_{fav}(j_t) = \frac{(j_t+2)|S_+(j_t)|^2 + (j_t-1)|S_-(j_t)|^2 - 3\sqrt{j_t(j_t+1)}\left[S_+(j_t)S_-^+(j_t)\right]}{(2j_t+1)(\ |S_+(j_t)|^2 + |S_-(j_t)|^2\ )} \qquad \text{Eq. 2.32}$$

$$\sigma_{fav}(j_t) = \frac{2j_t+1}{2L_0+1}[\ |S_+(j_t)|^2 + |S_-(j_t)|^2\ ] \qquad \text{Eq. 2.33}$$

where the subscripts ± or 0 on the amplitudes $S_l(j_t)$ indicate that the photoelectron orbital angular momentum $\bar{l}$ has the value $j_t \pm 1$ or j_t respectively[24].

When $\bar{j}_t$ is "parity unfavoured", $\pi_0\pi_c = (-1)^{j_t+1}$ and $\beta(j_t)$ and $\sigma(j_t)$ assume a particularly simple form[26]:

$$\beta_{unfav}(j_t) = -1 \qquad \text{Eq. 2.34}$$

$$\sigma_{unfav}(j_t) = \frac{2j_t+1}{2L_0+1}|S_0(j_t)|^2 \qquad \text{Eq. 2.35}$$

The angular momentum transfer theory expression for the asymmetry parameter β given in Eq. 2.31 is, in general, energy dependent due to the energy dependence of the scattering amplitudes $S_l(j_t)$[24], in terms of which both the cross sections $\sigma(j_t)$ and asymmetry parameters $\beta(j_t)$ are defined. Since β is defined in terms of a ratio of energy-dependent factors, the possibility exists that the energy dependence may cancel, leaving an analytically determined constant value for β. A necessary condition for this to occur is that only a single value of $\bar{j}_t$ contributes to the process under study. In general there are always at least two values of $\bar{j}_t$. In Russell-Saunders coupling, however, Eq. 2.28 implies that $\bar{j}_t$ will be *restricted to a single value* when either $\bar{L}_c$ or $\bar{L}_0$ is zero, in which case $\bar{j}_t$ will have the value of the other one of this pair. When only a single value of $\bar{j}_t$ is permitted, then the cross sections in Eq. 2.31 cancel, giving for the asymmetry parameter the expression:

$$\beta = \beta(j_t) \qquad \text{Eq. 2.36}$$

For an unfavoured value of $\bar{j}_t$, β=-1 and hence the angular distribution is energy independent. For a favoured value of $\bar{j}_t$ in general β is energy dependent. This energy dependence arises since the photoelectron orbital angular momentum can usually have two allowed values, $l = j_t \pm 1$, in favoured photoionization processes. The interference between the scattering amplitudes $S_l(j_t)$ for these two values of $\bar{l}$ causes $\beta(j_t)$ to vary with energy. In the special case of j_t=0, however, $\bar{l}$ has only the single value +1, due to angular momentum conservation, in which case Eq. 2.32 shows that $\beta(j_t{=}0){=}{+}2$. In all other cases in which only a single value of $\bar{j}_t$ contributes to a particular photoionization process, $\beta(j_t)$ is energy dependent.

When the photoelectron angular distribution is predicted to be energy dependent in Russell-Saunders coupling, then the evaluations of $\beta(j_t)$ and $\sigma(j_t)$ may be carried out in terms of the scattering amplitudes $S_l(j_t)$ for the photoionization process in Eq. 2.26. The scattering amplitudes $S_l(j_t)$ may be expressed in the Russell-Saunders coupling approximation in terms of reduced dipole matrix elements as follows[28]:

$$S_l(j_t) = \sqrt{\frac{4}{3.}\frac{\pi}{c}h\nu} \cdot i^l e^{-i\sigma_l} \Sigma_L \sqrt{2L+1} \begin{Bmatrix} L_c & l & L \\ 1 & L_0 & j_t \end{Bmatrix} \left\langle L_0 S_0 E_0 \middle\| \Sigma_{j=1}^{N} r_j \middle\| \Psi^{-}_{L_c S_c lLE} \right\rangle \qquad \text{Eq. 2.37}$$

where the initial state is indicated by its energy E_0 and term level L_0S_0, and the energy normalized channel function $\Psi^{-}_{L_c S_c lLE}$ describes the N-particle final state of energy $E=E_0+h\nu$. The phase factors $i^l e^{-i\sigma_l}$, where σ_l is the Coulomb phase shift, and the minus sign on the final state wavefunction, indicate that incoming wave boundary conditions have been imposed on the final state: namely at large separation, $r\rightarrow\infty$, where r is the photoelectron radial coordinate, the photoelectron has angular momentum $\bar{l}$, the core has $\bar{L}_c$, and the two are coupled to form the total angular momentum $\bar{L}$. For smaller separations r between the photoelectron and the ionic core, $\Psi^-_{L_cS_clLE}$ represents a multichannel wavefunction, having non-zero components in all allowed final state channels having the same total orbital and spin angular momentum $\bar{L}$ and $\bar{S}_0$. The initial state correspondingly is described by a multiconfiguration wavefunction, all of whose components have the same total orbital and spin angular momentum $\bar{L}_0$ and $\bar{S}_0$. In general, the reduced dipole amplitude in Eq. 2.37 contains contributions from all open and closed channels which may be populated from the ground state and which are then scattered by electron-electron interactions into the final state. When such interchannel scattering is not treated, when the initial state is represented by a single configuration rather than by a multiconfiguration wavefunction, and when the multiple structure of the photoionization transition is ignored, as is done in the central-potential model approximation[29,30], Eq. 2.37 reduces to the central-potential model in the limit of isotropic electron-ion interactions:

$$S_l(j_t) \propto \delta(j_t, l_0) \cdot i^l e^{-i\sigma_l} (-1)^{l_0 - l_{\max}} \sqrt{l_{\max}} (2l_0+1)^{-1} e^{-i\delta_{\varepsilon l}} R_{\varepsilon l} \qquad \text{Eq. 2.38}$$

where $\delta_{\varepsilon l}$ is the photoelectron's phase shift and $R_{\varepsilon l}$ is the radial dipole integral. Substituting Eq. 2.38 in Eq. 2.32 gives the Cooper-Zare result[23]:

$$\beta = \frac{l_0(l_0-1)R^2_{l_0-1} + (l_0+1)(l_0+2)R^2_{l_0+1} - 6l_0(l_0+1)R_{l_0-1}R_{l_0+1}\cos(\sigma_{l_0+1}+\delta_{l_0+1}-\sigma_{l_0-1}-\delta_{l_0-1})}{(2l_0+1)\cdot(\ l_0R^2_{l_0-1} + (l_0+1)R^2_{l_0+1}\ )}$$

Eq. 2.39

where the explicit dependence of the phase shift and radial dipole matrix elements on energy ε has been omitted for simplicity.

Using Eq. 2.39 it is possible calculate the β values for some atomic ionizations, summarized in Table 2.2.

Table 2.2: Calculated β values for the some atomic ionizations

Transition	β value
$s \rightarrow p$	β=2
$p \rightarrow s$	β=0
$p \rightarrow d$	β=1
$d \rightarrow p$	β=0.2
$d \rightarrow f$	β=0.8

Analogous behaviour is observed in molecules: if a molecular orbital is composed primarily of atomic *s* orbitals, β will be large and the outgoing electron wave will have predominately *p* character[5].

From an experimental point of view the β parameter can be evaluated applying Eq. 2.24 expressed as:

$$\frac{d\sigma}{d\theta} = \frac{\sigma}{4\pi}\left[1 + \frac{\beta}{4}(3P\cos 2\theta + 1)\right] \qquad \text{Eq. 2.40}$$

to the intensities measured at θ=0°

$$I_0 = \frac{\sigma}{4\pi}(1 + \beta) \qquad \text{Eq. 2.41}$$

and θ=60°

$$I_{60} = \frac{\sigma}{4\pi}\left(\frac{8 - \beta}{8}\right) \qquad \text{Eq. 2.42}$$

with linearly polarized radiation (P =1) and calculating the ratio R:

$$R = \frac{I_0}{I_{60}} = \frac{(1 + \beta)}{\left(\frac{8 - \beta}{8}\right)} \Rightarrow \beta = \frac{8(R - 1)}{R + 8} \qquad \text{Eq. 2.43}$$

or instead of recording spectra at $\theta = 60°$, measuring the intensity at $\theta = 54° 44'$ (in this case the measured intensity is proportional to the total photoionization cross section and independent by β)

$$I_{54°44'} = \frac{\sigma}{4\pi} \qquad \text{Eq. 2.44}$$

with linearly polarized radiation ($P = 1$) and calculating the ratio R:

$$R = \frac{I_0}{I_{54°44'}} = (1 + \beta) \Rightarrow \beta = R - 1 \qquad \text{Eq. 2.45}$$

By recording spectra at two or more angles, θ, it is possible to measure the β values, obtaining further information about the photoionization process, mainly concerning the character of the initial orbital and the nature of the free electron wavefunction.

2.3 Conclusions

In this Chapter a review of the fundamental principles related to photoelectron spectroscopy is presented. PES with a fixed wavelength radiation source and PES with a tuneable wavelength radiation source are considered from a fundamental point of view.

The basic relations governing the photoionization process have been outlined and have been applied to the analysis of the results obtained in this thesis in Chapter 5 to Chapter 8.

2.4 References

[1] H. Hertz
Annalen der Physik **31**, 983 (1887)

[2] A. Einstein
Annalen der Physik **17**, 132 (1905)

[3] J. W. Rabalais
Principles of Ultraviolet Photoelectron Spectroscopy
Wiley & Sons, New York, 1977

[4] H. Herzberg
Molecular Spectra and Molecular Structure
D. van Nostrand Company Inc., New York, 1966, Vol. III

[5] J. H. D. Eland
Photoelectron Spectroscopy
Butterworths&Co, Oxford, 1984

[6] A. B. F. Duncan
Rydberg series in atoms and molecules
Academic Press, New York, 1971

[7] M. B. Robin
Higher Excited State of Polyatomic Molecules
Academic Press, New York, 1974

[8] C. E. Moore
Atomic Energy Levels
National Bureau of Standards, Washington, 1949

[9] U. Fano and J. W. Cooper
Physics Review **137**, 1364 (1965)

[10] J. Berkowitz
Photoabsorption, Photoionization and Photoelectron Spectroscopy
Academic Press, New York, 1979

[11] F. B. Dunning and R. F. Stebbings
Rydberg States of Atoms and Molecules
Cambridge University Press, Cambridge, 1983

[12] P. M. Guyon and I. Nenner
Applied Optics **19**, 4068 (1980)

[13] K. P. Lawley and R. J. Donovan
Journal of The Chemical Society Faraday Transactions 2 **89**, 1885 (1993)

[14] R. S. Berry
Journal of Chemical Physics **45**, 1228 (1966)

[15] J. Berkowitz and W. A. Chupka
Journal of Chemical Physics **51**, 2341 (1969)

[16] A. L. Smith
Journal of Quantitative Spectroscopy and Radiative Transfer **10**, 1129 (1970)

[17] U. Fano
Physics Review **124**, 1866 (1961)

[18] F. H. Mies
Physics Review **175**, 164 (1968)

[19] H. N. Russell and F. A. Saunders
Astrophysic Journal **61**, 38 (1925)

[20] J. M. Hollas
Modern Spectroscopy
Wiley & Sons, Chichester, 1996

[21] H. G. Kuhn
Atomic Spectra
Longmans, London, 1964

[22] C. N. Yang
Physics Review **74**, 764 (1948)

[23] J. Cooper and R. N. Zare
Lectures in Theoretical Physics
edited by S. Geltman, K.T. Mahanthappa and W.E. Brittin, New York, 1967, Vol. XI-C

[24] V. Schmidt
Electron Spectrometry of Atoms using Synchrotron Radiation
Cambridge University Press, New York, 1997

[25] U. Fano and D. Dill
Physics Review A **6**, 185 (1972)

[26] D. Dill and U. Fano
Physics Review Letters **29**, 1203 (1972)

[27] D. Dill
Physics Review A **7**, 1976 (1973)

[28] A. F. Starace
Handbook der Physik
edited by W. Melhorn, Berlin, 1982, Vol. 31

[29] D. Dill, S. T. Manson and A. F. Starace
Physics Review Letters **32**, 971 (1974)

[30] D. Dill, A. F. Starace and S. T. Manson
Physics Review A **11**, 1596 (1975)

Chapter 3

3 SYNCHROTRON RADIATION

Synchrotron Radiation has a number of special characteristics which make electron synchrotron and storage ring sources powerful as research instruments and as facilities for technological applications. Synchrotron Radiation has a continuous spectrum ranging from infrared to X-ray wavelengths, it is highly intense and it is strongly polarized. A single storage ring can provide a considerable number of ports at which equipment for utilizing photon beams may be installed. The properties of a Synchrotron Radiation beam depend both on the emission process itself and on the electron optics of the storage ring or accelerator from which the radiation is obtained.

3.1 The Synchrotron Radiation

Natural Synchrotron Radiation from charged particles spiralling around magnetic field lines in space is as old as the stars, for example the light that is seen from the Crab Nebula[1] arises from this source.

Synchrotron Radiation and its use as a scientific tool have an interesting history. The prediction of the phenomenon, the search for this new kind of radiation, its discovery and the notion of its potential usefulness are indeed an interesting case history. The phenomenon that an electron in a circular trajectory would radiate was predicted in a pre-quantum and a pre-relativistic language almost 100 years ago. At that time, it was well known from classical electrodynamics that accelerated charged particles radiate. In 1897 Larmor[2] gave an expression for the instantaneous total power radiated by a single, nonrelativistic electron as:

$$P = \frac{2}{3}\frac{e^2}{c^2}\frac{dv^2}{dt} = \frac{2}{3}\frac{e^2}{m^2c^3}\frac{dp^2}{dt} \qquad \text{Eq. 3.1}$$

where e is the charge on the electron, c is the velocity of light, v and p are the velocity and momentum of the charged particle, respectively, and m is its rest mass. In 1898, Lienard[3] published an extension of Larmor's formula for the rate of radiation from the centripetal acceleration of an electron in a circular trajectory. Schott[4] further developed the classical theory in connection with early models of the atom and in an attempt to describe the discrete nature of atomic spectra. As is well known, the Bohr model of the atom described the regularities in atomic spectra elegantly and the results of Schott's work were forgotten for a long time. No attempts were made to verify experimentally the conclusions of the classical theory and for more than 30 years radiation from an accelerated charge was mentioned only in textbooks.

After this early work, quite some time elapsed without noticeable progress until, in the 1940's, the subject of radiation from relativistic electrons received new attention in university and industrial laboratories, when the building of multimillion volt accelerators began and the classical radiation loss of accelerated electrons was again investigated.

3.1.1 The usable Synchrotron Radiation

Short-wavelength Synchrotron Radiation generated by relativistic electrons in circular accelerators is only a half-century old. The first observation[5], since it was visible radiation that was seen, came at the General Electric Research Laboratory in Schenectady, New York, on April 24, 1947. In the 55 years since, Synchrotron Radiation has become a premier research tool for the study of matter in all its forms, as facilities around the world constantly evolved to provide this radiation in ever more useful forms.

3.2 Discovery and Development of Synchrotron Radiation

In 1945, the *synchrotron* was proposed as the latest accelerator for high-energy physics, designed to push particles, in this case electrons, to higher energies than a *cyclotron*, the particle accelerator of those days.

An accelerator takes stationary charged particles, such as electrons, protons and positrons, and drives them to velocities near the speed of light.

The General Electric (GE) Laboratory in Schenectady built the world's second synchrotron, and it was with this machine in 1947 that Synchrotron Radiation was first observed. The optical radiation from the electron beam was first seen on April the 24th 1947[5]. On that April day Robert Langmuir and Herbert Pollock were running the machine and were trying to push the electron gun and its associated pulse transformer to the limit. Some intermittent sparking had occurred, and the technician Floyd Haber was asked to observe this effect with a mirror around the protective wall which separated the machine from the control room. He signalled to turn off the synchrotron as "he saw an arc in the tube". Pollock recorded these observations in his laboratory notebook[5], noting that the beam was stable and of small cross section (approximately 1 mm square).

In May 1947, Elder, Gurewitsch, Langmuir and Pollok published a letter[6,7] in which they reported their visual observation of Synchrotron Radiation. In this letter the polarization properties were also noted.

For high-energy physicists performing experiments at an electron accelerator, Synchrotron Radiation is a nuisance which causes a loss of particle energy. However, condensed-matter physicists realized that this was exactly what was needed to investigate electrons surrounding the atomic nucleus and the position of atoms in molecules.

3.2.1 The first generation: parasitic operation

Under Codling and Madden[8], measurements began in the early 1960s at the new NBS facility in Washington (Synchrotron Ultraviolet Radiation Facility or SURF) to determine the potential of Synchrotron Radiation as a source for spectroscopy in the ultraviolet (the wavelength for peak radiated power per unit wavelength was 335 Å with this synchrotron). Absorption spectra of noble gases revealed a large number of previously unobserved resonances due to inner-shell and two-electron excitations, including doubly excited helium, which remains today a prime test bed for studying electron- electron correlation. These findings further stimulated the growing interest in Synchrotron Radiation. Establishment of SURF began the first generation of Synchrotron Radiation facilities, sometimes also called parasitic facilities because the accelerators were built and usually operated primarily for high-energy or nuclear physics. However, the NBS synchrotron had outlived its usefulness for nuclear physics and was no longer used for this purpose.

If SURF headed the first generation, it was not by much, as activity was also blossoming in both Europe and Asia. At the Frascati laboratory (Rome) in 1962, researchers began measuring absorption in thin metal films using a 1.15 GeV synchrotron[9]. In the same period scientists in Tokyo formed the INS-SOR (Institute for Nuclear Studies-Synchrotron Orbital Radiation) group and by 1965 were making measurements of soft X-ray absorption spectra of solids using radiation from a 750 MeV synchrotron[10,11]. The trend toward higher energy and shorter wavelengths took a big leap with the use of the 6 GeV Deutsches Elektronen-Synchrotron (DESY) in Hamburg, which began operating for both high-energy physics and Synchrotron Radiation in 1964. With Synchrotron Radiation available at wavelengths in the X-ray region down to 0.1 Å, experimenters at DESY were able to begin absorption measurements of solids, notably metals and alkali halides, and of photoemission in aluminium[12].

3.2.2 *The first generation storage rings*

While the number of synchrotrons was growing, the next major advance was the development of electron storage rings, the basis for all of today's synchrotron sources. Around 1970, Tantalus in Stoughton, Wisconsin, a 240 MeV storage ring, originally planned and operated in the 1960s as a test facility for the advanced accelerators concept, but later operated exclusively for Synchrotron Radiation work, came into full operation[13-15]. The first spectrum was measured in 1968. In subsequent years, improvements enabled Tantalus to reach its peak performance, add a full complement of ten beamlines with monochromators, and become in many respects a model for today's multi-user Synchrotron Radiation Facilities.

3.2.3 The second generation storage rings

The larger storage rings mentioned above were electron-positron colliding-beam machines that were operated to provide the highest possible collision rates without blowing up the beams, a condition that generally meant low beam currents. Under these conditions, parasitic operation meant a severely limited output of synchrotron radiation, thereby motivating a clamour for storage rings designed for and dedicated to the production of Synchrotron Radiation.

The Synchrotron Radiation Source[16] (SRS) at the Daresbury Laboratory in the UK was the first fruit of this movement. Synchrotron Radiation research had begun at Daresbury around 1970[17]. Elsewhere, some of the first generation facilities gradually evolved toward second generation status by means of upgrades and agreements with laboratory managements to dedicate a fraction and sometimes all of the yearly machine operations to Synchrotron Radiation, as the high-energy physics frontier advanced. All of these second generation facilities provide fine examples of the productivity of a dedicated source of Synchrotron Radiation. For example, over the years, the SRS at Daresbury has grown to about 40 experimental stations serving around 4000 users from physics and biology to engineering[17].

3.2.4 The third generation storage rings

Even before the second generation facilities were in full use, synchrotron users recognized that a new generation of storage rings with a still lower emittance and long straight sections for undulators would permit achieving even higher brightness and with it, a considerable degree of spatial coherence.

Third generation synchrotron radiation facilities represent the current state-of-the-art in synchrotron sources. The European Synchrotron Radiation Facility[18] (ESRF) in Grenoble was the first of the third generation hard X-ray sources to operate, coming on line for experiments by users with a 6 GeV storage ring and a partial complement of commissioned beamlines in 1994[17].

3.2.5 NEXT: The fourth generation storage rings

The race to develop a new generation of Synchrotron Radiation Sources with vastly enhanced performance has already begun, namely to the fourth generation.

The candidate with the best scientific case for a fourth generation source is the hard X-ray (wavelength less than 1 Å) free-electron laser (FEL) based on a very long undulator in a high-energy electron linear accelerator. Such a device would have a peak brightness many orders of magnitude beyond that of the third generation sources, as well as pulse lengths of 100 fs or shorter, and would be fully coherent. Research and development on the many technical challenges that must be overcome are well under way at many laboratories around the world[17].

3.3 Theory of Synchrotron Radiation

An accelerating charged particle, such as one travelling on a curved trajectory, emits radiation. For a slowly moving electron ($v \ll c$, where v is the velocity of the electron and c is the velocity of light) the expected radiation is emitted with a more or less doughnut shaped angular distribution with a single wavelength equal to the circumference of the orbit[19]. However, when moving at relativistic speeds ($v \approx c$), this radiation is emitted in a very narrow cone tangential to the path of the particle[20] as pictured in Figure 3.1.

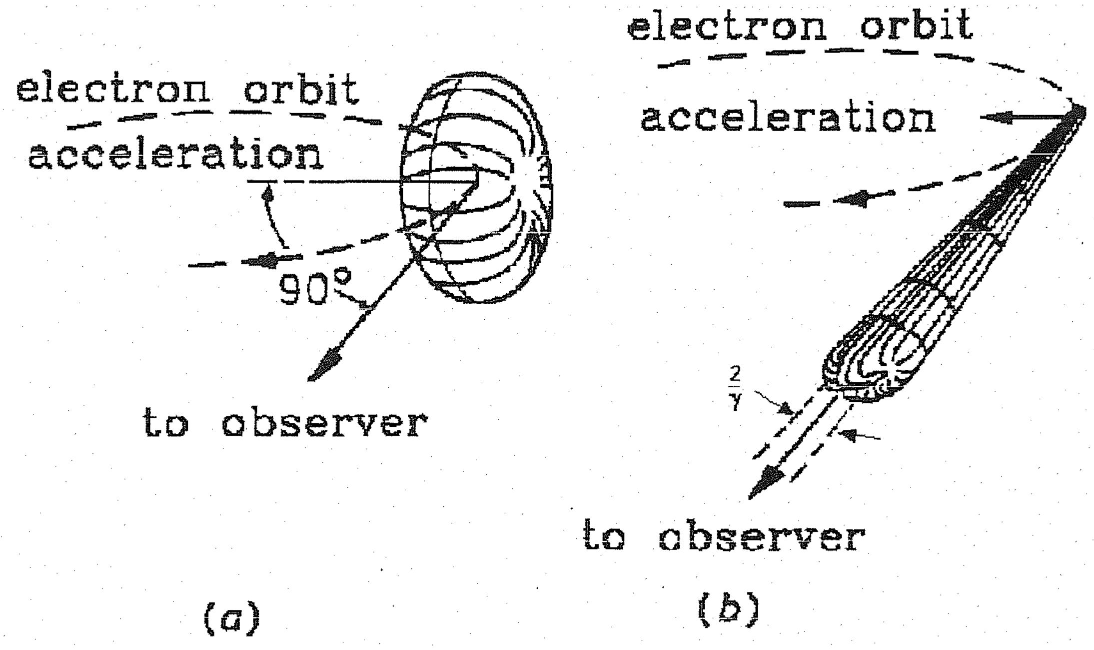

Figure 3.1: Emission pattern of an electron circulating with velocity v:
(a) $v \ll c$
(b) $v \approx c$

The properties of Synchrotron Radiation produced from an electron (or positron) beam traversing a magnetic field are determined essentially by those of a single electron moving along a macroscopic circle. However due to the relativistic velocity of the circulating electron, the radiation emission pattern is pushed into the forward direction. Because of this effect an observer fixed in space can see the Synchrotron Radiation only for a short time interval. According to Fourier analysis such a short pulse contains frequencies up to a critical value:

$$\omega_c = \frac{2\gamma^3 c}{R} \qquad \text{Eq. 3.2}$$

where γ is the Lorentz contraction factor[20] and R is the radius of the orbit. Thus the energy spectrum of Synchrotron Radiation extends up to very high harmonics, or equivalently to very high energies. Due to the longitudinal and transverse oscillations of the circulating electrons, the energy spectrum of Synchrotron Radiation is a continuous distribution.

There are three types of magnetic structures commonly used to produce Synchrotron Radiation: bending magnets, undulators and wigglers.

3.3.1 Bending magnet

A bending magnet causes a single curved trajectory as pictured in Figure 3.2. The result is a fan of radiation around a bend. The instantaneous power radiated[21] by a single electron around the whole orbit is:

$$P = \frac{2}{3}\frac{e^2 c\gamma^4}{R^2} \qquad \text{Eq. 3.3}$$

where e is the charge of an electron, c is the velocity of light, γ is the Lorentz contraction factor[20] and R is the radius of the orbit. From Eq. 3.3 the radiated power increases with the fourth power of the particle energy and decreases with the square of the orbital radius. Most radiation is emitted for high-energy electrons in a circular motion with a small radius. Since the radiation from different electrons is emitted incoherently, the total intensity is obtained by simply summing the contributions from all electrons[21].

Some useful equations are the energy radiated[21]:

$$\delta E(keV) = \frac{88.5E^4(GeV)}{R(m)} \qquad \text{Eq. 3.4}$$

where E is the electron energy and δE is the energy radiated by a single electron per revolution, and the critical photon energy[22]:

$$\varepsilon_c(eV) = \frac{3e\hbar B\gamma^2}{2m} = \frac{2218E^3(GeV)}{R(m)} \qquad \text{Eq. 3.5}$$

where ε_c is the critical photon energy, B is the magnetic field and m is the electron rest mass.

The critical photon energy is that for which half the radiated power is in higher energy photons and half is in lower energy photons. As such it provides a primary parameter for characterizing bending magnet radiation and it is a measure of how far the spectrum extends into the X-ray region[22].

The radiation spectrum from a bending magnet is very broad, analogous to white radiation from an X-ray light bulb and the emission angle is typically 1/γ.

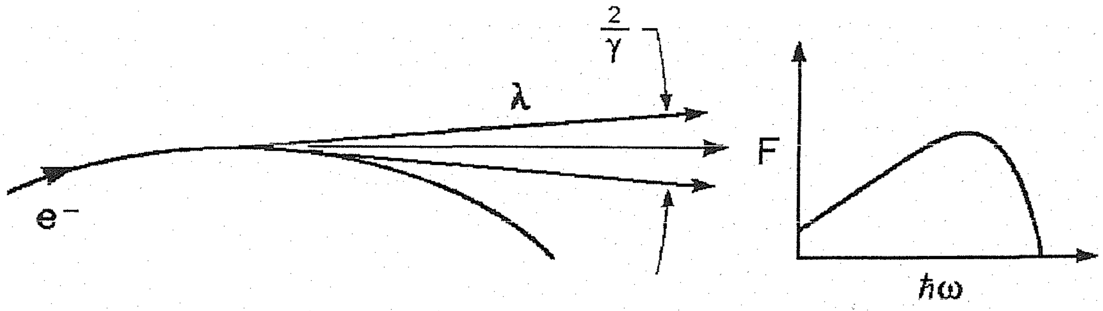

Figure 3.2: Bending magnet radiation and the related radiation spectrum

3.3.2 Undulators

Undulators are periodic magnetic structures with relatively weak magnetic fields. The periodicity and the weak magnetic field cause the electron to move in a harmonic oscillation when it moves in the axial direction, resulting in a motion characterized by small angular excursions as shown in Figure 3.3, smaller than the angular width of the natural radiation cone, $1/\gamma$, normally associated with Synchrotron Radiation. The characteristic emission angle is narrowed by a factor $\sqrt{N}$, where N is the number of magnetic periods (typically of order 100)[22].

In contrast to the smooth spectral distribution of radiation from a bending magnet, radiation from an undulator shows characteristic maxima due to the periodic magnetic structure of the undulator: the magnetic field with N periods of length λ_u produces an oscillatory path for the electrons which is similar to the response generated by $2N$ bending magnets.

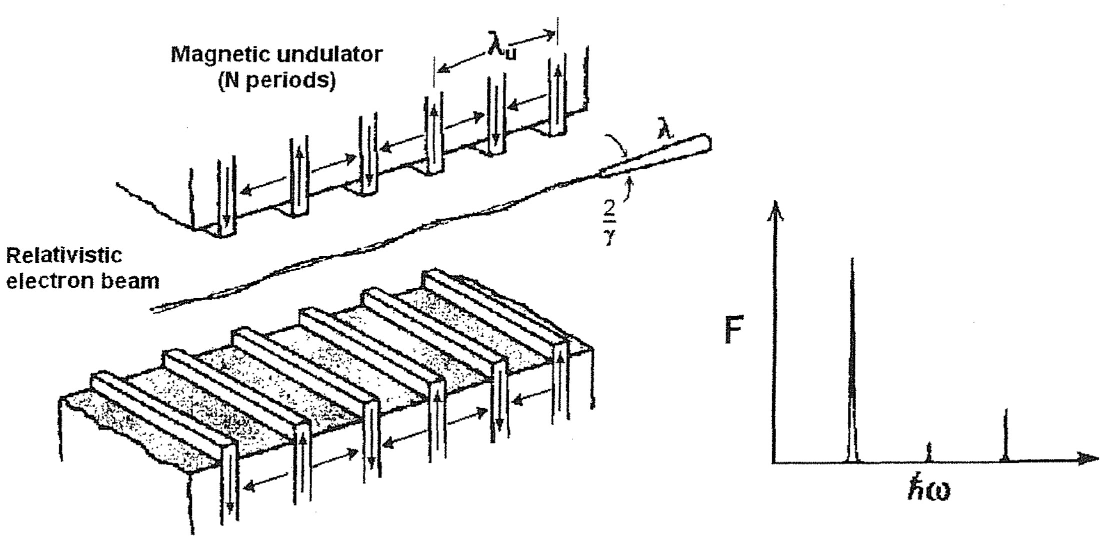

Figure 3.3: Undulator radiation and the related radiation spectrum

A characteristic parameter for a periodic magnet is the non-dimensional magnetic strength K[22] that relates the maximum deflection angle α of the electron path to the natural opening angle $1/\gamma$ of the natural radiation cone. It is given by:

$$K = \frac{\alpha}{1/\gamma} = \frac{1}{2\pi}\frac{eB_0\lambda_u}{mc} \qquad \text{Eq. 3.6}$$

where B_o is the magnet field strength.

For an undulator $K \leq 1$, hence the interference between electromagnetic waves emitted by the same electron at different undulators yields a redistribution of the spatial and spectral intensity. The condition for constructive interference follows from the proper timing for the movement of the electron and its emission of radiation with wavelength λ: the time taken by the electron to travel through one undulator period λ_u minus the time taken by radiation to travel this distance must equal to $n\lambda/c$, where n is an integer.

For radiation emitted at angles θ (in the plane of the undulator) and ψ (in the plane perpendicular of the undulator) with respect to the undulator axis, the wavelength of the nth harmonic radiation λ_n is[23]:

$$\lambda_n = \frac{1}{n}\frac{\lambda_u}{2\gamma^2}\left[1 + \frac{K^2}{2} + \gamma^2\theta^2 + \gamma^2\psi^2\right] \qquad \text{Eq. 3.7}$$

The harmonics are characteristic of the spectrum of the observed undulator radiation. Hence, it is advantageous to work at the energy of such harmonics and to adapt the value of λ_n for a given undulator to the experimental needs. This is done usually by changing the gap between the permanent magnets of the undulator, which, in turn, changes the parameter K, and thus λ_n .

Another important measure of the radiation emitted by electrons traversing a periodic magnet undulator is the brightness (the power ΔP radiated from an area ΔA into a solid angle $\Delta\Omega$), and in particular the spectral brightness in terms of photon flux within the central cone F_{cen}. This is defined as[22]:

$$B = \frac{F_{cen}\cdot(N/1000)}{\Delta A\cdot\Delta\Omega\cdot(0.1\%bandwidth)} \qquad \text{Eq. 3.8}$$

Synchrotron Radiation from undulators can have brightness three orders of magnitude higher than that from bending magnets. The narrowed resultant radiation cone in combination with a tightly confined electron beam leads to radiation with small angular divergence and relatively narrow spectral width, properties generally associated with coherence properties of lasers.

A further important property of undulator radiation concerns its polarization characteristics. The degree of linear polarization $P_L(\theta, \omega)$ is easily obtained from the power $P(\lambda, \psi)$ radiated around the whole orbit into a wavelength interval $d\lambda$ and an interval $d\psi$ of the angle ψ by a single ultra relativistic (γ >>1) monoenergetic electron[21]:

$$P(\lambda,\psi) = \frac{27}{32\pi^3}\frac{e^2 c}{R^2}\left(\frac{\lambda_c}{\lambda}\right)^4 \gamma^8 [1+(\gamma\psi)^2]^2 \left\{K^2_{2/3}(\xi) + \frac{(\gamma\psi)^2}{1+(\gamma\psi)^2} K^2_{1/3}(\xi)\right\} \qquad \text{Eq. 3.9}$$

$$\text{with} \quad \xi = \frac{\lambda_c}{2\lambda}[1+(\gamma\psi)^2]^{3/2} \qquad \text{Eq. 3.10}$$

where λ_c is the “characteristic wavelength”, R denotes the radius of curvature and $K_{1/3}$ and $K_{2/3}$ are modified Bessel functions of the second kind.

The two terms in the curly brackets of Eq. 3.9 are associated with the intensities in the two directions of polarization, $I_{//}$ and $I_{\perp}$, having the electric vector parallel and perpendicular to the plane of the orbit. It can be seen that:

$$P_L = \frac{I_{//} - I_{\perp}}{I_{//} + I_{\perp}} = \frac{K^2_{2/3}(\xi) - \frac{(\gamma\psi)^2}{1+(\gamma\psi)^2} K^2_{1/3}(\xi)}{K^2_{2/3}(\xi) + \frac{(\gamma\psi)^2}{1+(\gamma\psi)^2} K^2_{1/3}(\xi)} \qquad \text{Eq. 3.11}$$

Since the two components of the electric vector have a well defined phase relation with respect to each other, namely $+\pi/2$ or $-\pi/2$ above or below the plane of the orbit, respectively, the degree of circular polarization P_c can also be calculated with decomposition of the elliptically polarized wave into right-hand or left-hand waves with intensity I_R and I_L:

$$P_c = \frac{I_R - I_L}{I_R + I_L} = \pm\frac{2\sqrt{I_{//} I_\perp}}{I_{//} + I_\perp} = \pm\frac{2K_{1/3}(\xi)K_{2/3}(\xi)[\frac{(\gamma\theta)^2}{1+(\gamma\theta)^2}]^{1/2}}{K^2_{2/3}(\xi) + \frac{(\gamma\theta)^2}{1+(\gamma\theta)^2}K^2_{1/3}(\xi)} \qquad \text{Eq. 3.12}$$

where the positive and negative signs correspond to $\psi>0$ or $\psi<0$ respectively. The circular polarization is zero for $\theta=0$ and approaches one for $|\theta|\rightarrow\infty$. Above and below the plane the right-handed and left-handed components dominate respectively. In practice circularly polarized radiation can be obtained by masking part of the beam.

3.3.3 Wigglers

Wigglers are a strong magnetic field version of undulators. Due to strong fields, $K>>1$, and the oscillation amplitude and concomitant radiated power is larger. The radiation cone is broader in both space and angle. The radiation spectrum is similar to that of bending magnets, as pictured in Figure 3.4, but characterized by a much larger photon flux and a shift to harder X-rays (shorter wavelengths). Although more power is radiated, wiggler radiation is less bright because of the substantially increased radiation cone.

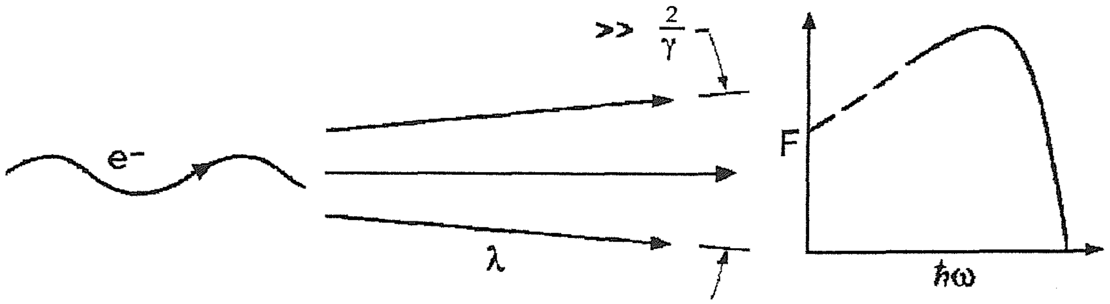

Figure 3.4: Wiggler radiation and the related radiation spectrum

The energy radiated in a single turn forms only a small fraction of the energy of the electron itself (<0.01%). This is why the effects of the emission of radiation on the motion of one electron can, to a first approximation, be neglected. However, this lost energy needs to be restored and this is achieved by incorporating radio frequency (RF) cavities around the orbit. For this reason the electron beam in a storage ring is not a continuous stream, but rather a highly modulated density function consisting of axial bunches. The spacing of these bunches is set by the RF used to restore power to the electrons to compensate for power lost to Synchrotron Radiation. The RF is fed to a microwave cavity operating in a mode with an axial electric field, synchronised to the orbit frequency so that slower electrons receive a small acceleration, while faster electrons receive a small deceleration. In this way, in a particular RF cavity, a potential well is set up that tends to trap available electrons into a series of bunches that travel around the ring at the speed of light with a separation equal to the RF wavelength[24].

3.4 The ELETTRA Synchrotron Radiation

ELETTRA[25] is a large multidisciplinary Synchrotron Radiation Laboratory, open for use by researchers in diverse basic and applied fields such as materials and life sciences, physics, chemistry and geology. ELETTRA is an ultra-bright radiation source in the spectral range from UV to X-rays. It offers an international and competitive environment to researchers from Universities, national Laboratories and enterprises from all over the world.

ELETTRA, a third generation electron storage_ring, has been in operation since October 1993. It has been optimised in the VUV and soft X-ray range, with an electron energy between 2.0 and 2.4 GeV. It has a spectral brightness of up to 10^{19} photons/s/mm^2/mrad^2/0.1%bw and feeds over 20 beam lines in the range from few eV to tens of keV (wavelengths from infrared to X-rays).

The storage ring is made up of four types of magnets: bending magnets that deflect the circulating electron beam into a closed circular path, quadrupoles that focus the beam, sextupoles that compensate chromatic and non-linear effects, and steering magnets that perform small adjustments to the circular trajectory. The ring is made up of twelve identical groups of magnets forming a ring roughly 260 m in circumference. The electrons are generated in a LINAC (LINear ACcelerator) and then injected into the ring. Electrons start off from a ceramic disc that is heated to very high temperature. An electric field of up to 100 kV draws out the electrons that are then accelerated through various RF structures that make up the LINAC. The LINAC is composed of the Gun (that houses the ceramic disc), a low energy bunching section and several high-energy sections. The overall length of the LINAC is 66 m and it contains seven high-energy sections each 6 m long. Between accelerating sections quadrupole magnets keep the beam focused. The LINAC operates at 3 GHz and generates a pulse of electron bunches that are accelerated to a final energy which can be as high as 1.2 GeV. In order not to lose electrons as they are accelerated, the entire LINAC is under vacuum, as is the transfer line and the storage ring. In this way collisions with gas molecules, that would otherwise cause the loss of electrons, are avoided. The electrons exiting the LINAC are then transported to the inner side of the storage ring by a transfer line (a series of deflection and focussing magnets). Both the LINAC and transfer line are below ground in order to not interfere with beamlines in the experimental hall and also for reasons of radiation safety. The storage ring is filled by a multi-turn injection process whereby pulses of electrons are gradually fed into the ring ten times a second until the desired current is achieved. Filling the ring to high currents takes usually several minutes. The electrons circulating in the ring do so in a metal vacuum chamber. The vacuum that is maintained in the ring must be of very high quality, since unlike the LINAC and transfer line where an electron passes through once, in the ring the electrons travelling close to the speed of light traverse a given point more than a million times in one second. To maintain a long beam lifetime the chance of electrons colliding with gas molecules has to be reduced. The situation is further complicated by the copious emission of Synchrotron Radiation, around 90 kW of power just from the bending magnets. The unused radiation must be absorbed in special places otherwise chamber deformation and photoelectron release of surface gases will occur. The energy lost by the electrons when emitting Synchrotron Radiation is compensated by RF cavities. Four single cell cavities are used and they are positioned between dipole magnets in the dispersion region thereby allowing maximum use of the long straight sections for insertion devices (wigglers and undulators). The cavities, operating at 500 MHz, produce a longitudinally bunched beam, in synchronization with the RF field. The maximum number of electron bunches, separated by 2 ns, that can fit in the ring circumference is 432.

The results presented in this Thesis have been obtained at the BL 4.2 Circular Polarized Beamline at ELETTRA.

3.4.1 The BL 4.2 Circular Polarized Beamline

The BL 4.2 Circular Polarized Beamline at ELETTRA provides radiation in the photon energy range 5-1000 eV (12-2500 Å)[26]. The photon source is an electromagnetic elliptical wiggler (EEW). In this EEW the vertical magnetic field due to the permanent magnet poles is combined with a horizontal field generated by a horizontal array of electromagnets. By moving the permanent magnets it is possible to modify the intensity of the vertical magnetic field and hence the horizontal displacement of the electrons, while the vertical displacement is slightly changed by changing the current intensity passing through the coils of the electromagnets. In this way there is the possibility of changing the mode of operation of the insertion device from elliptical wiggler to elliptical undulator mode, whilst maintaining optimum characteristics of polarization and photon flux over a wide spectral range. The polarization of the associated emitted radiation can be changed from left-handed to right-handed by reversing the horizontal field. Two independent monochromators, one working at normal incidence, from 5 to 35 eV, and the other working at grazing incidence, from 30 to 1200 eV, have been designed to cover efficiently the entire spectral range. In practice, during this project only the monochromator working at normal incidence was used with the gold coating.

A schematic layout of the beamline in the normal incidence configuration (NIM) is shown in Figure 3.5.

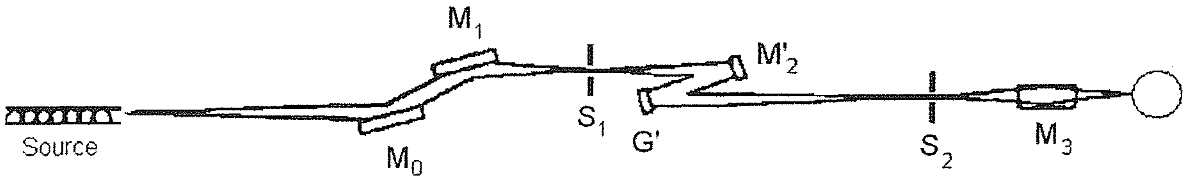

Figure 3.5: Layout of the beamline in Normal Incidence Configuration

The first mirror, M_0, of the beamline is a flat mirror used at 2.5° grazing incidence, which diverts vertically the radiation. This mirror protects the following optical elements from the hard portion of the radiation spectrum. The second mirror, M_1, has a toroidal shape and returns the radiation parallel to the orbit plane with 2.5° grazing incidence. It has been designed to focus the radiation into the entrance slit, S_1, of the monochromator along the tangential direction (magnification 1/3) and into the exit slit, S_2, of the monochromator along the radial direction (magnification 2/3). The monochromator consists of a cylindrical mirror, M'_2, and a set of two interchangeable spherical gratings, G'. After the entrance slit the radiation is deflected vertically by means of a normal incidence convex cylindrical mirror, M'_2, whose coating could be either gold or aluminium. The radiation is then diffracted and focused onto the exit slit by a spherical grating, G', illuminated at normal incidence with a constant 2° included angle. The combination of M'_2 and G' provides a focus at the exit slit S_2 with a degree of astigmatism correction. Only the first outside order of the diffracted beam is focused onto the exit slit. The radiation is then refocused onto the sample by the toroidal mirror, M_3, with a magnification equal to one. The mirror M_3 diverts the radiation by 5° in the horizontal plane. The positions of these mirrors can be manually adjusted to maximise the photon flux, measured by a photodiode at the end of the spectrometer. In order to protect the vacuum in the beamline and in the storage ring a series of valves are present along the beamline, which automatically shut when the pressure rises higher than preset limits. The last valve is a window valve transparent to visible light. This permits alignment of the spectrometer with the beamline, using the visible components of the zero order from the monochromator passing through the window valve.

3.5 Conclusions

In this Chapter a review of the properties of Synchrotron Radiation are presented.
A brief history from the first discovery of Synchrotron Radiation to the following developments until the present days has been outlined.
In this thesis, Synchrotron Radiation was used as tuneable wavelength radiation source and the results presented have been obtained at the BL 4.2 Circular Polarized Beamline at ELETTRA. A detailed description of this beamline has been given in section 3.4.1 of the present Chapter.

3.6 References

[1] http://hyperphysics.phy-astr.gsu.edu/hbase/astro/crab.html

[2] J. Larmor
Phil. Magazine **44**, 503 (1897)

[3] A. Lienard
L'Eclairage Elec. **16**, (1898)

[4] G. A. Schott
Electromagnetic Radiation
Cambridge University Press, Cambridge, 1912

[5] H. C. Pollock
American Journal of Physics **51**, 278 (1983)

[6] F. R. Elder, A. M. Gurewitsch, R. V. Langmuir and H. C. Pollock
Physical Review **71**, 829 (1947)

[7] F. R. Elder, R. V. Langmuir and H. C. Pollock
Physical Review **74**, 52 (1948)

[8] K. Codling and R. P. Madden
Journal of Applied Physics **36**, 380 (1965)

[9] A. Balzarotti, M. Grandolfo and M. Piacentini
Lettere al Nuovo Cimento **3**, 15 (1970)

[10] T. Sagawa, Y. M. Iguchi, M. Sasanuma, T. Wasu, S. Yamaguchi, A. Ejiri, S. Fujiwara, M. Nakamura, T. Masuoka, T. Sasaki and T. Oshio
Japanese Journal of Physical Society **21**, 2587 (1966)

[11] T. Sagawa, Y. M. Iguchi, M. Sasanuma, M. Yokota, S. Yamaguchi, A. Ejiri, S. Fujiwara, M. Nakamura, T. Masuoka, T. Sasaki and T. Oshio
Japanese Journal of Physical Society **21**, 2602 (1966)

[12] R. Haensel and C. Kunz
Zeitschrift fur Angewandte Physik **23**, 276 (1967)

[13] K. J. Button, H. A. Gebbie and B. Lax
Indian Economic Journal **2**, 202 (1966)

[14] E. M. Rowe and F. E. Mills
Particle Accelerator **4**, 221 (1973)

[15] C. Gahwiller, F. C. Brown and H. Fujita
Review of Scientific Instrumentation **41**, 1275 (1970)

[16] http://www.dl.ac.uk

[17] A. L. Robinson
X-Ray Data Booklet
Lawrence Berkeley National Laboratory, Berkeley, 2001, Vol. 2.2

[18] http://www.esrf.fr

[19] R. P. Feynman
The Feynman lectures of physics
Addison-Wesley, Reading, 1963

[20] J. D. Jackson
Classical Electrodynamics
Wiley, New York, 1962

[21] C. Kunz
Synchrotron Radiation
Kunz C., New York, 1979

[22] D. Attwood
Soft X-rays and extreme ultraviolet radiation
Cambridge University Press, New York, 2000

[23] V. Schmidt
Electron Spectrometry of Atoms using Synchrotron Radiation
Cambridge University Press, New York, 1997

[24] S. Krinsky, M. L. Perlman and R. E. Watson
Handbook on Synchrotron Radiation
edited by E.E. Koch, Amsterdam, 1983, Vol. 1A, Chapter 2

[25] http://www.elettra.trieste.it

[26] A. Derossi, F. Lama, M. Piacentini, T. Prosperi and N. Zema
Review of Scientific Instrumentation **66**, 1718 (1995)

Chapter 4

4 EXPERIMENTAL DETAILS

A number of ultraviolet photoelectron spectrometers have been built at Southampton and elsewhere[1-6] to study short-lived molecules. The spectrometer used in this work was specially designed by Dr. Alan Morris to be utilised initially at the Daresbury Laboratory Synchrotron Radiation Source[7], and later at ELETTRA[8]. Angle resolved studies can be performed with this instrument[9].

The essential components of a photoelectron spectrometer are a source of suitable radiation, an ionization chamber in which molecules or atoms can be ionized, an electron energy analyser, an electron detector and a recorder. Additionally, the spectrometer must be evacuated, otherwise the VUV radiation will be absorbed, photoelectrons will be scattered and the detector will not operate. In the next sections the spectrometer used in this thesis is described and all these components are discussed.

4.1 The spectrometer

This spectrometer was built at Southampton, mainly in aluminium and nonmagnetic material. It is modular, with separate chambers for the ionization region and the electron analyser, separated by narrow entrance slits. Each chamber is evacuated by a turbomolecular pump; this differential pump system prevents contamination of the Synchrotron Radiation beamline optics. Moreover an electrostatic lens system was introduced between the ionization chamber and the analyser to allow the operation of the analyser at constant pass energy, and to further reduce contamination of the analyser.

The supporting frame incorporates several features to facilitate alignment of the spectrometer with the (non moveable) photon beam; this is depicted schematically in Figure 4.1. The base of the frame, labelled A in Figure 4.1, has wheels for mobility and has adjustable legs that allow the spectrometer to be raised for alignment purposes. Plate B is pivoted at a point directly under the photon beam axis, again to assist with alignment. Plate C slides in and out of the horizontal plane in Figure 4.1, so that the spectrometer may be moved into position before connection to the beamline system. The upper supporting section, labelled D, may be used to translate the spectrometer in the other horizontal direction.

Further schematic diagrams of the spectrometer are presented in Figure 4.2 and Figure 4.3, showing the principal features of the design.

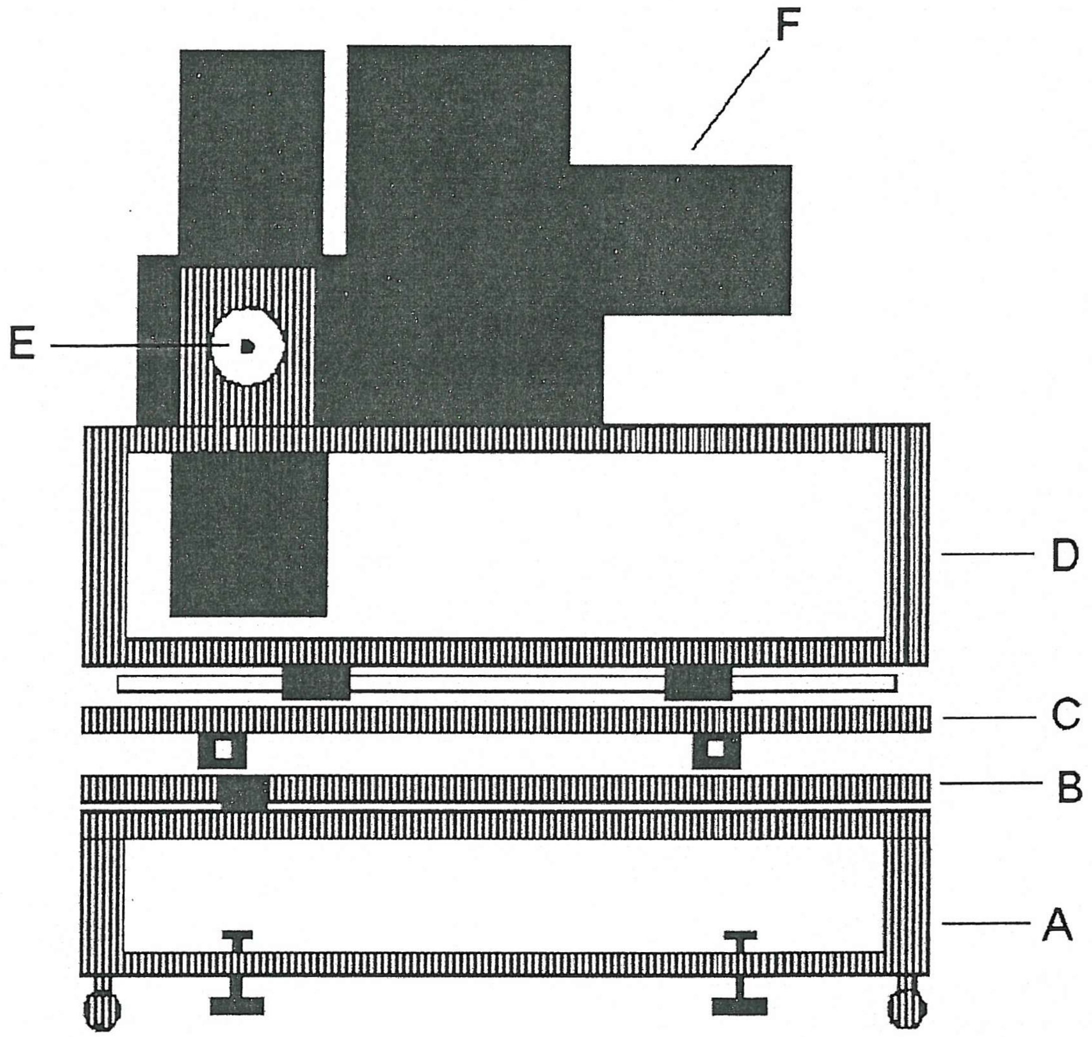

Figure 4.1: Schematic picture of the spectrometer and supporting frame

A: Wheeled Base Frame	*D: Translation Plate 2*
B: Pivoted Plate	*E: Photon Beam axis*
C: Translation Plate 1	*F: Spectrometer*

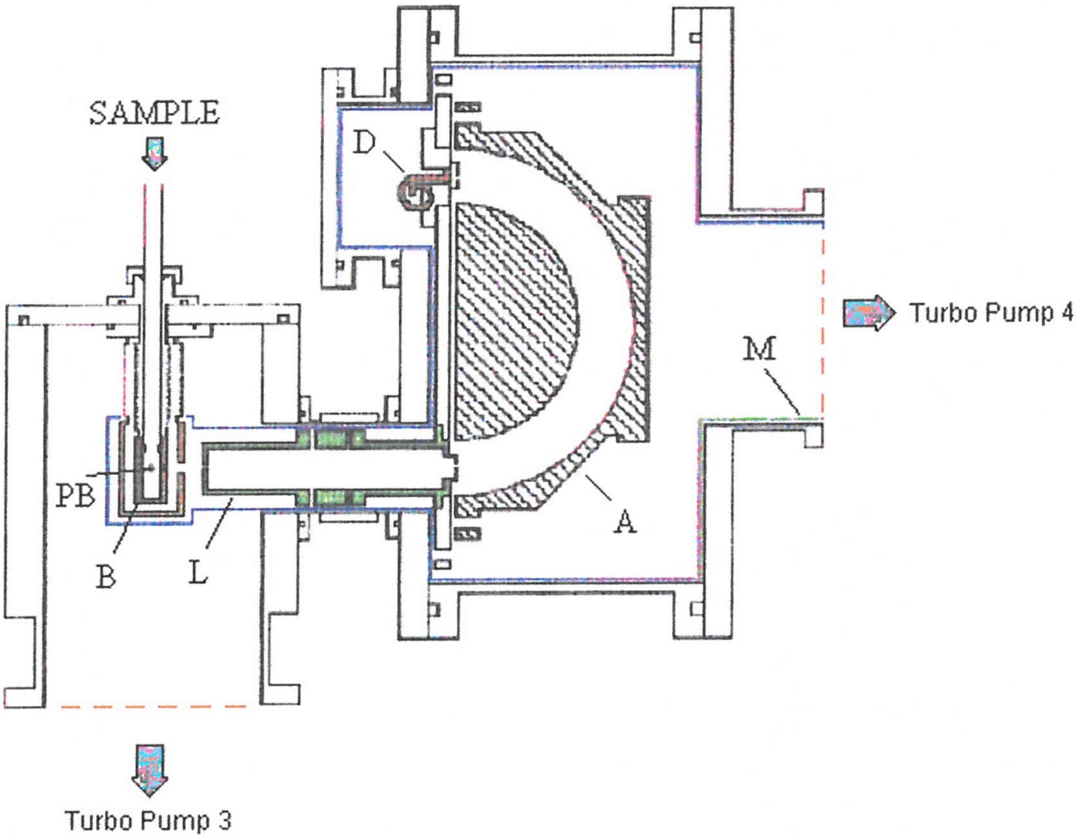

Figure 4.2: Cross section of the Analyser system

A: Hemispherical analyser	*L: Electron Lens*
B: Boxes for differential Pumping	*M: μ-metal Shield*
D: Electron Detector	*PB: Ionization Chamber*

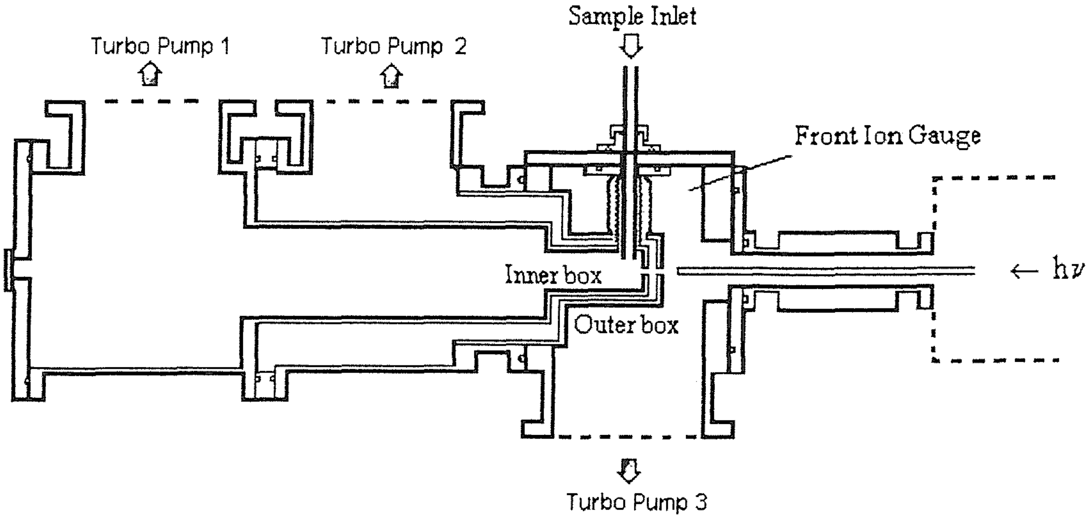

Figure 4.3: The Pumping System of the Spectrometer

Figure 4.2 shows a cross section of the spectrometer in the plane perpendicular to the photon beam (PB in Figure 4.2).

The sample gases are introduced through an inlet system into the ionization chamber of the spectrometer, where they interact with the photon beam.

The ionization chamber consists of two metallic boxes (B in Figure 4.2) differentially pumped in order to prevent contamination of the spectrometer and of the monochromator optics. The inner metal box is earthed and coated with a conductive graphite layer in order to reduce local electric fields that could degrade the spectra. The boxes are connected to two turbomolecular pumps to allow differential pumping, as can be seen in Figure 4.3.

As the electrons leave the boxes they enter a three elements lens system (L in Figure 4.2). The main reasons for using the lens are to use the analyser at constant pass energy and to keep the analyser far away from the photoionization region reducing its contamination. The first lens element (nearest the ionization region PB) is electrically connected to the outer box, the third element is kept at a positive (negative) voltage in order to accelerate (decelerate) the electrons, and the second element is at a voltage chosen to optimize the focus of the electron beam onto the entrance slit of the analyser.

This voltage depends on the kinetic energy of the electrons and is experimentally pre-determined from a focus voltage curve.

A 180° 100 mm mean radius hemispherical electron energy analyzer (A in Figure 4.2) is used. It is operated at fixed pass energy, usually 5 eV, which should ensure constant resolution and transmission throughout the spectral range.

The ionization and analyzer chamber must be at sufficiently low pressure to ensure that the electrons can travel from the point of production to the detector without undergoing collisions with the background gas. Two turbomolecular pumps, each backed by a rotary pump, evacuate the ionization chamber and the analyzer; typical pressures are in the range 10^{-5}-10^{-6} mbar.

As local electric and magnetic fields could affect the motion of the electrons, shielding is extremely important. The spectrometer is made entirely of non magnetic metals and any unwanted local electrostatic fields inside sensitive regions should be avoided. In order to eliminate any magnetic field effects the ionization region, the lens, the analyser and the detector are enclosed in a shielding made by μ-metal (M in Figure 4.2); this is a material especially produced to have a high magnetic permeability to constrain magnetic fields to pass within the metal rather than through the metal.

The electrons are detected by a channeltron (D in Figure 4.2). The final electron signal is transmitted to a standard electronic counting system.

The cross section of the ionization region, depicted in Figure 4.3, shows the differential pumping which has to be used to prevent contamination of the beam-line optics when working at the Synchrotron Radiation Source.

4.1.1 The vacuum system

The spectrometer must be evacuated to low pressures ($P < 10^{-5}$ mbar), otherwise the VUV radiation will be absorbed, photoelectrons will be scattered, and the detector will not operate.

The differential pumping system[10] adopted in the apparatus consists of four turbomolecular pumps, each backed by its own rotary pump. The ionization region is enclosed within two boxes. The boxes are closed, apart from a 2 mm circular aperture at the front to collimate the photon beam, the slits (10 mm × 2 mm) which point towards the electron analyser, and a 12 mm diameter hole at the top for the introduction of the sample gas. Most of the sample gas in the inner box is removed via a 360 ls^{-1} turbo pump (Turbo Pump 1 in Figure 4.3, Leybold Turbovac 361C). The gas that escapes through the slits on the inner box is pumped away by a 360 ls^{-1} turbomolecular pump (Turbo Pump 2 in Figure 4.3, Leybold Turbovac 361C). A third turbomolecular pump, speed 1000 ls^{-1} (Turbo Pump 3 in Figure 4.3, Leybold Turbovac 1000) maintains the vacuum between the spectrometer and the Synchrotron Radiation Source by collecting any gas that enters the ionization chamber. An ionization gauge measures the pressure outside the boxes, whose base value is 8×10^{-8} mbar, rising to 5×10^{-6} mbar when gas is admitted. The pressure inside the inner box is estimated to be at least one order of magnitude higher. No appreciable change in the beamline pressure is observed when gas is admitted. Pressure in the spectrometer in the analyser region is measured by an ionization gauge and read by an Edwards AGC controller. Because Turbo Pumps 1 and 2 receive a heavy load of gases, which are often corrosive, both have corrosion resistant coatings. They are also fitted with purge valves to reduce bearing contamination and extend the operational lifetime when pumping corrosive gases. The electron analyser region is also held under vacuum using a fourth, horizontally mounted tubomolecular pump (Turbo Pump 4 in Figure 4.2, Leybold Turbovac 600). Using this pumping arrangement and a 4 mm diameter stainless steel lightguide to connect the spectrometer to the beamline, contamination of the monochromator optics is kept to a minimum.

4.1.2 The hemispherical electron analyser

The electron analyser, labelled A in Figure 4.2, consists of two concentric 180° hemispherical electrodes. The inner and outer sectors are constructed from aluminium; they have radii R_i and R_o of 80 mm and 120 mm respectively and an internal separation of 40 mm. In order to select electrons with mean pass energy E_{pass}, the sectors must be at potentials V_i and V_0 given respectively by[11,12]:

$$V_i = E_{pass}\frac{R_0}{R_i} \qquad \text{Eq. 4.1}$$

$$V_0 = E_{pass}\frac{R_i}{R_0} \qquad \text{Eq. 4.2}$$

The contribution of the finite width of the analyser slits to the full width at half maximum (FWHM) of a photoelectron band is approximately[13]:

$$\Delta E_{FWHM} = \frac{\Delta S}{R_i + R_0}E_{pass} \qquad \text{Eq. 4.3}$$

where ΔS is the common width of the entrance and exit slits, $\Delta S=\Delta S_{entrance}=\Delta S_{exit}$. For the analyser geometry used in this work ΔS =1 mm and the ΔE_{FWHM} is equal to 25 meV for pass energies of E_{pass}=5 eV. This is the contribution from the analyser itself, and neglects the small effect arising from the angular acceptance of the analyser, α[14]. Narrower slits or lower pass energy would give rise to better resolution, but at the expense of a lower electron transmission. Other broadening effects arise from the radiation bandwidth, Doppler broadening in the sample beam and thermal motion of the sample molecules[15]. A further important contribution to the ΔE_{FWHM} arises from local potentials that may deflect the electrons, accelerate them, decelerate them or cause them not to reach the entrance slit of the hemispheres. To minimise these potentials all the inner surfaces of the analyser are coated with a conductive layer of graphite.

The transmission efficiency of the analyser is a linear function of the pass energy, except at very low energies (<1 eV) as such electrons are more strongly affected by stray fields[16]. Contamination of the electron optics from the reactive gases used usually leads to the resolution and transmission of the spectrometer deteriorating with time so that regular cleaning and replacement of the graphite coating is essential to regenerate the best conditions for recording high quality spectra.

4.1.3 The electron lenses

Usually photoelectron spectrometers record spectra by sweeping the voltages on the hemispheres, so that the kinetic energy of the transmitted electrons is scanned. This procedure has the disadvantage of giving different resolution and transmission for electrons with different kinetic energies. The apparatus used in this work was built in such a way that the spectrometer has an analyser that operates at constant pass energy E_{pass} typically of 5 eV. The electrons are accelerated (or decelerated) by a lens, labelled L in Figure 4.2, so that they enter the analyser with the appropriate fixed energy. Hence spectra are recorded with constant transmission and resolution.

The lens is constructed from three electrically isolated, coaxial, cylindrical aluminium elements. The first element is earthed, so that electrons in this segment maintain their initial kinetic energy after ionization. The third element is at a voltage $V_3 = E_{pass}-E_i$, where E_i is the original energy of the electrons, so that when moving from the first to the third element these electrons are accelerated or decelerated to the pass energy E_{pass}. The plate on which the analyser is mounted is in electrical contact with the third element lens.

The second element of the lens is at a potential V_2, and acts as a focusing element. The value of V_2 must be such that the exit slit of the lens becomes the optical image of the entrance slit. A focus curve is generated by plotting acceptable values of V_2 against the electron kinetic energy. Focus curves for various lens geometries have been calculated by Harting and Read[17]. In practice, the focus curve was determined empirically in this work. This is performed by optimising V_2 so that the intensity of a particular electron signal is maximized for a range of kinetic energies at the selected analyser pass energy. A fourth order polynomial is fitted to a plot of $(E_i+ V_2)/E_i$ vs E_{pass}/E_i, and the coefficients are passed to the controlling software which is then able to calculate the optimum focusing voltage V_2 at a particular electron kinetic energy.

In Southampton only the HeI (21.22 eV) discrete line source is available, and different electron kinetic energies are obtained by observing the photoelectron bands of molecular oxygen and applying positive and negative external voltages to the inner boxes to obtain an energetic shift of the bands.

4.1.4 Shielding

External electric and magnetic fields must be removed since these can affect the paths of the electrons which are to be analysed. Electrostatic fields cannot penetrate the metal frame of the spectrometer, but extra effort must be made to minimize the magnetic fields. One possible way to avoid this problem is by enclosing the spectrometer with three pairs of mutually orthogonal Helmholtz coils, in which the field produced by the current passing in any pair of coils compensates the component of the earth's field in a plane perpendicular to that of the coils. The photoelectron resolution and count-rate can be optimised by adjusting the current through the coils. However space constraints at the Synchrotron Radiation Source do not permit such an arrangement; hence the critical regions of the spectrometer (the ionization region, the lens, the analyser and the detector) are surrounded by a 2 mm-thick layer of μ-metal, labelled M in Figure 4.2, an alloy with high magnetic permeability that tends to constrain the magnetic field to pass within it rather than through it.

4.1.5 Electron detection and control system

Electrons that traverse the analyser and pass through the exit slit are detected by a single channel electron multiplier (channeltron), labelled D in Figure 4.2. The electron pulses produced by the channeltron are preamplified and passed to an Ortec 590A amplifier, whose output goes to a "General Purpose I/O" National Instrument card plugged into a computer.

The potentials for the focussing and retarding elements of the lens are set by Kepco APH500M and BOP100-1M power supplies respectively, controlled by digital-to-analog converters (DACs), supplied by a Keatly board with 2 channels 20 bit analog output plugged into a computer.

The control software written with the programme LABVIEW allows the collection of photoelectron spectra and to interface with the beamline control system to record constant ionic state spectra at ELETTRA.

4.1.6 The rotation mechanism

Angle resolved photoelectron and constant ionic state spectra are conventionally recorded by rotating the analyser in the plane perpendicular to the linearly polarized photon beam. This spectrometer was built in such a way that the whole apparatus can be rotated, vacuum system included. Figure 4.4 shows the two extreme cases in which the lens axis, that defines the direction of the electrons collected, is positioned at an angle of *(a)* θ=0° and *(b)* θ=73.5° with respect to the horizontal direction of polarization of the photon beam (at right angles to the direction of propagation of the radiation). A fixed vertical screw-drive is mounted in bearings located at the top and bottom of the fitting. When rotated this moves the threaded block and the attached arm up or down, as shown in Figure 4.4. For the measurements of angular distribution it is important to make sure that the efficiency of the analyser does not change when the spectrometer is rotated. The biggest contribution to the change of the efficiency of the analyser comes from small misalignments between the axis of rotation and the direction of the photon beam. This contribution is minimised by slight adjustments, after each rotation of the spectrometer, of the direction of the photon beam in such a way as to maximise the signal from the detector and the current measured by the photodiode at the back of the spectrometer. Moreover to minimize this contribution all the experiments related to angle resolved studies were performed at θ values of 0°, 54° 44' and 60°. These three values were extensively tested to ensure the reliability of this kind of experiment by measuring photoelectrons from gases of known angular distribution parameters at known photon energies.

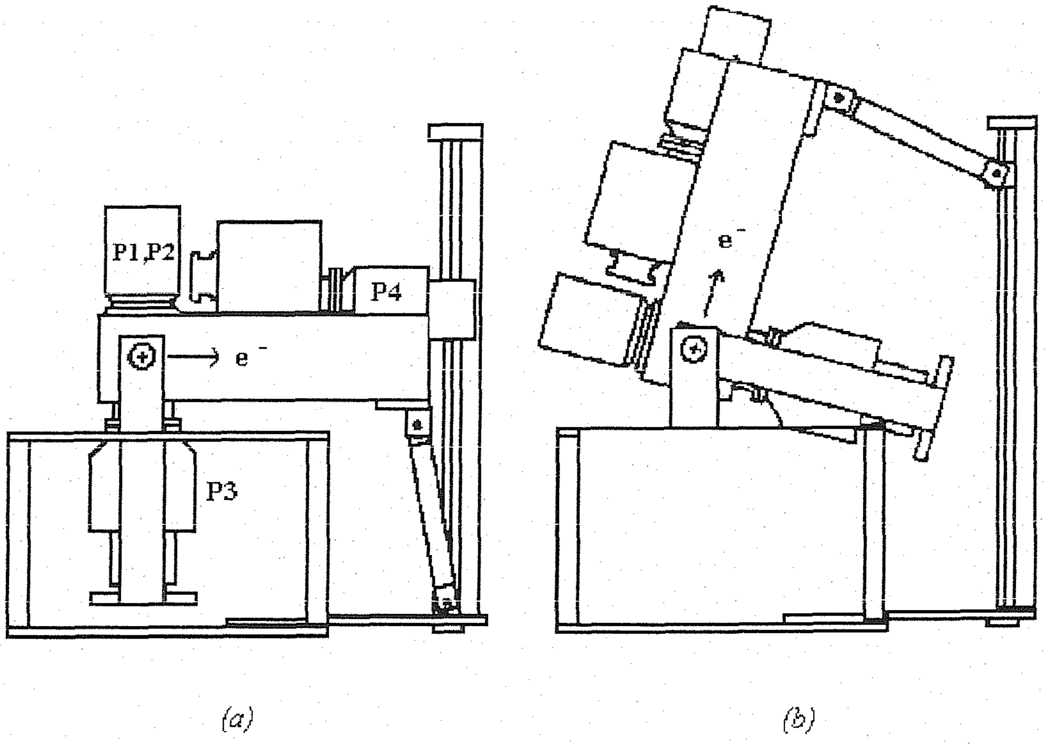

Figure 4.4: A view in the photon beam direction showing the mechanism for rotating the spectrometer
(a) θ =0 ° *(b) θ =73.5 °*

4.1.7 The laboratory radiation source

The inert gas discharge lamp is the most common photon source used in gas phase ultraviolet photoelectron spectroscopy[18].

The most useful and widely used photon source in photoelectron spectroscopy is a discharge in pure helium, which gives the He(I)α (He(1s2p ^{1}P)→He(1s^2 ^{1}S)+$h\nu$) resonance line at 584 Å, corresponding to a photon energy of 21.22 eV, as its main output. This radiation is energetic enough to cause ionization of valence electrons in most molecules. The He(I)α line is accompanied by lines of higher energy, e.g. the HeI β (He(1s3p ^{1}P)→He(1s^2 ^{1}S)+$h\nu$) resonance line at 537 Å, equivalent to a photon energy of 23.08 eV; this is much lower in intensity and approximately 98% of the radiation emitted in the vacuum ultraviolet region is HeI α[11].

In Southampton this kind of discharge lamp (Fisons/VG 232) is fitted to record test photoelectron spectra when beamtime is not available. The radiation from the He lamp is unpolarized. With unpolarized radiation to performed angular resolved experiments the signal must be measured as a function of the angle θ' away from the direction of the radiation beam[11]; for this reason no angle resolved experiments were performed in Southampton.

4.2 Types of spectra

The spectrometer has been designed to allow two different kinds of spectra to be recorded: photoelectron (PE) spectra and constant ionic state (CIS) spectra.

4.2.1 Photoelectron Spectra (PES)

In a PE spectrum the yield of the electrons is measured as a function of their kinetic energy, with the wavelength of the incident radiation fixed at a particular value, as explain extensively in Chapter 2.1. This kind of spectrum is recorded scanning the voltage of the third lens element to obtain a photoelectron spectrum at fixed pass energy. An electron energy spectrum of this type provides a map of the ionic states that are accessed, and allows ionization energies to be measured. The overall resolution, that is the combination of the resolution of the analyser and the bandwidth of the radiation, is normally of the order of 50 meV. This allows vibrational progressions to be resolved in the photoelectron spectra of most light molecules.

4.2.2 Constant Ionic State Spectra (CIS)

In addition to a photoelectron (PE) spectrum, a constant ionic state (CIS) spectrum can also be recorded with a Synchrotron Radiation Source by sweeping the energy of the monochromatized Synchrotron Radiation and monitoring the intensity of a selected photoelectron feature, see Chapter 2.2.

In a CIS spectrum the yield of electrons corresponding to a selected ionization process, normally a vibrational component of a photoelectron band, is measured as a function of the energy of the incident radiation.

In this kind of spectrum the kinetic energy of the electrons to be detected is scanned simultaneously with the energy of the radiation, while maintaining their difference equal to the ionization energy of the process under investigation, i.e. the energy separation between the initial molecular state and the final ionic state does not change. This is possible to perform because the acquisition program when using the

Synchrotron Radiation Source is written in such a way that the potential of the third lens is scanned with the monochromator of the beamline, which selects the photon beam energy, in order to keep the electrons of a selected ionization process focused on the detector.

A CIS spectrum can show discrete structure when the radiation is resonant with an excited neutral state that autoionizes to the ionic state under investigation, as explain extensively in Chapter 2.2.

The resolution in a CIS spectrum depends only on the radiation bandwidth, and not on the analyser resolution, and it allows vibrational and rotational progressions in neutral excited states to be resolved. By recording such a spectrum, a map of autoionizing states, usually Rydberg states, is obtained. The nature of these states may be deduced and new ionization limits may be extrapolated from these spectra.

To run a CIS spectrum it is usual to first acquire a conventional PE spectrum, from which an accurate ionization energy to the particular ionic state and vibrational component of interest can be determined.

4.3 Sample production

The short lifetimes (≈0.1 msec) of the reactive molecules studied in this work mean that they must be produced *in situ* for spectroscopic investigation and then rapidly pumped into the photon beam[19]. Methods that are commonly used to produce such species are fast atom-molecule reactions, pyrolysis, photolysis and gas-solid reactions, and are based on the safe handling of reactive intermediates in photoelectron spectroscopy[20].

In Figure 4.5 are shown the inlet systems utilized during this work in which the samples under investigation were produced.

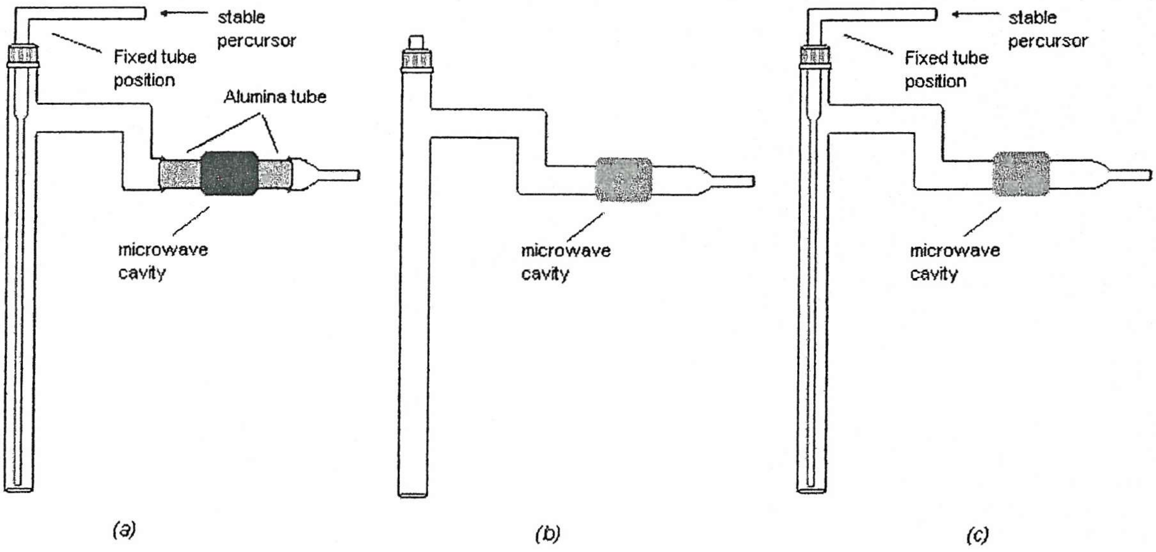

Figure 4.5: Schematic inlet system used for producing reactive intermediates by a rapid atom-molecule reaction

As can be seen in Figure 4.5, in order to prevent low energy electrons produced in the discharge from entering the ionization region, the side inlet tube has three 90° bends.

Typically, in these inlet systems atoms are produced in the microwave discharge and subsequently they react with a stable target molecule which is flowed down the central tube, usually the inner inlet system. Depending on the rate constant of the primary reaction and on the lifetime of the reactive molecule of interest, the position of the inner inlet system above the photon beam, which is called mixing distance, can be adjusted to give the maximum signal of the molecule of interest.

4.3.1 Atoms production

Oxygen atoms, as well as nitrogen atoms, were produced by microwave discharging (2.45 GHz, P~50/60 W) a flowing mixture of molecular oxygen (or molecular nitrogen), with argon (or helium) as carrier, flowing through a boric acid (or phosphoric acid) coated inlet system. A schematic drawing of the inlet system is shown in Figure 4.5 *(b)*. This inlet system is the simplest one because both the gas and the carrier are introduced via the same aperture.

4.3.2 Radicals production

The fast atom-molecule route was used to produce OH radicals via the rapid reaction:

$$H + NO_2 \rightarrow OH + NO \qquad \text{Eq. 4.4}$$

The rate constant of this reaction is 1.1×10^{-10} $cm^3 molecule^{-1} sec^{-1}$ at room temperature[21].

Hydrogen atoms were produced by microwave discharging a flowing mixture of molecular hydrogen and helium through a coated inlet system, Figure 4.5 *(c)*. Helium is added to help sustain the discharge, and the inner surface of the glass tube is coated with phosphoric acid to reduce hydrogen atom recombination. NO_2 is added, as a stable precursor, to the $H/H_2/He$ mixture through a 3 mm inner inlet system which passes down the centre of the main inlet system. At ELETTRA the inner tube should not be moved to adjust the position of the mixing point, but the optimum mixing distance must be accurately determined during several test experiments performed in Southampton.

The OH radicals produced by the reaction Eq. 4.4 undergo rapid secondary reactions:

$$OH + OH \rightarrow H_2O + O \qquad \text{Eq. 4.5}$$

$$O + O + M \rightarrow O_2 + M \qquad \text{Eq. 4.6}$$

These reduce the yield of OH radicals and also give rise to H_2O bands in the spectra that can overlap with those from OH. This is a common problem when studying the PES of reactive intermediates.

In order to reduce the concentration of secondary products in the ionization region, the precursors must be mixed close to the photon beam, but not so close that an insufficient partial pressure of OH is produced.

For OH produced from the $H+NO_2$ reaction in the apparatus used, the optimum mixing distance was found to be 3 cm above the photon beam.

OD was produced via the same method as OH, using D_2 instead of H_2.

The fast atom-molecule route was also used to produce the S atoms and SH radicals via the rapid reactions:

$$F + H_2S \rightarrow SH + HF \qquad \text{Eq. 4.7}$$

$$F + HS \rightarrow S + HF \qquad \text{Eq. 4.8}$$

Fluorine atoms were produced by passing a flowing mixture of F_2 in 5% helium through a microwave discharge in a glass inlet tube coated with teflon.

The rate constant of the $F+H_2S$ reaction is 1.33×10^{-10} $cm^3molecule^{-1}s^{-1}$ at room temperature[22].

In order to avoid attack of the glass of the inlet system by the fluorine atoms produced by the discharge, the inner surface of the tube is coated with a thin layer of teflon, while the discharge cavity was positioned on an alumina section of the inlet system to prevent melting of the teflon due to heating from the discharge[19], as shown in Figure 4.5 *(a)*.

The optimum mixing distance for production of both S and SH was found to be 2 cm above the photon beam, with the inner-inlet system longer than the outer inlet system by about 2 mm.

An initial study was also performed at ELETTRA on the CF radicals. These radicals can be produced by reaction of fluorine atoms with a secondary gas which can be chosen from acetaldehyde, acetone, acetonitrile or acetylene[23,24]. All these reactions produced a low yield of CF and also species as CO (AIE 14.018 eV[25]) which contribute to the region of interest around 13.8-14.2 eV. For these reasons the reaction used for producing CF was F+ CH_3F.

The following species are also produced with CF as reaction products depending on the reaction time and partial pressure of F and CH_3F: C_2H_2, C_2HF and HF. However, they do not contribute any signals within the ionization energy region of interest.

As for the production of S and SH radicals, in order to avoid attack of the glass of the inlet system, the inner surface of the tube is coated with a thin layer of teflon, while the discharge cavity was positioned on an alumina section in the inlet system to prevent melting of the teflon due to heating from the discharge[19], as shown in Figure 4.5 *(a)*.

The optimum mixing distance for production of CF was found to be 4 cm above the photon beam.

Some test experiments were also performed at Southampton to produce the NH_2 radicals. The fast atom-molecule route was also used to produce these radicals via the rapid reaction:

$$F + NH_3 \rightarrow HF + NH_2 \qquad \text{Eq. 4.9}$$

where fluorine atoms were produced by passing a flowing mixture of F_2 in 5% helium through a microwave discharge in a glass inlet tube coated with teflon.

The rate constant of the F+NH_3 reaction is 1.1×10^{-10} $cm^3 molecule^{-1} s^{-1}$ at room temperature[22].

NH radicals were produced by the rapid secondary reaction of atomic fluorine with NH_2:

$$F + NH_2 \rightarrow HF + NH \qquad \text{Eq. 4.10}$$

As for all the reactions using fluorine atoms, in order to avoid attack of the glass of the inlet system by the fluorine atoms produced by the discharge, the inner surface of the tube is coated with a thin layer of teflon, while the discharge cavity was positioned on an alumina section in the inlet system to prevent melting of the teflon due to heating from the discharge[19], as shown in Figure 4.5 *(a)*.

The same conditions for the production of S and SH were found also for the production of both NH_2 and NH: an optimum mixing distance of 2 cm above the photon beam, with the inner-inlet system longer than the outer inlet system by about 2 mm.

4.4 Conclusions

The photoelectron spectrometer used in this thesis for the study of reactive intermediates with a Synchrotron Radiation Source has been fully described in this Chapter. This spectrometer has been used to study the photoionization behaviour of several reactive intermediates (namely O, N and S atoms, OH, OD, and SH radicals) and the results of this work are presented in Chapters 5 to 8.

4.5 References

[1] D. C. Frost, S. T. Lee, C. A. McDowell and N. P. C. Westwood
Journal of Electron Spectroscopy and Related Phenomena **12**, 95 (1977)

[2] N. Jonathan, D. J. Smith and K. J. Ross
Chemical Physics Letters **9**, 217 (1971)

[3] J. M. Dyke, L. Golob, N. Jonathan, A. Morris and M. Okuda
Journal of The Chemical Society and Faraday Transactions 2 **70**, 1828 (1974)

[4] J. M. Dyke, N. Jonathan and A. Morris
Electron Spectroscopy: Theory, Techniques and Applications
edited by C.R. Brundle and A.D. Baker, Academic Press, London, 1979

[5] A. Morris, N. Jonathan, J. M. Dyke, P. D. Francis, N. Keddar and J. D. Mills
Review of Scientific Instruments **55**, 172 (1984)

[6] J. M. Dyke, A. Morris and N. Jonathan
International Review of Physical Chemistry **2**, 3 (1982)

[7] http://www.dl.ac.uk

[8] www.elettra.trieste.it

[9] J. M. Dyke, S. D. Gamblin, A. Morris, T. G. Wright, A. E. Wright and J. B. West
Journal of Electron Spectroscopy and Related Phenomena **97**, 5 (1998)

[10] D. J. Hucknall and A. Morris
Vacuum technology calculations in chemistry
Rs C, Cambridge, 2003

[11] J. H. D. Eland
Photoelectron Spectroscopy
Butterworths & Co, Oxford, 1984

[12] J. W. Rabalais
Principles of Ultraviolet Photoelectron Spectroscopy
Wiley & Sons, New York, 1977

[13] A. Poulin and D. Roy
Journal of Physics E **11**, 35 (1978)

[14] G. K. Ovrebo and J. L. Erskine
Journal of Electron Spectroscopy and Related Phenomena **24**, 189 (1981)

[15] J. M. Hollas
Modern Spectroscopy
Wiley & Sons, New York, 1996

[16] J. L. Gardner and J. A. R. Samson
Journal of Electron Spectroscopy and Related Phenomena **8**, 123 (1976)

[17] E. Harting and F. H. Read
Electrostatic Lenses
Elsevier, Amsterdam, 1976

[18] J. A. R. Samson
Tecniques of Vacuum Ultraviolet Spectroscopy
Wiley & Sons, New York, 1967

[19] M. C. R. Cockett, J. M. Dyke and H. Zamanpour
Vacuum Ultraviolet Photoionization and Photodissociation of Molecules and Clusters
edited by C.Y. Ng, World Scientific, London, 1991, Chapter 2

[20] A. Morris and J. M. Dyke
Vacuum **53**, 339 (1999)

[21] P. P. Benard and M. A. A. Clyne
Journal of The Chemical Society and Faraday Transactions 2 **73**, 394 (1977)

[22] http://kinetics.nist.gov/index.php

[23] J. M. Dyke, A. E. Lewis and A. Morris
Journal of Chemical Physics **80**, 1382 (1984)

[24] J. M. Dyke, N. Hooper and A. Morris
Journal of Electron Spectroscopy and Related Phenomena **119**, 49 (2001)

[25] K. Kimura, S. Katsumata, Y. Achiba, T. Yamazaki and S. Iwata
Handbook of HeI photoelectron spectra of fundamental organic molecules
Japan Scientific Societies Press, Tokyo, 1981

Chapter 5

5 PHOTOELECTRON SPECTROSCOPY OF O ATOMS

This Chapter reports studies of ultraviolet photoelectron spectroscopy using Synchrotron Radiation on O atoms.

The Chapter is organized as follows. In section 5.1 previous spectroscopic investigations on O atoms that are considered important for the present work are briefly reviewed. Section 5.2 presents experimental constant ionic state (CIS) spectra, and resonant photoelectron spectra, together with their interpretations. Section 5.3 summarizes the results obtained.

5.1 Previous photoelectron spectroscopy investigations on O atoms

In the earth's ionosphere, atomic oxygen is the dominant neutral species above 150 km for average solar conditions. The solar spectrum between 9.50 eV and 45.90 eV consists of numerous lines, arising from emissions from multiply ionized atoms, superimposed on a broad continuum[1]. In the ionosphere, photoionization of atomic oxygen by radiation from the sun is the major source of photoelectrons. The electrons produced can travel a considerable distance along geomagnetic field lines before losing their energy. It is therefore important to know the photoionization cross section of atomic oxygen, as well as the relative contributions from autoionization and direct ionization, as a function of photon energy in order that the photoelectron flux in the upper atmosphere and its energy distribution can be estimated[2,3].

The first HeI photoelectron spectrum of atomic oxygen was obtained by Jonathan *et al.*[4,5]. This showed three bands arising from the O $(2p)^{-1}$ ionization corresponding to the ionizations $O^+(^4S, ^2D, ^2P) \leftarrow O(^3P)$. Subsequently, the branching ratios for the production of these $O^+(^4S, ^2D$ and $^2P)$ states, as well as the angular distribution parameters for these ionizations, were measured at the HeI, HeII and NeI photon energies[6-8]. The partial photoionization cross sections for these ionizations have been measured by Hussein *et al.*[9] from 17.10 to 21.40 eV using Synchrotron Radiation, the absolute values for the O (^3P) photoionization cross section have been measured from threshold (13.60 eV) up to 103.00 eV by Samson and Pareek[10] using monochromatized radiation from a helium continuum discharge lamp, and the absolute value for the photoionization cross section for the $O^+(^4S) \leftarrow O(^3P)$ ionization was determined by de Lange *et al.*[11] at the HeI photon energy. Later, using Synchrotron Radiation, Prümper *et al.*[12] measured angular distribution parameters for ionization to all three ionic states at several photon energies between 24.00 and 70.00 eV, and van der Meulen *et al.*[13] measured the relative partial photoionization cross sections and angular distribution parameters for the $O^+(^4S, ^2D) \leftarrow O(^3P)$ ionizations from threshold up to 30.00 eV. This latter investigation[13] was the first study of atomic oxygen in which the angular distribution parameter, β, was measured across autoionization resonances.

Recently, Tayal[14] calculated the angular distribution parameters for these autoionizations from 13.60 to 50.00 eV using the R matrix method with configuration interaction included in the wavefunctions for both the initial O(^{3}P) and the final continuum states.

Absorption and emission studies of atomic oxygen in the energy region 13.60-19.00 eV above the ground state[15,16], as well as photoionization investigations of O(^{3}P) in this photon energy region, using a mass spectrometer as the ion detector and a helium discharge with a vacuum ultraviolet monochromator as the tunable photon source, have also been made[17,18].

5.2 Results and discussion

The purpose of this present work was to measure relative partial photoionization cross sections and angular distribution parameters for the $O^+(^4S)\leftarrow O(^3P)$ and $O^+(^2D)\leftarrow O(^3P)$ ionizations, in the photon energy range 14.00-19.00 eV.

Initially these experiments were performed to compare the Daresbury Synchrotron Radiation Source[19] (a second generation source) with the ELETTRA Synchrotron Radiation Source[20] (a third generation source) in order to establish the characteristics of the ELETTRA source when used to study reactive intermediates and to quantify the improvement in intensity and resolution that can be obtained at ELETTRA when studying short lived species. The CIS spectra obtained were of higher resolution than previous CIS measurements and this allowed detailed comparison to be made of the relative photoionization cross sections and angular distribution parameters, recorded as a function of photon energy, with previous experiments and calculations.

Oxygen atoms were produced by passing a flowing mixture of molecular oxygen and argon as a carrier, through a microwave discharge (2.45GHz) in a glass inlet tube, coated with boric acid, attached to the ionization chamber of the spectrometer.

The photon energy was calibrated by recording the CIS spectrum of the $O^+(^4S)\leftarrow O^*\leftarrow O(^3P)$ process in the photon energy region 14.00-19.00 eV, and comparing the positions with known $O^*\leftarrow O$ transition energies above the first ionization energy[17]. Intensities of the CIS spectra were normalised by the photon flux and then corrected for the transmission function of the spectrometer.

The degree of linear polarization of the photon source was well established[21,22], as $P=1$. As a result, the asymmetry parameter, β, could be measured for oxygen atoms at selected photon energies and over a photon energy range, by recording CIS spectra at two different angles, $\theta=0°$ and $\theta=60°$, at each photon energy; the β parameter could then be calculated from the expression (see Chapter 2.2.6):

$$\beta=\frac{8(R-1)}{R+8} \qquad \text{Eq. 5.1}$$

where $R=\frac{I_0}{I_{60}}$ is the ratio of the experimental intensities at the two angles.

Photoelectron spectra recorded at a photon energy of 21.22 eV, for molecular oxygen with the microwave discharge on and off, are shown in Figure 5.1. These spectra were recorded at a detection angle $\theta = 60°$ with respect to the direction of polarization of the radiation.

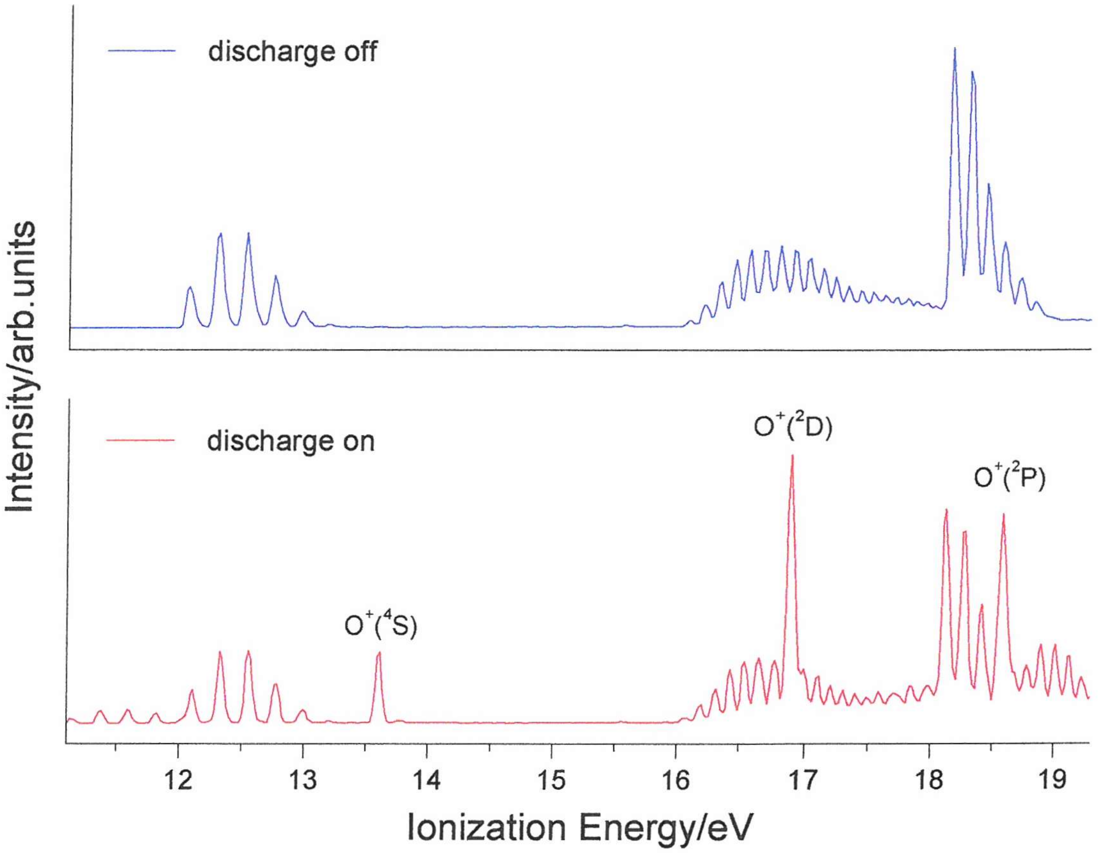

Figure 5.1: Photoelectron spectra recorded for molecular oxygen with discharge off (blue trace) and discharge on (red trace) at $h\nu = 21.22$ *eV*

As can be seen from the discharge on spectrum, there are sharp bands at 13.62, 16.94 and 18.63 eV, corresponding to the $O^+(^4S) \leftarrow O(^3P)$, $O^+(^2D) \leftarrow O(^3P)$, and $O^+(^2P) \leftarrow O(^3P)$ ionizations respectively. The other features seen in the spectra arise from molecular ionizations of O_2 ($X\ ^3\Sigma_g$) and O_2 ($a\ ^1\Delta_g$).

CIS spectra could be successfully recorded for the $O^+(^4S) \leftarrow O(^3P)$ and $O^+(^2D) \leftarrow O(^3P)$ ionizations but this was not possible for the $O^+(^2P) \leftarrow O(^3P)$ band, as it was too heavily overlapped by molecular features. The band-pass of the monochromator, which in a CIS scan is the only factor contributing to the overall resolution, was normally set to 3 meV. The step-size in the CIS scans was 1 meV. The Daresbury SRS experiments were performed on beamline 3.2 with the same spectrometer as used in the ELETTRA experiments. This beamline uses a 5 metre normal incidence monochromator. The transmitted radiation from the monochromator had a typical width of 15 meV and the step-size used in the CIS scans was 5 meV.

The first step was to make a comparison between the SRS Beamline 3.2 and the ELETTRA Beamline 4.2. These two beamlines are the most suited to photoionization studies of reactive intermediates in the vacuum ultraviolet region, at the SRS[19] and at ELETTRA[20] respectively.

First, comparison of photoelectron count-rates of atomic oxygen and other reactive species at the same gas pressure, production conditions and synchrotron ring currents gave an intensity improvement of 75-125 in favour of ELETTRA, for PE spectra of similar photoelectron resolution. Also, measurements of the current at a photon energy of 21.22eV on the aluminium photodiode in the ionization chamber opposite the photon source, gave the following results. At SRS on BL 3.2, at a ring current of 200 mA and at 15 meV photon width, a current of 0.1 nA was measured. At ELETTRA on BL 4.2 at a ring current of 200 mA and at 4 meV photon width, a current of 7.5 nA was measured.

This corresponds to an intensity improvement of 75.

The improvement in resolution can be demonstrated by comparing CIS spectra recorded for oxygen atoms, as shown in Figures 5.2.

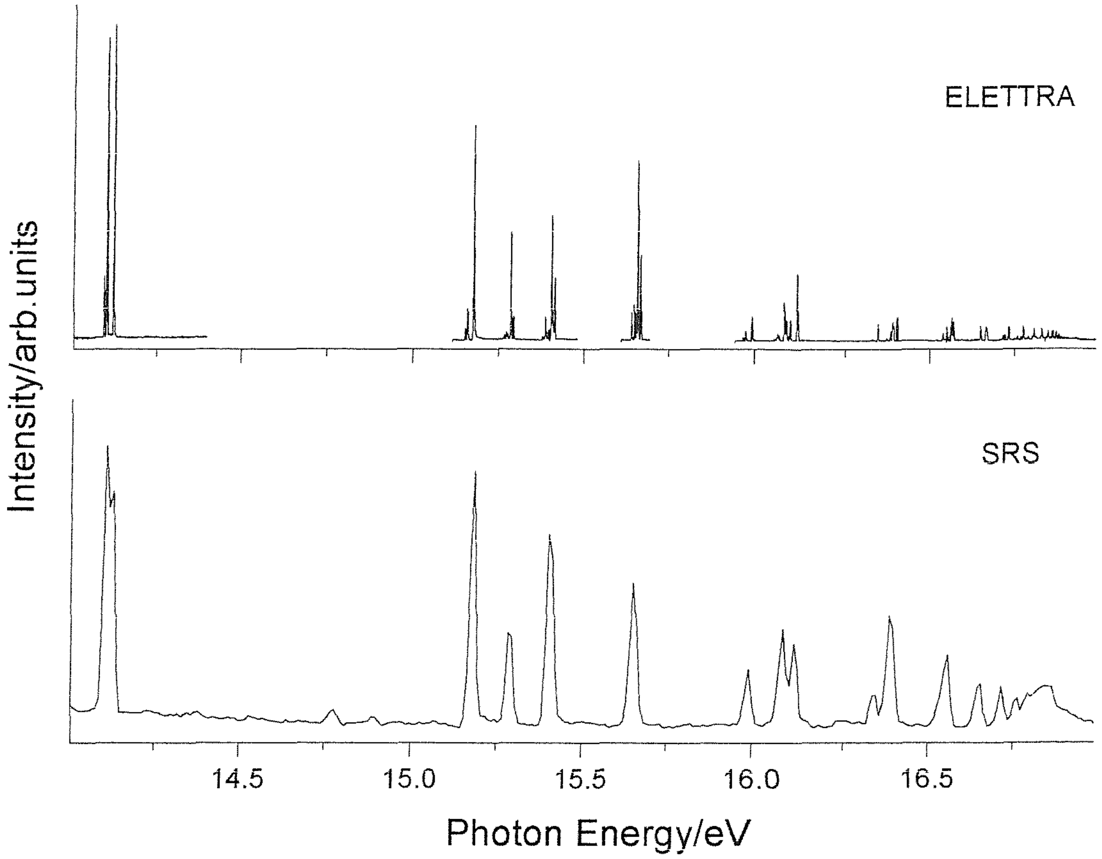

Figure 5.2: CIS spectra of atomic oxygen recorded at $\theta = 0°$ at ELETTRA on BL 4.2 (upper plot) and at SRS on BL 3.2 (lower plot)

The spectra, which were both recorded at θ=0° with respect to the major polarization axis of the photon source, are CIS spectra for the process $O^+(^4S) \leftarrow O^* \leftarrow O(^3P)$ in the photon energy region 14.00-17.00 eV recorded at the two synchrotron sources.

It should be noted that the polarization of the radiation from the beam line at the SRS was substantially less than 1 ($P \approx 0.6$); a comparison between the relative intensities of the individual lines in the above spectra is therefore not meaningful.

The Rydberg states observed in Figure 5.2 are part of series which converge mostly to the second ionization limit but autoionize to $O^+(^4S)$.

A full assignment of these structures will be given later.

On expanding a section of the photon energy range in Figure 5.2 (15.15-15.45 eV), the improvement in resolution can be seen more clearly (see Figures 5.3). The bandwidth in Figure 5.3 *(a)* is 2.5 meV whereas that in Figure 5.3 *(b)* is 20 meV, demonstrating the clear improvement in resolution on the ELETTRA beamline 4.2 compared to the SRS beamline 3.2.

The full O atom CIS spectrum in the photon energy region 14.00-19.00 eV with the first, second and third ionization limits marked in, is shown in Figure 5.4.

This was recorded at $\theta = 0°$ and consists of the $O^+(^4S) \leftarrow O^* \leftarrow O(^3P)$ CIS spectrum between 14.00 and 19.00 eV and the $O^+(^2D) \leftarrow O^* \leftarrow O(^3P)$ CIS spectrum between 17.00 and 19.00 eV photon energy. It is convenient to record spectra in these sections as the first ionization energy, $O^+(^4S) \leftarrow O(^3P)$, is 13.62 eV and the second ionization energy, $O^+(^2D) \leftarrow O(^3P)$, is 16.94 eV.

The bands observed in Figure 5.4 can be readily assigned to known $O^* \leftarrow O(^3P_{J''})$ transitions by comparison with known O^* term values[17,23].

The assignments are shown in Figure 5.4, where transitions have been denoted as *(J'', J')*.

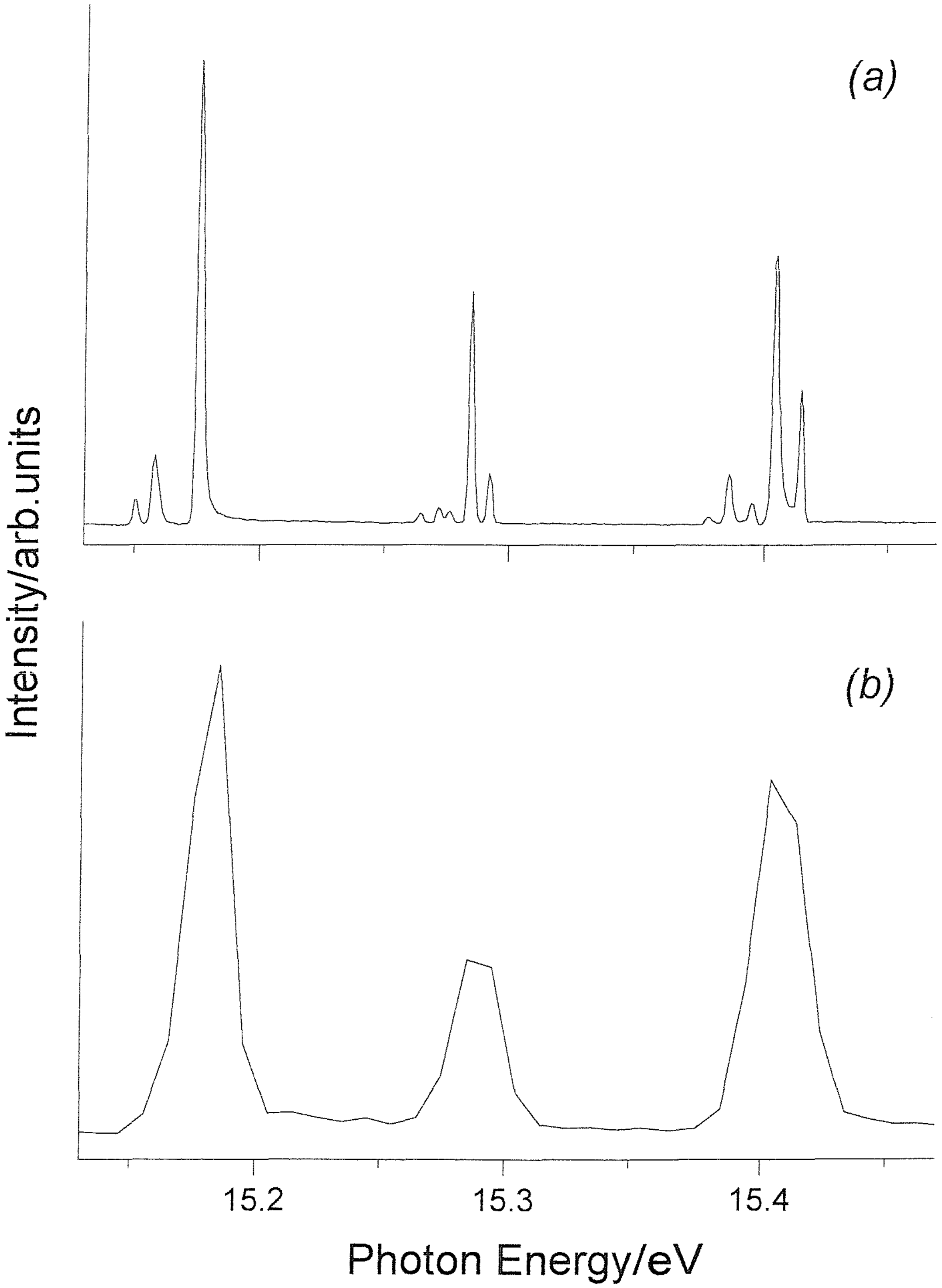

Figure 5.3: The 15.1-15.5 eV photon energy regions of Figure 5.2 expanded show a comparison of resolution in CIS spectra recorded with (a) the ELETTRA BL 4.2 and (b) the SRS BL 3.2 synchrotron sources

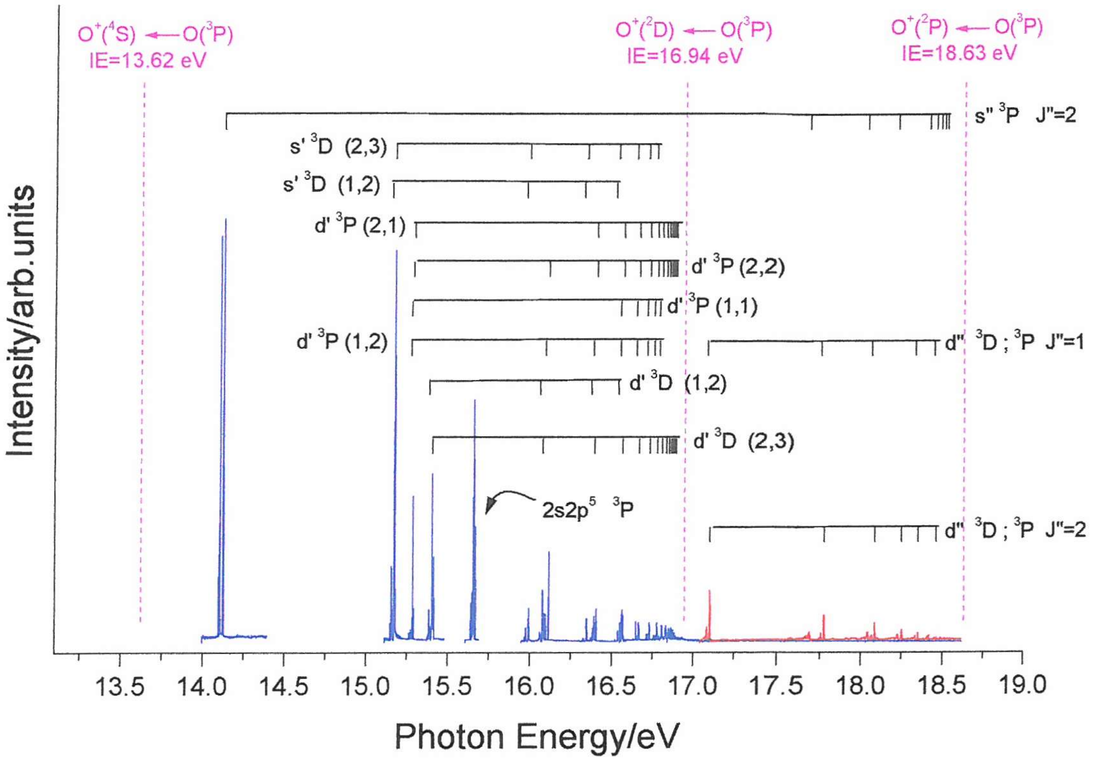

Figure 5.4: O atoms CIS spectra recorded at $\theta = 0°$, with the first, second and third ionization limits marked (magenta trace)
This spectrum is made up of the $O^+(^4S) \leftarrow O^* \leftarrow O(^3P)$ CIS spectrum in the 14.0-18.6 eV (blue trace) and the $O^+(^2D) \leftarrow O^* \leftarrow O(^3P)$ CIS spectrum in the 16.9-18.6 eV photon energy region (red trace)
$O^* \leftarrow O$ transitions are labelled as (J", J')
To simplify this diagram, the labelling of bands associated with $O^*(^3S)$ states between 13.9 eV and 16.9 eV has been omitted
Single and double prime on running electron designates terms converging to the second (IE=16.94 eV) and to the third (IE=18.63 eV) ionization limit respectively

In order to assign the spectra in Figure 5.4 it is helpful to determine the energy levels to which transitions are allowed from the ground state $2s^22p^4\ {}^3P_{2,1,0}$.

The upper level can be restricted to triplet terms, since the spin selection rule[24,25], $\Delta S=0$, should be strictly obeyed for a light atom such as oxygen. The most likely transitions will be those with $\Delta l=\pm1$, or s←p and d←p in this case[24,25]. The terms involved may be considered to be the result of adding an s or d electron to the three terms of O^+ resulting from the electron configuration $2s^22p^3$. These O^+ core states are ^4S, ^2D, ^2P, in order of increasing energy. The resulting terms are obtained by combining the angular momentum of the s or d electron with the core-state angular momentum. From these terms the selection rules[24,25] $\Delta L=0, \pm 1$ reduces the possible transitions to the nine allowed term series given in Table 5.1. Single and double prime on running electron designates terms converging to the second (IE=16.94 eV) and to the third (IE=18.63 eV) ionization limit respectively.

Table 5.1: Energy levels to which transitions are allowed from the ground state $2s^2 2p^4\ ^3P_{2,1,0}$ assuming Russell-Saunders coupling is valid

Series	Ionic Core	Ionic State after Autoionization
$[2s^22p^3(^4S_{3/2})\ ns]\ ^3S_1$	$^4S_{3/2}$	-
$[2s^22p^3(^4S_{3/2})\ nd]\ ^3D_1$	$^4S_{3/2}$	-
$[2s^22p^3(^2D_{5/2,3/2})\ ns']\ ^3D_{3,2,1}$	$^2D_{5/2,3/2}$	$^4S_{3/2}$, εd
$[2s^22p^3(^2D_{5/2,3/2})\ nd']\ ^3S_1$	$^2D_{5/2,3/2}$	$^4S_{3/2}$, εs
$[2s^22p^3(^2D_{5/2,3/2})\ nd']\ ^3P_{2,1,0}$	$^2D_{5/2,3/2}$	None
$[2s^22p^3(^2D_{5/2,3/2})\ nd']\ ^3D_{3,2,1}$	$^2D_{5/2,3/2}$	$^4S_{3/2}$, εd
$[2s^22p^3(^2P_{3/2,1/2})\ ns'']\ ^3P_{2,1,0}$	$^2P_{3/2,1/2}$	$^2D_{5/2,3/2}$, εd
$[2s^22p^3(^2P_{3/2,1/2})\ nd'']\ ^3P_{2,1,0}$	$^2P_{3/2,1/2}$	$^2D_{5/2,3/2}$, εd
$[2s^22p^3(^2P_{3/2,1/2})\ nd'']\ ^3D_{3,2,1}$	$^2P_{3/2,1/2}$	$^4S_{3/2}$, εd ; $^2D_{5/2,3/2}$, $\varepsilon s/\varepsilon d$

Of the nine predicted series in Table 5.1 only the ones converging to the second and third ionization limits can be observed.

Inspection of Figure 5.4 shows that in the photon energy region 15.00-16.90 eV, all the transitions can be assigned to excitation to Rydberg states which are members of series which converge to the second ionization energy, apart from a group of bands associated with excitation to a $2s2p^5\ ^3P$ state. This inner-electron transition is very prominent in the spectrum and five of the expected six members[17] are resolved.

The observed Rydberg states correspond to $1s^22s^22p^3$ *n*s and $1s^22s^22p^3$ *n*d configurations accessed from the $1s^22s^22p^4\ ^3P$ state. Transitions from J"=1 and J"=2 components of the ^3P state can readily be identified.

To simplify Figure 5.4 the labelling of bands associated with $O^*(^3S_1)$ states between 14.00 and 17.00 eV has been omitted.

The bands in the 14.00-14.20 eV region are the most intense bands in the spectrum. They arise from a $[2s^22p^3\ (^2P_{3/2,1/2})\ 3s"]\ ^3P_{2,1,0} \leftarrow 2s^22p^4\ ^3P_{2,1,0}$ excitation and components arising from transitions from J"=0, 1, 2 can be identified in this spectral region, as can be seen in Figure 5.5.

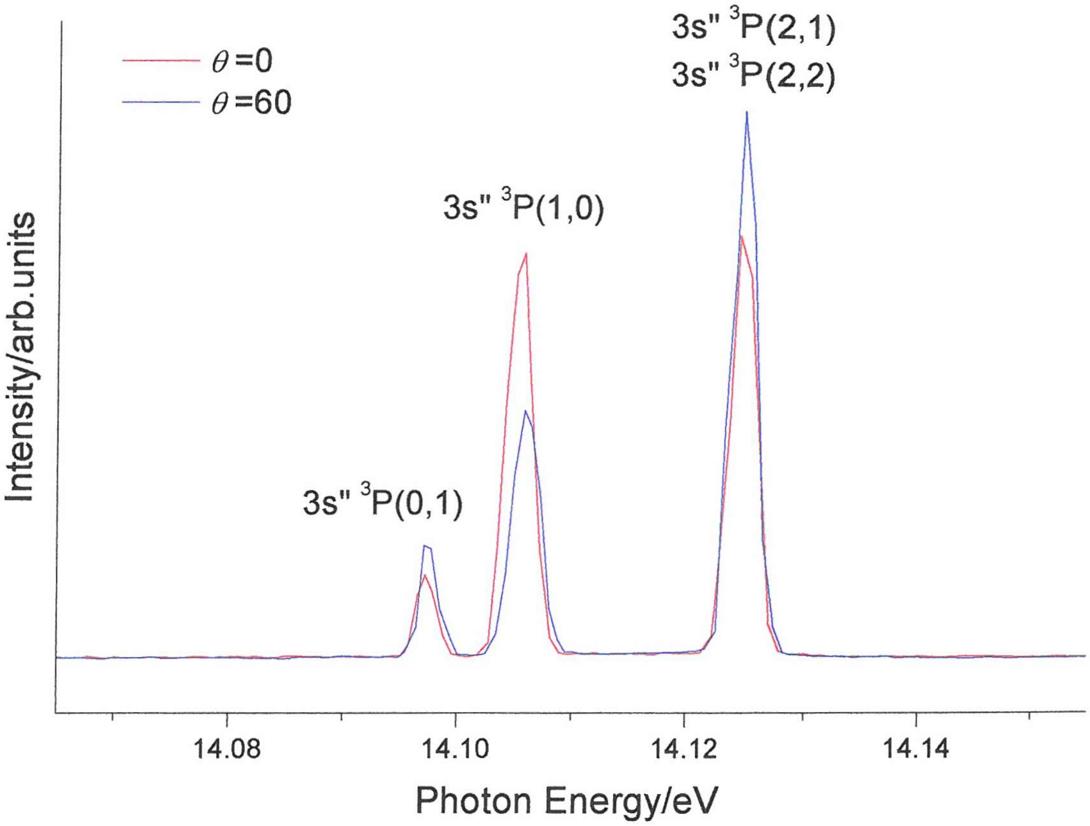

Figure 5.5: CIS spectra recorded for the $O^+(^4S) \leftarrow O^* \leftarrow O(^3P)$ *process in the 14.07–14.15 eV photon energy region, at two detection angles* ($\theta = 0°, 60°$) *with respect to the horizontal direction of polarization of the photon source*
Transitions are labelled at (J", J'); the transitions from J"=0,1,2 from the initial $O(^3P)$ *state are clear*

In the photon energy region 14.00-17.00 eV, the bands associated with s' ^3D and d' ^3S excited states are allowed on the basis of Russell-Saunders selection rules[24,25], summarized in Table 5.2, for the two steps transitions:

$$O^+(^4S) + e^- \xleftarrow{Monopole} O^* \xleftarrow{Dipole} O(^3P) + h\nu \qquad \text{Eq. 5.2}$$

Table 5.2: Summary of selection rules for dipole and monopole transitions[24,25]

Dipole transition	Monopole transition
ΔL=0, ±1 L=0 ←/→ L=0	ΔL=0
ΔS=0	ΔS=0
ΔJ=0, ± 1 J=0 ←/→ J=0	ΔJ=0
Δl=± 1	-
Laporte rule (even ↔ odd parity)	No change of parity (even ←/→ odd)

In the case of an O^* (s' ^3D) state, $O^+(^4S)$ will be produced with a d free electron and for a O^* (d' ^3S) state, $O^+(^4S)$ will be produced with an s free electron. However, for the bands at ~14.1 eV (corresponding to excitation to a 3s'' ^3P state) and the bands in the 14.00-16.93 eV region (corresponding to excitation to a d' ^3P states), even though they can be accessed by an allowed transition from the ^3P initial state, the parity selection rule forbids production of a ^3P continuum with a $O^+(^4S)$ ionic state.

The continuum $O^+(^4S)$ plus a p free electron is parity forbidden from these O^* states. However, as has been pointed out previously[15,16], autoionization becomes allowed if a coupling scheme which is intermediate between the Russell-Saunders and j-j limits is more appropriate. Then, for example, the 3s'' $^3P_{1,2}$ state can interact with nearby $^3S_1$, $^5S_2$ and $^3D_{1,2}$ states allowing the J'=1 and J'=2 levels of the O^* excited state to autoionize to ^3S, ^5S and ^3D continua with an $O^+(^4S)$ ionic core , hence satisfying the parity selection rule. Similarly, in intermediate coupling, the nominal $O^+(^4S_{3/2})$ ionic ground state acquires a small amount of $^2P_{3/2}$ character which, when combined with s and d free electron character, provides an allowed autoionization route from the O^*(3s'' ^3P) state. These mechanisms will also apply to the *n*d' ^3P states and the $2s2p^5$ ^3P O^* state, although it is noted that in the latter case an extra important factor is that this state interacts strongly with the 3d' ^3P state, which itself relies on a departure from Russell-Saunders coupling for its autoionization strength.

Above the second ionization energy (16.94 eV), all the observed O^* states are allowed in a Russell-Saunders scheme for both the resonance step and the autoionization step. For example, the 4s" ^3P state is produced by an allowed transition from the ground ^3P state and the autoionization to $O^+(^2D)$ plus a d free electron is allowed. Similarly, an O^* (*n*d" ^3D) state can be produced from $O(^3P)$ by an allowed transition and can autoionize to $O^+(^2D)$ and an s or d free electron.

5.2.1 Photoionization cross sections and asymmetry parameter

At each photon energy, the relative photoionization cross sections can be evaluated by taking the intensity measurements made at $\theta = 0°$and $\theta = 60°$, and calculating the relative integrated cross section and asymmetry parameter, β[26].

This has been carried out to give the spectrum shown in Figure 5.6, where comparison has been made with a spectrum obtained by photoionization mass spectrometry (PIMS)[15].

In this PIMS work, an effusive beam of O atoms was produced and relative photoionization cross sections were measured in the photon energy region 13.75 to 18.75 eV using a mass spectrometer to detect O^+ production. The nature of the experiment meant that no state selective measurements were made to determine the state (or states) that O^+ is produced at a particular photon energy.

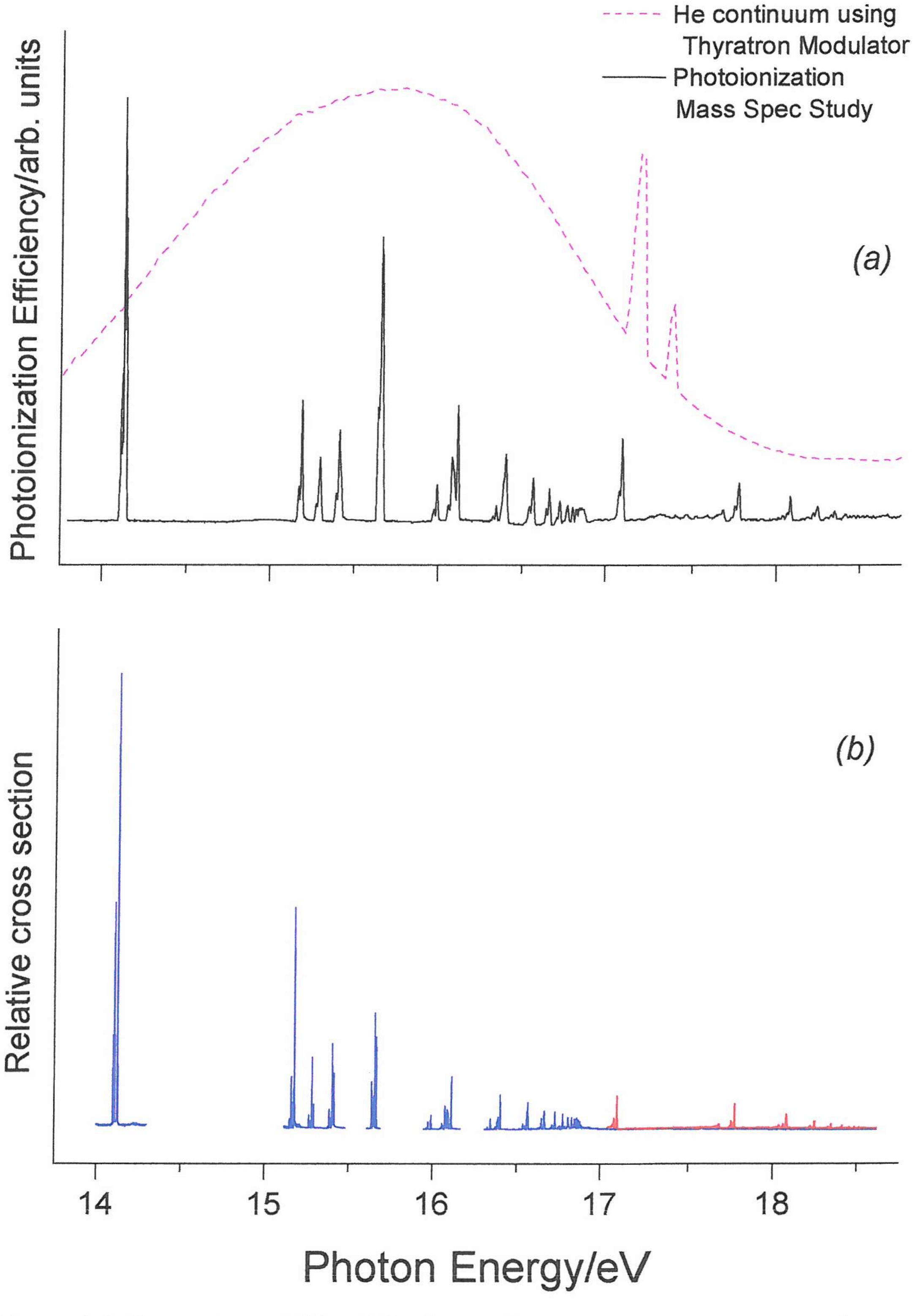

Figure 5.6: Comparison of (b) a CIS relative photoionization cross section plot, derived for $\theta = 54°44'$ in this work with (a) a PIMS $O^+ \leftarrow O^* \leftarrow O(^3P)$ spectrum obtained in Ref. (15). As in Figure 5.4, the blue trace is obtained from $O^+(^4S) \leftarrow (^3P)$ ionization and the red trace is obtained from $O^+(^2D) \leftarrow (^3P)$ ionization.

Comparison of Figures 5.6 *(a)* and 5.6 *(b)* shows that $O^+(^4S)\leftarrow O(^3P)$ is the ionization route in the photon energy region 13.63-16.93 eV, as expected as it is the only available channel, and $O^+(^2D)\leftarrow O(^3P)$ is the main ionization route in the photon energy region 16.95-18.62 eV. This means that ionization of an O^* state occurs mainly to the nearest available ionic state. Also, comparison of the relative band intensities in Figures 5.6 *(a)* and 5.6 *(b)* shows good overall agreement. In particular, for the spectrum recorded in this work, the intensities of the bands in the 14.08-14.14 eV region relative to the intensity of bands at higher photon energy shows good agreement with those of the PIMS study[15].

The bands in the 14.08-14.14 eV photon energy region, and other bands associated with ^3P excited states, were weaker in an angle resolved PES study of van der Meulen *et al.*[13]. The explanation put forward in reference (13) to account for these weak ^3P features was that in the PIMS study[15] traces of oxygen were present in the helium discharge photon source and these led to production of $O^*(^3P)$ states in the discharge which decay by photon emission and these photons then enhance population of O^* states in the photoionization region[27,28]. However, this appears not to be valid given the good agreement of the relative intensities of this present work, the relative intensities measured in earlier work at SRS (see Figure 5.2 *(b)*) and that of the PIMS study[15], and it should be noted that due to the hight vacuum at which the synchrotron is operative (see Chapter 3.4) the partial pressure of oxygen present outside the experimental chamber and inside the beamline is extremely low and this would not support Meulen *et al.* explanation[13].

Comparison of the relative photoionization cross section and asymmetry parameter, β, as a function of photon energy derived from this work with that obtained in the earlier work of van der Meulen *et al.*[13] in a lower resolution study at the ALADDIN Wisconsin Synchrotron Radiation Source[29], has been made over the full photon energy range studied. Examples are shown in Figure 5.6 where comparison of the two β parameter plots indicates that off resonance the values of the asymmetry parameter, β, evaluated in this work agree with those of van der Meulen *et al.*[13], within experimental error. However, the better resolution obtained with the ELETTRA Synchrotron Radiation Sourse[20] makes comparison of the β plots obtained in resonance regions with the results obtained by van der Meulen *et al.*[13] difficult.

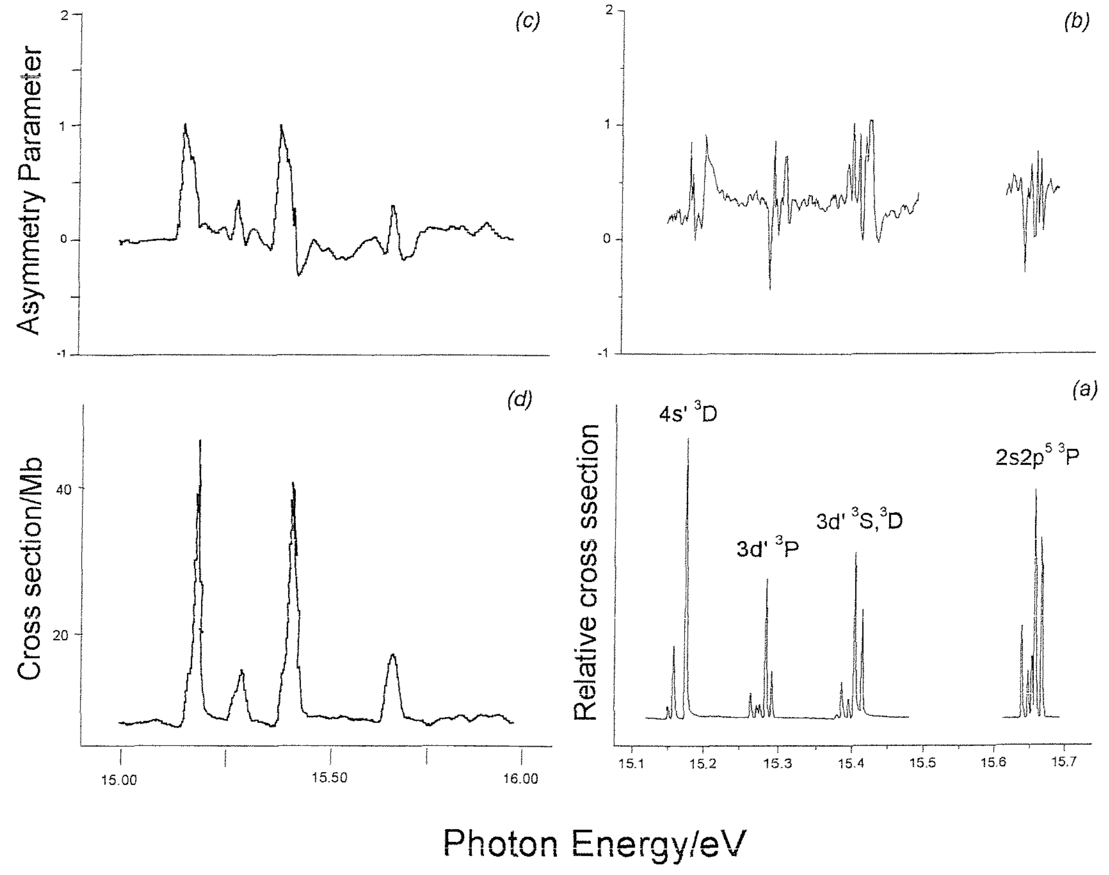

Figure 5.7: Comparison of (a) the relative cross section and (b) the derived asymmetry parameter β plots in the photon energy range 15.1-15.7 eV obtained in this work with (c), (d) the results of van der Meulen et al.[13]. The resolution in the CIS plots of this work is 4 meV compared with the resolution in the CIS plots of Ref. (13) of ~15 meV

A more meaningful comparison of cross sections can be made if the resolution in the relative photoionization cross section plot is reduced from 3 meV to 15 meV(FWHM values), the estimated CIS resolution of the work of van der Meulen *et al.*[13].

This has been done and the results are shown in Figure 5.8.

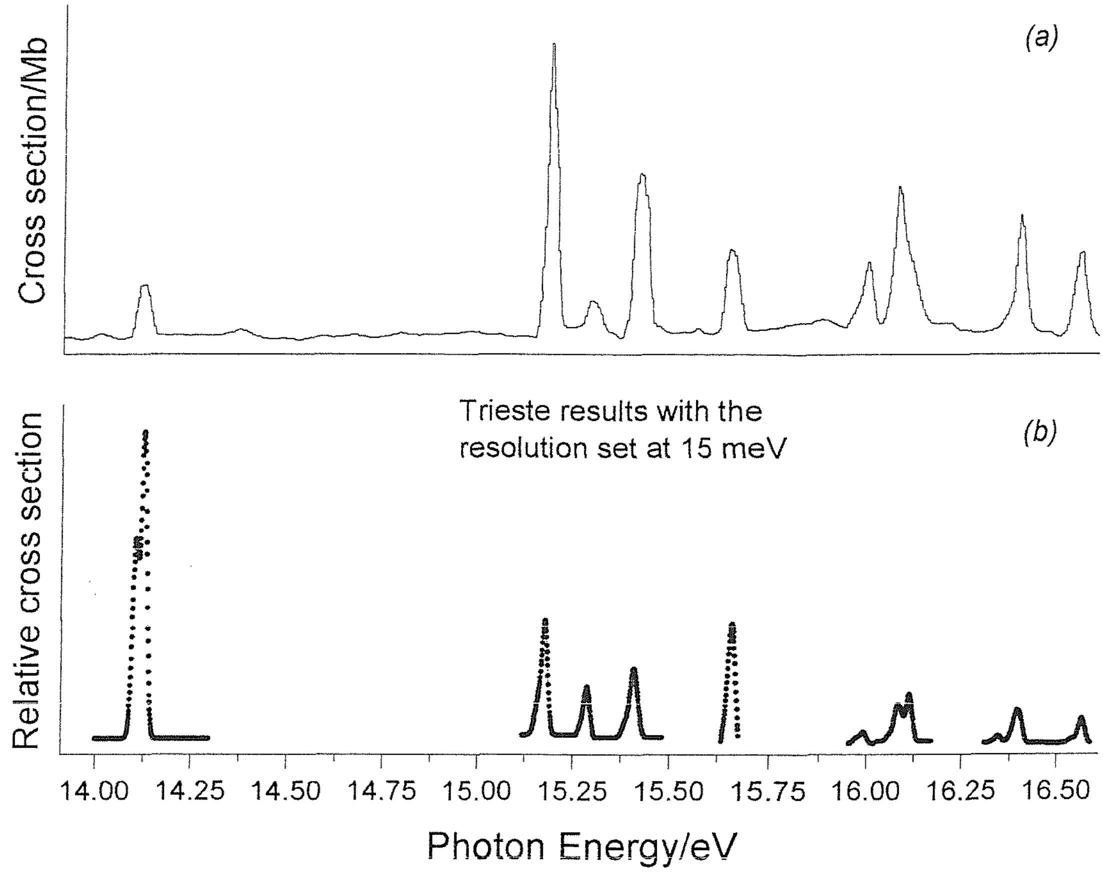

Figure 5.8: Comparison of (b) the relative photoionization cross section as a function of photon energy obtained in this work (with a resolution, FWHM, reduced from 4 meV to ~15 meV) with (a) the corresponding plot obtained by van der Meulen et al.[13]

As can be seen in this figure, the agreement between the two cross section plots is poor. It has already been noted that the relative intensities measured here show much better agreement with the relative intensities measured in a PIMS study[15] (see Figure 5.6), and with the relative intensities obtained in a lower resolution study at Daresbury Synchrotron Radiation Source[19]; therefore the present results are considered more reliable.

Recently, Tayal[14] presented the first detailed theoretical calculations of the asymmetry parameters for photoionization of atomic oxygen across autoionization resonances. Values of β were calculated for the $O^+(^4S, ^2D, ^2P) \leftarrow O(^3P)$ ionizations from threshold to 50 eV photon energy using the R matrix method with extensive configuration interaction being used to describe the ^3P initial state and the final ^3S, ^3P

and ^3D continuum states. As already noted, between the ^4S and ^2D thresholds, the ^3S and ^3D Rydberg states are allowed to autoionize but autoionization of the ^3P states is forbidden in an Russell-Saunders coupling scheme, j-j interaction is required to enable these ^3P excited states between the first and second threshold to autoionize. As this is not taken into account in the work of Tayal[14], the values of β calculated in reference (14) are expected to be in only semi-quantitative agreement with experiment, particularly for ^3P resonances between the first and second thresholds. Comparisons of the computed[14] and experimental β values for the $O^+(^4S) \leftarrow O(^3P)$ and $O^+(^2D) \leftarrow O(^3P)$ ionizations in the photon energy regions 15.00-19.00 eV and 17.05-18.60 eV respectively is shown in Figures 5.9 and 5.10 respectively.

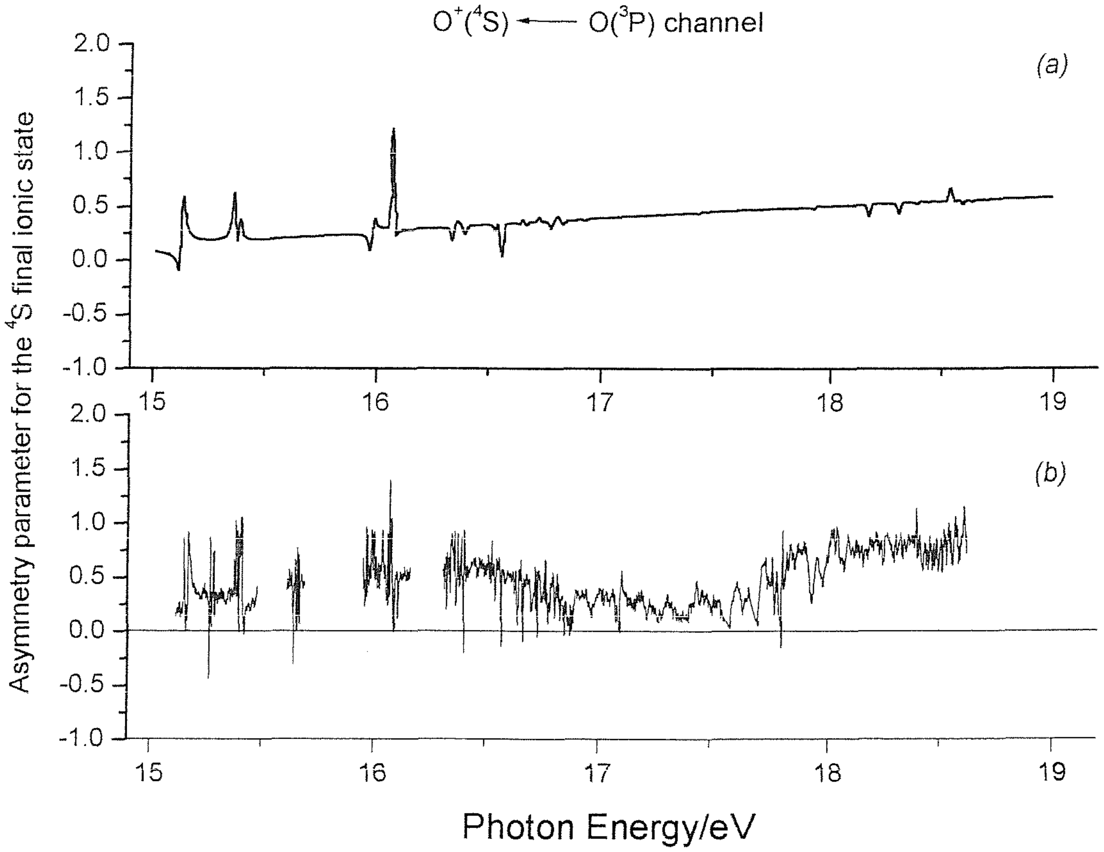

Figure 5.9: Comparison of plots of the asymmetry parameter as a function of photon energy for the $O^+(^4S) \leftarrow O^* \leftarrow O(^3P)$ ionization in the photon energy region 15.00-19.00 eV:
(a) from the calculations of Tayal[14]
(b) derived from the measurements of this work

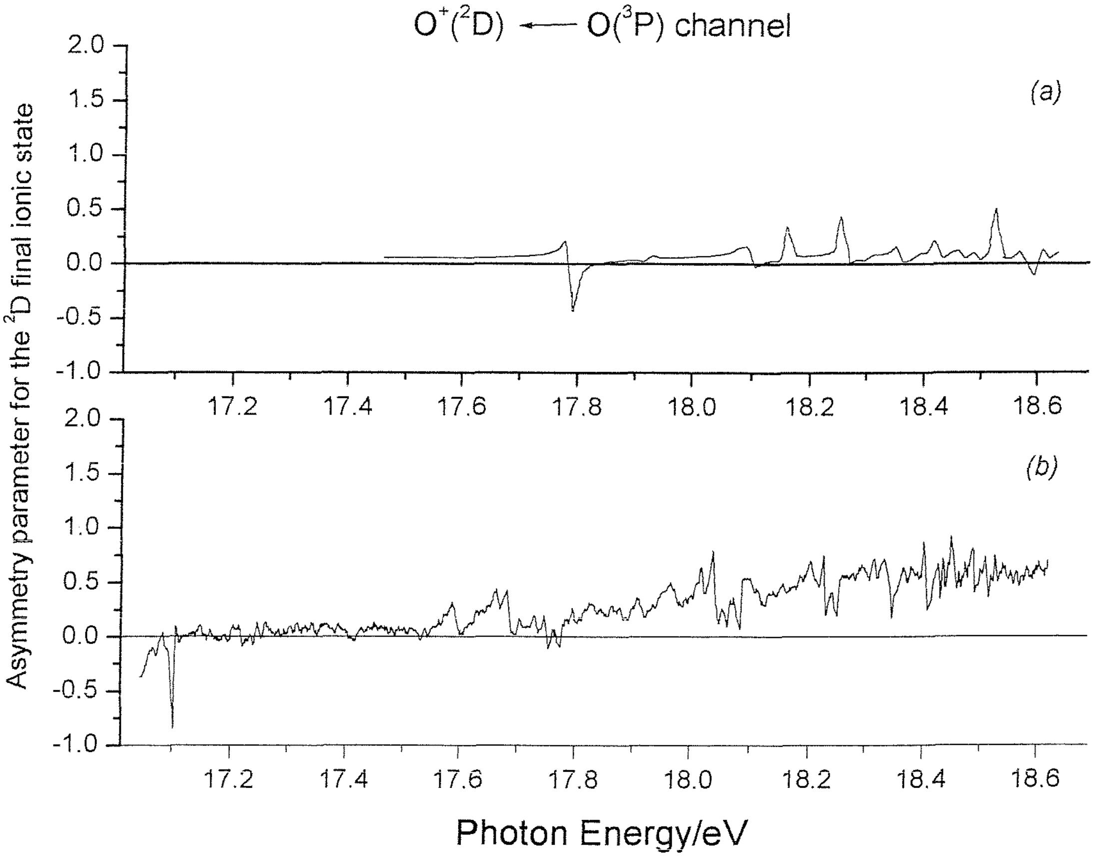

Figure 5.10: Comparison of plots of the asymmetry parameter as a function of photon energy for the $O^+(^2D) \leftarrow O^* \leftarrow O(^3P)$ ionization in the photon energy region 17.05-18.60 eV:
(a) from the calculations of Tayal[14]
(b) derived from the measurements of this work

Figure 5.9 shows reasonable agreement between Tayal's calculations and the experimental results of this work, except for the ^3P resonances which occur below the second ionization threshold, e.g., the bands at ca. 15.28 eV and ca. 15.66 eV where large changes in β are observed experimentally but no change in β relative to the off-resonance background is seen in the calculations. Clearly, this is because these ^3P states derive their autoionization intensities as a result of departure from Russell-Saunders coupling and this is not included in the calculations of reference (14). Figure 5.10 shows poorer agreement between the experimental β and the calculations of Tayal[14] possibly because of the low statistics of the experimental data in the photon energy region 17.05-18.60 eV for the $O^+(^2D) \leftarrow O(^3P)$ ionization.

5.3 Conclusions

In this work, the feasibility of performing angle resolved PES and CIS measurements on reactive species on the vacuum ultraviolet beamline at the ELETTRA Synchrotron Radiation Source at Trieste has been demonstrated by taking oxygen atoms as an example. The relative photoionization cross sections and angular distribution parameters for the $O^+(^4S) \leftarrow O(^3P)$ and $O^+(^2D) \leftarrow O(^3P)$ ionizations have been measured from threshold (13.62 eV) to 19.00 eV, at the highest resolution yet reported. The results obtained have been compared with recent experimental measurements and calculations. Relative photoionization cross sections in some recent experimental studies are only in moderate agreement with those measured in this work. Also, the need for including coupling which is intermediate between the Russell-Saunders and j-j limits in calculations of photoionization cross sections and angular distribution parameters of atomic oxygen is emphasized.

5.4 References

[1] L. A. Hall and H. E. Hinteregger
Journal of Geophysical Research **75**, 6959 (1970)

[2] K. Takayanagi and Y. Itikava
Space Science Reviews **11**, 380 (1970)

[3] R. C. Whitten and I. G. Popoff
Fundamentals of Aeronomy
Wiley & Sons, New York, 1971

[4] N. Jonathan, D. J. Smith and K. J. Ross
Journal of Chemical Physics **53**, 3758 (1970)

[5] N. Jonathan, A. Morris, D. J. Smith and K. J. Ross
Chemical Physics Letters **7**, 497 (1970)

[6] J. A. R. Samson and V. E. Petrosky
Physical Review A **9**, 2449 (1974)

[7] J. A. R. Samson and W. H. Hancock
Physics Letters **61 A**, 380 (1977)

[8] J. L. Dehmer and P. M. Dehmer
Journal of Chemical Physics **67**, 1782 (1977)

[9] M. I. A. Hussein, D. M. P. Holland, K. Codling, P. R. Woodruff and E. Ishiguro
Journal of Physics B **18**, 2827 (1985)

[10] J. A. R. Samson and P. N. Pareek
Physical Review A **31**, 1470 (1985)

[11] W. J. van der Meer, P. van der Meulen, M. Volmer and C. A. de Lange
Chemical Physics **126**, 385 (1988)

[12] G. Prumper, B. Obst, W. Benten, B. Zimmermann, P. Zimmermann and U. Becker
Journal of Physics B **32**, 4101 (1999)

[13] P. van der Meulen, M. O. Krause and C. A. deLange
Physical Review A **43**, 5997 (1991)

[14] S. S. Tayal
Journal of Physics B **34**, 2215 (2001)

[15] P. M. Dehmer, J. Berkowitz and W. A. Chupka
Journal of Chemical Physics **59**, 5777 (1973)

[16] P. M. Dehmer, W. L. Luken and W. A. Chupka
Journal of Chemical Physics **67**, 195 (1977)

[17] R. E. Huffman, J. C. Larrabee and Y. Tanaka
Journal of Chemical Physics **46**, 2213 (1967)

[18] P. M. Dehmer
Journal of Chemical Physics **62**, 584 (1975)

[19] http://www.dl.ac.uk

[20] http://www.elettra.trieste.it

[21] A. Derossi, F. Lama, M. Piacentini, T. Prosperi and N. Zema
Review of Scientific Instrumentation **66**, 1718 (1995)

[22] D. Desiderio, S. DiFonzo, B. Diviacco, W. Jark, J. Krempasky, R. Krempaska, F. Lama, M. Luce, H. C. Mertins, M. Piacentini, T. Prosperi, S. Rinaldi, F. Schefers, F. Schmolla, G. Soulle, L. Stichauer, S. Turchini, R. P. Walker and N. Zema
Synchrotron Radiation News **12**, 34 (1999)

[23] C. E. Moore
Atomic Energy Levels
U.S. Government Printing Office, Washington DC, 1952, Vol. 1

[24] J. M. Hollas
Modern Spectroscopy
Wiley & Sons, Chichester, 1996

[25] H. G. Kuhn
Atomic Spectra
Longmans, London, 1964

[26] C. N. Yang
Physical Review **74**, 764 (1984)

[27] D. M. de Leeuw and C. A. de Lange
Chemical Physics **54**, 123 (1980)

[28] J. A. R. Samson and V. E. Petrosky
Journal of Electron Spectroscopy and Related Phenomena **3**, 461 (1974)

[29] http://www.src.wisc.edu/default.html

Chapter 6

6 PHOTOELECTRON SPECTROSCOPY OF OH AND OD RADICALS

This Chapter reports studies of photoelectron spectroscopy using Synchrotron Radiation on the OH and OD radicals.

The Chapter is organized as follows. In section 6.1 previous spectroscopy investigations on OH and OD that are considered important for the present work are briefly reviewed. Section 6.2 presents the results of the measured CIS spectra, and resonant photoelectron spectra, together with their interpretations. Section 6.3 summarizes the results obtained.

6.1 Previous investigations on OH and OD radicals with photoelectron spectroscopy

Over the past 30 years, the hydroxyl radical, OH, has been one of the most thoroughly studied simple diatomic hydrides due to its importance in the chemistry of the Earth's atmosphere[1], combustion processes[2,3], and the interstellar medium[4].

During this time, OH has been the focus of several different experimental and theoretical studies. Of particular interest has been an investigation of its electronic structure via experimental studies involving its interaction with ultraviolet (UV) and vacuum ultraviolet (VUV) radiation. The low-lying electronic states of the neutral molecule have been extensively studied by experiment[5-15] and theory[16-18].

The ground state electronic configuration of OH and OD is $1\sigma^2 2\sigma^2 3\sigma^2 1\pi^3$,which gives rise to a $^2\Pi$ state.

Photoionization from the valence 1π molecular orbital produces the X $^3\Sigma^-$, a $^1\Delta$ and b $^1\Sigma^+$ ionic states at adiabatic ionization energies (AIEs) of 13.01, 15.17 and 16.61 eV respectively[8]. The potential energy curves of these ionic states are very similar to that of the ground state of the neutral because of the non-bonding character of the 1π orbital. The removal of one electron from the 3σ shell gives rise to the A $^3\Pi$ and c $^1\Pi$ ionic states at AIEs of 16.48 and 18.30 eV respectively[8].

Photoabsorption measurements in the 1830-1150 Å region (6.8-10.8 eV) have been carried out by Douglas[5], Viney[6] and Nee *et al.*[7].

Photoelectron spectra of OH and OD have been recorded with HeI radiation by Katsumata *et al.*[19] and more recently by van Lonkhuyzen *et al.*[8]. In the first study[19] the H+NO_2 reaction was used to produce OH and OD, and the first and second PE bands were observed, while bands at higher ionization energies could not be observed because of the overlap with bands from secondary reaction products. In the second PE investigation[8], where OH and OD were produced by the F+H_2O and the F+D_2O reactions, four of the five expected OH (OD) bands could be observed.

Little information is available concerning autoionization of OH and OD. The UV absorption spectrum at wavelengths shorter than 1200 Å (10 eV) is poorly resolved and resonant states above the first ionization energy have only been observed by photoionization mass spectrometry (PIMS)[9,15]. In the work of Dehmer[9], performed with a high-intensity VUV helium continuum radiation source and an near-normal incidence monochromator over the photon energy region 13.0-16.5 eV, only one Rydberg series was identified converging to the second ionization limit (a $^1\Delta$). Most bands associated with excitation to Rydberg states were unassigned.

In an attempt to assign these Rydberg bands to particular Rydberg series, Cutler *et al.*[15] repeated this work, on both OH and OD. They performed a higher resolution study at the Aladdin Synchrotron Radiation Source[20] in Wisconsin, over the photon energy range 13.0-18.2 eV. Two additional Rydberg series were observed, converging to the fourth and third ionization limits, b $^1\Sigma^+$ and A $^3\Pi$ respectively. Rotational structure associated with the transition $OH^*(a\ ^1\Delta, 3d) \leftarrow OH(X\ ^2\Pi, v''=0)$ was recorded, although no analysis of this structure was presented. Also, for the $OH^*(A\ ^3\Pi, 3d) \leftarrow OH(X\ ^2\Pi, v''=0)$ absorption, components were observed with $v'=0$, 1, and 2. For higher values of principal quantum number (n=4-8), only the $v'=0 \leftarrow v''=0$ components could be identified but positions of the other vibronic transitions (i.e. $v'=1, 2 \leftarrow v''=0$ for each n) were suggested based on results of earlier PES work.

The Southampton PES group has previously carried out an investigation into the photoelectron spectroscopy of OH and OD radicals[21] using Synchrotron Radiation at the SRS in Daresbury[22]. Rydberg states which are parts of series which converge to the second and third ionization limits, a $^1\Delta$ and A $^3\Pi$ respectively, were observed in the CIS spectra of the first and second PE bands of both OH and OD. These were confidently assigned by comparison with previous work as autoionizations via Rydberg states.

To evaluate the viability of further synchrotron studies on small radicals using the third generation Synchrotron Radiation Source ELETTRA[23], a selection of the measurements previously made at SRS[22] were repeated (see also Chapter 5).

The (a $^1\Delta$, nd) Rydberg series observed previously was re-investigated, to try to take advantage of the increased flux and improved narrow bandwidth available at ELETTRA[23], with the aim of obtaining assignments of the observed bands.

6.2 Results and discussion

As already discussed, natural extension of the previous work made by the PES Southampton group was to repeat some of the PES and CIS measuremnts at the SRS in Daresbury[22] using the third generation Synchrotron Radiation Source ELETTRA[23]. Moreover evidence for different states that arise from the different coupling of the angular momentum of the Rydberg orbital with the ionic core has been found[21], and this issue has been investigated more in depth using the high resolution radiation available from ELETTRA[23].

As described in the previous instrumental section (see Chapter 4.3.2), OH (OD) radicals were produced by the fast reaction of atomic hydrogen (deuterium) with nitrogen dioxide:

$$H(D) + NO_2 \rightarrow OH(OD) + NO \qquad \text{Eq. 6.1}$$

Hydrogen (deuterium) atoms were produced by passing a flowing mixture of H_2 (D_2) and He through a microwave discharge at 2.45 GHz in a glass inlet tube coated with phosphoric acid[21]. NO_2 was introduced into the $H_2(D_2)/H(D)/He$ mixture, about 3 cm above the photon beam, through an inner inlet tube, 3 mm internal diameter, see Figure 4.5 *(c)*. Test experiments were carried out in Southampton in order to find out the optimum pressures and mixing distance above the photon beam which maximise the intensities of OH bands with respect to the bands from the secondary reactions:

$$OH + OH \rightarrow H_2O + O \quad \text{and} \quad O + O + M \rightarrow O_2 + M \qquad \text{Eq. 6.2}$$

CIS spectra were then recorded for the $OH^+(X\ ^3\Sigma^+, v^+=0) \leftarrow OH(X\ ^2\Pi, v''=0)$ and $OD^+(X\ ^3\Sigma^+, v^+=0) \leftarrow OD(X\ ^2\Pi, v''=0)$ vibrational components, in the photon energy range 13.1-15.1 eV, where structure is expected to be observed.

Figure 6.1 shows the photoelectron spectra acquired in ELETTRA at $h\nu = 21.22$ eV for the $H+NO_2$ reaction with the H_2/He discharge on and off and at a mixing distance above the photon beam of 3 cm.

The spectra obtained are in good agreement with those previously recorded by Katsumata *et al.*[19] and by the Southampton PES group[21].

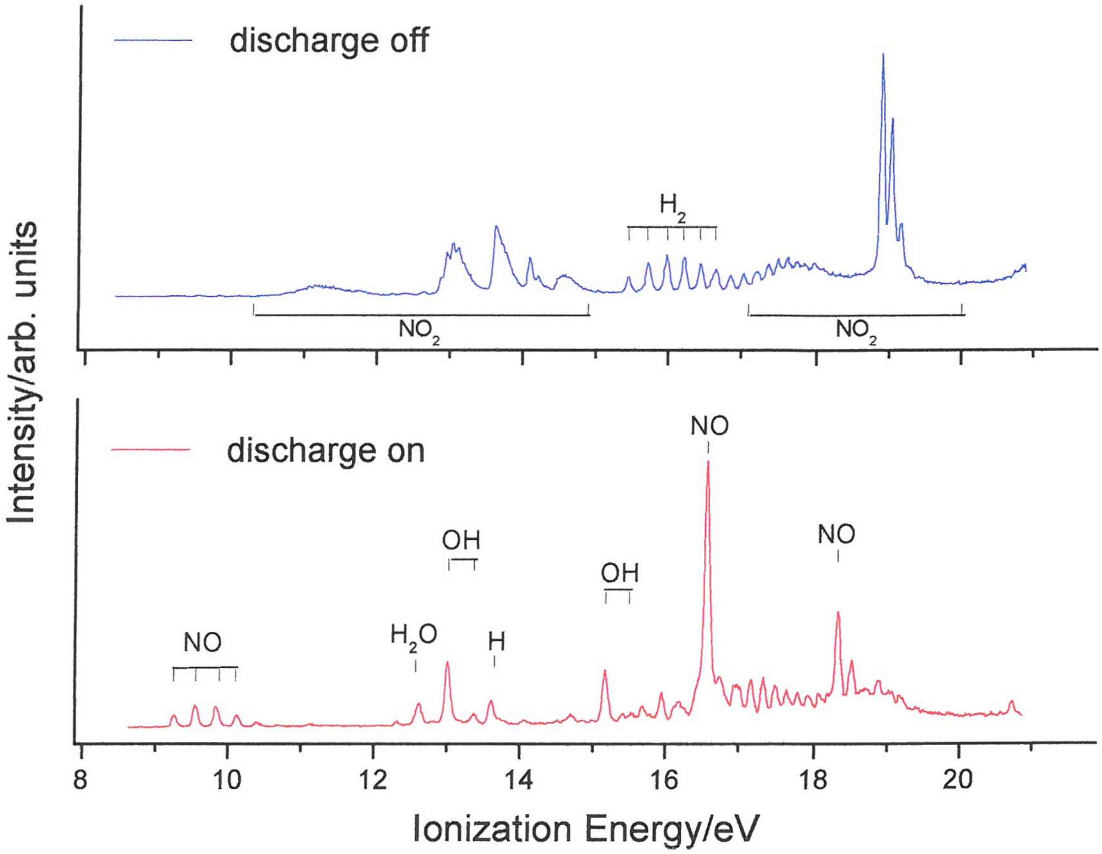

Figure 6.1: Photoelectron spectrum recorded at hν =21.22 eV of the reaction
$H+NO_2 \rightarrow OH+NO$
with discharge off (blue trace) and discharge on (red trace)

As can be seen from Figure 6.1 there is almost a complete reaction of the NO_2 in the discharge-on spectrum. This was the first objective, to use sufficient H atoms to remove all the NO_2 and observe bands of OH.

The first two photoelectron bands of OH at 13.01 eV and 15.17 eV AIEs corresponding to the ionizations $OH^+(X\ ^3\Sigma^-, v^+=0) \leftarrow OH(X\ ^2\Pi, v''=0)$ and $OH^+(a\ ^1\Delta, v^+=0) \leftarrow OH(X\ ^2\Pi, v''=0)$ have been maximized with respect to the H_2O band at 12.62 eV (by optimizing the mixing distance and reagent partial pressures, in Southampton) and the first vibrational component of each OH band can be observed. Bands associated with H_2, H and NO were observed in the discharge on spectrum, along with signals arising from H_2O produced by secondary reactions.

In this study the most intense vibrational component for the first band of OH $OH^+(X\,^3\Sigma^-, v^+=0) \leftarrow OH(X\,^2\Pi, v''=0)$ was selected for CIS studies.

Figure 6.2 shows the photoelectron spectrum acquired in ELETTRA at $h\nu=21.22$ eV for the D+NO_2 reaction with the H_2/He discharge on and at a mixing distance above the photon beam of 3 cm.

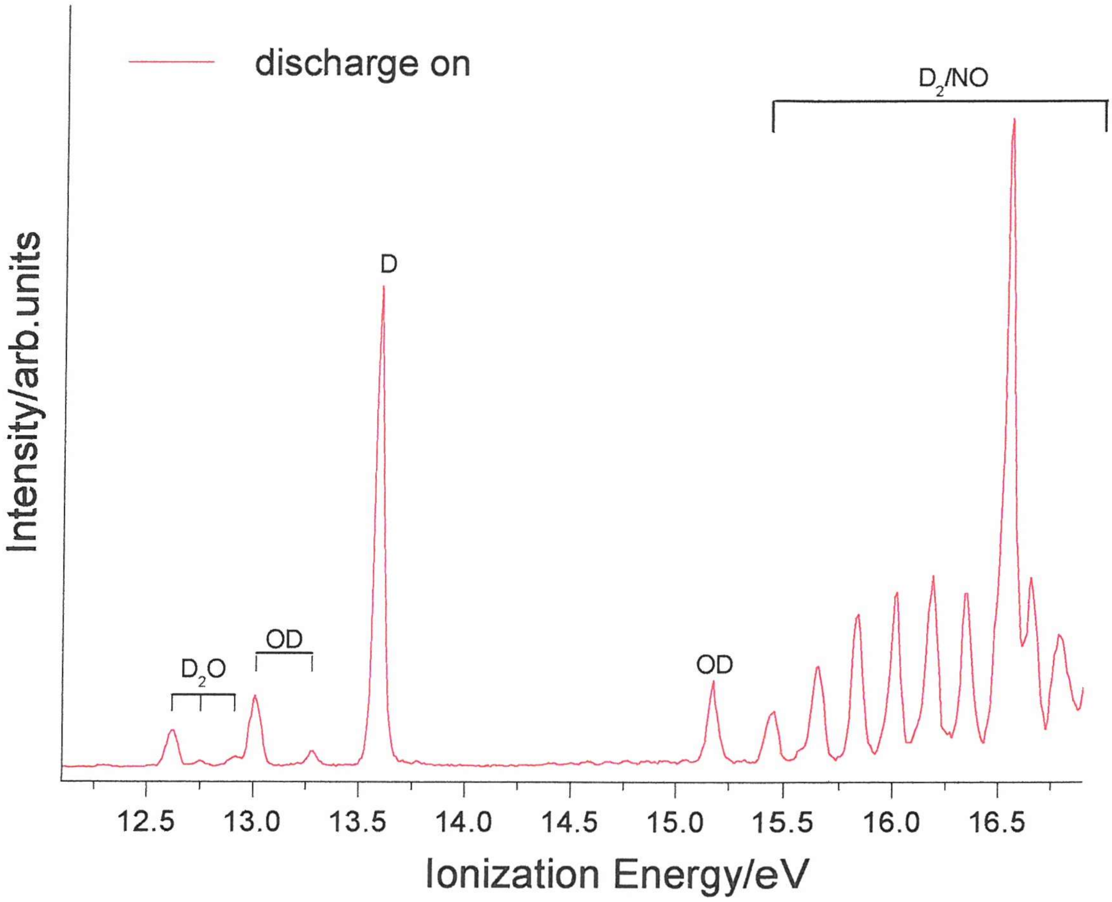

Figure 6.2: Photoelectron spectrum at $h\nu=21.22$ *eV of the reactions*
$D+NO_2 \rightarrow OH+NO$
with discharge on

The photoelectron spectrum of the D_2/He+NO_2 mixture recorded in ELETTRA, shown in Figure 6.2 is very similar to the spectrum shown in Figure 6.1. The main difference is that the vibrational separations in the D_2, D_2O and OD bands are smaller than in the corresponding bands of H_2, H_2O and OH. The measured vibrational separations for the first photoelectron bands of OH and OD are 366 and 266 meV respectively and they are compatible with the values known from other spectroscopic investigations[19] (366 and 280 meV).

6.2.1 *CIS spectra for the ($X\,^3\Sigma^-$, $v^+=0$)← ($X\,^2\Pi$, $v''=0$) ionizations of OH and OD in the photon energy range $h\nu=13.10\text{-}15.01$ eV*

CIS spectra have been recorded for the (X $^3\Sigma^-$, $v^+=0$)←(X $^2\Pi$, $v''=0$) ionizations of OH and OD in the photon energy range 13.10–15.10 eV, and the spectrum obtained for OH$^+$(X $^3\Sigma^-$, $v^+=0$)←OH(X $^2\Pi$, $v''=0$) has been compared with the spectrum of reference (21) previously recorded at the SRS[22]. The CIS technique cannot distinguish between different photoionization processes with the same ionization energy. Potential contaminants for this reaction are NO_2, H_2O and NO. CIS spectra of these molecules at the ionization energy used to record spectra of OH and OD (13.01 eV) have been previously recorded[21] by the Southampton PES group and the conclusion is that only NO contributes to peaks in the CIS spectra of OH and OD. The peak due to NO is marked with an asterisks (*) in the following CIS spectra.
In Figures 6.3-6.8 the CIS spectra recorded for the (X $^3\Sigma^-$, $v^+=0$)←(X $^2\Pi$, $v''=0$) ionization of both OH and OD in the photon energy range 13.10–15.10 eV and at $\theta=60°$ with respect to the major polarization axis of the photon source, are shown.
The spectrum shown in Figure 6.3 is in good agreement with spectra of reference (21) recorded at the SRS[22]; however, a much higher resolution is obtained in this present work and rotational structure can be observed in the vibrational components. This is demonstrated in Figure 6.5, which expands the photon energy range 13.45-14.00 eV. In Figures 6.5 and 6.6 rotationally resolved features are shown for autoionization via OH/OD*(a $^1\Delta$, 3d) Rydberg states, recorded in the (X $^3\Sigma^-$, $v^+=0$)←(X $^2\Pi$, $v''=0$) CIS spectrum. In Figures 6.7 and 6.8 the results of this investigation are compared with the results obtain in the PIMS studies of references (9) and (15).

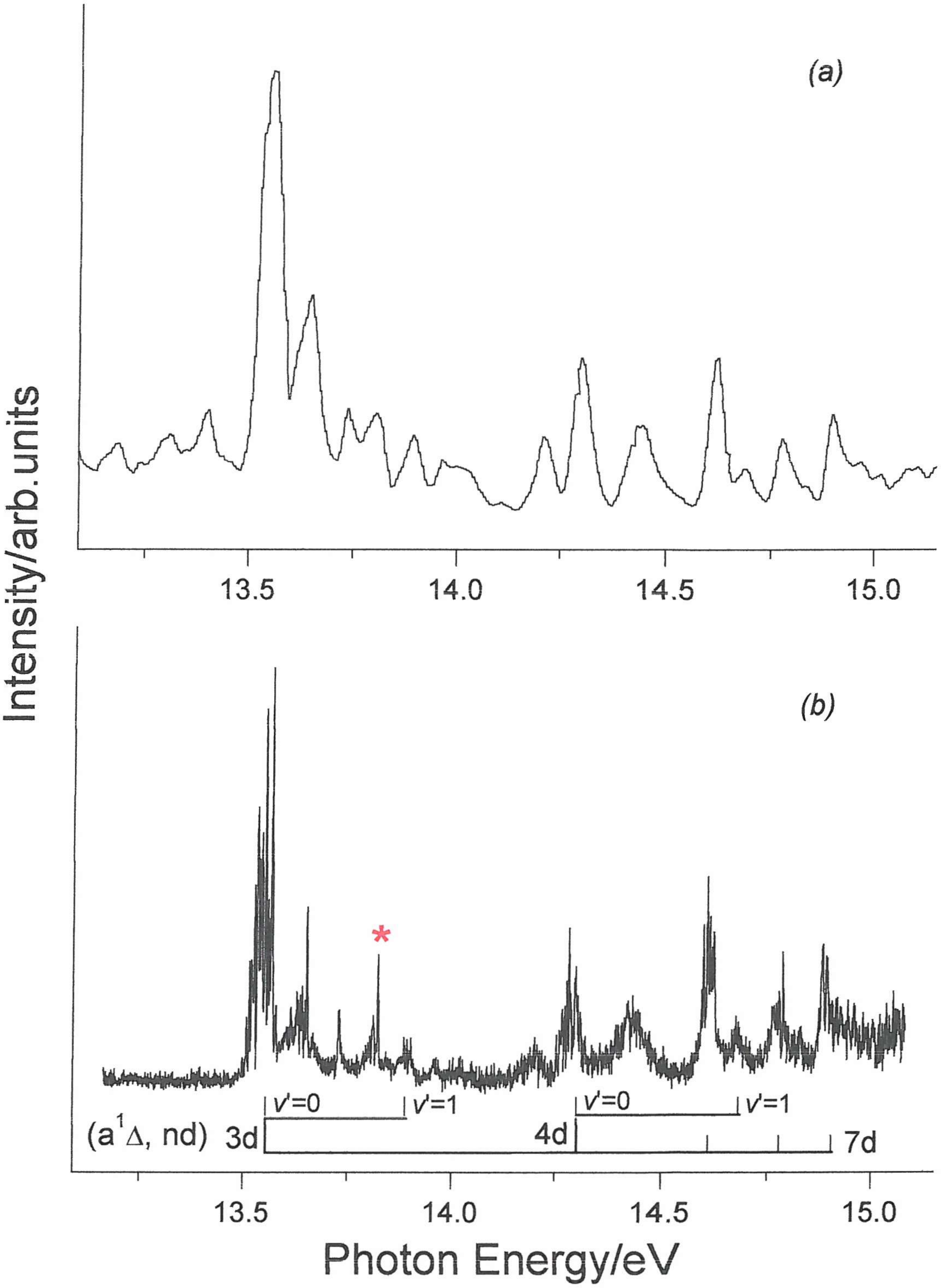

Figure 6.3: CIS spectrum for the $OH^+(X\,^3\Sigma^-, v^+=0) \leftarrow OH(X\,^2\Pi, v''=0)$ ionization in the photon energy range 13.05–15.05 eV recorded at $\theta=60^\circ$ (a) at Daresbury on BL 3.2 and (b) at ELETTRA on BL 4.2
The peak due to NO is marked with an asterisks (*) in the CIS spectrum
Positions of $OH^*(a\,^1\Delta, nd)$ Rydberg states are indicated

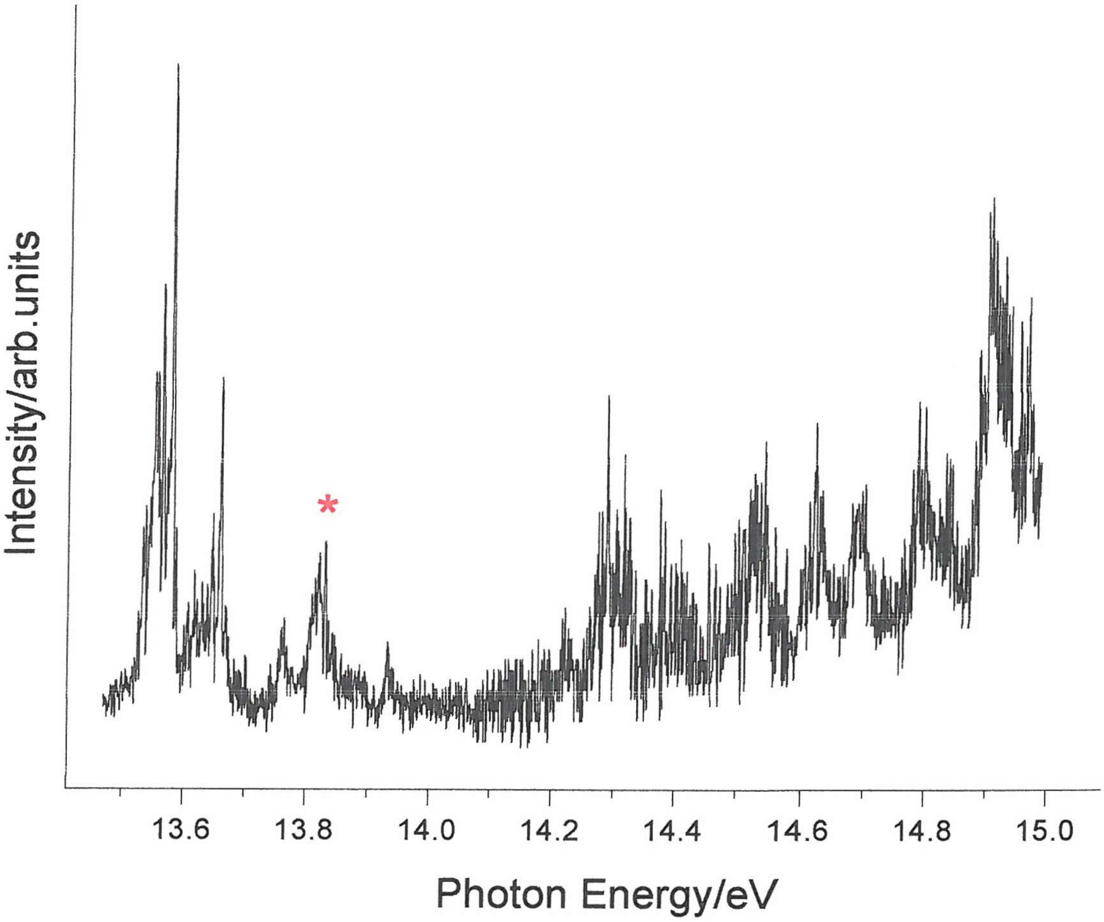

Figure 6.4: CIS spectrum for the $OD^+(X\,^3\Sigma^-,\ v^+=0) \leftarrow OD(X\,^2\Pi,\ v''=0)$ *ionization in the photon energy range 13.10–15.10 eV*
The peak due to NO is marked with an asterisks (*) in the CIS spectrum

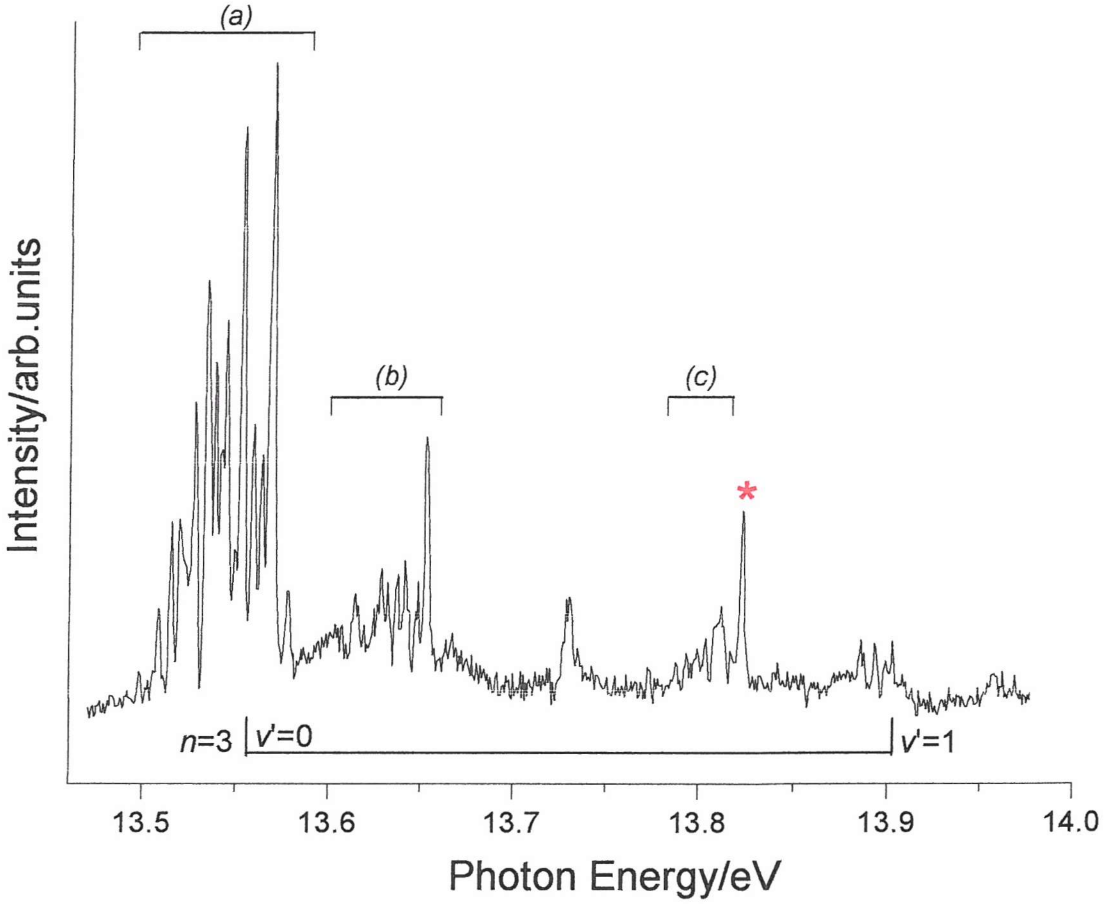

Figure 6.5: CIS spectrum of the $OH^+(X\,^3\Sigma,\ v^+=0) \leftarrow OH(X\,^2\Pi,\ v''=0)$ *ionization in the photon energy range 13.45–14.00 eV*
The peak due to NO is marked with an asterisks (*) in the CIS spectrum

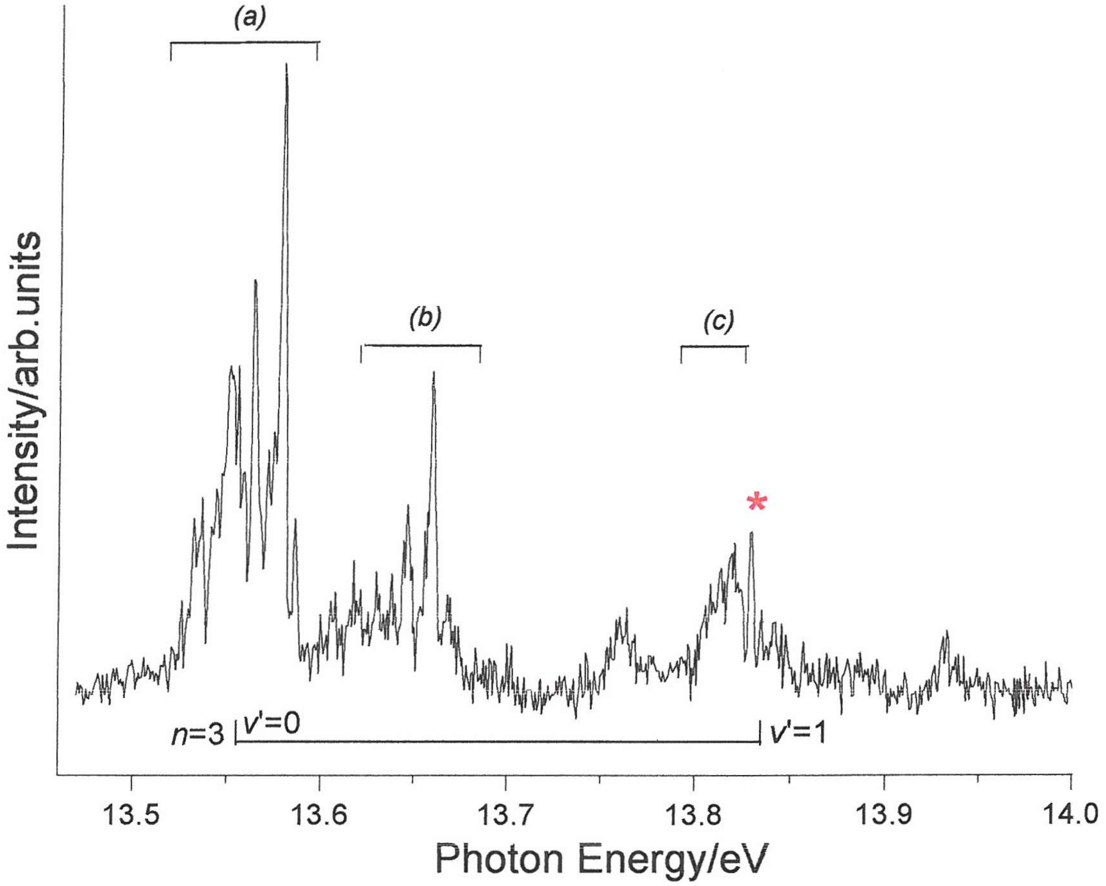

Figure 6.6: CIS spectrum of the $OD^+(X\,^3\Sigma,\ v^+=0) \leftarrow OD(X\,^2\Pi,\ v''=0)$ *ionization in the photon energy range 13.45–14.00 eV*
The peak due to NO is marked with an asterisks (*) in the CIS spectrum

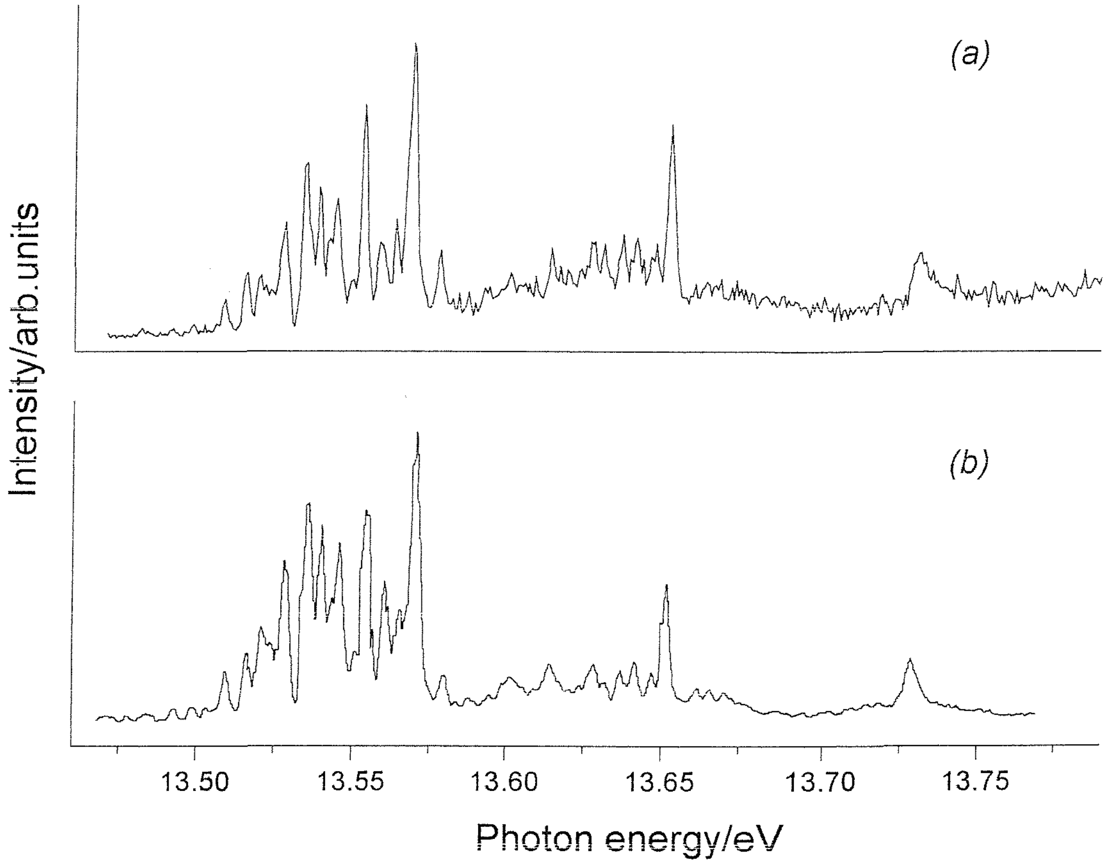

Figure 6.7: Comparison of:

(a) a CIS spectrum of the $OH^{+}(X\,^{3}\Sigma,\ v^{+}=0) \leftarrow OH(X\,^{2}\Pi,\ v''=0)$ *ionization in the photon energy range 13.45–13.80 eV with*

(b) a PIMS spectrum obtained by Dehmer[9]

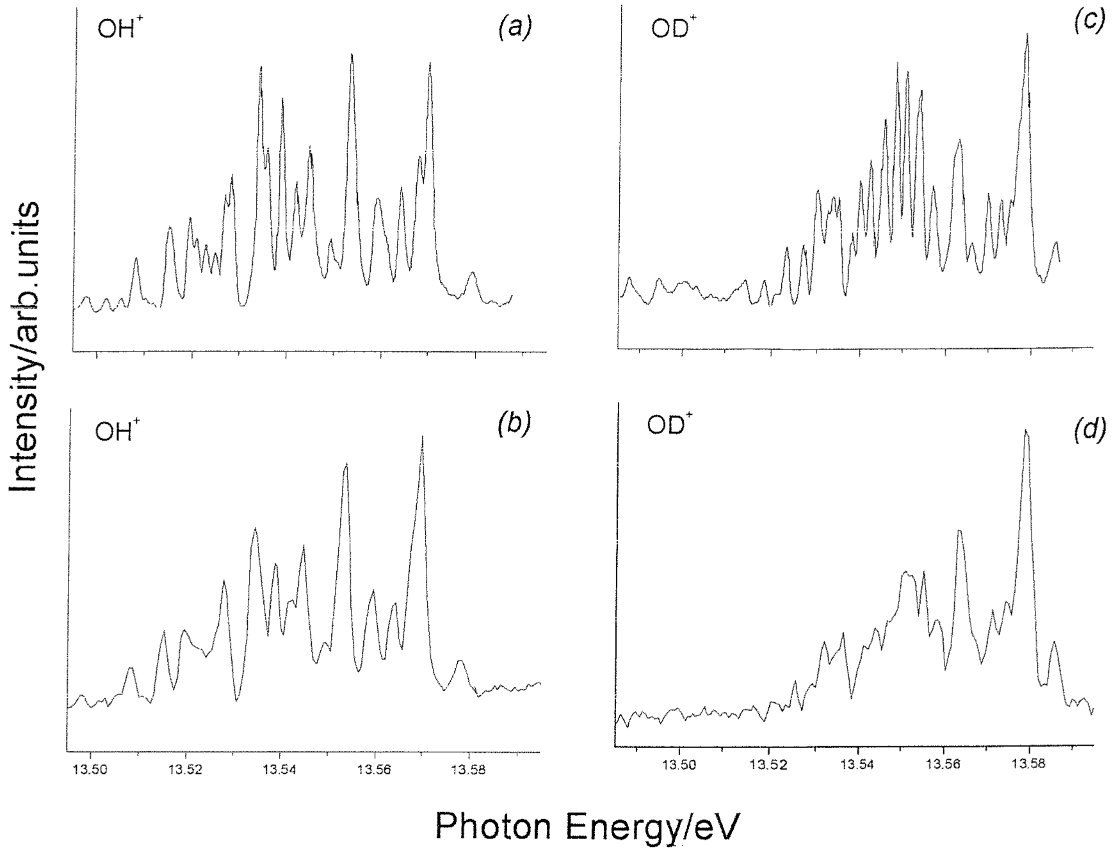

Figure 6.8: Comparison of:

(a) a PIMS spectrum of OH obtained in Ref. (15) with

(b) a CIS spectrum of the $OH^+(X\,^3\Sigma,\ v^+=0) \leftarrow OH(X\,^2\Pi,\ v''=0)$ *ionization in the photon energy range 13.50–13.60 eV, this work*

(c) a PIMS spectrum of OD obtained in Ref. (15) with

(d) a CIS spectrum of the $OD^+(X\,^3\Sigma,\ v^+=0) \leftarrow OD(X\,^2\Pi,\ v''=0)$ *ionization in the photon energy range 13.50–13.60 eV, this work*

Figure 6.7 shows a good agreement with the previously recorded PIMS spectrum recorded by Dehmer[9], with features with linewidths of ~2meV.

Figure 6.8 shows a good agreement of the results of this work for both OH and OD with the previously recorded PIMS spectra recorded by Cutler *et al.*[15], with features with linewidths of ~2meV.

From references (9) and (15), all the rotationally resolved features in this region can be assigned to autoionization via $OH^*(a\,^1\Delta, 3d)$ Rydberg states.

The rotational structure shown in Figures 6.5 and 6.6 has not yet been assigned. The spin-orbit splitting in the $^2\Pi$ state (139.1 cm^{-1}, 0.017 eV)[24] means that the $^2\Pi_{1/2}$ state will be 139.1 cm^{-1} above the $^2\Pi_{3/2}$ state with a relative population of 51% at 300 K. From the method used to make OH, ionization will occur from both spin-orbit components with a Boltzmann population of the rotational levels at ≈300 K.

In the CIS experiments, the OH$^+$(X $^3\Sigma^-$, v^+=0)←OH(X $^2\Pi$, v''=0) ionization is selected and the structure shown in Figure 6.5 must arise from the OH$^+$(a $^1\Delta$, 3d, v''=0, J')←OH(X $^2\Pi_{1/2,\,3/2}$, v''=0, J") transitions.

The OH*(a $^1\Delta$, 3d) Rydberg state is expected to give the (a $^1\Delta$, 3dσ), (a $^1\Delta$, 3dπ) and (a $^1\Delta$, 3dδ) components in $C_{\infty v}$ symmetry. These give rise to the following states:

OH*[a $^1\Delta$, 3dσ] ($^2\Delta$)
OH*[a $^1\Delta$, 3dπ] ($^2\Pi$)/($^2\Phi$)
OH*[a $^1\Delta$, 3dδ] ($^2\Sigma$)/($^2\Gamma$)

According to the selection rules for an electric dipole transition (see Chapters 2.2 and 5.2), only the $^2\Sigma$←$^2\Pi$, $^2\Pi$←$^2\Pi$ and $^2\Delta$←$^2\Pi$ transitions are allowed.

Bearing in mind that the 3d and 4s Rydberg orbitals in OH and OD are oxygen in character and considering the value of the quantum defects for molecular oxygen[25,26] [*n*sσ=1.06, *n*dσ=0.18, *n*dπ=0.11, *n*dδ=0.02], then using the known second AIE of OH as 15.17 eV, excitation energies can be calculated from the OH(X $^2\Pi$) state as follows:

the excitation energy (ExEn) of the [$\sigma^2\pi^2$ $^1\Delta$, 4sσ] ($^2\Delta$) state is 13.595 eV
the ExEn of the [$\sigma^2\pi^2$ $^1\Delta$, *n*dδ] ($^2\Sigma$) state is 13.639 eV
the ExEn of the [$\sigma^2\pi^2$ $^1\Delta$, *n*dπ] ($^2\Pi$) state is 13.542 eV
the ExEn of the [$\sigma^2\pi^2$ $^1\Delta$, *n*dσ] ($^2\Delta$) state is 13.460 eV

For these reasons the suggested assignment of the 3d bands is $^2\Delta<^2\Pi<^2\Sigma$, corresponding to *(a)* < *(b)* < *(c)* as shown in Figure 6.5. However, these values should only be used as a guide as to where the actual values are as they were obtained for molecular oxygen and do not apply to OH. However, the transitions to the 3d states are expected to be more intense than the transitions to the 4s Rydberg state. This is due to the fact that the s Rydberg states are more prone to predissociation than the d Rydberg state because of their bigger electron densities close to the core, and the transition moments to *n*s Rydberg states are smaller than those to (*n*-1)d Rydberg states.

Attempts have been made to simulate this structure using computed one-photon Rotational Line Strengths[27-30] (RLS). In Figure 6.9 the experimental first band envelope at ≈13.55 eV (left hand side) is compared with results of rotational line strength calculations for the $^2\Pi\leftarrow^2\Pi$, $^2\Delta\leftarrow^2\Pi$ and $^2\Sigma\leftarrow^2\Pi$ transitions (right hand side). These calculations were performed assuming a rotational temperature T=300 K, a resolution of 15 cm^{-1} and using *Hund's case a* for the $^2\Pi$ and $^2\Delta$ states, and *Hund's case b* for the $^2\Sigma$ state.

Comparison of the RLS envelopes with the experimental envelope in Figure 6.9 shows that the range covered by the experimental envelope (0.08 eV) is approximately the same as the range covered by the simulations. Although the comparison of the computed envelopes with the experimental one is only moderate, it appears that the experimental envelope at ≈13.55eV excitation energy fits best with a $^2\Pi\leftarrow^2\Pi$ transition. The second band at ≈13.66 eV would then fit best as a $^2\Delta\leftarrow^2\Pi$ transition and the third band at ≈13.81 eV would fit best as a $^2\Sigma\leftarrow^2\Pi$ transition. With this assignment the quantum defects can be calculated as $nd\sigma=0.006$, $nd\pi=0.085$, $nd\delta=-0.165$ with a relative excited state order $^2\Pi<^2\Delta<^2\Sigma$.

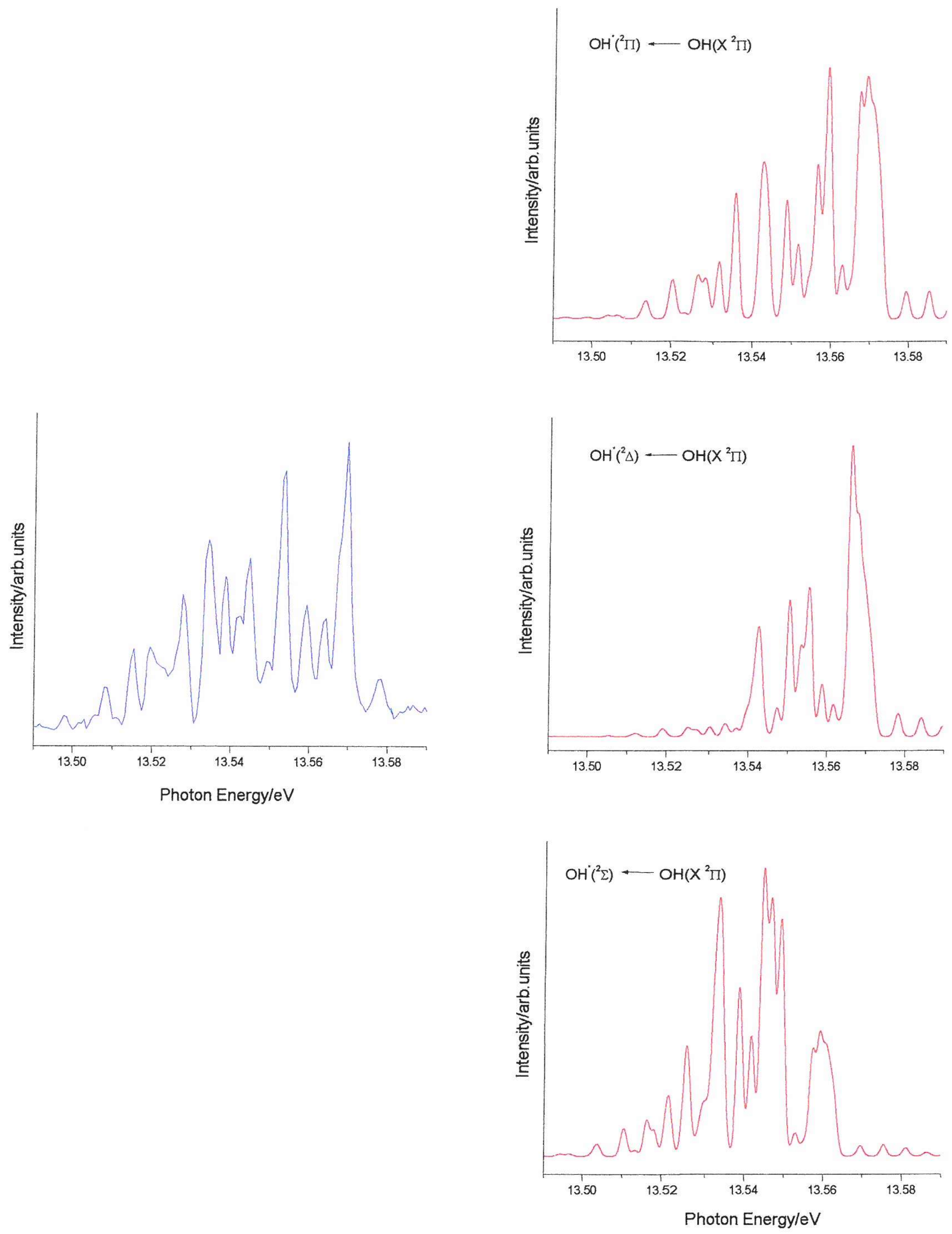

Figure 6.9: Result of rotational line strength calculations, right hand black trace, compared to the experimental band at ≈13.55 eV, left hand blue trace

Inspection of published papers[31-36] on NO reveals why the simulated rotational envelopes of the first observed 3d band in the OH$^+$(X $^3\Sigma^+$, v^+=0)←OH(X $^2\Pi$, v''=0)

CIS spectrum cannot be adequately simulated using one-photon rotational line strengths. The reason is that there is l-mixing between the 3dσ and 4sσ states (both give rise to $^2\Delta$ excited states and interact) and l-uncoupling between close lying 3dσ and 3dπ components (l-uncoupling causes mixing between the $^2\Delta$ and $^2\Pi$ states). Any further simulation of the rotational envelopes in the observed CIS spectra would have to take these effects into account.

However the spectra obtained in this work were felt to be not sufficiently well resolved to warrant attempting simulations which include these effects (although interaction with the Orsay group of Prof. D. Gauyacq[37] was considered to achieve this).

The [a $^1\Delta$, 3dδ] ($^2\Sigma$) states are unaffected by the 3d-4s interaction and l-uncoupling (there are no orbitals of 3dδ symmetry in the core) and hence the OH^*(a $^1\Delta$, 3dδ] ($^2\Sigma$)←OH(X $^2\Pi$) band should be well represented by *Hund's case a/b* RLS calculations. Unfortunately, the band at ≈13.81 eV is only poorly observed in our spectra and hence a meaningful comparison with the RLS calculations cannot be made because of its low intensity.

6.3 Conclusions

The work in this Chapter is presented to demonstrate the feasibility of synchrotron studies on short-lived radicals. The increased photon flux and improvement in spectral resolution available at the ELETTRA[23] third generation Synchrotron Radiation Source, makes the study of short-lived molecules possible with PES, CIS and angle-resolved measurements.

6.4 References

[1] R. P. Wayne
Chemistry of Atmospheres
Claredon Press, Oxford Science Publications, Oxford, 1991

[2] G. J. Mintoff and C. F. H. Tipper
Chemistry of Combustion Reactions
Butterworths, London, 1962

[3] D. J. Hucknall
Chemistry of Hydrocarbon Combustion Reactions
Chapman Hall, London, 1985

[4] W. D. Watson
Review of Modern Physics **48**, 513 (1976)

[5] A. E. Douglas
Canadian Journal of Physics **52**, 318 (1974)

[6] J. C. Viney
Journal of Molecular Spectroscopy **83**, 465 (1980)

[7] J. B. Nee and L. C. Lee
Journal of Chemical Physics **81**, 31 (1984)

[8] H. van Lonkhuyzen and C. A. De Lange
Molecular Physics **51**, 551 (1984)

[9] P. M. Dehmer
Chemical Physics Letters **110**, 79 (1984)

[10] R. J. Cody, C. Maralejo and J. E. Allen
Journal of Chemical Physics **95**, 2491 (1991)

[11] M. Collard, P. Kerwin and A. Hodgson
Chemical Physics Letters **179**, 422 (1991)

[12] E. De Beer, M. P. Koopmans, C. A. De Lange, Y. Wang and W. A. Chupka
Journal of Chemical Physics **94**, 7634 (1991)

[13] E. De Beer, C. A. De Lange, J. A. Stephens, Y. Wang and V. McKoy
Journal of Chemical Physics **95**, 714 (1991)

[14] C. A. De Lange
High Resolution Laser Photoionization and Photoelectron Studies
edited by I. Powis, T. Baer and C.Y. Ng, Wiley, Chichester, 1995

[15] J. N. Cutler, Z. X. He and J. A. R. Samson
Journal of Physics B **28**, 4577 (1995)

[16] E. F. van Dishoeck, S. R. Langhoff and A. Dalgarno
Journal of Chemical Physics **78**, 4552 (1983)

[17] E. F. van Dishoeck and A. Dalgarno
Journal of Chemical Physics **79**, 873 (1983)

[18] A. V. Nemukhin and B. L. Grigorenko
Chemical Physics Letters **276**, 171 (1997)

[19] S. Katsumata and D. R. Lloyd
Chemical Physics Letters **45**, 519 (1977)

[20] http://www.src.wisc.edu/facilities/default.html

[21] J. D. Barr, A. DeFanis, J. M. Dyke, S. D. Gamblin, N. Hooper, A. Morris, S. Stranges, J. B. West and T. G. Wright
Journal of Chemical Physics **110**, 345 (1999)

[22] http://www.dl.ac.uk

[23] http://www.elettra.trieste.it

[24] H. Herzberg
Molecular Spectra and Molecular Structure
D. van Nostrand Company Inc., New York, 1966, Vol. IV

[25] E. Lindholm
Arkiv för Fysik **9**, 117 (1968)

[26] C. Y. R. Wu
Journal of Quantitative Spectroscopy Radiative Transfer **37**, 1 (1987)

[27] J. Baker
Ph.D Thesis
University of Southampton, 1991

[28] D. L. Andrews and W. A. Ghoul
Journal of Chemical Physics **75**, 530 (1981)

[29] M. N. R. Ashfold
Molecular Physics **58**, 1 (1986)

[30] C. Mainos, M. C. Castex and H. Nkwawo
Journal of Chemical Physics **93**, 5370 (1990)

[31] C. Jungen
Journal of Chemical Physics **53**, 4168 (1970)

[32] E. Miescher
Canadian Journal of Physics **54**, 2074 (1976)

[33] S. Fredin, D. Gauyacq, M. Horani, C. Jungen, G. Lefevre and F. Masnou-Seeuws
Molecular Physics **60**, 825 (1987)

[34] S. T. Pratt, C. Jungen and E. Miescher
Journal of Chemical Physics **90**, 5971 (1989)

[35] D. Gauyacq, A. L. Roche, M. Seaver, S. D. Colson and W. A. Chupka
Molecular Physics **71**, 1311 (1990)

[36] A. Vient, N. Shafizadeh, J. H. Fillion, D. Gauyacq, M. Horani and J. L. Lemaire
Journal of Physical Chemistry **99**, 1666 (1995)

[37] http://www.chem.uva.nl/imc/reactive_intermediates.html

Chapter 7

7 PHOTOELECTRON SPECTROSCOPY OF N ATOMS

This Chapter reports studies on N atoms with ultraviolet photoelectron spectroscopy using Synchrotron Radiation.

The Chapter is organized as follows. In section 7.1 previous spectroscopic investigations on N atoms that are considered important for the present work are briefly reviewed. Section 7.2 presents experimental constant ionic state (CIS) spectra, and resonant photoelectron spectra of N atoms, together with their interpretations. Section 7.3 summarizes the results obtained.

7.1 Previous investigations on N atoms with photoelectron spectroscopy

Photoionization of atomic nitrogen is an important process in the physics and chemistry of the ionosphere[1]. There has been considerable theoretical work carried out on the photoionization cross section of N atoms from threshold at 14.54 eV to energies greater than 40 eV[1-5]. An accurate calculation of the photoionization cross section is difficult due to the open-shell electronic structure and consequent high degree of electron correlation in this atom. Henry[2] computed the photoionization cross section for N atoms over the energy range 14.6-20.6 eV using the continuum Hartree-Fock approximation. Later Henry[3] extended these calculations to higher energies (19-130 eV). Le Dourneuf *et al.*[4] and Bell *et al.*[5], in their work with R-matrix calculations, calculated the photoionization cross section of ground state of atomic nitrogen from threshold up to 95 eV. Experimentally, the total photoionization cross section of atomic nitrogen was measured in photoabsorption by Ehler *et al.*[6] and by Comes *et al.*[7]. The first measurements of the photoionization cross section were reported by Ehler *et al.*[6] in the region 17-31 eV; later Comes *et al.*[7] carried out measurements in the range 14-31 eV. Recently, Samson *et al.*[8] have made measurements of the absolute photoionization cross section for single and double ionization of atomic nitrogen in the range from 45 eV to 280 eV and from 14 eV to 24 eV performing ion mass spectrometry at the Synchrotron Radiation Center at the University of Wisconsin[9]. Carroll *et al.*[10] recorded the absorption spectrum of atomic nitrogen and observed for the first time Rydberg series which have been attributed to excitation to $[2s2p^3\ (^5S)\ np]\ ^4P$ autoionizing states. The shape of the line of an autoionizing resonance is a sharp feature and it can be observed as a decrease, an increase or an asymmetric profile in the cross section. The reason for this is the interference between the amplitudes of the direct and indirect processes resulting in a characteristic Fano profile[11].

Near the ionization threshold the asymmetry parameter β may vary with electron kinetic energy, but it is normally constant within a particular photoelectron band since it is determined mainly by the character of the ionised orbital. The asymmetry parameter may vary sharply as resonant states are accessed due to the enhancement of electron interactions[12].

The line-shape parameters Γ, q and ρ^2 characterize the autoionizing resonances revealing information on the dynamics of the photoionization process and they are expected to have certain characteristics[13]. The relative photoionization cross section for atomic nitrogen from 14 eV to 21 eV and, for the first time, the line-shape parameters and oscillator strengths for the $N^*[2s2p^3\ (^5S),\ 3p]\ (^4P) \leftarrow N(^4S)$ and $N^*[2s2p^3\ (^5S),\ 4p]\ (^4P) \leftarrow N(^4S)$ resonances were measured by Dehmer *et al.*[14] using a photoionization mass spectrometer coupled with the helium Hopfield continuum as incident radiation.

The Dehmer work has been extended by Schaphorst *et al.*[15], who performed electron spectroscopy at the Synchrotron Radiation Center at the University of Wisconsin[9], to the $N^*[2s2p^3\ (^5S),\ np]\ (^4P) \leftarrow N(^4S)$ resonances with $n = 5$ and reporting for the first time the angular distribution of photoelectrons for the $n = 3$ and $n = 4$ resonances.

7.2 Results and discussion

The purpose of the work presented in this Chapter was to extend the data analysis of Schaphorst *et al.*[15], in particular to evaluate the line-shape parameters and oscillator strengths for the $N^*[2s2p^3\ (^5S),\ np]\ (^4P) \leftarrow N(^4S)$ resonances for $n \geq 5$, using the ELETTRA Synchrotron Radiation Source on the BL 4.2 Circular Polarized Beamline[16] as described in Chapter 3.4.1.

The constant ionic state (CIS) spectra obtained were of higher resolution than previous measurements[15] and this allowed the data analysis to be extend to higher resonances.

Nitrogen atoms were produced by passing a flowing mixture of molecular nitrogen mixed with helium as a carrier, through a microwave discharge (2.45 GHz) in a glass inlet tube, coated with phosphoric acid[17], attached to the ionization chamber of the spectrometer, as described in Chapter 4.3.1.

The photon energy was calibrated against the energy values of the N autoionizing resonances obtained from the study of Schaphorst *et al.*[15].

The intensities of the bands in the experimental PE and CIS spectra were normalized by the photon flux and then by the transmission correction of the spectrometer. The photon flux was estimated as a function of photon energy from the current measured on an aluminium photodiode placed on the opposite side of the spectrometer ionization chamber from the photon source. The transmission function of the spectrometer, for electrons of different initial electron kinetic energy, was determined by measuring the intensity of the helium $(1s)^{-1}$ photoelectron band at different photon energies. The intensity of the helium $(1s)^{-1}$ band was measured in the VUV photon energy range used and then it was normalized using the absolute photoionization cross section of helium in this range[18]; finally the normalized intensity was plotted as function of the kinetic energy. This curve was used to correct the experimental PE and CIS spectra for the transmission of the spectrometer.

The degree of linear polarization ($P = 1$) of the radiation was well established[19]. The asymmetry parameter (β) was measured for nitrogen atoms at selected photon energies and over a photon energy range, by recording CIS spectra at two different θ

angles (0° and 54° 44') at each photon energy (at 54°44' the measured intensity is proportional to the total photoionization cross section, independent of β).

The β parameter was then calculated from the expression (see Chapter 2.2.6):

$$\beta = (R-1) \qquad \text{Eq. 7.1}$$

where $R = \frac{I_0}{I_{54°44'}}$ is the ratio of the experimental intensities at these two angles, after applying the above corrections.

For the measurements of angular distribution it is important that the efficiency of the analyser does not change when the spectrometer is rotated. The change of the efficiency of the analyser on rotation arises from small misalignments between the axis of rotation and the direction of the photon beam. In order to quantify this contribution a correction factor is evaluated by measuring the intensity of bands at θ=0° and at θ=54° 44', usually at 21.22 eV photon energy, from a sample (usually Ar) where the asymmetry parameter is well established. From the comparisons between the calculated asymmetry parameter and the known asymmetry parameter, the correction factor was determined.

Test experiments were carried out in Southampton in order to determine the optimum nitrogen and helium pressures to be used in the experiments at ELETTRA, which maximise the intensities of the atomic nitrogen bands. Figure 7.1 shows the photoelectron spectrum recorded at $h\nu$=21.22 eV with the following partial pressures measured on an ionization gauge positioned on the wall of the ionization chamber with respect to the background pressure: $\Delta p(N_2)=2.52\times10^{-7}$ mbar and $\Delta p(He)=1.55\times10^{-7}$ mbar.

The ground state configuration of N is $1s^2 2s^2 2p^3$; three ionic states should arise from ionization from the 2p level corresponding to the ionization: $N^+(^3P)\leftarrow N(^4S)$, $N^+(^1D)\leftarrow N(^4S)$ and $N^+(^1S)\leftarrow N(^4S)$. The first ionization is clearly observed in Figure 7.1 at 14.54 eV[17] ionization energy. The second and third ionizations, expected at 16.44 eV and 18.59 eV ionization energies respectively, can only be observed if Russell-Saunders selection rules are broken[17], as the $N^+(^1D)\leftarrow N(^4S)$ and the $N^+(^1S)\leftarrow N(^4S)$ ionizations are both spin forbidden (see Chapter 2.2.5).

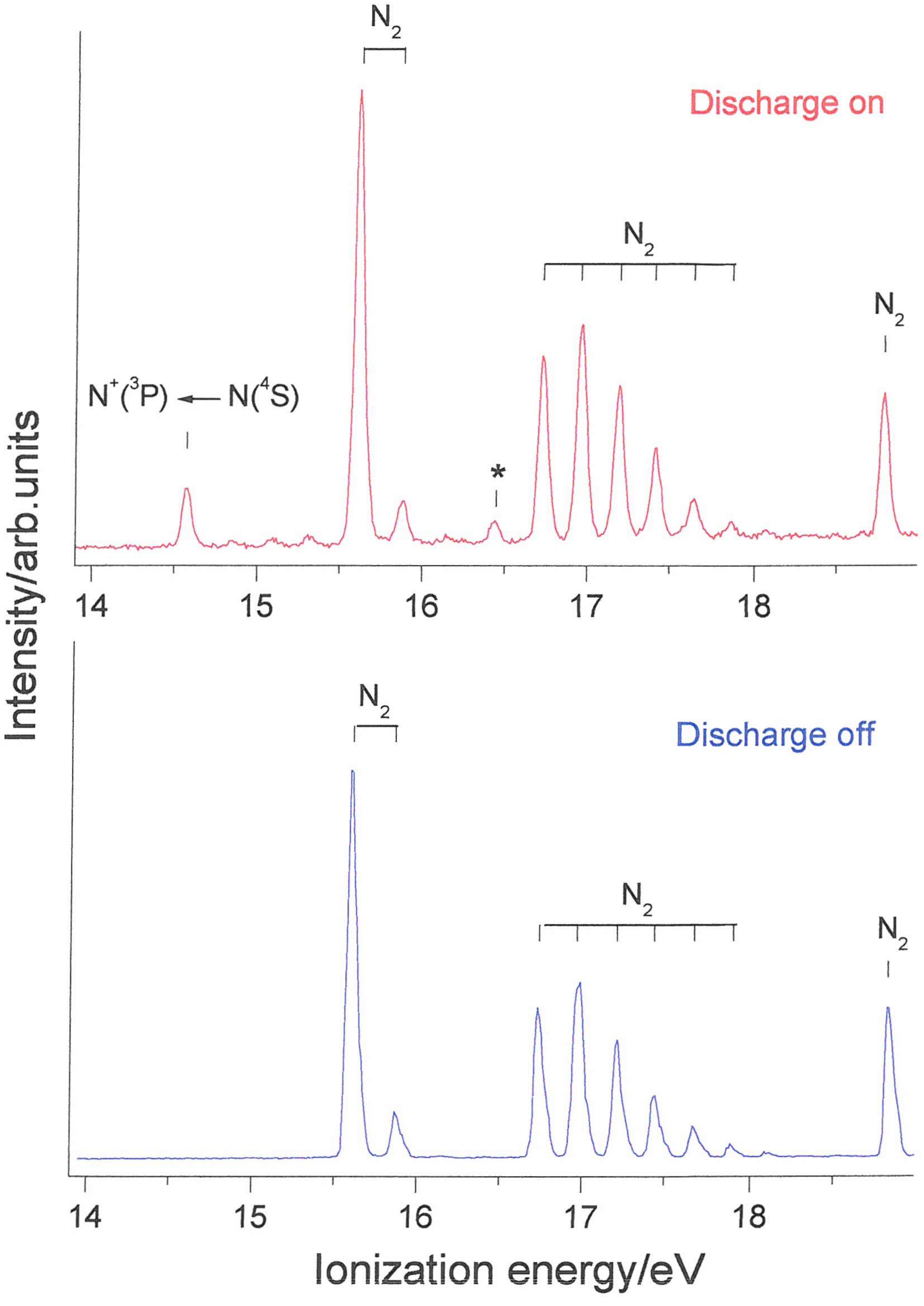

Figure 7.1: PE spectrum recorded at photon energy $h\nu = 21.22$ eV with the microwave discharge on (upper panel) and off (lower panel) of a He/N_2 mixture

The peak labelled with (*) at 16.44 eV is believed to result from the ionization $N_2^+(A\ ^2\Pi_u, v^+=0) \leftarrow N_2(X\ ^1\Sigma_g^+, v''=1)$

The small band labelled (*) in Figure 7.1 at 16.45 eV is believed to result from the ionization $N_2^+(A\ ^2\Pi_u, v^+=0) \leftarrow N_2(X\ ^1\Sigma_g^+, v''=1)$[15,20].

For the $(2s)^{-1}$ ionization of $N(^4S)$, bands are expected at 20.39 eV $[N^+(^5S) \leftarrow N(^4S)]$, 25.98 eV $[N^+(^3D) \leftarrow N(^4S)]$, 28.08 eV $[N^+(^3P) \leftarrow N(^4S)]$, and 33.77 eV $[N^+(^3S) \leftarrow N(^4S)]$ respectively[21].

In Figure 7.2 PE spectra recorded at $h\nu$ =29.99 eV with and without discharge are shown.

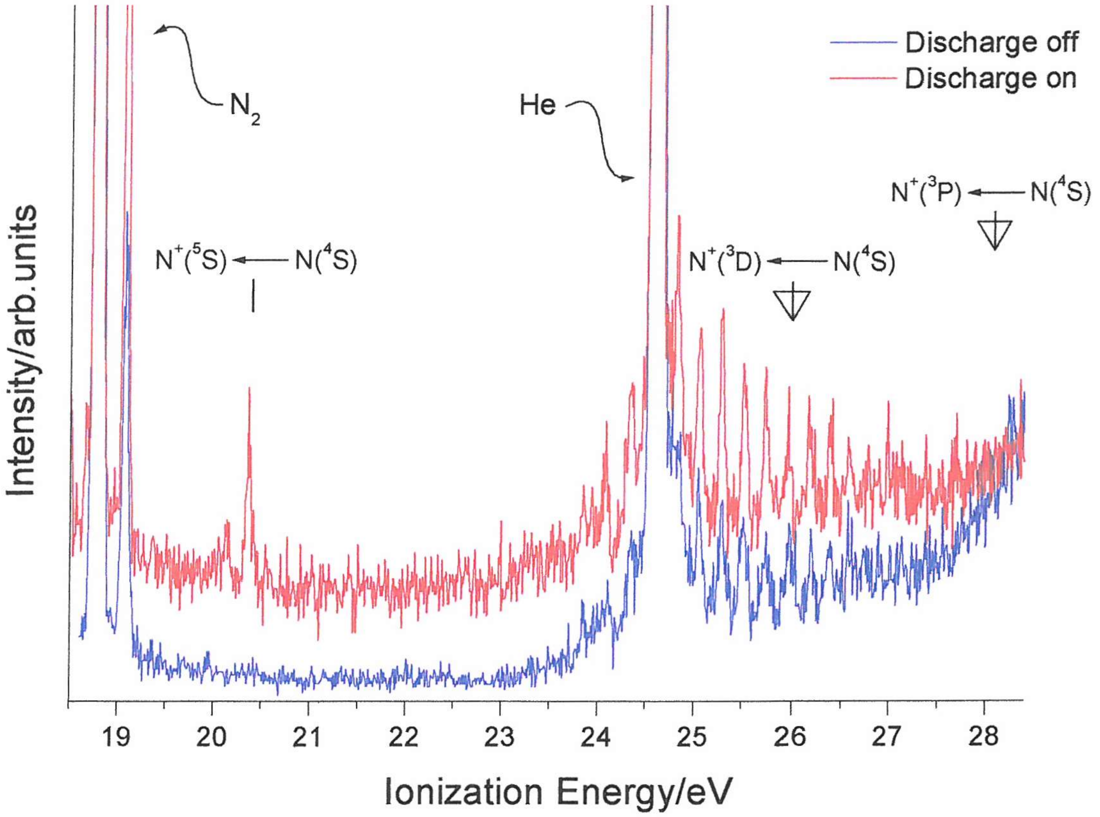

Figure 7.2: PE spectrum recorded at photon energy $h\nu$ =29.99 eV with the microwave discharge on (red line) and off (blue line) of a He/N_2 mixture

The position of the $N^+(^5S) \leftarrow N(^4S)$, $N^+(^3D) \leftarrow N(^4S)$ and $N^+(^3P) \leftarrow N(^4S)$ ionizations are indicated as well as N_2 and He features

In Figure 7.2 the band at 20.39 eV corresponding with the ionization $N^+(^5S) \leftarrow N(^4S)$, is clearly observed, while the bands arising from the ionizations $N^+(^3D) \leftarrow N(^4S)$ and $N^+(^3P) \leftarrow N(^4S)$ are completely overlapped by the molecular features.

These molecular features arise from the $N_2^+(C\ ^2\Sigma_u^+) \leftarrow N_2(X\ ^1\Sigma_g^+)$ ionization and are in good agreement with the study of Asbrink *et al.*[22], where the photoelectron spectrum of N_2 was recorded between 23.50 and 28.00 eV ionization energy using a HeII lamp. The vertical ionization energy (VIE) for this ionization is measured in the spectrum in Figure 7.2 at 25.29 eV, while the adiabatic energy is not observed due to low intensity at the band onset. Also the vibrational spacings of the band at 25.29 eV are in agreement with those of Asbrink *et al.*[22].

Due to an intrinsic limitation of the normal incidence monochromator used, the photon flux at energies above the 30.00 eV is not sufficient to record PE spectra. For this reason it was not possible check for the presence of the atomic nitrogen band at 33.77 eV.

7.2.1 CIS of $N^+(^3P) \leftarrow N(^4S)$, $h\nu$=19.4-20.5 eV

Constant ionic state spectra have been recorded for the first atomic nitrogen band, $N^+(^3P) \leftarrow N(^4S)$, at the ionization energy of 14.54 eV with a 1 meV/channel stepwidth. All spectra were recorded at two angles, $\theta = 0°$ and $\theta = 54° 44'$, with respect to the polarization axis of the photon source.

The relative integrated cross section and the β parameter as a function of photon energy are shown in Figures 7.3 and 7.4. The asymmetry parameter has been evaluated as a function of photon energy applying Eq. 7.1. The β parameter across the 5p and 6p resonances varies sharply between +2 and -0.3. Similar behaviour was reported by Schaphorst *et al.*[15] for the 3p and 4p resonances. The variation of the β parameter across the autoionizing resonances for $n \geq 7$ shows smoother behaviour.

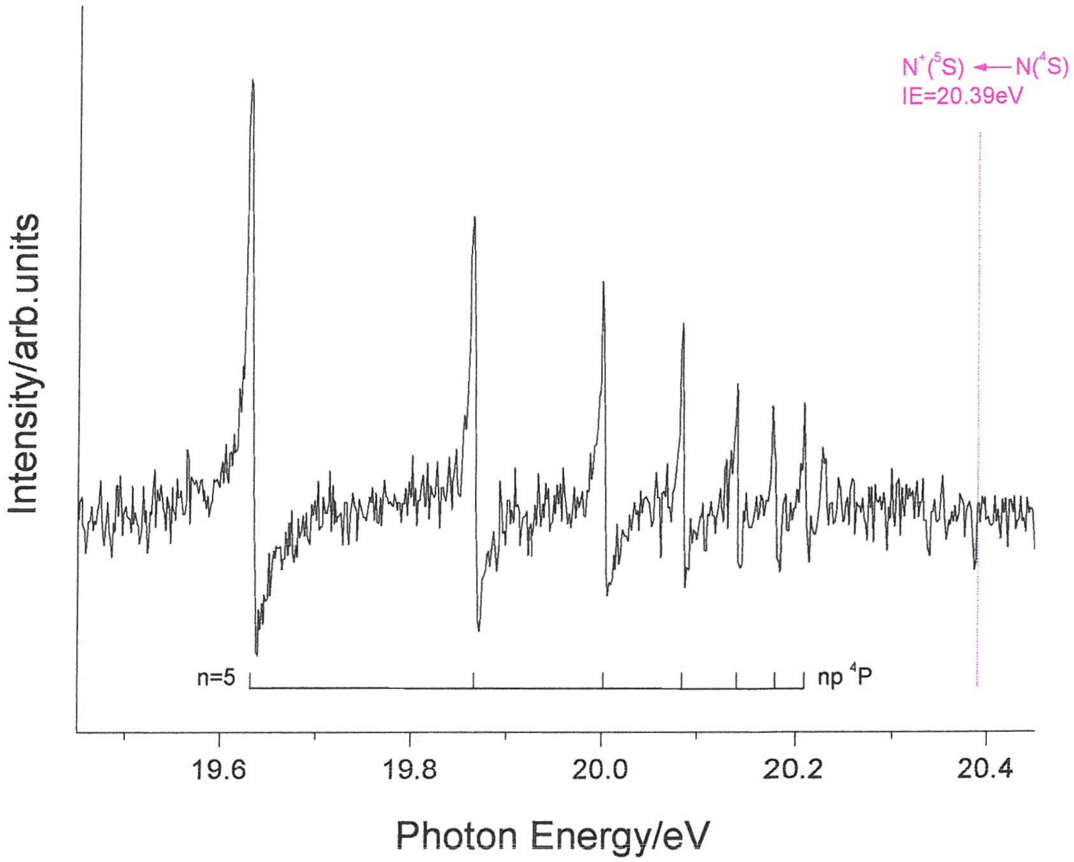

Figure 7.3: Relative integrated cross section of atomic nitrogen across the $N^+(^3P) \leftarrow N^* \leftarrow N(^4S)$ autoionizing resonances for $n \geq 5$, over the photon energy range 19.4–20.5 eV
The spectrum was recorded at $\theta = 54° 44'$ and 1 meV/channel stepwidth

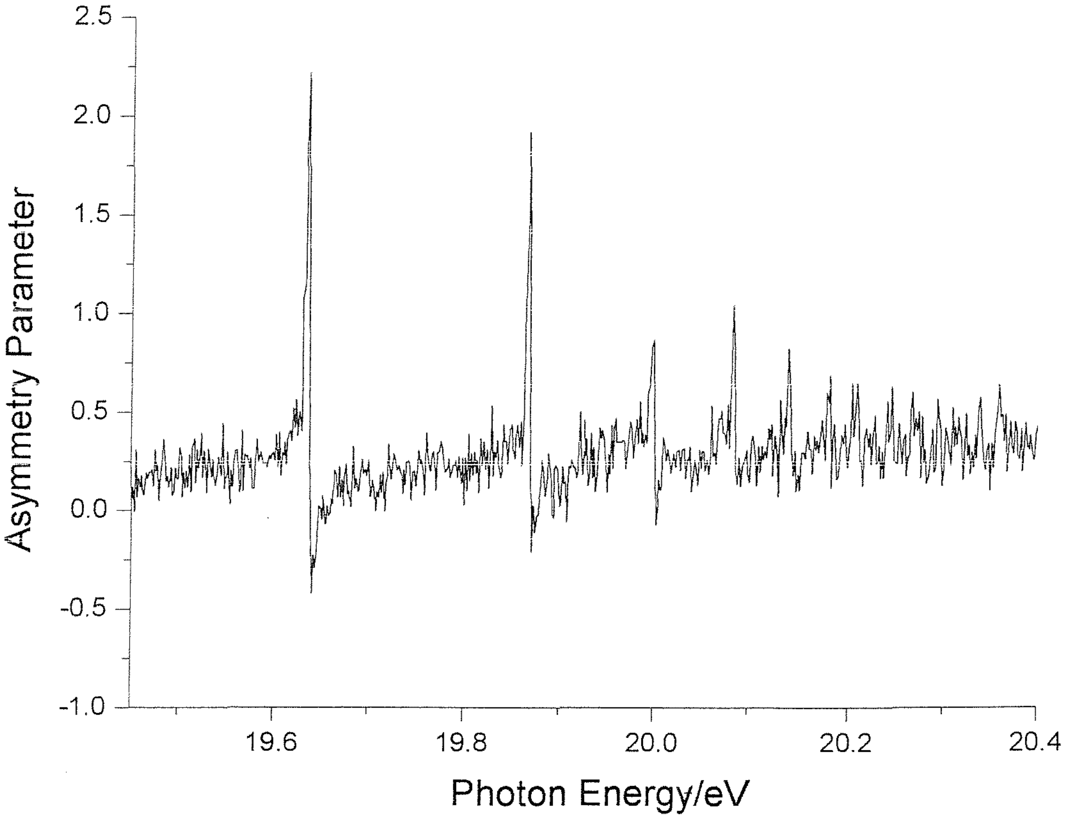

Figure 7.4: Asymmetry parameter for atomic nitrogen across the $N^*[2s2p^3\ (^5S),\ np]\ (^4P) \leftarrow N(^4S)$ *autoionizing resonances for* $n \geq 5$*, over the photon energy range 19.4–20.5 eV*

The lines shown in Figure 7.3 have a characteristic asymmetric profile due to the interference between the amplitudes of the direct and indirect processes resulting in a characteristic Fano profile[11,23] where the cross section can be expressed as (see Chapter 2.2.3):

$$\sigma(E) = \sigma_a \frac{(q+\varepsilon)^2}{1+\varepsilon^2} + \sigma_b \qquad \text{Eq. 7.2}$$

In this equation σ_a and σ_b represent two portions of the cross section which correspond respectively to transitions to states of the continuum that do and do not interact with the discrete autoionizing state. The reduced energy ε is defined as:

$$\varepsilon = \frac{E - E_r}{\frac{1}{2}\Gamma} \qquad \text{Eq. 7.3}$$

where E_r is the resonance energy and Γ is the natural width of the autoionizing state which represents the bound-continuum mixing of the resonance state[11].

The q parameter characterises the line profile: neglecting the background cross section, the resonance has a maximum at $\varepsilon_{max}=1/q$ and is zero at $\varepsilon_0=-q$. The sign of q thus determines whether the maximum occurs before or after the minimum. The magnitude of q indicates qualitatively the relative probabilities of the transition to the Rydberg state and direct ionization[11].

Another parameterization of Eq. 7.2 that is frequently used defines a correlation index ρ^2 and a cross section for photon energies outside of the resonance region σ_c as:

$$\rho^2 = \frac{\sigma_a}{\sigma_a + \sigma_b} \qquad \text{Eq. 7.4}$$

In this case Eq. 7.2 can then be rewritten as:

$$\sigma(E) = \sigma_c\left[\frac{(q+\varepsilon)^2}{1+\varepsilon^2}\rho^2 + \left(1-\rho^2\right)\right] \qquad \text{Eq. 7.5}$$

A direct numerical fit of the observed spectrum to the Fano formula of Eq. 7.5 may become unreliable for an atomic transition involving a narrow resonance[24]. The fitting function used in this work is the convolution of the Fano profile in Eq. 7.5 and the instrumental function $F(E,\Omega)$ where Ω is the energy resolution measured by the full width at half maximum (FWHM):

$$\sigma(E,\Omega) = \int_{-\infty}^{\infty} \sigma(E-E')\cdot F(E',\Omega)dE' \qquad \text{Eq. 7.6}$$

It is often a good approximation to assume a Gaussian distribution as the instrumental function; alternatively a weighted combination of a Gaussian and Lorentzian distributions can be used[24]. In order to evaluate the Fano profile parameters of the autoionizing resonances for $n \geq 5$, several fits have been performed using either a Gaussian distribution or a weighted combination of a Gaussian and Lorentzian distribution as the instrumental function and varying the CIS energy resolution Ω from 1 to 7 meV.

The fits with the best χ^2 values have been obtained using a pure Gaussian distribution as the instrumental function and an energy resolution of 3 meV. Figure 7.5 shows the Fano profile fits compared with the experimental data for the n =6, 7, 8, 9 and 10 resonances.

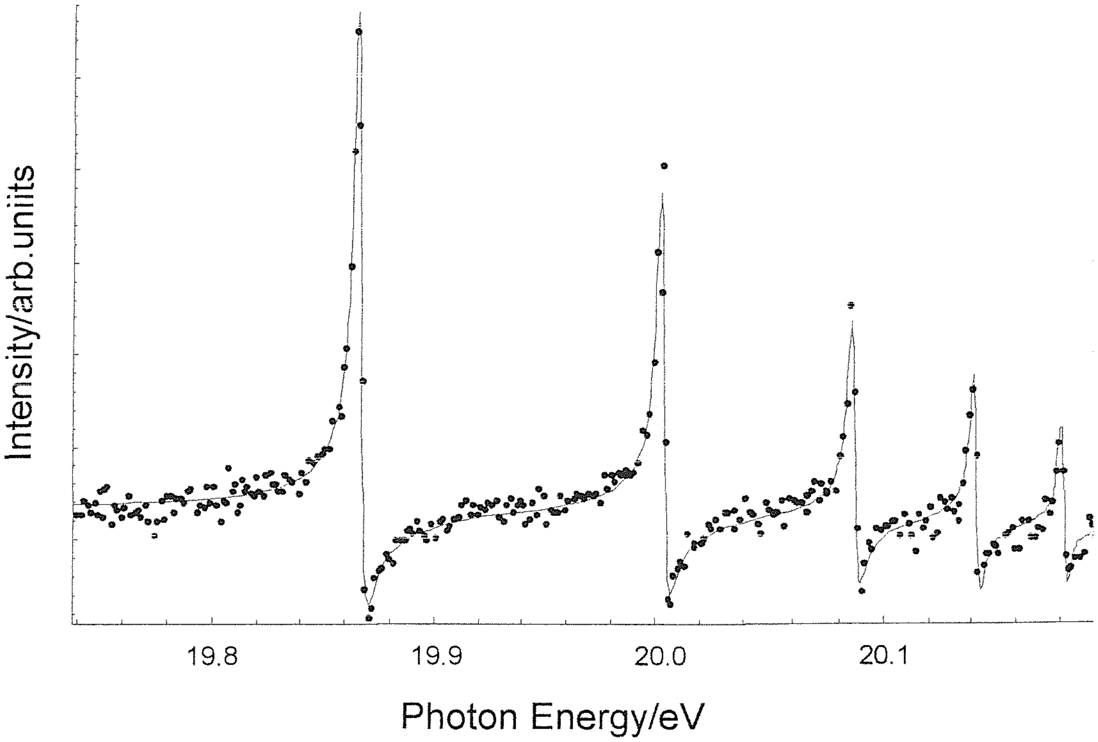

Figure 7.5: The solid line is the Fano profile fit to the data (dots) for the n=6, 7, 8, 9 and 10 autoionizing resonances

The discrete oscillator strengths for the resonances have been calculated from the expression[13]:

$$f = \frac{mc^2}{2e^2}\sigma_c \rho^2 \Gamma q^2$$ Eq. 7.7

where c is the speed of the light, e and m are the charge and the mass of the electron, respectively. To express the oscillator strengths on an absolute scale and for comparison with the value for $n=5$ obtained by Schaphorst *et al.*[15], the cross section σ_c has been set to 11 Mb in agreement with the results of the multiconfiguration Hartree-Fock calculation at a photon energy of 18.6 eV obtained in reference (15).

Values of Γ, q, ρ^2 and f are reported in Table 7.1 for the autoionizing resonances from $n=5$ to $n=10$. The present results for the 5p resonance agree with those of Schaphorst *et al.*[15] within experimental error. The ρ^2 value is nearly equal for the autoionizing resonances, as expected for the members of a Rydberg series with an approximately constant quantum defect δ[13,23]. The same behaviour is expected for the q value. Experimentally the q value becomes more negative from $n=3$ to $n=7$, taking in account the values of -1.60 and -1.70 obtained by Shaphorst *et al.*[15] for the 3p and 4p resonances respectively. For autoionizing resonances for $n>7$ the q value becomes less negative although it can be considered constant within experimental error.

If the mean separation of the energy levels N_n adjacent to the energy level E_n is cosidered[23]:

$$N_n^2 = \frac{1}{2}\left(E_{n+1} - E_{n-1}\right) = R\frac{2(n-\delta_n)}{\left((n-\delta_n)^2 - 1\right)^2} \qquad \text{Eq. 7.8}$$

the dependence of N_n on the quantum number n is:

$$N_n \propto \frac{1}{n^3} \qquad \text{Eq. 7.9}$$

The same procedure yields a relationship among the widths of successive lines of a Rydberg series, namely:

$$\Gamma_n = R\frac{2(n-\delta_n)}{\left((n-\delta_n)^2 - 1\right)^2}\overline{\Gamma} \qquad \text{Eq. 7.10}$$

where $\overline{\Gamma} = \Gamma(n-\delta_n)^3$ represents the ratio of each line width to the average separation of the adjacent lines; this ratio is constant for the whole series and it is called "reduced linewidth"[23]. However for n>250 the presence of weak electric fields inevitably present in the ionization region are sufficient to causes l as well as m_l mixing (l and m_l represent the Rydberg electron orbital angular momentum and magnetic quantum numbers, respectively) both of which contribute to the lengthening of the lifetime (≡ drop in $\bar{\Gamma}$)[25].

In Table 7.1 are reported the value of $\bar{\Gamma} = \Gamma n^{*3}$ where $n^* = (n-\delta_n)$. In the calculations the quantum defect parameters, δ_n , obtained by Schaphorst *et al.*[15] from the expression:

$$E_n = E_\infty - \frac{R}{(n-\delta_n)^2} \qquad \text{Eq. 7.11}$$

have been used, where E_∞ is the adiabatic ionization energy of the molecule and R is the Rydberg constant. This choice is justified by the fact the photon energy source has been calibrated using the resonance energies obtained by Schaphorst *et al.*[15] and the resonance positions determined by the fit. For all the resonances the $\bar{\Gamma}$ values are approximately constant, within experimental error, as expected[13,23], as the n values are well below the high values where lengthening of Rydberg state lifetime occurs through l and m_l mixing.

Table 7.1: Widths (Γ), line-shape parameters (q and ρ^2) and oscillator strengths (f) for the $N^*[2s2p^3\,(^5S), np]\,(^4P) \leftarrow N(^4S)$ autoionizing resonances for $n \geq 5$

		Γ(meV)	q	ρ^2 ($\times 10^2$)	f ($\times 10^3$)	Γn^{*3} ($\times 10^2$)
5p	Ref. (15)	4.4 ± 0.3	-1.9 ± 0.3	65 ± 15	1.6 ± 0.6	37.3 ± 2.5
5p	Present work	4.77 ± 0.15	-1.85 ± 0.08	62.1 ± 1.9	1.59 ± 0.15	40.1 ± 1.3
6p	Present work	2.60 ± 0.15	-2.07 ± 0.10	56.5 ± 3.0	0.99 ± 0.12	40.5 ± 2.4
7p	Present work	1.80 ± 0.15	-2.22 ± 0.10	61.6 ± 4.9	0.86 ± 0.13	47.1 ± 3.9
8p	Present work	1.19 ± 0.27	-1.84 ± 0.14	55.8 ± 12.0	0.35 ± 0.12	47.9 ± 10.9
9p	Present work	0.89 ± 0.39	-1.58 ± 0.16	61.9 ± 25.1	0.22 ± 0.14	52.0 ± 22.8
10p	Present work	0.62 ± 0.59	-1.31 ± 0.19	81.0 ± 66.6	0.14 ± 0.17	51.2 ± 48.7

7.3 Conclusions

The natural width Γ, line shape parameters q and ρ^2 and discrete oscillator strengths f have been measured for the members of the $N^*[2s2p^3\ (^5S),\ np]\ (^4P) \leftarrow N(^4S)$ autoionizing resonances for $n \geq 5$. The 5p parameters calculated in this work are in good agreement with the values obtained by previous experiment. The constancy of the parameters ρ^2 and Γn^{*3} for the whole series of autoionizing resonances has been demonstrated while the parameter q shows a non constant behaviour.

7.4 References

[1] J. U. Koppel
Journal of Chemical Physics **55**, 123 (1971)

[2] R. J. W. Henry
Journal of Chemical Physics **44**, 4357 (1966)

[3] R. J. W. Henry
Journal of Chemical Physics **48**, 3635 (1968)

[4] M. Le Dourneuf, L. Vo Ky and A. Hibbert
Journal of Physics B **9**, L359 (1976)

[5] K. L. Bell and K. A. Berrington
Journal of Physics B **24**, 933 (1991)

[6] A. W. Ehler and G. L. Weissler
Journal of the Optical Society of America **45**, 1035 (1955)

[7] F. J. Comes and A. Elzer
Physics Letters A **25**, 334 (1967)

[8] J. A. R. Samson and G. C. Angel
Physical Review A **42**, 1307 (1990)

[9] http://www.src.wisc.edu/default.html

[10] P. K. Carroll, R. E. Huffman, J. C. Larrabee and Y. Tanaka
Astrophysical Journal **146**, 553 (1966)

[11] U. Fano
Physics Review **124**, 1866 (1961)

[12] D. Dill
Physical Review A **7**, 1976 (1973)

[13] U. Fano and J. W. Cooper
Review of Modern Physics **40**, 441 (1968)

[14] P. M. Dehmer, J. Berkowitz and W. A. Chupka
Journal of Chemical Physics **60**, 2676 (1974)

[15] S. J. Schaphorst, S. B. Whitfield, H. P. Saha, C. D. Caldwell and Y. Azuma
Physical Review A **47**, 3007 (1993)

[16] http://www.elettra.trieste.it

[17] J. M. Dyke, N. Jonathan, A. Morris and T. Sears
Journal of The Chemical Society and Faraday Transition 2 **72**, 597 (1976)

[18] J. B. West and G. V. Marr
Atomic Data and Nuclear Data Tables **18**, 497 (1976)

[19] J. B. West, J. M. Dyke, A. Morris, T. G. Wright and S. D. Gamblin
Journal of Physics B **32**, 276 (1999)

[20] J. M. Dyke, N. Jonathan and A. Morris
Electron Spectroscopy: Theory, Techniques and Applications
edited by C.R. Brundle and A.D. Baker, Academic Press, London, 1979

[21] C. E. Moore
Atomic Energy Levels
U.S. Government Printing Office, Washington DC, 1952, Vol. 1

[22] L. Asbrink and C. Fridh
Physica Scripta **9**, 338-340 (1974)

[23] U. Fano and J. W. Cooper
Physics Review **137**, 1364 (1965)

[24] T. K. Fang and T. N. Chang
Physical Review A **57**, 4407 (1998)

[25] W. A. Chupka
Journal of Chemical Physics **98**, 4520 (1993)

Chapter 8

8 PHOTOELECTRON SPECTROSCOPY OF S ATOMS AND SH RADICALS

This Chapter reports studies of photoelectron spectroscopy using Synchrotron Radiation on S atoms and SH radicals.

The Chapter is organized as follows. In section 8.1 previous spectroscopic investigations on S atoms and SH radicals that are considered important for the present work are briefly reviewed. Section 8.2 presents experimental photoelectron spectra at different photon energies and at two angles with respect to the major polarization axis of the photon source, together with their interpretations. The results have been obtained during two different beamtimes at ELETTRA[1] and two techniques, photoelectron (PE) spectroscopy and constant ionic state (CIS) spectroscopy, have been used to study S and SH. Section 8.3 summarizes the results obtained.

Because to the large number of plots presented in this Chapter, all the Figures have been grouped at the end of the Chapter.

8.1 Previous investigations on S atoms and SH radicals with photoelectron spectroscopy and related methods

In the extreme ultraviolet wavelength region, absorption, photoionization and autoionization of sulphur atoms are of fundamental interest for understanding the spectroscopy and photoionization dynamics of open-shell atoms. Moreover, due to its relatively high solar abundance, atomic sulphur plays an important role in determining solar and stellar opacities[2-4] and interaction of S atoms with ultraviolet radiation is important in the solar atmosphere[5].

The ground state configuration of S atoms is $1s^22s^22p^63s^23p^4$, ^3P. Three ionic states arise on $(3p)^{-1}$ ionization from this state: the ^4S, ^2D and ^2P states at ionization energies of 10.35, 12.21 and 13.40 eV respectively[6].

There has been considerable theoretical work carried out on the photoionization cross section of S atoms over a wide photon energy range. Conneelly *et al.*[7] computed photoionization cross sections for atomic systems with incomplete outer 3p subshells using the continuum Hartree-Fock approximation, and Dill *et al.*[8] derived expressions for the angular distribution of photoelectrons produced by ionization of open shell atoms including sulphur. The asymmetry parameter, β, as function of photon energy was calculated for each of the three ionic channels resulting from the $(3p)^{-1}$ ionization of sulphur atoms using both Hartree-Fock and Herman-Skillman wavefunctions for the atom, ion and free electron from threshold up to 60 eV.

Later, Manson *et al.*[9] presented results of calculations of the photoionization cross sections and angular distributions of the outer p sub-shell of chalcogen and halogen atoms from 13 to 100 eV photon energy, using the continuum Hartree-Fock approximation. In the theoretical work on S atoms[8,9], the general shape of the cross section for each of the three ionic channels shows a clear Cooper minimum around 40 eV. The calculated asymmetry parameters as a function of photon energy have a small value near threshold, rise rapidly to a maximum then fall to a minimum with negative β values at the Cooper minimum of the cross section; they subsequently increase smoothly (the S 3p orbital is expected to show a Cooper minimum since the number of nodes in the atomic wavefunction, n-l-1, is greater than zero). The $(3p)^{-1}$

photoionization cross section of S atoms has also been calculated at a number of photon energies by Yeh *et al.*[10] using Hartree-Fock-Slater calculations.

Experimentally, a number of studies have been made on S atoms[11-14]. Tondello[11] measured and analysed the absorption spectrum of S in the vacuum ultraviolet region 1830-900 Å (6.77-13.77 eV), below and above the ionization threshold. An attempt to derive the absolute value of the photoionization cross section from the ground state in the 1197-940 Å region (10.36-13.19 eV) was made in this work. Modifications and additions to this spectrum have been made using a similar technique by Sarma *et al.*[12] and, more recently, by Joshi *et al.*[13].

Subsequently, Gibson *et al.*[14] studied the photoionization spectrum of atomic sulphur using photoionization mass spectrometry from the ionization threshold, 10.35 to 13.40 eV.

The SH radical is a molecule of environmental importance which plays a role in the ultraviolet photochemistry of several small sulphur-containing compounds which are released into the earth's atmosphere from natural and anthropogenic sources[15]. For example, hydrogen sulphide, carbonyl sulphide and carbon disulphide are released from the earth and its oceans as a consequence of microbiological processes. They react with the hydroxyl radical in the atmosphere to yield SH, which is then oxidized by O_2 and O_3 to SO_2.

Although SH has been studied with various spectroscopic techniques[16-19] and theoretical methods[20,21], information on its electronic states is still somewhat limited. A multiphoton ionization study of the SH radical in the single photon energy range 4.68-3.91eV has been performed by Ashfold *et al.*[16] The observation and partial characterization of three Rydberg states of SD and SH, accessed via 2-photon resonances from the ground state was achieved in this work. More recently, thirteen Rydberg states converging to the second and third ionic states have been observed and characterised by two-photon resonance enhanced multiphoton ionization spectroscopy and multiphoton ionization photoelectron spectroscopy[22]. Also, the electronic absorption spectrum of SH has been investigated from the near ultraviolet into the vacuum ultraviolet region and several electronic transitions have been identified[17,18].

The adiabatic ionization energies of SH(X $^2\Pi$) to the first five ionic states have been established from HeI vacuum ultraviolet (VUV) photoelectron spectroscopy measurements to an accuracy of ± 0.01eV[6]. Recently a more accurate determination of the ionization energies to the X $^3\Sigma^-$ and a $^1\Delta$ ionic states[23,24] from SH(X $^2\Pi$) have been achieved by the pulsed field ionization zero electron kinetic energy method.

The ground state electronic configuration of the SH radical is $1\sigma^2 2\sigma^2 3\sigma^2 1\pi^4 4\sigma^2 5\sigma^2 2\pi^3$; photoionization from the valence 2π molecular orbital produces the X $^3\Sigma^-$, a $^1\Delta$ and b $^1\Sigma^+$ ionic states at adiabatic ionization energies (AIEs), equal to the vertical ionization energies (VIEs), of 10.42, 11.64 and 12.76 eV respectively[6,23,24]. The potential energy curves of these ionic states are very similar to that of the ground state of the neutral because of the non-bonding S 3p character of the 2π orbital. The removal of one electron from the 5σ shell gives rise to the A $^3\Pi$ and c $^1\Pi$ ionic states at AIEs of 14.11 and 15.69 eV respectively[6].

The SH^+(A $^3\Pi$)←SH(X $^2\Pi$) and SH^+(c $^1\Pi$)←SH(X $^2\Pi$) bands are broad and vibrationally resolved, with the AIE equal to the VIE for both bands. AIE values for these bands are 14.11 eV and 15.69 eV respectively[6].

Until now, no attempts have been made to measure asymmetry parameters (β) and photoionization cross sections (σ) of either S or SH. The purpose of this present work was to measure angular distribution parameters and relative photoionization cross sections for the $S^+(^4S)$←$S(^3P)$, $S^+(^2D)$←$S(^3P)$ and $S^+(^2P)$←$S(^3P)$ bands and the SH^+(X $^3\Sigma^-$, $v^+=0$)←SH(X $^2\Pi$, $v''=0$), SH^+(a $^1\Delta$, $v^+=0$)←SH(X $^2\Pi$, $v''=0$) and SH^+(b $^1\Sigma^+$, $v^+=0$)←SH(X $^2\Pi$, $v''=0$) bands as a function of photon energy from threshold (~10.3 eV) to 30.0 eV with the ELETTRA Synchrotron Radiation Source. This should allow comparison to be made with available calculations.

8.2 Results and discussion

Photoelectron (PE) spectra were recorded in the constant pass energy mode, by scanning the voltage on a lens which accelerates (or decelerates) the photoelectrons before they enter the analyser, as explained in Chapter 4.2.1.

In this work, S atoms and the SH radicals were produced by the following consecutive reactions (see also Chapter 4.3.2):

$$F + H_2S \rightarrow SH + HF \qquad \text{Eq. 8.1}$$

$$F + HS \rightarrow S + HF \qquad \text{Eq. 8.2}$$

The room temperature rate constants for the above reactions are 1.33×10^{-10} and 2.01×10^{-10} cm^{3}molecule^{-1}s^{-1} respectively[25]. To obtain a high F-atom yield, fluorine atoms were produced by flowing 5% F_2 in helium through a microwave discharge at 2.45 GHz in the side arm of a glass inlet system[26], with an inner inlet system which is the inlet used for the target molecules (in this case H_2S). In order to avoid attack of the glass system by the fluorine atoms produced by the discharge, the inner surface of the tube was coated with a thin layer of teflon, while the discharge cavity was positioned on an alumina section of the inlet system to prevent melting of the teflon due to heating from the discharge[26], as explained in Chapter 4.3. The intensities of the bands in the experimental PE spectra were normalized by the photon flux and then by the transmission correction of the spectrometer. The transmission function of the spectrometer, for electrons of different initial electron kinetic energy, was determined by measuring the intensity of the helium (1s) $^{-1}$ photoelectron band at different photon energies. The intensity of the helium (1s)$^{-1}$ band was measured in the VUV photon energy range used and then it was normalised using the absolute photoionization cross section of helium in this range[27]; finally the normalized intensity was plotted as function of the electron kinetic energy. This curve was used to correct the experimental PE spectra for the transmission of the spectrometer.

The degree of linear polarization (P =1) of the radiation was well established[28,29]. The asymmetry parameter (β) was measured for S and SH at selected photon energies and over a photon energy range, by recording PE spectra at two different θ angles (0° and 54° 44') at each photon energy (at 54° 44' the measured intensity is proportional to the total photoionization cross section, independent of β); the β parameter was then calculated from:

$$\beta = (R-1) \qquad \text{Eq. 8.3}$$

where $R = \frac{I_0}{I_{54°44'}}$ is the ratio of the experimental intensities at these two angles, after applying the above corrections.

Test experiments were carried out in Southampton in order to determine the optimum pressures and mixing distance above the photon beam to be used in the experiments at ELETTRA which maximise the intensities of the second and third photoelectron bands of SH at 11.64 eV and 12.76 eV AIE respectively, corresponding to the ionizations $SH^+(a\ ^1\Delta, v^+=0) \leftarrow SH(X\ ^2\Pi, v''=0)$ and $SH^+(b\ ^1\Sigma^+, v^+=0) \leftarrow SH(X\ ^2\Pi, v''=0)$, and the second and third ionizations of S at 12.21 eV and 13.40 eV IE respectively, corresponding to the ionizations $S^+(^2D) \leftarrow S(^3P)$ and $S^+(^2P) \leftarrow S(^3P)$[6]. The following conditions were found to be the optimum for production of both S and SH: a mixing distance above the photon beam of 2 cm, with the inner-inlet system used for H_2S longer than the outer inlet system by about 2 mm, and the partial pressures measured on an ionization gauge positioned on the wall of the ionization chamber of $\Delta p(H_2S)=2.4\times10^{-7}$ mbar and $\Delta p(F_2/He)=4.6\times10^{-6}$ mbar.

The PE spectra recorded at a photon energy of $h\nu=21.64$ eV with Synchrotron Radiation at $\theta=0°$ and at two different angles with respect to the polarization axis of the photon source ($\theta=0°$ and $\theta=54°\ 44'$) of the products of the $F+H_2S$ reaction are shown in Figures 8.1 and 8.2 with the assignment of the major features indicated.

These spectra show sharp bands at 11.64 and 12.76 eV, which are the second and third bands of SH, and sharp bands at 12.21 and 13.40 eV which are the second and third bands of S atoms. The sharp band at $\approx$10.5eV arises from overlap of the first band of S atoms at 10.35 eV, and the first band of SH at 10.42 eV as well as a small contribution from the first band of residual H_2S at 10.48 eV[6]. Bands associated with F and F_2 were also observed in the spectra[30,31], as well as a small contribution from SF_2 which is a secondary reaction product[32] (see Figure 8.3).

The vibrationally resolved band of SH at 14.11 eV AIE is the fourth band of SH (the $SH^+(a\ ^3\Pi) \leftarrow SH(X\ ^2\Pi)$ ionization). Unfortunately, the fifth band of SH (the $SH^+(c\ ^1\Pi) \leftarrow SH(X\ ^2\Pi)$ ionization) AIE 15.69 eV, was not observed because it was too weak and overlapped with the first band of F_2.

The broad band on the low energy side of the $S^+(^2P) \leftarrow S(^3P)$ ionization at 13.40 eV ionization energy is mainly due to the presence of unreacted H_2S, along with SF_2 produced by secondary reactions. Confirmation of the presence of SF_2 can be easily obtained from the observation of the first two vibrational components of the first band of SF_2 on the low ionization energy side of the sharp band at ≈10.5 eV (1st AIE of SF_2 10.08 eV)[32], as shown in Figure 8.3. The spectra obtained are in good agreement with those previously recorded in Southampton by Dunlavey *et al.*[6] with HeI radiation source.

In Figure 8.4, an expanded version of the composite band at ≈10.5 eV is shown.

Figure 8.4 clearly shows two maxima. Deconvolution of this band into two Gaussians was performed and the fitted Gaussians were centred at 10.36±0.02 and 10.45±0.03 eV. These energies are in agreement with the known energies of the $S^+(^4S) \leftarrow S(^3P)$ and $SH^+(X\ ^3\Sigma^-) \leftarrow SH(X\ ^2\Pi)$ ionizations at 10.35 eV and 10.42 eV respectively. The small contribution of the $H_2S^+(X\ ^2B_1) \leftarrow H_2S(X\ ^1A_1)$ ionization at 10.48 eV is included in the band centred at 10.45 eV. This is consistent with a slightly larger full width at half maximum (FWHM) of the second fitted Gaussian compared to the first Gaussian.

The values obtained from the fit are $FWHM_1$=72±3 meV and $FWHM_2$=95±3 meV for the first and second Gaussians, respectively.

8.2.1 Preliminary studies by PES

Because of a problem with the software used to obtain CIS spectra in the first visit to ELETTRA at which S and SH were studied, only PES spectra were recorded. CIS spectra were obtained during the second visit, see section 8.2.2.

PE spectra were recorded in the ionization energy region 9.600-15.200 eV using 23 different photon energies from 13.205 to 21.640 eV. A step size of 0.20 eV was used from $h\nu$=13.205 eV to $h\nu$=16.420 eV and a step size of 0.40 eV was used from $h\nu$=16.420 eV to $h\nu$=18.494 eV. PE spectra were also recorded at $h\nu$=21.640 eV.

In Figures 8.5 and 8.6 the renormalized PE spectra recorded at θ=0° and θ=54° 44' with respect to the major polarization axis of the photon source are shown.

Due to significant variations in the intensities of the 12.21 eV band (second band of S) and the 11.64 eV band (second band of SH) with photon energy, the ionization energy region 11.500-12.400 eV was re-examined by recording a new series of 21 PE spectra with photon energies from $h\nu$ =13.205 eV to $h\nu$ =13.411 eV, with a smaller step size of 0.01 eV.

In Figures 8.7 the re-examined sections are shown for the two different angles of detection.

The strong band present in each of the PE spectra shown in Figures 8.5 and 8.6 at photon energies between 13.20 eV and 14.30 eV, shown by arrows in these diagrams, is due to ionization of helium by second order radiation. In this photon energy region second order radiation can ionize helium (IE=24.58 eV[33]) with consequent emission of electrons. This helium $(1s)^{-1}$ band was used as an internal check for the correction factor applied for the evaluation of the asymmetry parameter for the observed bands of S and SH. Indeed, with the procedure used, β was always obtained as 2.00, within experimental error, for this helium $(1s)^{-1}$ band. In practice, for measurements of angular distribution parameters it is important to make sure that the efficiency of the analyser does not change when the spectrometer is rotated. The biggest contribution to the change of the efficiency of the analyser comes from small misalignments between the axis of rotation and the direction of the photon beam. This contribution is minimized by adjusting, after each rotation of the spectrometer, the direction of the photon beam in such a way as to maximize the signal coming from the detector and the current measured by the photodiode on the opposite side of the ionization chamber of the spectrometer from the direction of the photon beam. However, to quantify this contribution for all the angle resolved experiments a correction factor is evaluated at each set of experiments by measuring the intensity of bands at θ =0° and at θ =54° 44', usually at 21.22 eV photon energy, from a sample (usually Ar) where the asymmetry parameter is well established. From the comparisons between the calculated asymmetry parameter and the known asymmetry parameter, the correction factor was determined. Then, at each photon energy, the asymmetry parameter can be calculated for an S or SH band using Eq. 8.3 with this correction factor, and relative photoionization cross sections can be evaluated by integrating the area of the bands at θ=54° 44'. This has been carried out to give the plots shown in Figures 8.8 to 8.12.

Inspection of existing angular distribution and relative cross section (σ) measurements for H_2S[34-37], indicates that for the S photoelectron bands arising from a $(3p)^{-1}$ ionization, the angular distribution parameter (β) plotted as function of photon energy is expected to show an initial increase, a maximum at ≈25 eV and a minimum at ≈40 eV, the Cooper minimum, whereas the σ plot is expected to show a regular decrease from threshold, the shallow Cooper minimum at ≈40 eV and then a slow increase. The first, second and third bands of S, and SH, and the first band of H_2S are expected to be very similar in their β and σ plots as they all correspond to ionization from a S 3p lone-pair orbital. Comparisons of the measured asymmetry parameters as a function of photon energy for the three ionization channels resulting from the $(3p)^{-1}$ photoionization of S derived from this work with results of the angular distribution Hartree-Fock calculations of Dill *et al.*[8] have been made over the photon energy range 10-22 eV. These calculations[8] used Russell-Saunders coupling and were based on an angular momentum transfer expansion for the differential photoionization cross section. Dill *et al.*[8] showed that the three ionic channels resulting from photoionization of $S(^3P)$ should show significantly different behaviour from each other when plotted as function of photon energy, in contrast to identical behaviour expected in the Cooper-Zare model[38,39]. In Figure 8.8, the three different angular distribution plots are shown as a function of photon energy and comparisons with the results of Dill *et al.*[8] are presented in Figures 8.9-8.11.

Figure 8.8 *(b)* also shows data points taken from reference (34) for the first band of H_2S. This shows reasonable agreement with the S atom results of this work but again more H_2S data points are required for a more meaningful comparison.

As can be seen in Figures 8.9-8.11, the experimental results obtained in this work are in reasonable agreement with the results of the calculations[8] for the $S^+(^4S) \leftarrow S(^3P)$

and $S^+(^2D) \leftarrow S(^3P)$ ionization channels, Figures 8.9 and 8.10 respectively, but are in poorer agreement for the $S^+(^2P) \leftarrow S(^3P)$ ionization, Figure 8.11. However, for all three ionizations, data points are required to higher photon energy than the range covered in this work for a more detailed comparison between experiment and theory. Figure 8.12 shows similar β plots for the first three bands of SH, with Figure 8.12 *(b)* again showing the available data for the first band of H_2S from reference (34).

No previous measurements or calculations of the β parameter as a function of photon energy have been made for SH. However, as with the S atom data, more data points are required notably at higher photon energy. Also, it should be borne in mind that, as stated earlier, the first band of SH contains a small contribution from H_2S and this will contribute to Figure 8.12 *(a)*.

In Figures 8.13 and 8.14 the relative photoionization cross sections for the second S atom band and for the first three S atom bands are plotted as a function of photon energy in the energy region 13.2-13.8 eV and 13.0-21.5 eV respectively.

In Figure 8.13, the relative cross section of the second S atom band, the $S^+(^2D) \leftarrow S(^3P)$ ionization, is plotted as function of the photon energy in the interval 13.20-13.80 eV. As can be seen, this plot shows clear structure in the region 13.205-13.350 eV. The observed maxima can be assigned to excitation to ^3P Rydberg states derived from $3s^2 3p^3$ *n*d configurations accessed from the $3s^2 3p^4$ ^3P ground state. These Rydberg states are parts of a series which converges to the third ionization limit at 13.400 eV[13,14].

To estimate the behaviour of the absolute photoionization cross section for the three ionic states of sulphur, the integrated area of each band was estimated at a photon energy of 16.7 eV, an energy at which the total photoionization cross section has been calculated by Yeh *et al.*[10] as 18.2 Mb, using Hartree-Fock-Slater calculations. While for the second and third bands, corresponding to the $S^+(^2D) \leftarrow S(^3P)$ and the $S^+(^2P) \leftarrow S(^3P)$ ionizations, the integrated areas could be easily measured, for the first S atom band, the $S^+(^4S) \leftarrow S(^3P)$ ionization, that strongly overlaps with the first band of SH, the result of the double-Gaussian deconvolution shown in Figure 8.4 was used. The contribution of the first H_2S band at 10.48 eV is included with the first band of SH in the second Gaussian band and it does not affect the calculated intensity of the first S band, which corresponds to the first fitted band.

As a result, the intensity ratios of the first three bands of S atoms, were measured at an angle of 54° 44′, as (6.2±1.0):10:(5.7±0.5) at 16.7 eV. The relatively high experimental uncertainty of the first band relative intensity is due to overlap of the first S atom band with the first bands of SH and H_2S, as stated earlier. In order to estimate the absolute cross sections for these ionizations at 16.7 eV, the total areas of these bands were normalized to the total cross section of the $(3p)^{-1}$ ionization of 18.2 Mb, calculated by Yeh *et al.*[10].

Once this had been done, the experimental results could be used to estimate the photoionization cross section at 13.8 eV, an energy at which the total photoionization cross section has been determined in an experimental study of the absorption spectrum of S atoms. In this investigation, Tondello[11] determined the photoionization cross section over the energy region investigated, 10.3 to 13.8 eV. In the photon energy region 12.8 to 13.8 eV, which overlaps with the photon energy region investigated in the present work, the photoionization cross section decreases regularly from 90 to 79 Mb. At 13.8 eV, values for the photoionization cross sections of the first two bands of atomic S could be obtained from the plots made in the present study, whereas the photoionization cross section for the third band was obtained by extrapolation of the plot shown in Figure 8.14 *(c)* to lower energy. This gave estimates of the photoionization cross section for the first three bands of S atoms at 13.8 eV, which when summed gave a total photoionization cross section of 58 Mb, which can be compared with the photoionization cross section value determined in Tondello's work of 79 Mb[11]. Given the approximations involved, most notably that the total photoionization cross section in the present work has been referenced to the photoionization cross section calculated at 16.7 eV by Hartree-Fock-Slater calculations[10], it is not surprising that only moderate agreement is obtained. Nevertheless, this comparison indicates there is a clear need for a direct measurement of the photoionization cross section of atomic sulphur in the vacuum ultraviolet region, most notably above the third ionization energy of 13.4 eV i.e. at photon energies which include all three ionic states arising from the $(3p)^{-1}$ ionization.

The general behaviour of the photoionization cross sections for the first three ionizations of sulphur atoms are shown in Figure 8.14. In Figure 8.14 *(a)* the relative photoionization cross section of the first S atom band is plotted as a function of the photon energy in the interval 13.205-18.494 eV. In this Figure the maximum at 13.30 eV corresponds to excitation to the [$3s^23p^3$ (^{2}P) *n*d] ^{3}P Rydberg states seen in Figure 8.13, recorded with a smaller photon energy increment.

In Figure 8.14 it can be seen that except for the resonance at 13.30 eV, already assigned to excitation to [$3s^23p^3$ (^{2}P) *n*d] ^{3}P Rydberg states, at least two other small maxima are seen at 14.96 eV and 15.37 eV (these features will be discussed later in this Chapter). These probably correspond to excitation to [$3s^13p^4$ (^{4}P) *n*p] ^{3}D/ ^{3}P/ ^{3}S or [$3s^13p^4$ (^{2}D) *n*p] ^{3}D/ ^{3}P/ ^{3}S states accessed from the $3s^23p^4$ (^{3}P) state. However, because of the stepwidth used to record these spectra (0.20 eV) and the limited number of data points, assignment of these features will only be achieved when spectra of the type shown in Figures 8.13 and 8.14 are recorded over a wider photon energy range and with a smaller stepwidth.

Figures 8.15 and 8.16 show plots of relative photoionization cross sections for the first three bands of SH. They show similar overall behaviour to that observed for the equivalent plots for S atoms (Figure 8.14) and H_2S^{34}, but, as with the S atom plots, they need to be recorded over a wider photon energy range with a smaller stepwidth. Figures 8.14 *(b)* and 8.16 *(b)* also include the experimental photoionization cross section for the first band of H_2S as a function of photon energy, taken from reference (40), for comparison.

This initial study of S and SH has shown that PES measurements need to be extended over a wider photon energy range and should be recorded with a smaller stepwidth to allow a more detailed comparison to be made. Ideally, CIS measurements need to be made on the first three bands of S and SH.

This is what has been done during the next beamtime and the results obtained are discussed in the following section.

8.2.2 CIS spectroscopy studies

During the next beamtime, better experimental conditions allowed studies to be performed on S and SH over wider photon energy. This was because new software was written to allow PES and CIS spectra to be acquired and the experimental resolution was better, which allowed the first bands of S and SH to be resolved. In Figure 8.17, PE spectra recorded at ELETTRA of the products of the F+H_2S reaction at a photon energy of $h\nu$=21.26 eV and at two different angles with respect to the polarization axis of the photon source (θ=0° and θ=54° 44') are shown with the assignment of the major features indicated. These spectra show sharp bands at 11.64 and 12.76 eV, which are the second and third bands of SH, and sharp bands at 12.21 and 13.40 eV which are the second and third bands of S atoms. Also, observed is the first bands of O atoms (13.62 eV[41]) and H_2O (12.62 eV[41]). The H_2O arises from residual water in the inlet system and O atoms probably arise from reaction of F atoms with H_2O. Compared with Figure 8.2, in Figure 8.17 the bands at ≈10.5 eV arising from the first bands of S and SH/ H_2S could be resolved. As can be seen in the expanded plot of the 10.0-11.0 eV IE region in Figure 8.18, the first band of S atoms at 10.35 eV is resolved from the first band of SH at 10.42 eV, and the small contribution from the first band of residual H_2S at 10.48 eV[6].

The vibrationally resolved band of SH at 14.11 eV AIE is the fourth band of SH (the $SH^+(a\ ^3\Pi)\leftarrow SH(X\ ^2\Pi)$ ionization).

CIS spectra, recorded as described in Chapter 4.2.2, could be successfully recorded for the $S^+(^4S)\leftarrow S(^3P)$ ionization at 10.35 eV, for the $S^+(^2D)\leftarrow S(^3P)$ ionization at 12.21 eV and for the $S^+(^2P)\leftarrow S(^3P)$ ionization at 13.40 eV. All spectra were recorded at two angles, θ=0° and θ=54° 44', with respect to the polarization axis of the photon source and with a 1 meV/channel stepwidth. In Figures 8.19-8.32 the CIS spectra for the $S^+(^4S)\leftarrow S(^3P)$, $S^+(^2D)\leftarrow S(^3P)$ and $S^+(^2P)\leftarrow S(^3P)$ ionizations are shown. Figure 8.19 shows the $S^+(^4S)\leftarrow S(^3P)$ CIS spectrum in the photon energy region 11.5-30.0 eV, Figure 8.26 shows the $S^+(^2D)\leftarrow S(^3P)$ CIS spectrum in the photon energy region 13.5-30.5 eV and Figure 8.30 shows the $S^+(^2P)\leftarrow S(^3P)$ CIS spectrum in the photon energy region 14.5-30.5 eV. These spectra were recorded at

θ =54° 44' (at this angle the measured intensity is proportional to the total photoionization cross section, independent of the asymmetry parameter).

To estimate the behaviour of the absolute cross sections for the three ionic states of sulphur, the relative cross sections off resonance for the atomic sulphur CIS bands were estimated at a photon energy of 14.76 eV, an energy at which the total photoionization cross section has been obtained by extrapolation of Tondello's absolute measurements[11] as 82 Mb, based on the linewidths of Tondello's lines and the absorption oscillator strength measured in emission by Muller[42].

In order to estimate the absolute cross section for these ionizations at 14.76 eV, the sum of the relative cross sections of these bands were normalized to the total cross section of 82 Mb, determined by Tondello[11].

Once this had been done, the experimental results could be used to estimates of the photoionization cross section for the first three bands of S atoms at 16.7 eV, which when summed gave a total photoionization cross section of 68.7 Mb, which can be compared with the total photoionization cross section calculated by Yeh *et al.*[10] as 18.2 Mb, using Hartree-Fock-Slater calculations.

Bearing in mind that values of absolute cross sections can be obtained only if all the parameters are measured simultaneously, or consecutively in the same experiment and under experimental conditions, values of "absolute cross sections" using data extrapolations from other work, both experimental and theoretical, can be used only as a relative indication. Therefore, given the approximations involved, most notably that the total photoionization cross section in the present work has been referenced to the extrapolated photoionization cross section at 14.76 eV determined by Tondello's measurements[11], it is not surprising that an unsatisfactory agreement is obtained with the computed value of Yeh *et al.*[10]. Nevertheless, this comparison indicates there is a clear need for a direct measurement of the absolute photoionization cross section of atomic sulphur in the vacuum ultraviolet region.

The results of the above relative-absolute normalization obtained from Tondello results[11] have been applied in Figures 8.19-8.32. In this section this normalization has been preferred over the one carried out in section 8.2.1 using the value byYeh *et al.*[10] from Hartree-Fock-Slater calculations, because it is obtained from experimental measurements.

The $S^+(^4S) \leftarrow S^* \leftarrow S(^3P)$ and $S^+(^2D) \leftarrow S^* \leftarrow S(^3P)$ CIS spectra in the photon energy region 11.60-13.45 eV with the second and third ionization limits marked in, are shown in Figures 8.20-8.22 and 8.27, recorded at θ=54° 44'.

The bands observed in these Figures can be readily assigned to known $S^* \leftarrow S(^3P)$ transitions by comparison with known S^* term values[11,13,14]. The energy positions of the resonances have been fitted using the Rydberg formula and good agreement has been found with the results of previous studies of Joshi *et al.*[13] and Gibson *et al.*[14]. Examples of the results obtained for the *n* =7 *n*s' ^{3}D, *n*d' ^{3}D and *n*d' ^{3}S Rydberg states by these fits have been summarized in Table 8.1 using the band maxima shown, where they are compared with the results obtained by Joshi *et al.*[13] and Gibson *et al.*[14] for the Rydberg series which converges to the second ionization limit shown in Figure 8.20.

Table 8.1: Examples for n =7 ns' ^{3}D, nd' ^{3}D and nd' ^{3}S Rydberg states which are parts of a Rydberg series converging to the second ionization limit listing the fitted quantum defects and fitted ionization limits obtained in this work compared with the results of ref. (13,14)
The weighted average of the $^2D_{3/2}$ and $^2D_{5/2}$ limits has been used in ref. (13,14) to calculate the quantum defects

		Present work		Results of ref. (13,14)	
Excitation energy/eV	Rydberg series	Quantum defect δ	Ionization limit IE/eV	Quantum defect δ	Ionization limit IE/eV
11.907	*n*d' ^{3}D	0.313	12.204	0.272	12.204
11.633	*n*s' ^{3}D	2.134	12.204	2.118	12.204
11.929	*n*d' ^{3}S	0.039	12.204	-0.030	12.204

Inspection of the CIS spectrum recorded for the first PE band of S atoms shows that in the photon energy region 11.60-12.20 eV, all the bands can be assigned to excitation to Rydberg states which are members of series which converge to the second ionization energy, apart from a couple of bands associated with Rydberg states which are part of series converging to the third ionization energy, see

Figure 8.21. On expanding a section of the first band CIS spectrum for the photon energy range 12.30-13.42 eV (see Figure 8.22), the structures observed in Figure 8.21 in the region 12.205-13.350 eV were investigated and assigned to the [$3s^23p^3$ (^{2}P) *n*s] ^{3}P, [$3s^23p^3$ (^{2}P) *n*d] ^{3}P and [$3s^23p^3$ (^{2}P) *n*d] ^{3}D Rydberg series accessed from the $3s^23p^4$ ^{3}P ground state. These Rydberg states are parts of series which converge to the third ionization limit at 13.400 eV[13,14].

Figures 8.22 and 8.27 show CIS spectra of the first PE band and second PE band of S atoms recorded in the photon energy region 12.30-13.42 eV and 13.10-13.42 eV respectively. Resonances are observed which are consistent with excitations to Rydberg states which are part of series converging to the third ionization limit. The position and assignment of these states has been established previously by Joshi *et al.*[13], using an absorption technique, and by Gibson *et al.*[14], using photoionization mass spectrometry. Examples of the results obtained for the *n* =9 *n*d" ^{3}P and *n*d" ^{3}D Rydberg states by these fits have been summarized in Table 8.2 using the band maxima shown, where they are compared with the results obtained by Joshi *et al.*[13] and Gibson *et al.*[14] for the Rydberg series which converge to the third ionization limit shown in Figure 8.22.

Table 8.2: Examples for n =9 nd" ^{3}P and nd" ^{3}D Rydberg states which are parts of a Rydberg series converging to the third ionization limit listing the fitted quantum defects and fitted ionization limits obtained in this work compared with the results of ref. (13,14)
The weighted average of the $^2P_{1/2}$ and $^2P_{3/2}$ limits has been used in ref. (13,14) to calculate the quantum defects

		Present work		Results of ref. (13,14)	
Excitation energy/eV	Rydberg series	Quantum defect δ	Ionization limit IE/eV	Quantum defect δ	Ionization limit IE/eV
13.226	*n*d" ^{3}P	0.296	13.441	0.264	13.404
13.229	*n*d" ^{3}D	0.340	13.410	0.194	13.404

Comparing Figure 8.13 with Figure 8.27, it can be seen that in the CIS scan several structures are present in the energy region 13.3-13.4 eV. These resonances could be easily misunderstood in the PES study as background noise due to the low count rate and big stepwidth while the CIS study confirms the presence of real structures converging to the third ionization limit.

The structure observed in Figure 8.14 *(c)* of the relative cross section for the $S^+(^2P)\leftarrow S(^3P)$ ionization in the 14.00-16.00 eV photon energy region have been investigated again to see if the small maxima presented (at 14.96 eV and 15.37 eV) are really part of excitation to $[3s^13p^4\ (^4P)\ np]\ ^3D/\ ^3P/\ ^3S$ or $[3s^13p^4\ (^2D)\ np]\ ^3D/\ ^3P/\ ^3S$ states accessed from the $3s^23p^4\ (^3P)$ state as proposed in the PE study. In Figure 8.30, where the $S^+(^2P)\leftarrow S(^3P)$ CIS spectrum in the photon energy region 14.5-30.5 eV is presented, no consistent structures were observed in these positions. Also, no maxima were seen in CIS scans of the first and second bands at these photon energies (see Figures 8.23 and 8.26). Unfortunately the results of the CIS investigation of this region (14-16 eV) are less reliable than CIS results obtained in other regions due to several problems that occurred during the acquisition (i.e. instability of the reaction followed by switch-off of the discharge caused by an electrical shutdown of the entire synchrotron facility due to a thunderstorm). However, in this region the cross section for the $S^+(^2P)\leftarrow S(^3P)$ ionization is increasing with increasing photon energy and an incorrect maximum could have been inferred from the previous PE study especially because the data points were taken with big stepwidth.

In Figures 8.24, 8.28 and 8.31, Rydberg series converging to the fourth ionization limit at 20.204 eV are presented. This is the first time that a Rydberg series converging to this limit has been observed.

Photoabsorption cross sections in regions of autoionization can be parameterized with a lineshape formula based on multichannel quantum defect theory (MQDT) analogous to the Fano's resonance formula[43,44].

Fano's parametrization considers isolated autoionizing states coupled to degenerate continua. It is valid for the case in which the widths of the resonances are comparable with the separation of the resonances in a Rydberg series.

A way of describing an entire series of interacting autoionizing series is to use an MQDT approach first developed by Seaton[45]. Variants of MQDT have been developed by Seaton[45,46], Giusti-Suzor *et al.*[47] and other workers[48,49].

A simple special case involves one series of Rydberg states autoionizing in one continuum. Dubau *et al.*[50] derived a parameterization for this case of two interacting channels, one open and one closed. Connerade[48] has given a detailed discussion of this parameterization while Giusti-Suzor *et al.*[47] derived the same formula using an alternative set of MQDT parameters.

The compact expression of the cross section is:

$$\sigma(E) = \sigma_a \frac{(\varepsilon + q)^2}{\varepsilon^2 + 1} \qquad \text{Eq. 8.4}$$

where σ_a is the cross section averaged over resonances, q is a profile index and the periodic energy scale ε is defined as:

$$\varepsilon = \frac{\tan[\pi(\upsilon + \delta)]}{W} \qquad \text{Eq. 8.5}$$

where δ is the quantum defect. The quantity W is related to the resonance width Γ_n via:

$$\Gamma_n = \frac{2W\,R}{\pi(n - \delta)^3} \qquad \text{Eq. 8.6}$$

while the effective principal quantum number $\upsilon = (n-\delta)$ is related to the photon energy E_n and the series limit I via:

$$\upsilon = n - \delta = \sqrt{\frac{R}{I - E_n}} \qquad \text{Eq. 8.7}$$

Eq. 8.5 gives $\varepsilon = 0$ for $\upsilon_n = (n-\delta)$ and this corresponds to the centre of a resonance[46] for each n. From Eq. 8.7, the values of these resonance energies E_n are:

$$E_n = I - \frac{R}{(n-\delta)^2} \qquad \text{Eq. 8.8}$$

An extension of Eq. 8.4 to include many channel cases using procedures outlined by Seaton[46], Giusti-Suzor *et al.*[47] and Cooke[49] has been presented by Ueda[51].

In the case of one closed channel and many open channels, a term σ_b is added to Eq. 8.4 which expresses the non resonant contribution of the open channels[51].

$$\sigma(E) = \sigma_a \frac{(q+\varepsilon)^2}{1+\varepsilon^2} + \sigma_b \qquad \text{Eq. 8.9}$$

If more than one closed channel exists in the region of interest and, if these channels do not interact either directly or through open channels, the photoionization cross section can be given by a superimposition of Eq. 8.9 over the *k* closed channels i.e.:

$$\sigma(E) = \sum_k \sigma_{ak} \frac{(q_k+\varepsilon_k)^2}{1+\varepsilon_k^2} + \sigma_b \qquad \text{Eq. 8.10}$$

If an energy region contains one open channel and many degenerate closed channels, the photoionization cross section can be written:

$$\sigma(E) = \sigma_a \frac{\left(1+\sum_k q_k/\varepsilon_k\right)^2}{\left(1+\left(\sum_k q_k/\varepsilon_k\right)^2\right)} \qquad \text{Eq. 8.11}$$

In this work, codes for fitting the experimental data to Eq. 8.9-8.11 have been written by the PES group in Southampton using the program Mathematica.

The parameters σ_a, σ_b, δ, q and W in equations 8.9-8.11 are energy independent. However, a slowly variation with the energy has to be introduced to obtain a better fit of the experimental data[50]. This is achieved using a set of parameters linear in the reduced energy $X=(I-E)/R$. The parameters (generically named p) are then written as $p = p_a + p_b X$.

In Figures 8.24, 8.28 and 8.31, the $S^+(^4S) \leftarrow S^* \leftarrow (^3P)$, $S^+(^2D) \leftarrow S^* \leftarrow (^3P)$ and $S^+(^2P) \leftarrow S^* \leftarrow (^3P)$ CIS spectra are shown. Ejection of a 3s electron from the ground state of atomic sulphur gives rise to $3s3p^4$ (^4P), $3s3p^4$ (^2D), $3s3p^4$ (^2S) ionic states at ionization energies of 20.204 eV, 22.497 eV and 25.211 eV, respectively[33].

In order to attempt to assign the bands in Figures 8.24, 8.28 and 8.31, it is helpful to determine the energy levels to which transitions are allowed from the ground state $3s^23p^4\ ^3P$. The upper level can be restricted to triplet terms, since the spin selection rule[52,53], $\Delta S=0$, should be strictly obeyed for a light atom such as sulphur. The most likely transitions will be those with $\Delta l=\pm1$, or $p \leftarrow s$ in this case[52,53]. The terms involved may be considered to be the result of adding a p electron to the term of S^+ resulting from the electronic configuration $3s3p^4$.

The lowest S^+ ($3s^13p^4$) core state is ^4P, and the resulting terms are obtained by combining the angular momentum of the p electron with the core-state angular momentum. From these term symbols the selection rule[52,53] $\Delta L=0, \pm1$ reduces the possible transitions to the allowed states given in Table 8.3.

Table 8.3: Energy levels to which transitions are allowed from the ground state $3s^23p^4\ ^3P$ assuming Russell-Saunders coupling is valid

Excited State	Ionic State after Autoionization
$[3s3p^4(^4P)\ np]\ ^3D$	$S^+(^4S)$, εd
$[3s3p^4(^4P)\ np]\ ^3P$	-
$[3s3p^4(^4P)\ np]\ ^3S$	$S^+(^4S)$, εs
$[3s3p^4(^4P)\ np]\ ^3D$	$S^+(^2D)$, εs; $S^+(^2D)$, εd
$[3s3p^4(^4P)\ np]\ ^3P$	$S^+(^2D)$, εd
$[3s3p^4(^4P)\ np]\ ^3S$	$S^+(^2D)$, εd
$[3s3p^4(^4P)\ np]\ ^3D$	$S^+(^2P)$, εd
$[3s3p^4(^4P)\ np]\ ^3P$	$S^+(^2P)$, εs; $S^+(^2P)$, εd
$[3s3p^4(^4P)\ np]\ ^3S$	-

The ^4P core state of S^+ is spin-orbit split into three states $^4P_{5/2}$, $^4P_{3/2}$ and $^4P_{1/2}$ at ionization energies from $S(^3P)$ of 20.204, 20.249 and 20.274 eV, respectively[33]. The ground state of S, ^3P, is spin-orbit split into three states as well, $^3P_{2,1,0}$. The energy differences between the $^3P_2$ ground state and $^3P_1$, and $^3P_2$ and $^3P_0$ are 49 meV and 71 meV respectively. The $^3P_2$ state will be the most populated at room temperature. Therefore it should be possible to observe nine series for the $S^+(^2D)\leftarrow S^*\leftarrow(^3P)$ process (i.e. 3 Rydberg series each converging to 3 ionic limits) and six series for the $S^+(^4S)\leftarrow S^*\leftarrow(^3P)$ and $S^+(^2P)\leftarrow S^*\leftarrow(^3P)$ processes (i.e. in each case two Rydberg series each converging to three ionic limits).

Several fits of the experimental data to Eq. 8.10 have been performed for the case of many open and closed channels, varying the number k of the closed channels.

The best results for all the three experimental spectra have been obtained fitting the data with a function with only two closed channels (k =2). For k =1 it is impossible to fit the spectra where there are clearly at least two Rydberg series. The fits with three Rydberg series (k =3) gave the same two series obtained with k =2 and physically unrealistic parameter values for the third series. In Figures 8.33-8.35 are shown the fits for the three CIS spectra shown in Figures 8.24, 8.28 and 8.31 and recorded at θ=54° 44'.

Figure 8.36 shows the experimental CIS spectra for the three different ionic channels and the resonance energies obtained by fitting them. These values are also reported in Table 8.4 for each final ionic state.

Table 8.4: Energy resonance positions, expressed in eV, from the fits of the CIS spectra on the three different ionic states

n	4	5	6	7	∞
$S^+(^4S)$ *Series 1*	17.844 ± 0.006	19.053 ± 0.002	19.521 ± 0.001	19.753 ± 0.001	20.212
$S^+(^4S)$ *Series 2*	17.876 ± 0.011	19.064 ± 0.002	19.525 ± 0.001	19.755 ± 0.001	20.212
$S^+(^2D)$ *Series 1*	17.962 ± 0.011	19.077 ± 0.003	19.527 ± 0.001	19.753 ± 0.001	20.212
$S^+(^2D)$ *Series 2*	18.093 ± 0.034	19.122 ± 0.009	19.566 ± 0.004	19.793 ± 0.003	20.255
$S^+(^2P)$ *Series 1*	17.867 ± 0.008	19.058 ± 0.002	19.523 ± 0.001	19.753 ± 0.001	20.212
$S^+(^2P)$ *Series 2*	17.944 ± 0.011	19.077 ± 0.003	19.551 ± 0.002	19.789 ± 0.001	20.255

For the $S^+(^4S)\leftarrow S^*\leftarrow S(^3P)$ process, the fit showed that there are two series converging to the same limit at 20.212 eV while for the $S^+(^2D)\leftarrow S^*\leftarrow S(^3P)$ and $S^+(^2P)\leftarrow S^*\leftarrow S(^3P)$ processes the fits showed that there are two series converging to two different limits at 20.212 eV and 20.255 eV. These two limits are near to the energy values founded in literature for the ionization energies from $S(^3P_2)$ to the $S^+(^4P_{5/2})$ and $S^+(^4P_{3/2})$ states of 20.204 eV and 20.249 eV respectively[33].

According to Table 8.3, the $S^+(^4S)\leftarrow S^*\leftarrow S(^3P)$ CIS spectrum has a ^3S and a ^3D Rydberg series while the $S^+(^2P)\leftarrow S^*\leftarrow S(^3P)$ CIS spectrum has a ^3P and a ^3D Rydberg series.

Series 1 of the $S^+(^2P)\leftarrow S^*\leftarrow S(^3P)$ CIS spectrum has the resonance energies values which are similar to the values of both Rydberg series of the $S^+(^4S)\leftarrow S^*\leftarrow S(^3P)$ CIS spectrum and the same limit. This means that *Series 1* of the $S^+(^2P)\leftarrow S^*\leftarrow S(^3P)$ CIS spectrum should be ^3D Rydberg series but it is not sure which of *Series 1* and *2* of the $S^+(^4S)\leftarrow S^*\leftarrow S(^3P)$ CIS spectrum is the ^3D Rydberg series; once this assignment is made the other series is a ^3S Rydberg series.

Series 1 of the $S^+(^2D)\leftarrow S^*\leftarrow S(^3P)$ CIS spectrum should be a ^3P Rydberg series converging to the $^4P_{5/2}$ limit since the ^3S and a ^3D Rydberg series have already been assigned at different resonance energies.

Series 2 of the $S^+(^2D)\leftarrow S^*\leftarrow S(^3P)$ CIS spectrum converges to the $^4P_{3/2}$ limit at 20.255 eV and it could be a ^3S, ^3P and ^3D Rydberg series. If it is a ^3P Rydberg series, the resonance energy difference between the two *n* =4 ^3P Rydberg states converging to the $^4P_{5/2}$ and $^4P_{3/2}$ limits is about 130 meV. If it is a ^3S or a ^3D Rydberg series, the resonance energy differences between the two *n* =4 ^3S or ^3D Rydberg states converging to the $^4P_{5/2}$ and $^4P_{3/2}$ limits are 217 and 249 meV (i.e. the differences in Table 8.4 between $S^+(^2D)$ *Series 2* and $S^+(^4S)$ *Series 2* and *1*, respectively).

Series 2 of the $S^+(^2P)\leftarrow S^*\leftarrow S(^3P)$ CIS spectrum converges to the $^4P_{3/2}$ limit at 20.255 eV and it could be a ^3P and ^3D Rydberg series. If it is ^3P series, its energy position for *n* =4 would be higher than the corresponding ^3P resonance converging to the $^4P_{5/2}$ limit, which is not the case. It is therefore possible to identify this series as a ^3D Rydberg series. At *n* =4, the resonance energy difference between the two ^3D Rydberg states converging to the $^4P_{5/2}$ and $^4P_{3/2}$ limits is about 80 meV. It is likely then that *Series 2* of the $S^+(^2D)\leftarrow S^*\leftarrow S(^3P)$ CIS spectrum is a ^3P Rydberg series since at *n* =4 the resonance energy difference between the two ^3P Rydberg series, converging to the $^4P_{5/2}$ and $^4P_{3/2}$ limits, is 130 meV.

In this way, the only series that are not unequivocally identified are the two in the $S^+(^4S)\leftarrow S^*\leftarrow S(^3P)$ CIS spectrum. In order to obtain more information, a study of the asymmetry parameter has been performed (see later in this Chapter).

As was done in the previous PES study of section 8.2.1, at each photon energy, the asymmetry parameter can be calculated for an S band using Eq. 8.3. Comparisons of the measured asymmetry parameters as a function of photon energy for the three ionization channels resulting from the $(3p)^{-1}$ photoionization of S derived from this work with results of the angular distribution Hartree-Fock calculations of Dill *et al.*[8] have been made over the photon energy range 10-30 eV. This has been carried out to give the plots shown in Figures 8.37 to 8.40.

In Figure 8.37 the three different angular distribution plots are shown as a function of photon energy and comparisons with the results of Dill *et al.*[8] are presented in Figures 8.38-8.40.

As can be seen in Figures 8.38-8.40, the experimental results obtained in this work are in reasonable agreement with the results of the calculations[8] for the all three ionization channels. However, the high resolution obtained with the ELETTRA synchrotron and the abundance of resonances resolved make a comparison difficult. Indeed, the calculations made by Dill *et al.*[8] were intended to provide a theoretical framework that allows angular distribution calculations comparable to calculations of total photoionization cross sections, without taking into account resonances in the β-results.

Figures 8.41 to 8.43 show the measured asymmetry parameters as a function of photon energy for the three ionization channels resulting from the $(3p)^{-1}$ photoionization of S.

Fits of the experimental spectra recorded at $\theta=0°$ have been performed as well.

It was then possible to calculate the asymmetry parameters for each ionization channels from the two fitted spectra at $\theta=0°$ and $\theta=54°\ 44'$. The asymmetry parameters evaluated in this way as a function of the photon energy are shown in Figures 8.44-8.46.

The agreement between the experimental and calculated asymmetry parameters is good although at higher n resonances there are more spikes in the calculated spectra. This is principally due to a small misalignment of the resonance positions between the fitted spectra at $\theta=0°$ and $\theta=54°\ 44'$. A small misalignment of 0.5 meV becomes important at higher n where the width of the resonances is small and gives this spike effect. This effect is increased by the fact that the fits are performed without deconvoluting the data with the instrumental resolution[54]. A fit without instrumental deconvolution may become unreliable for an atomic transition involving narrow resonances[55].

Nevertheless, a qualitative agreement for $n=4$, 5 and 6 is good for the purpose of this work.

The behaviour of the total asymmetry parameters as a function of photon energy in Figures 8.44-8.46 cannot help the assignment of the Rydberg series. More information could be obtained from the asymmetry parameter plot of each Rydberg series. To calculate them, the parameters of the fits at $\theta=0°$ and $\theta=54°\ 44'$ are separated for the two series of each ionization process.

The asymmetry parameters so obtained are plotted in Figures 8.47 to 8.52.

The asymmetry parameters of the two series in each of the two $S^+(^2D)\leftarrow S^*\leftarrow S(^3P)$ and $S^+(^2P)\leftarrow S^*\leftarrow S(^3P)$ CIS spectra have very similar behaviour in proximity of the resonances as can be observed in Figures 8.49-8.52. Crossing a resonance, the asymmetry parameter firstly increases its value then decreases to its value out of resonance. According to these observations and Table 8.3, the free electron of all the four series has a pure d character; therefore similar behaviour of all the four asymmetry parameters is expected.

The asymmetry parameter of the Rydberg *Series 2* of the $S^+(^4S)\leftarrow S^*\leftarrow S(^3P)$ CIS spectrum has a behaviour similar to the four series previously analysed. This means the free electron should have a d character. This property, as can be seen in Table 8.3, is satisfied by the ^3D Rydberg series. By elimination, the Rydberg *Series 1* of the $S^+(^4S)\leftarrow S^*\leftarrow S(^3P)$ CIS spectrum is a ^3S Rydberg series with a s wavefunction free electron. Indeed, Figures 8.47 shows the asymmetry parameter decreasing and then increasing while crossing a resonance.

Table 8.5 shows the six Rydberg series observed with the assignments made in this work.

Table 8.5: Summary of the assignment made for the six Rydberg series observed

Final CIS Ionic State	Fitted Limit	Ionic Limit	Excited State	Free Electron
$(3s^23p^3)$ $S^+(^4S)$ *Series 1*	20.212 eV	$^4P_{5/2}$	$[3s3p^4(^4P)\,np]\ ^3S$	εs
$(3s^23p^3)$ $S^+(^4S)$ *Series 2*	20.212 eV	$^4P_{5/2}$	$[3s3p^4(^4P)\,np]\ ^3D$	εd
$(3s^23p^3)$ $S^+(^2D)$ *Series 1*	20.212 eV	$^4P_{5/2}$	$[3s3p^4(^4P)\,np]\ ^3P$	εd
$(3s^23p^3)$ $S^+(^2D)$ *Series 2*	20.255 eV	$^4P_{3/2}$	$[3s3p^4(^4P)\,np]\ ^3P$	εd
$(3s^23p^3)$ $S^+(^2P)$ *Series 1*	20.212 eV	$^4P_{5/2}$	$[3s3p^4(^4P)\,np]\ ^3D$	εd
$(3s^23p^3)$ $S^+(^2P)$ *Series 2*	20.255 eV	$^4P_{3/2}$	$[3s3p^4(^4P)\,np]\ ^3D$	εd

In summary, for the first time Rydberg series converging to the fourth ionization limit (IE=20.204 eV) have been observed for the $S^+(^4S) \leftarrow S^*[3s3p^4\ (^4P)\ np] \leftarrow S(^3P)$, $S^+(^2D) \leftarrow S^*[3s3p^4\ (^4P)\ np] \leftarrow S(^3P)$ and $S^+(^2P) \leftarrow S^*[3s3p^4\ (^4P)\ np] \leftarrow S(^3P)$ ionization processes. The ionic core of the excited S^* atom is split into three spin-orbit states $^4P_{5/2}$, $^4P_{3/2}$ and $^4P_{1/2}$. A total of six Rydberg series have been observed experimentally. Using MQDT it has been possible to fit the experimental spectra with parameterized lineshape formula and to assign the Rydberg series.

^3S, ^3P and ^3D Rydberg series converging to the $^4P_{5/2}$ limit have been identified as well as ^3P and ^3D Rydberg series converging to the higher $^4P_{3/2}$ limit.

For the $S^+(^4S) \leftarrow S^* \leftarrow S(^3P)$ CIS spectrum, two series were observed which converge to the $S^+(^4P_{5/2}) \leftarrow S(^3P)$ limit. *Series 1* (the series with lower resonance energies for a given *n*) arises from ^3S excited states whereas *Series 2* corresponds to ^3D excited states.

For the $S^+(^2D) \leftarrow S^* \leftarrow S(^3P)$ CIS spectrum, two series were observed which converge to the $S^+(^4P_{5/2}) \leftarrow S(^3P)$ and $S^+(^4P_{3/2}) \leftarrow S(^3P)$ limits. Both the series correspond to ^3P excited states.

For the $S^+(^2P) \leftarrow S^* \leftarrow S(^3P)$ CIS spectrum, two series were observed which converge to the $S^+(^4P_{5/2}) \leftarrow S(^3P)$ and $S^+(^4P_{3/2}) \leftarrow S(^3P)$ limits. Both the series correspond to ^3D excited states.

In Figures 8.53 to 8.56 the CIS spectra recorded for the $SH^+(a\ ^1\Delta, v^+=0) \leftarrow SH(X\ ^2\Pi, v''=0)$ and $SH^+(b\ ^1\Sigma^-, v^+=0) \leftarrow SH(X\ ^2\Pi, v''=0)$ ionizations at $\theta=54^\circ\ 44'$ with respect to the polarization axis of the photon source are presented.

In Figures 8.54 and 8.55, the CIS of the second band $SH^+(a\ ^1\Delta, v^+=0) \leftarrow SH(X\ ^2\Pi, v''=0)$, the expected position of the $SH^*(b\ ^1\Sigma, nd)$, $SH^*(A\ ^3\Pi, nd)$ and $SH^*(c\ ^1\Pi, nd)$ Rydberg states, which are parts of series converging to the third, fourth and fifth ionization limits, are indicated. The excitation energies have been obtained applying the Rydberg formula with the 3d quantum defect values $\delta=0.17$ obtained by Gibson *et al.*[14] for S atoms. These spectra are only poorly resolved and hence a positive identification cannot be made. However, the structures seen in Figure 8.55 in the energetic region 13.0-14.5 eV look to be part of a series converging to a limit at

14.5 eV, but unfortunately there is no SH ionization limit at this energy and attempts to fit some of the components to a series converging to a limit at 14.11 eV (the fourth AIE of SH) proved unsuccessful. In view of these results, CIS measurements were not made at $\theta=0°$, hence β as a function of the photon energy was not obtained for SH.

8.3 Conclusions

In this investigation on S with Synchrotron Radiation, the angular distribution parameters and relative photoionization cross section for the $S^+(^4S) \leftarrow S(^3P)$, $S^+(^2D) \leftarrow S(^3P)$ and $S^+(^2P) \leftarrow S(^3P)$ ionizations have been evaluated as a function of photon energy from threshold to 31 eV, with both PE and CIS spectroscopy techniques. All spectra were recorded at two angles, $\theta = 0°$ and $\theta = 54° 44'$, with respect to the polarization axis of the photon source. In the first attempt, PE spectra were recorded in the ionization energy region 9.600-15.200 eV using 23 different photon energies from 13.205 to 21.640 eV.

Later, CIS spectra were successfully recorded for the $S^+(^4S) \leftarrow S(^3P)$ ionization at 10.35 eV, for the $S^+(^2D) \leftarrow S(^3P)$ ionization at 12.21 eV and for the $S^+(^2P) \leftarrow S(^3P)$ ionization at 13.40 eV. This second study has highlighted the presence of several structures that were not observed in the previous PE investigation. Inspections of the CIS spectra have shown that all the bands converging to the second and third ionization limits can be assigned to excitation to known Rydberg states. For the first time Rydberg series converging to the fourth ionization limit have been observed and assignments have been proposed according with Russell-Saunders selection rules[52,53].

The results obtained have been compared, where available, with previous experiments and calculations.

Also the $SH^+(X\ ^3\Sigma^-, v^+=0) \leftarrow SH(X\ ^2\Pi, v''=0)$, $SH^+(a\ ^1\Delta, v^+=0) \leftarrow SH(X\ ^2\Pi, v''=0)$ and $SH^+(b\ ^1\Sigma^-, v^+=0) \leftarrow SH(X\ ^2\Pi, v''=0)$ ionizations have been investigated as a function of photon energy from threshold to 21.64 eV by the PE and CIS spectroscopy techniques.

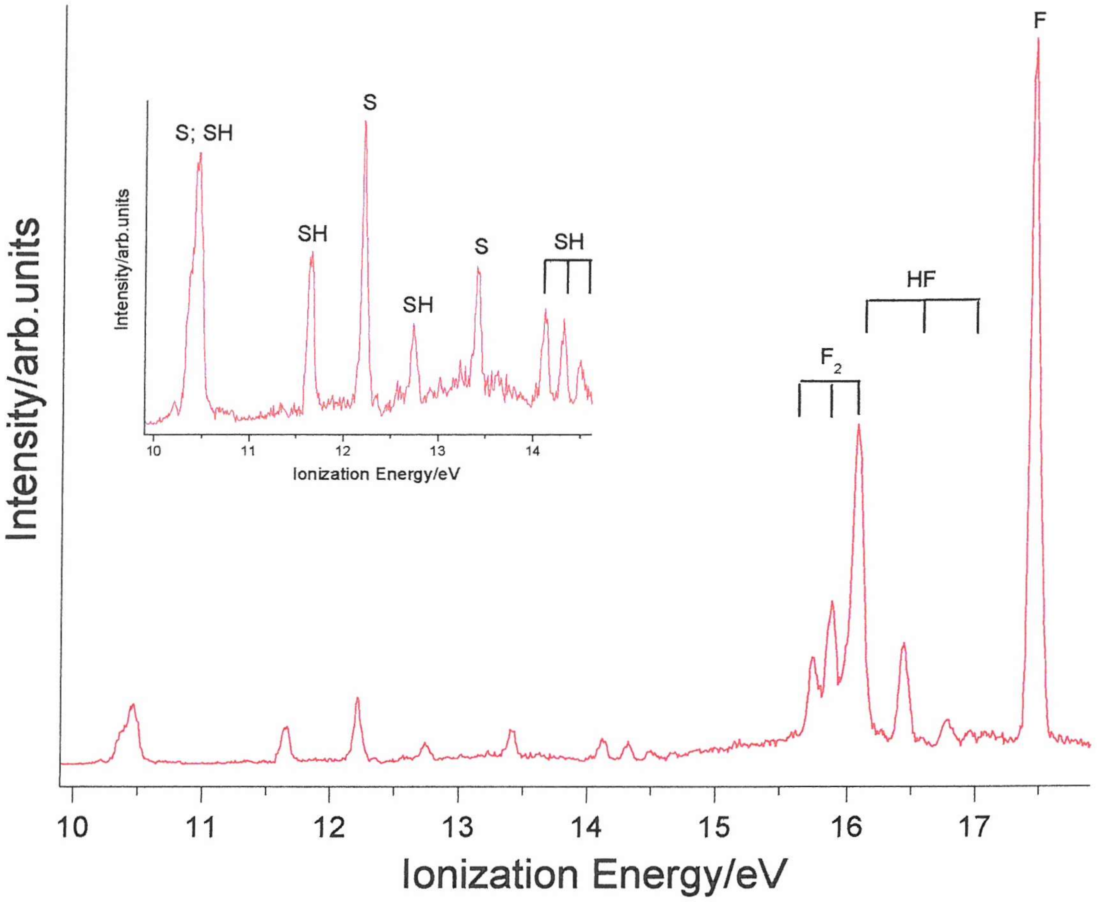

Figure 8.1: Photoelectron spectrum at hν =21.64 eV of the reactions

$F + H_2S \rightarrow SH + HF$

$F + HS \rightarrow S + HF$

measured at the angles with respect to the major polarization axis of the photon source θ =0 °

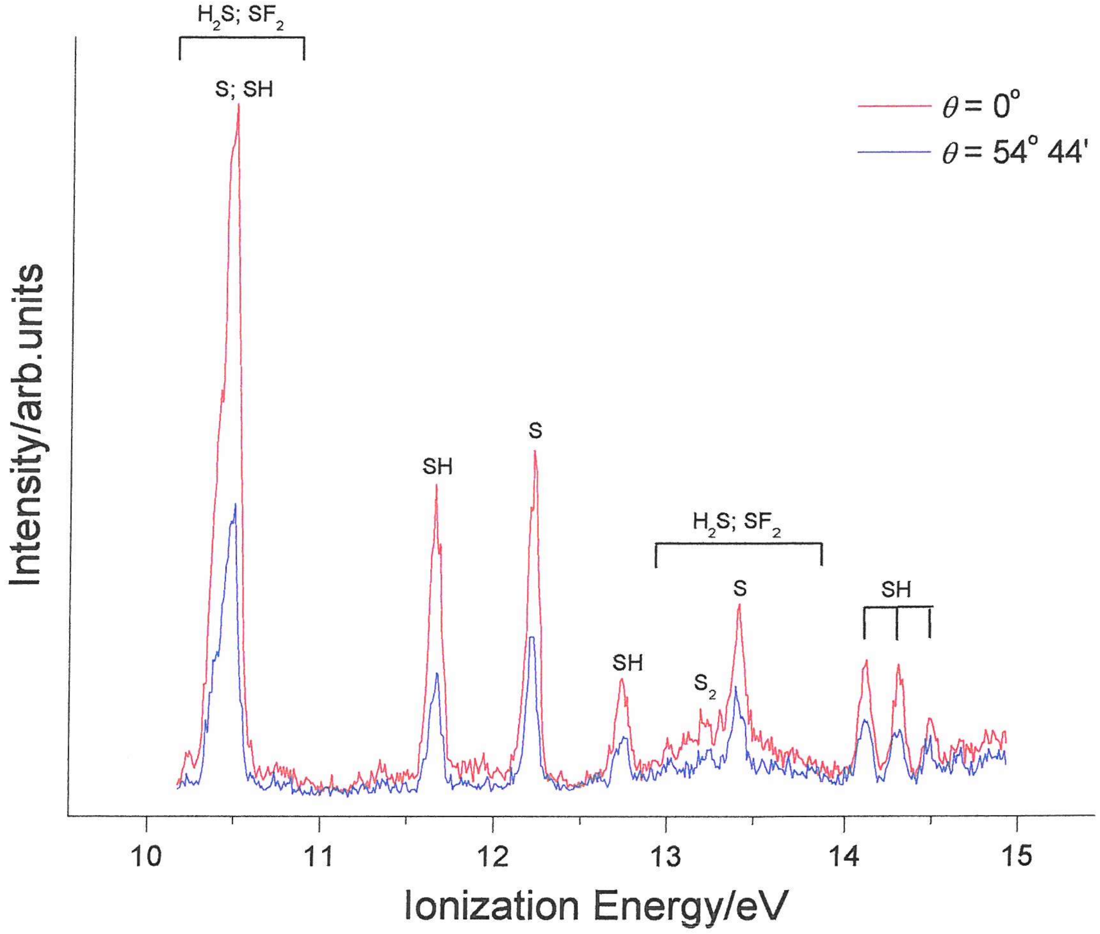

Figure 8.2: Photoelectron spectrum at hν =21.64 eV of the reactions

$F + H_2S \rightarrow SH + HF$

$F + HS \rightarrow S + HF$

measured at two different angles θ =0 ° (red trace) and θ =54 ° 44' (blue trace) with respect to the major polarization axis of the photon source in the 10.0-15.0 eV ionization energy region

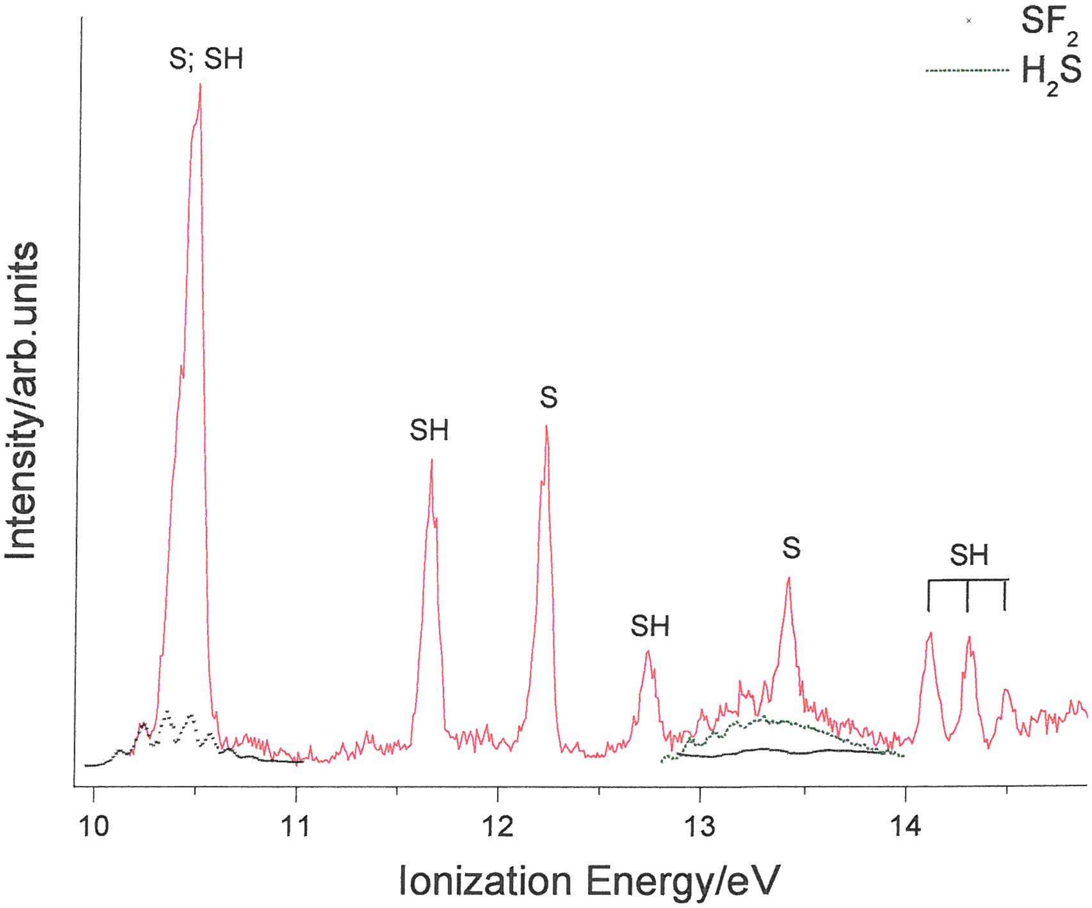

Figure 8.3: Photoelectron spectrum recorded at $h\nu = 21.64$ *eV at* $\theta = 0°$ *for the reaction F +* H_2S *at a mixing distance of 2 cm above the photon beam Estimated contributions from* SF_2 *(first and second bands) and* H_2S *(second band) are shown*

The asymmetry parameter of the first vibrational component of the 4^{th} *band of SH at IE of 14.11 eV has been measured as* $\beta = 1.04 \pm 0.39$ *at this photon energy*

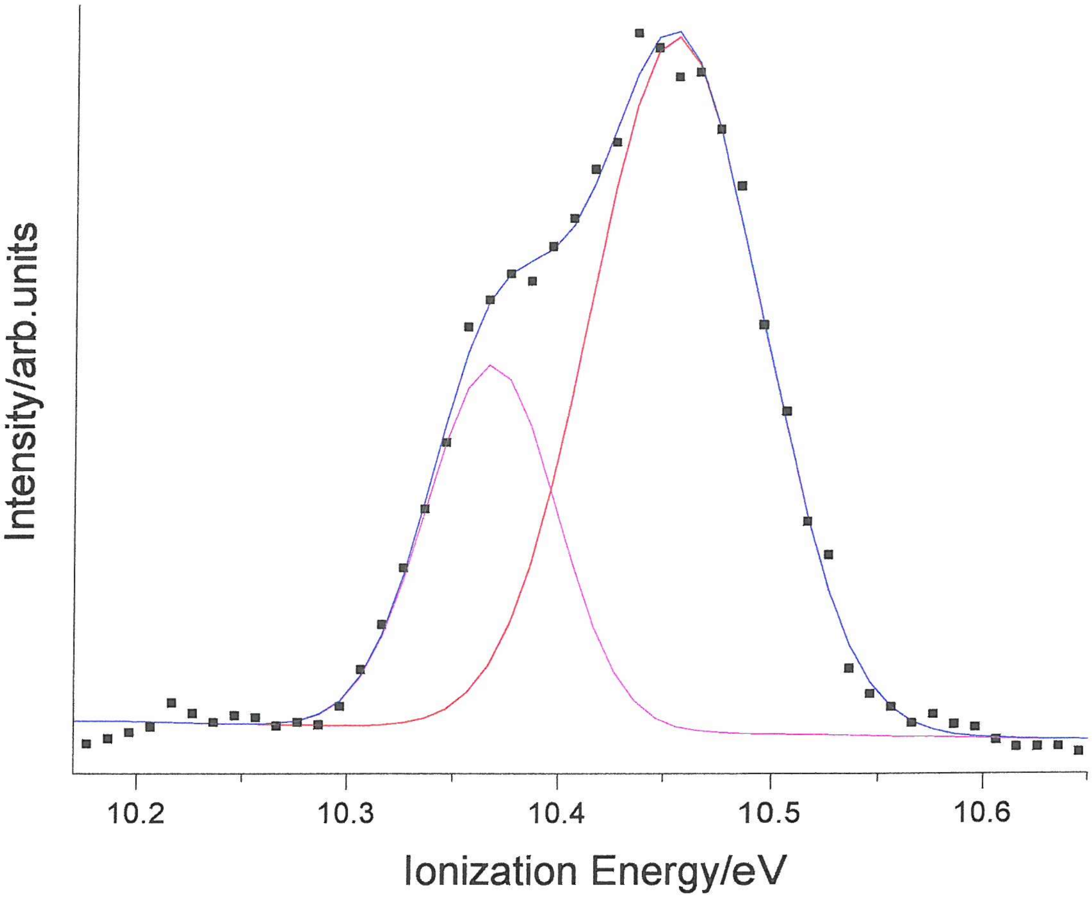

Figure 8.4: Deconvolution of the band shown in Figure 8.3 at ≈10.4 eV ionization energy into two Gaussian components. The band centred at 10.36 eV is the first band of S atoms ($S^+(^4S) \leftarrow S(^3P)$) whereas the band at 10.45 eV contains contributions from the first band of SH ($SH^+(X\,^3\Sigma^-) \leftarrow SH(X\,^2\Pi)$) and from the first band of H_2S (see text for further details)

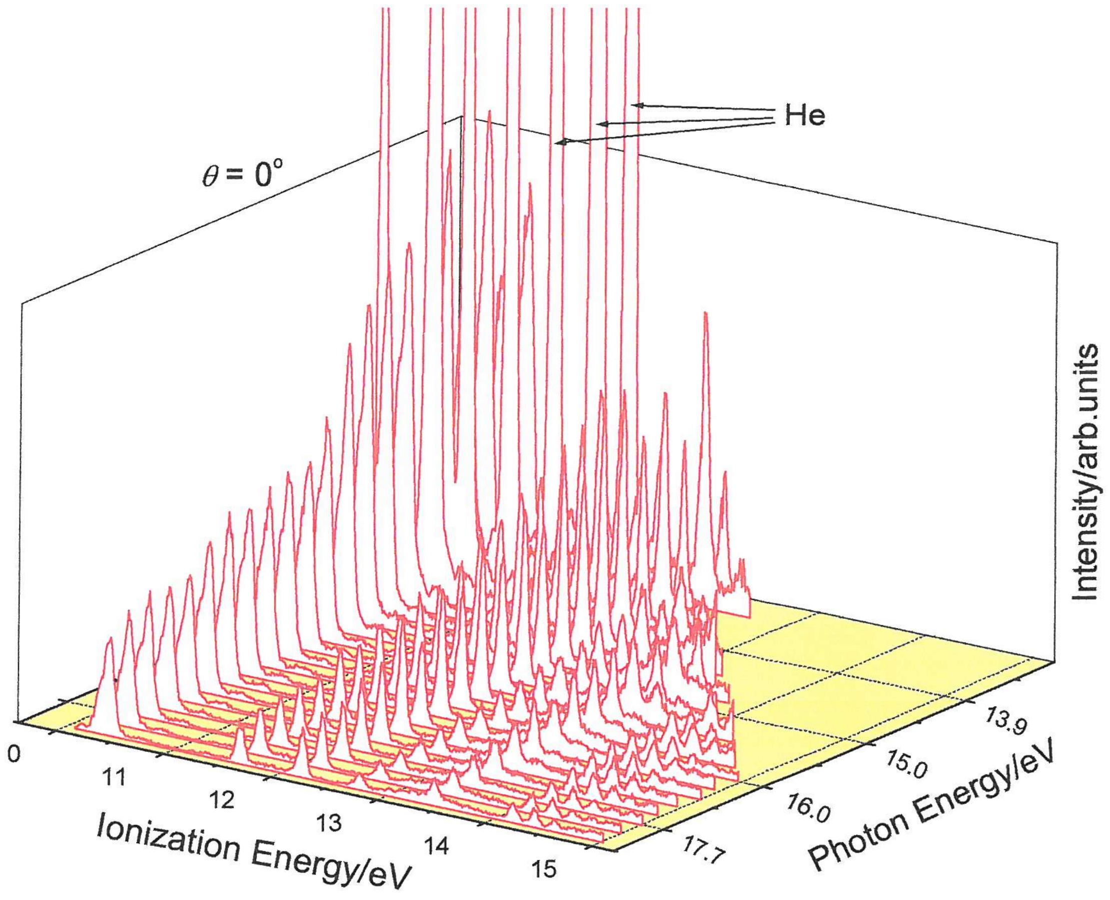

Figure 8.5: PE spectra recorded at 22 different photon energies from hν =13.2 eV to hν =18.5 eV (with a ~200 meV of stepwidth in the photon energy region 13.2-16.4 eV; with a ~400 meV of stepwidth in the photon energy region 16.4-18.5 eV) in the ionization energy region 9.6-15.2 eV, at θ =0° The band at photon energies between 13.20 eV and 14.30 eV, shown by arrows, is due to ionization of helium by second order radiation

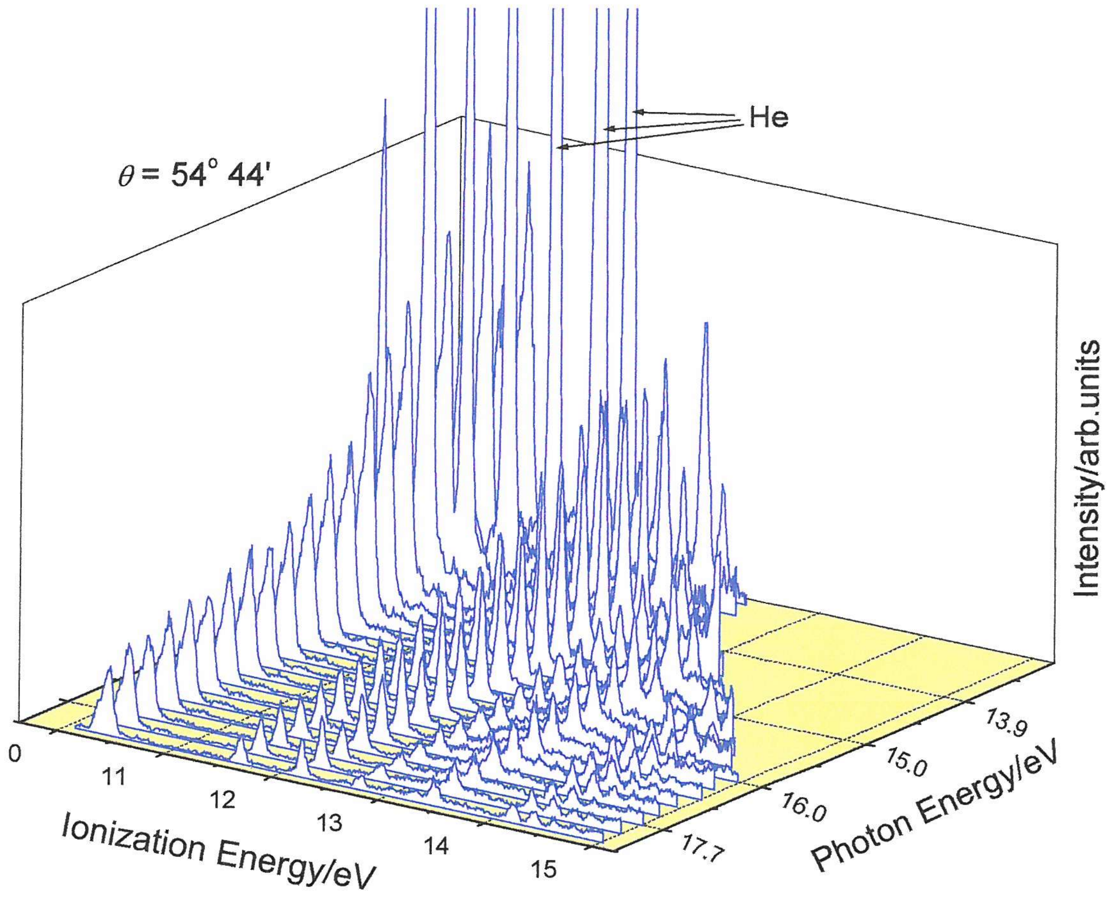

Figure 8.6: PE spectra recorded at 22 different photon energies from hν =13.2 eV to hν =18.5 eV (with a ~200 meV of stepwidth in the photon energy region 13.2-16.4 eV; with a ~400 meV of stepwidth in the photon energy region 16.4-18.5 eV) in the ionization energy region 9.6-15.2 eV, at θ =54° 44' The band between 13.20 eV and 14.30 eV photon energy, shown by arrows, is due to ionization of helium by second order radiation

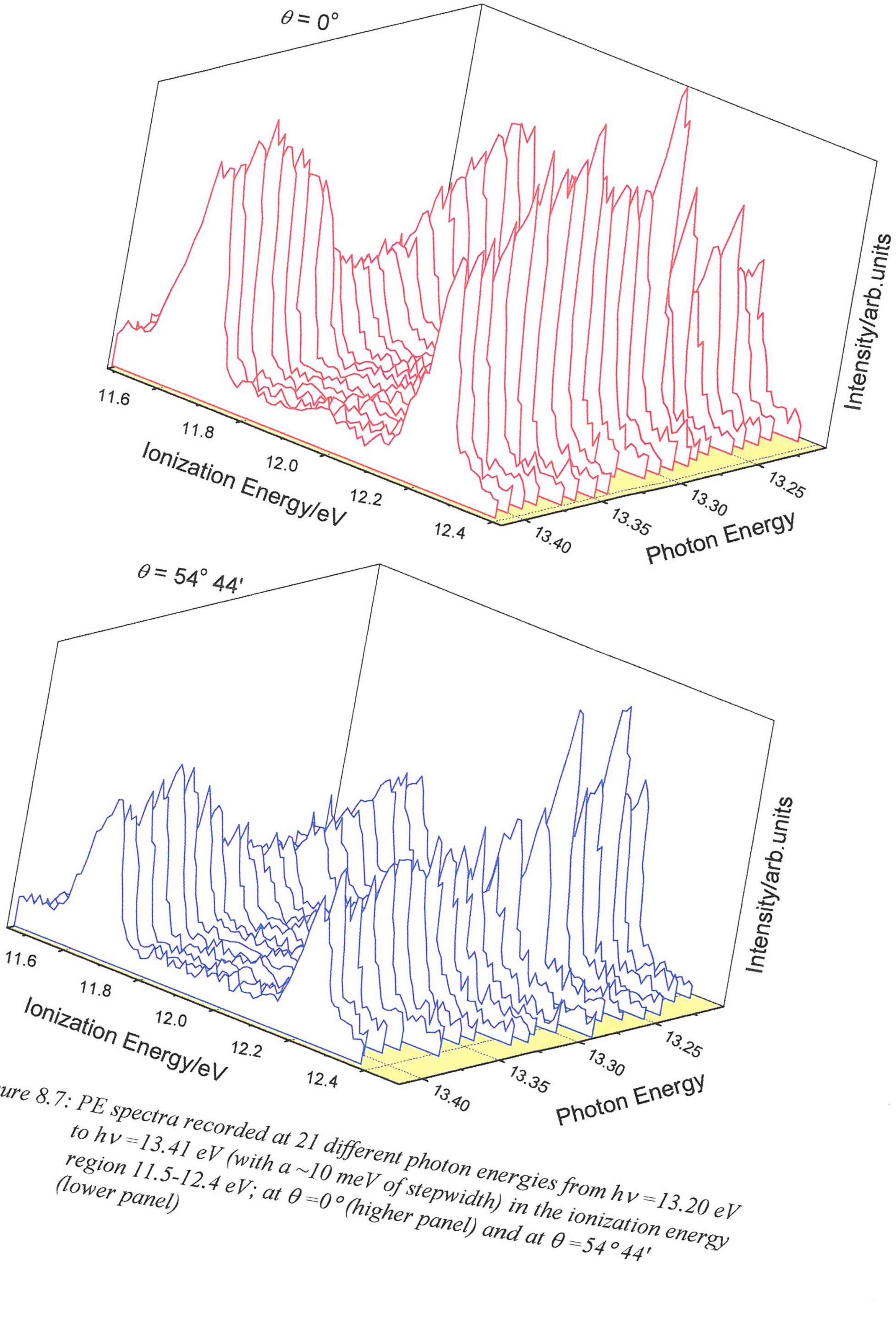

Figure 8.7: PE spectra recorded at 21 different photon energies from $h\nu = 13.20$ *eV to* $h\nu = 13.41$ *eV (with a ~10 meV of stepwidth) in the ionization energy region 11.5-12.4 eV; at* $\theta = 0°$ *(higher panel) and at* $\theta = 54°44'$ *(lower panel)*

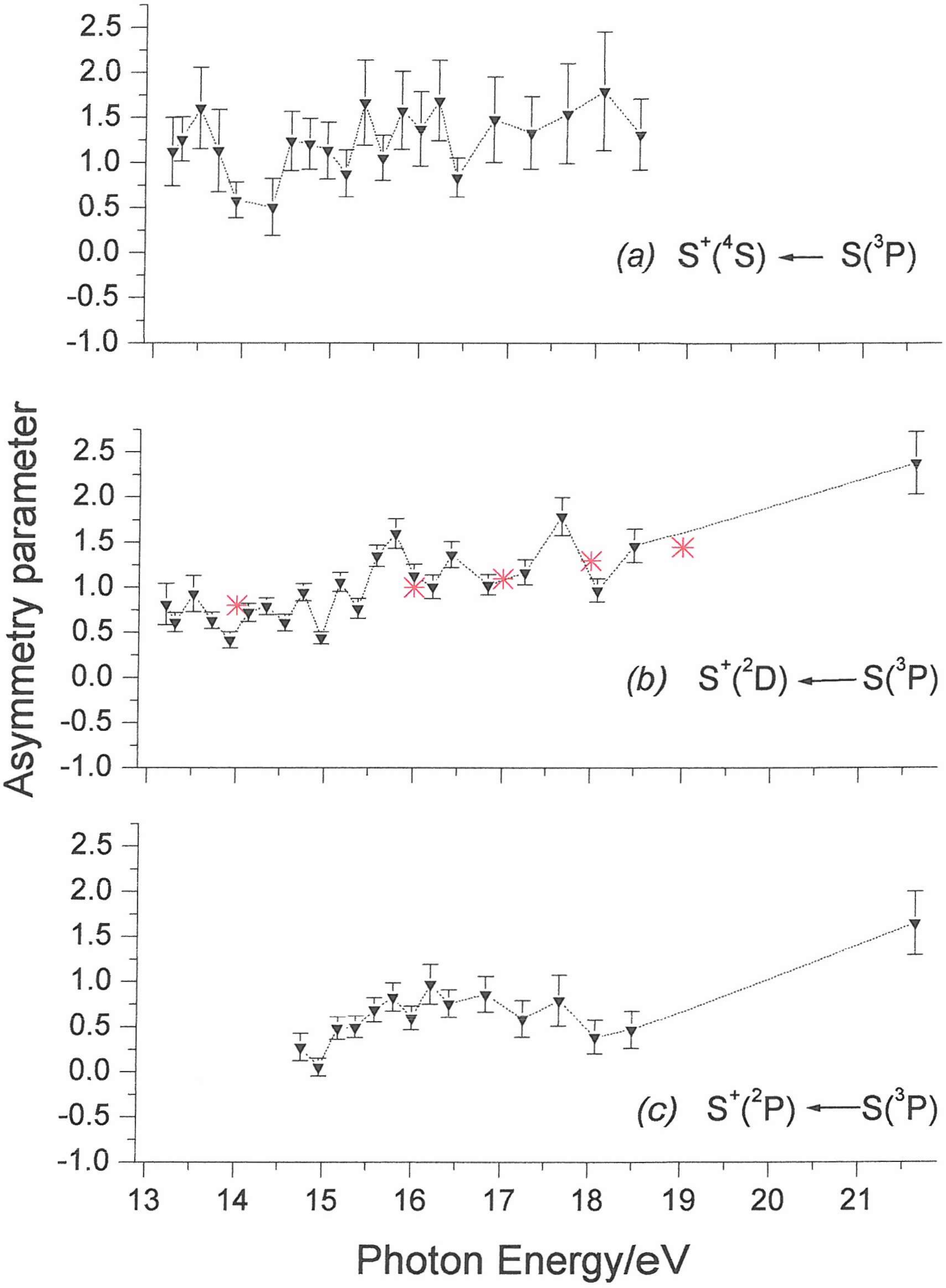

Figure 8.8: Plots of the asymmetry parameter (β) as a function of photon energy over the range hν =13.0–21.0 eV, for the first three photoelectron bands of S atoms

Plot (b) includes β values for the first band of H_2S measured at different photon energies in Ref.(34), denoted with the symbol (*)

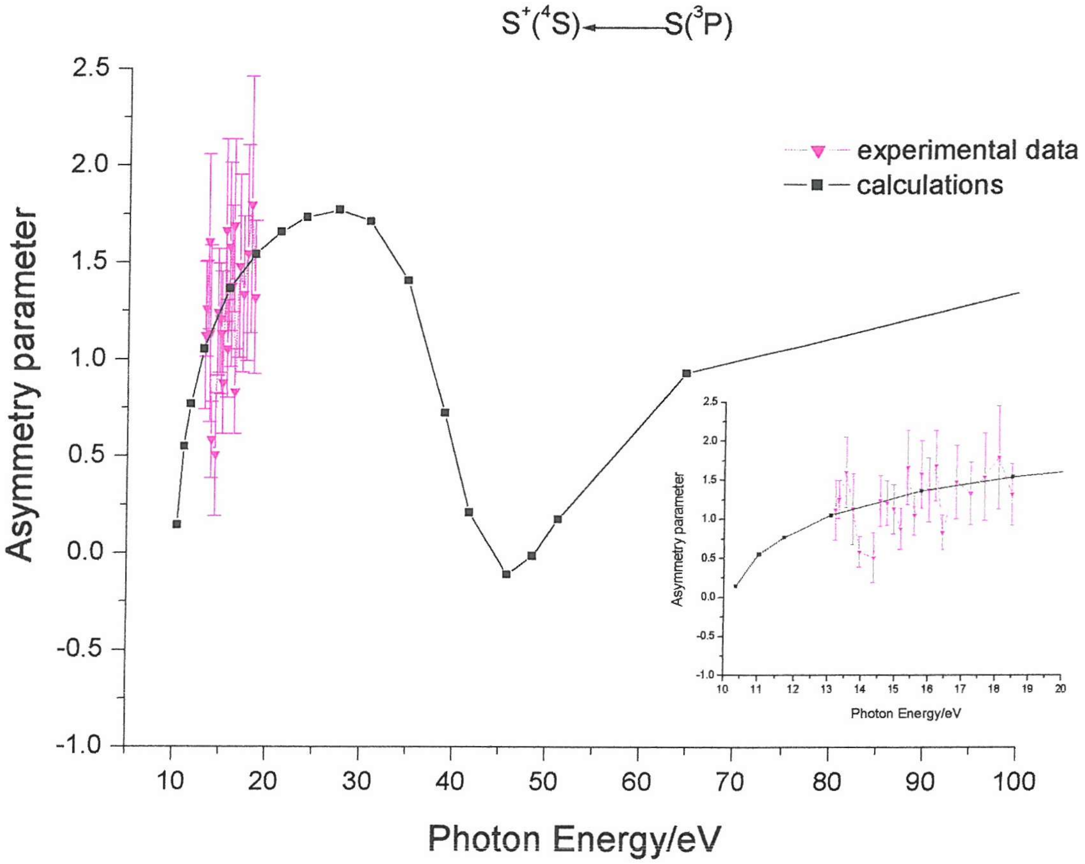

Figure 8.9: Asymmetry parameters for S atoms plotted as a function of photon energy and compared with the results of Dill et al.[7]*, for the first S atom band* $S^+(^4S) \leftarrow S(^3P)$

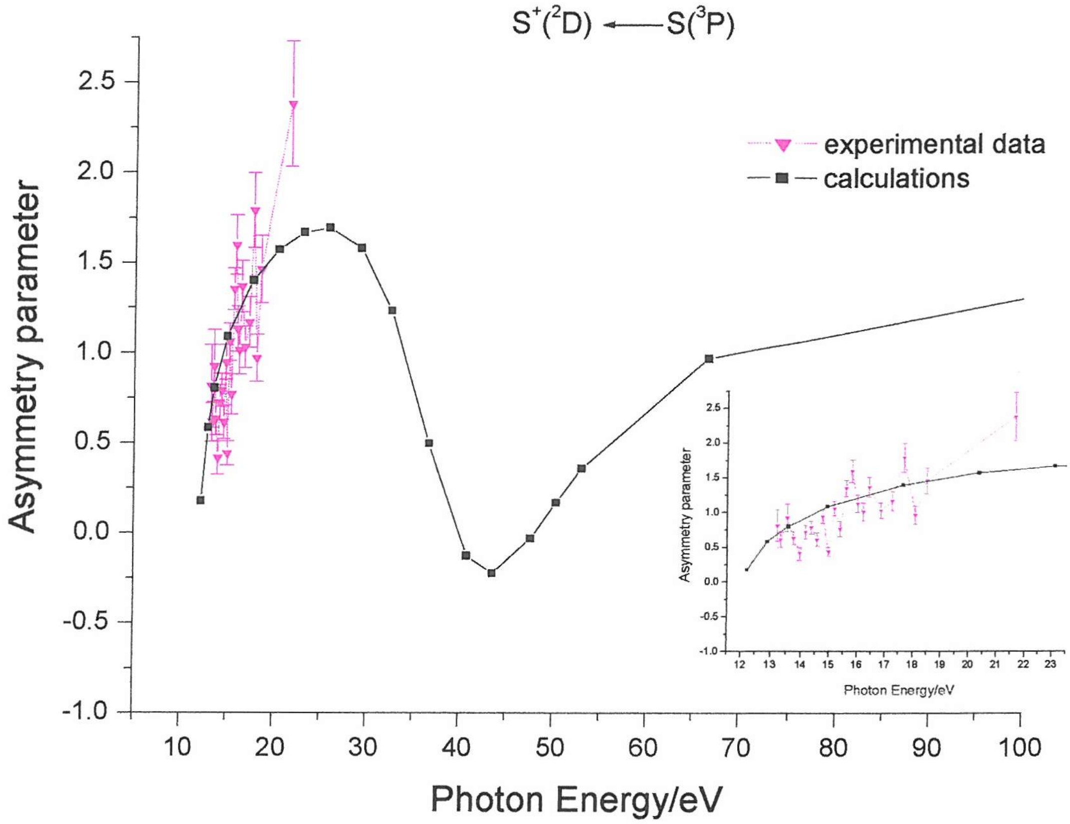

Figure 8.10: Asymmetry parameters for S atoms plotted as a function of photon energy and compared with the results of Dill et al.[7]*, for the second S atom band* $S^+(^2D) \leftarrow S(^3P)$

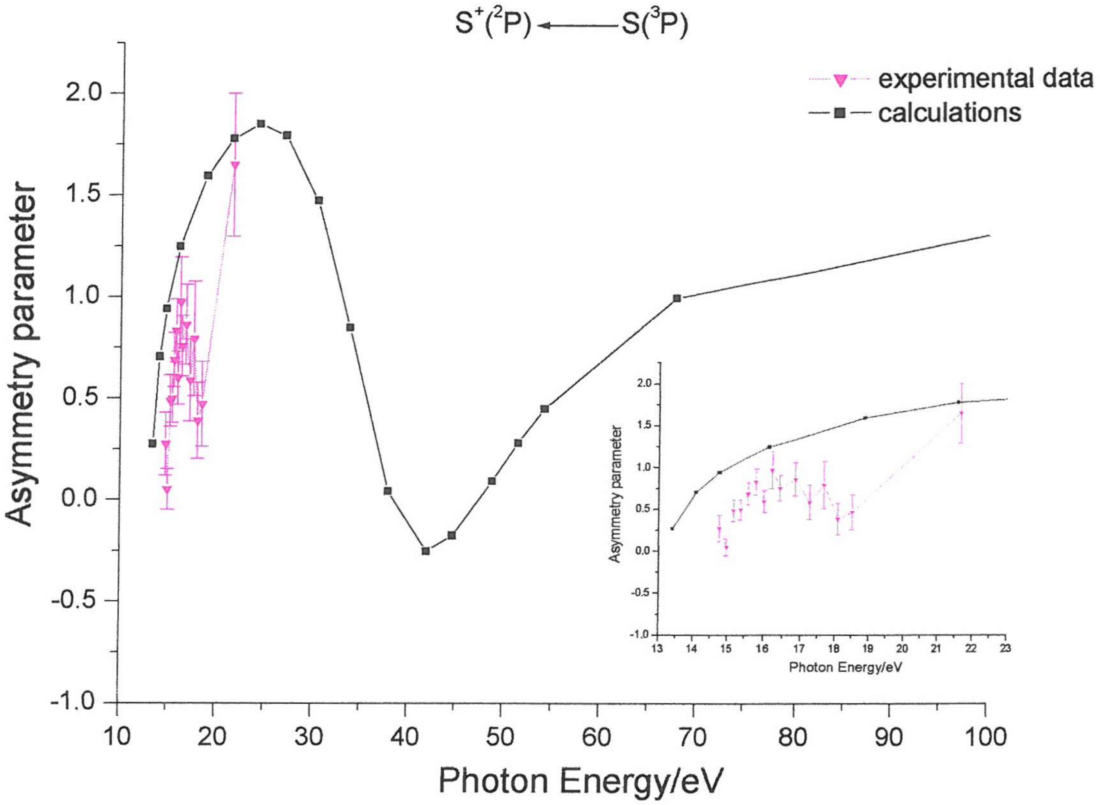

Figure 8.11: Asymmetry parameters for S atoms plotted as a function of photon energy and compared with the results of Dill et al.[7] *for the third S atom band* $S^+(^2P) \leftarrow S(^3P)$

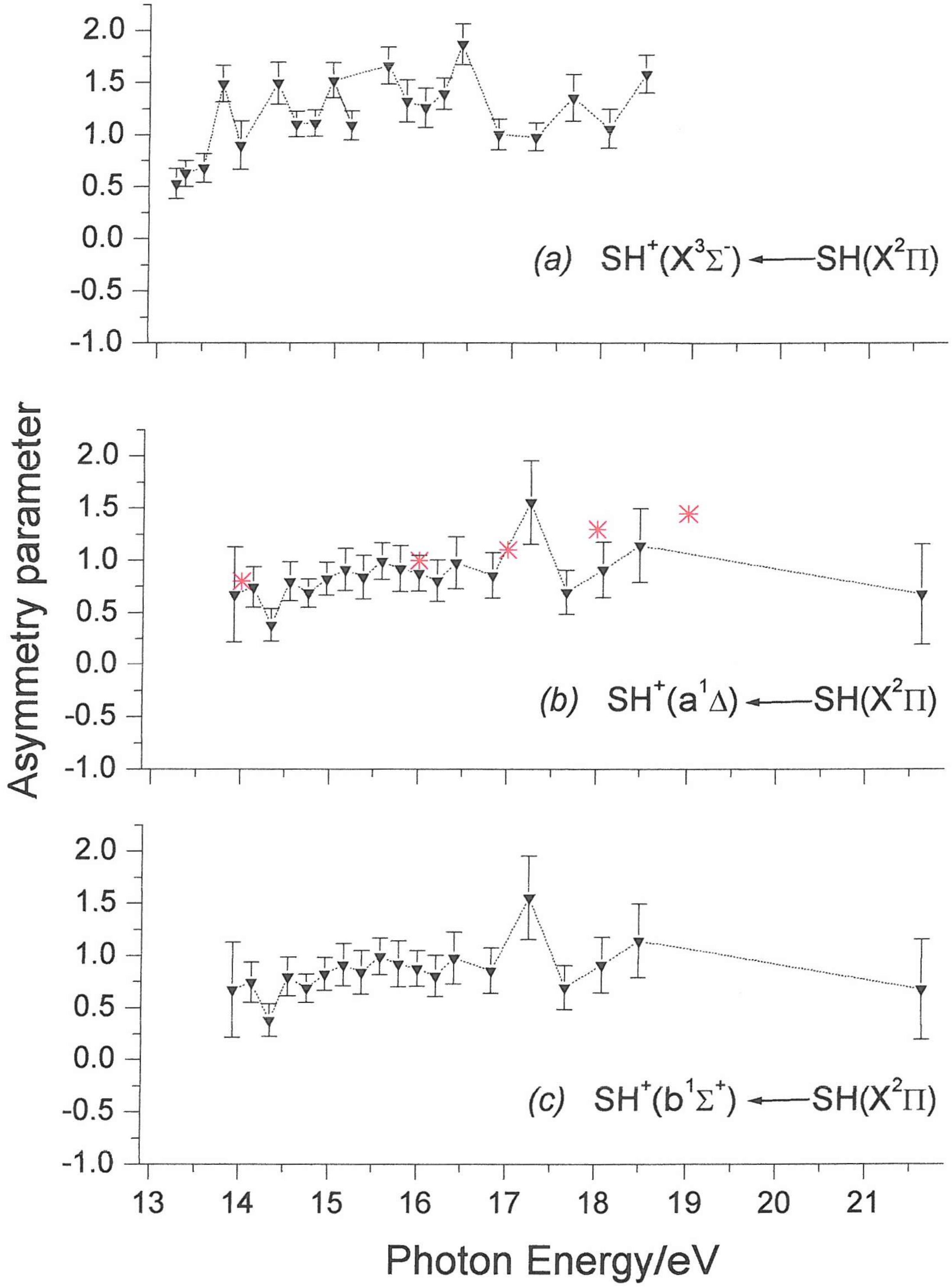

Figure 8.12: Plots of the asymmetry parameter (β) as a function of photon energy over the range $h\nu$ =13.0–18.5 eV, for the first three photoelectron bands of SH

Plot (b) includes β values for the first band of H_2S measured at different photon energies in Ref.(34), denoted with the symbol (*)

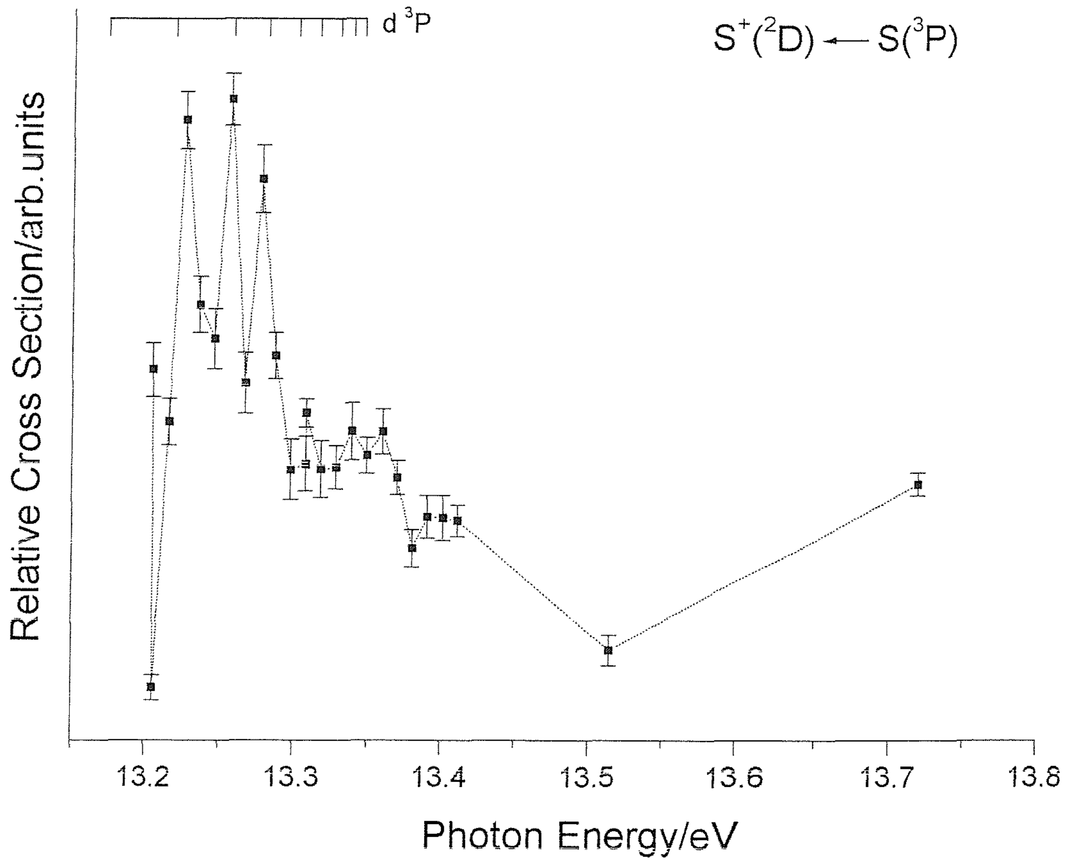

Figure 8.13: Relative cross sections for the $S^+(^2D) \leftarrow S(^3P)$ band in the photon energy region 13.205-13.800 eV

The resonances present in the region 13.205–13.350 eV have been assigned to excitations to $[3s^2 3p^3(^2P)\ nd]\ ^3P$ Rydberg states which are part of a series which converges to the third ionization limit at 13.400 eV

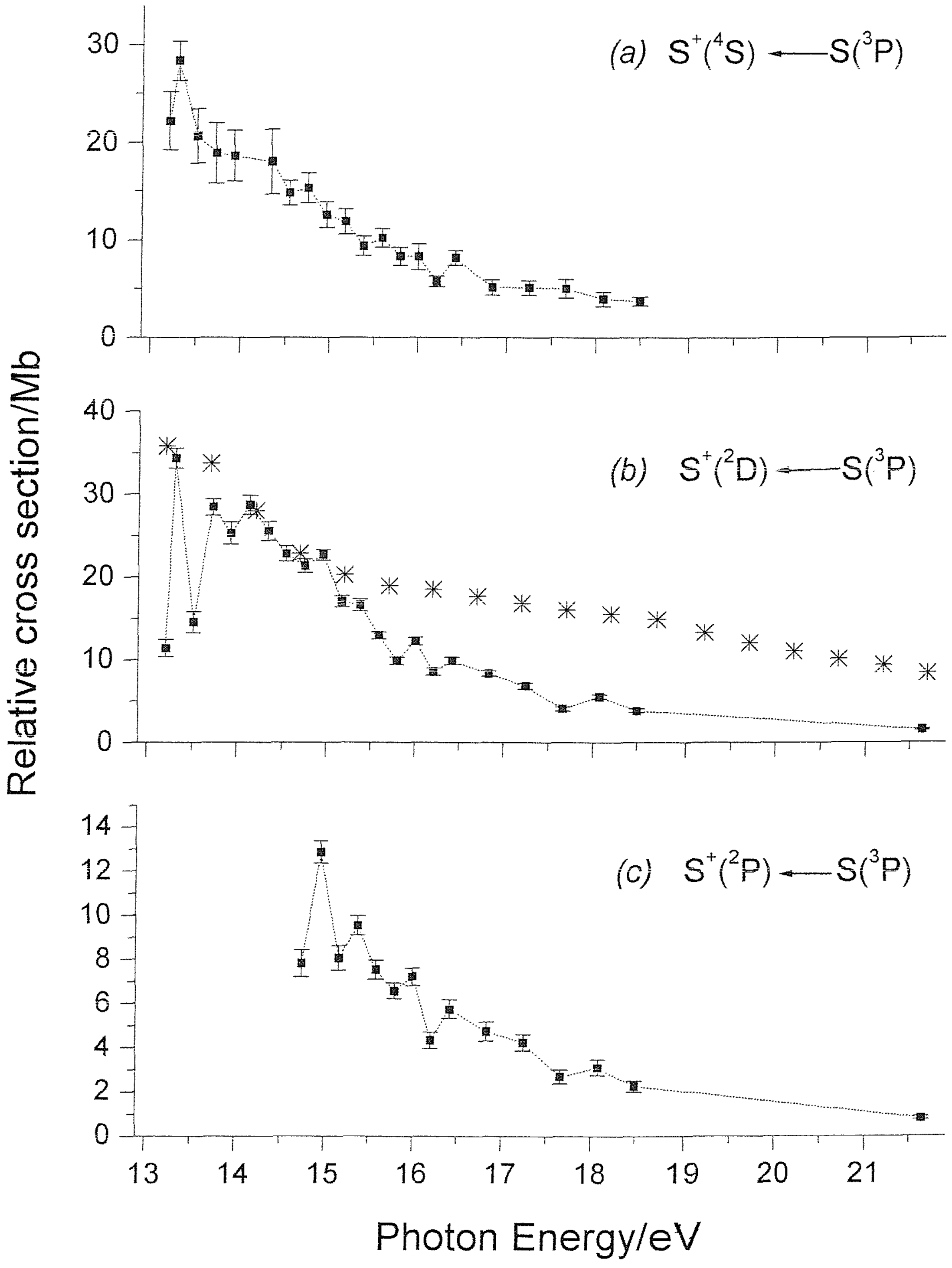

Figure 8.14: Relative photoionization cross sections for the first three bands of S atoms in the photon energy region 13.0–21.5 eV
In plot (a) the maximum observed at 13.30 eV corresponds to excitation to unresolved [$3s^2 3p^3(^2P)$ nd]^{3}P Rydberg states
Plot (b) includes σ values for the first band of H_2S measured at different photon energies in Ref.(40), denoted with the symbol (*)

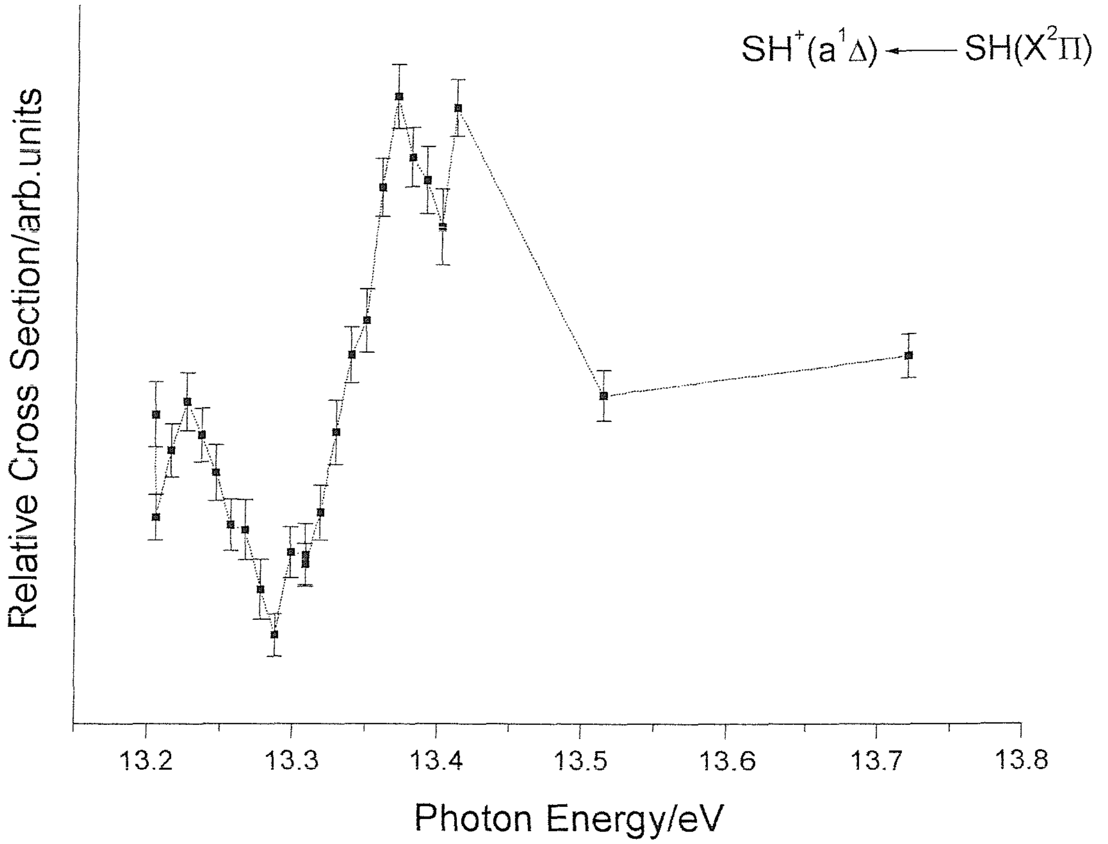

Figure 8.15: Relative photon ionization cross sections for SH plotted as a function of photon energy for the second band of SH in the photon energy region 13.2–13.8 eV

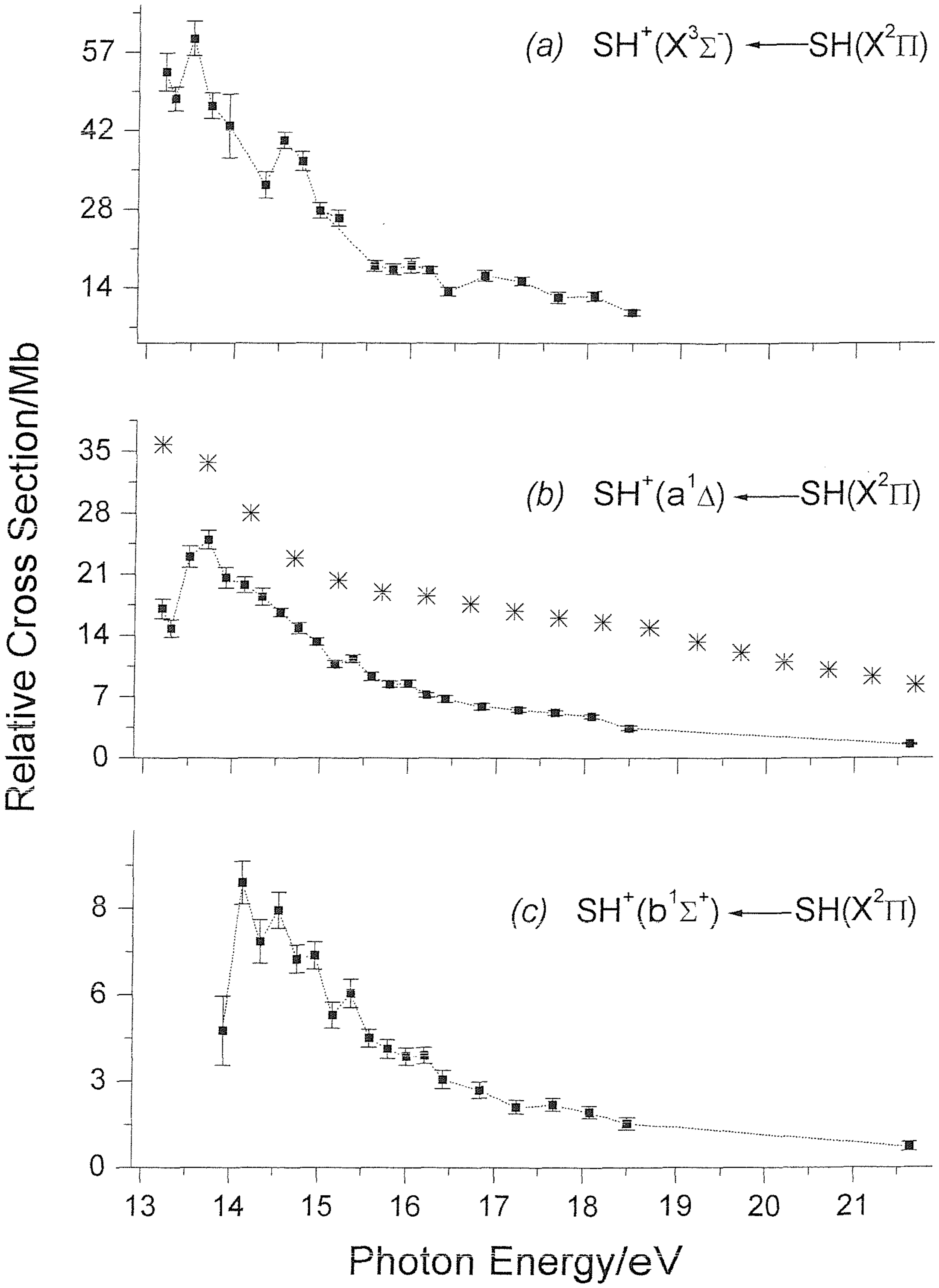

Figure 8.16: Relative photon ionization cross sections for SH plotted as a function of photon energy for the first three bands of SH in the photon energy region 13.0 21.5 eV

Plot (b) includes σ values for the first band of H_2S measured at different photon energies in Ref.(40), denoted with the symbol (*)

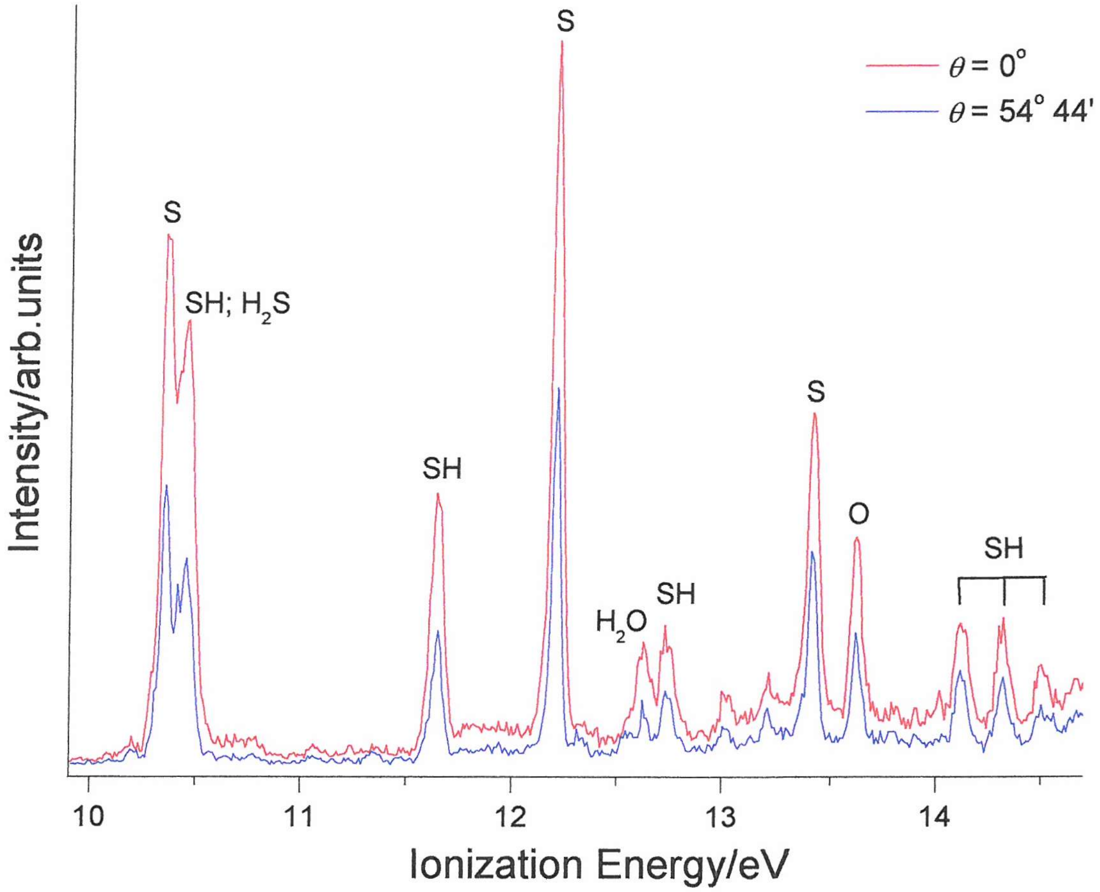

Figure 8.17: Photoelectron spectrum at $h\nu = 21.264$ *eV of the reactions*

$F + H_2S \rightarrow SH + HF$

$F + HS \rightarrow S + HF$

measured at two different angles $\theta = 0°$ *(red trace) and* $\theta = 54° 44'$ *(blue trace) with respect to the major polarization axis of the photon source in the 10.0-15.0 eV ionization region*

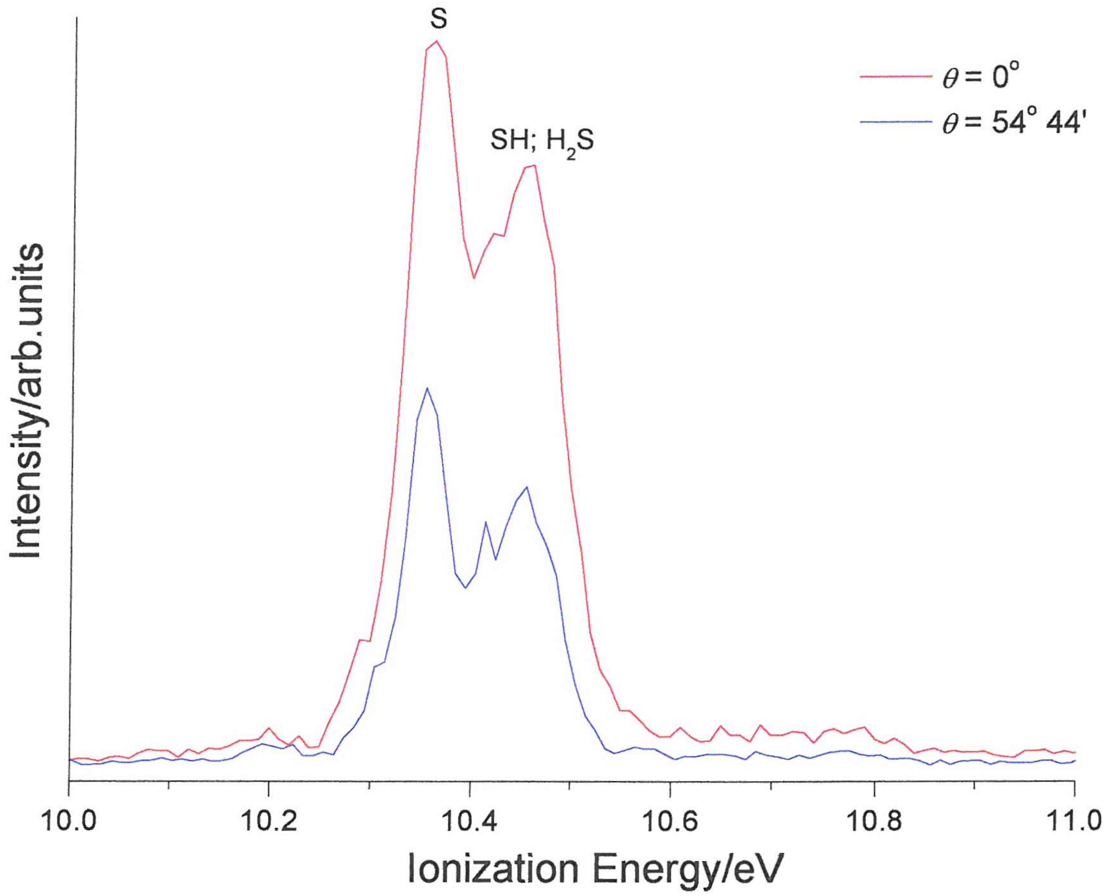

Figure 8.18: Band shown in Figure 8.17 at ≈10.4 eV ionization energy The band centred at 10.35 eV IE is the first band of S atoms ($S^+(^4S) \leftarrow S(^3P)$) whereas the band at 10.45 eV contains contributions from the first band of SH ($SH^+(X\,^3\Sigma^-) \leftarrow SH(X\,^2\Pi)$) at 10.42eV IE and from the first band of H_2S at 10.48 eV IE[6]

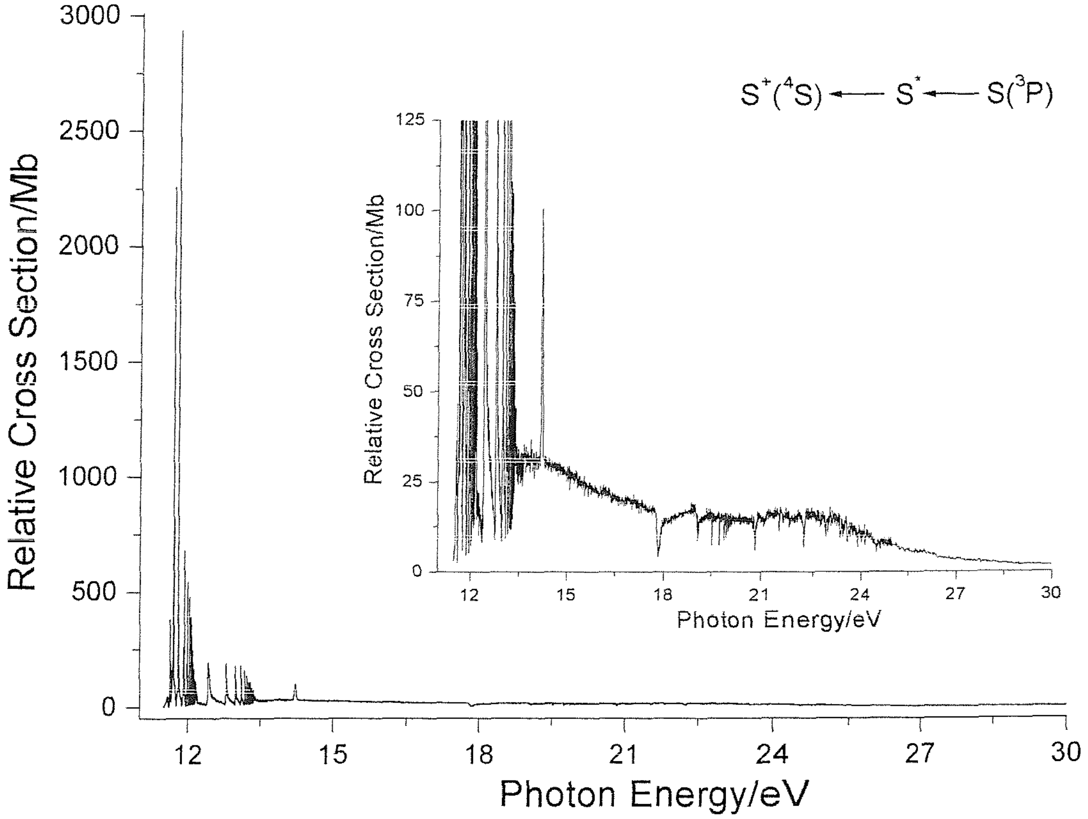

Figure 8.19: CIS spectrum recorded for the $S^+(^4S) \leftarrow S^* \leftarrow S(^3P)$ process in the 11.5-30.0 eV photon energy region, at $\theta = 54°44'$ detection angle

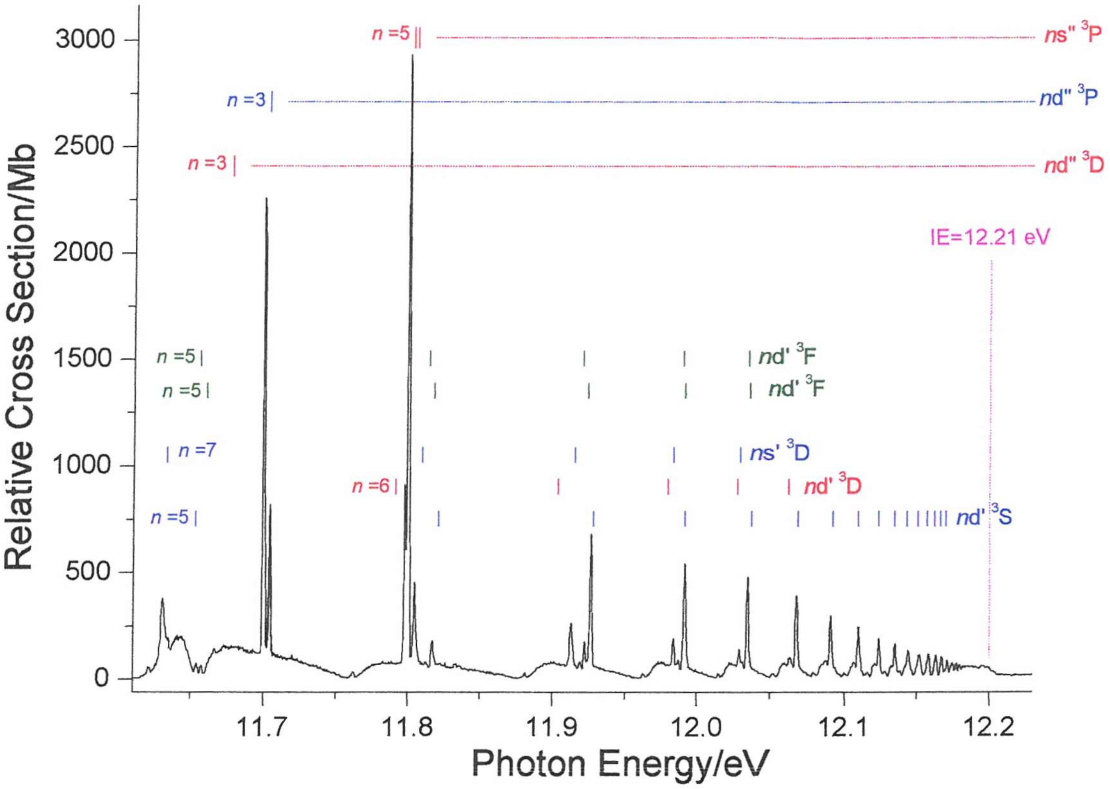

Figure 8.20: CIS spectrum recorded for the $S^+(^4S) \leftarrow S^* \leftarrow S(^3P)$ process in the 11.50-12.25 eV photon energy region, at θ =54°44' detection angle, with the second ionization limit marked (magenta trace) $S^* \leftarrow S$ transitions are indicated according with references (13) and (14), single prime on the Rydberg electron in the excited state (e.g. nd') designates terms converging to the second ionization limit

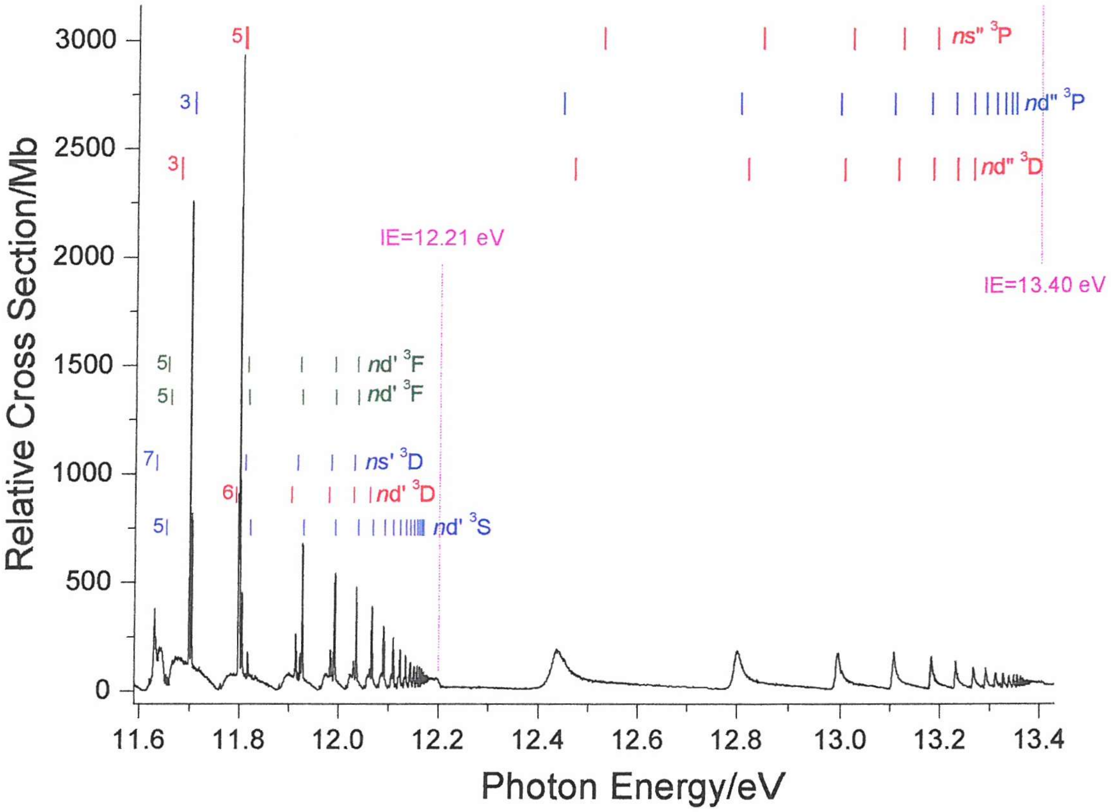

Figure 8.21: CIS spectrum recorded for the $S^+(^4S) \leftarrow S^* \leftarrow S(^3P)$ process in the 11.60-13.45 eV photon energy region, at θ =54° 44' detection angle, with the second and third ionization limits marked (magenta trace) $S^* \leftarrow S$ transitions are indicated according with references (13) and (14), single and double prime on the Rydberg electron in the excited state designates terms converging to the second (IE =12.21 eV) and to the third (IE =13.40 eV) ionization limit respectively

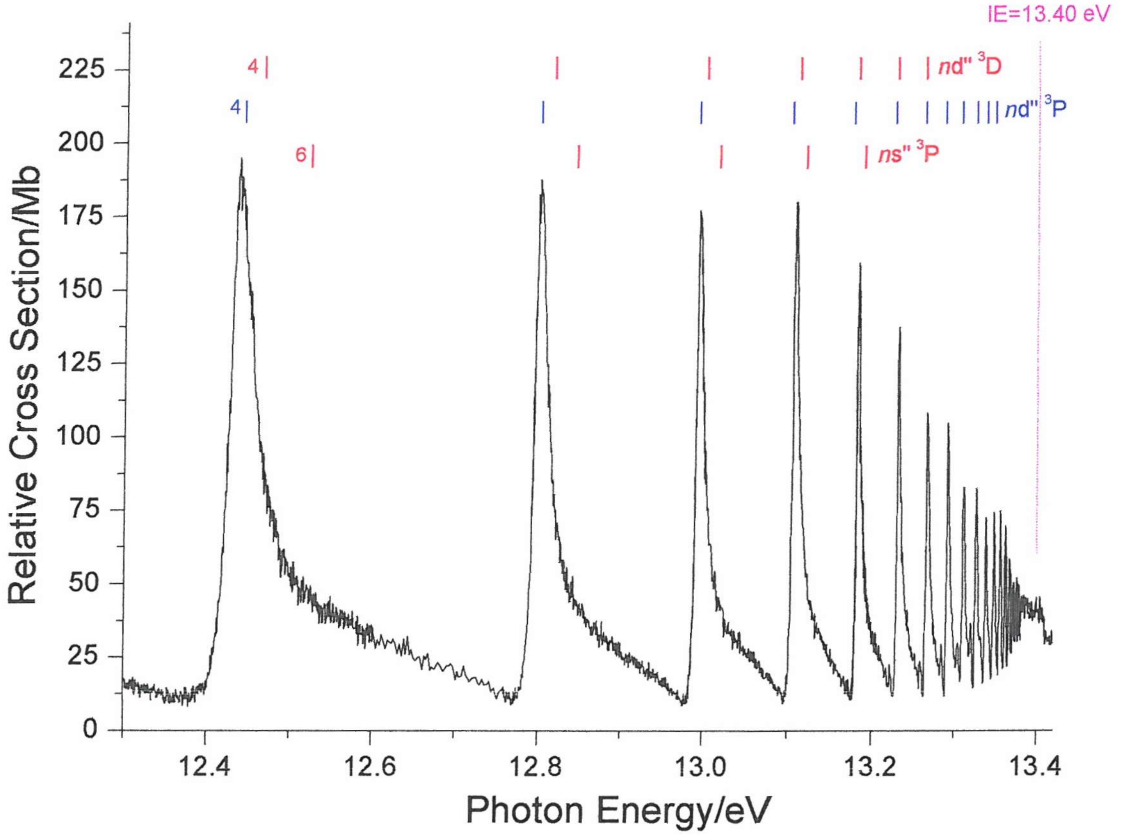

Figure 8.22: CIS spectrum recorded for the $S^+(^4S)\leftarrow S^*\leftarrow S(^3P)$ process in the 12.30-13.42 eV photon energy region, at θ=54°44' detection angle, with the third ionization limits marked (magenta trace) $S^*\leftarrow S$ transitions are indicated according with references (13) and (14), double prime on the Rydberg electron in the excited state designates terms converging to the third ionization limit

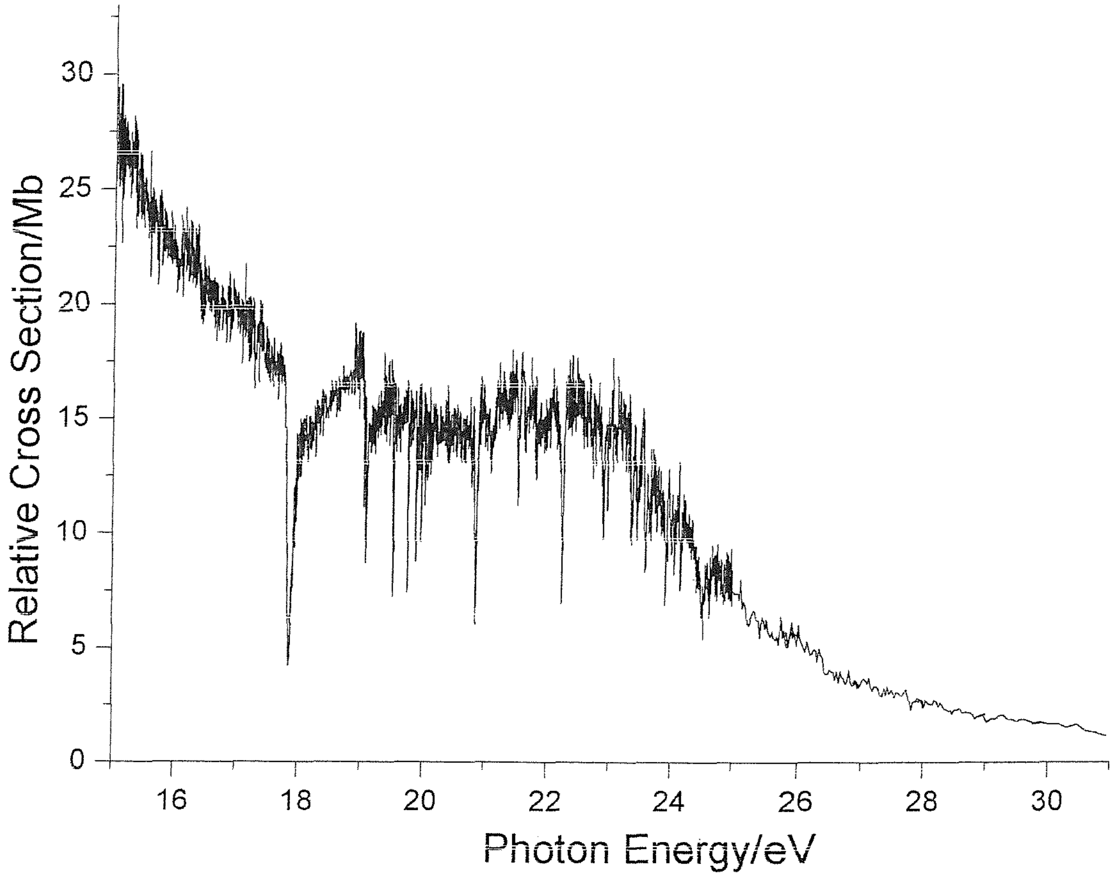

Figure 8.23: CIS spectrum recorded for the $S^{+}(^{4}S) \leftarrow S^{*} \leftarrow S(^{3}P)$ *process in the 15.0-31.0 eV photon energy region, at* $\theta = 54°44'$ *detection angle*

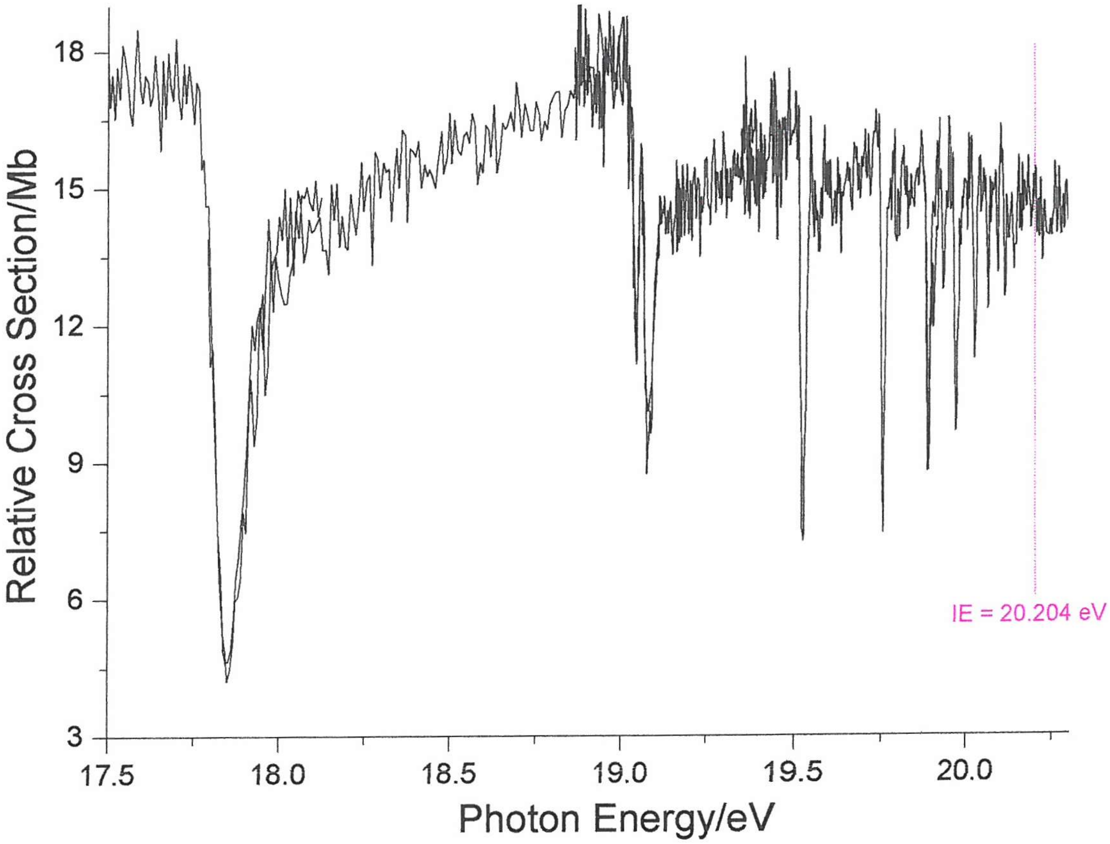

Figure 8.24: CIS spectrum recorded for the $S^+(^4S) \leftarrow S^* \leftarrow S(^3P)$ process in the 17.50-20.55 eV photon energy region, at $\theta = 54°44'$ detection angle, with the fourth ionization limit marked (magenta trace)

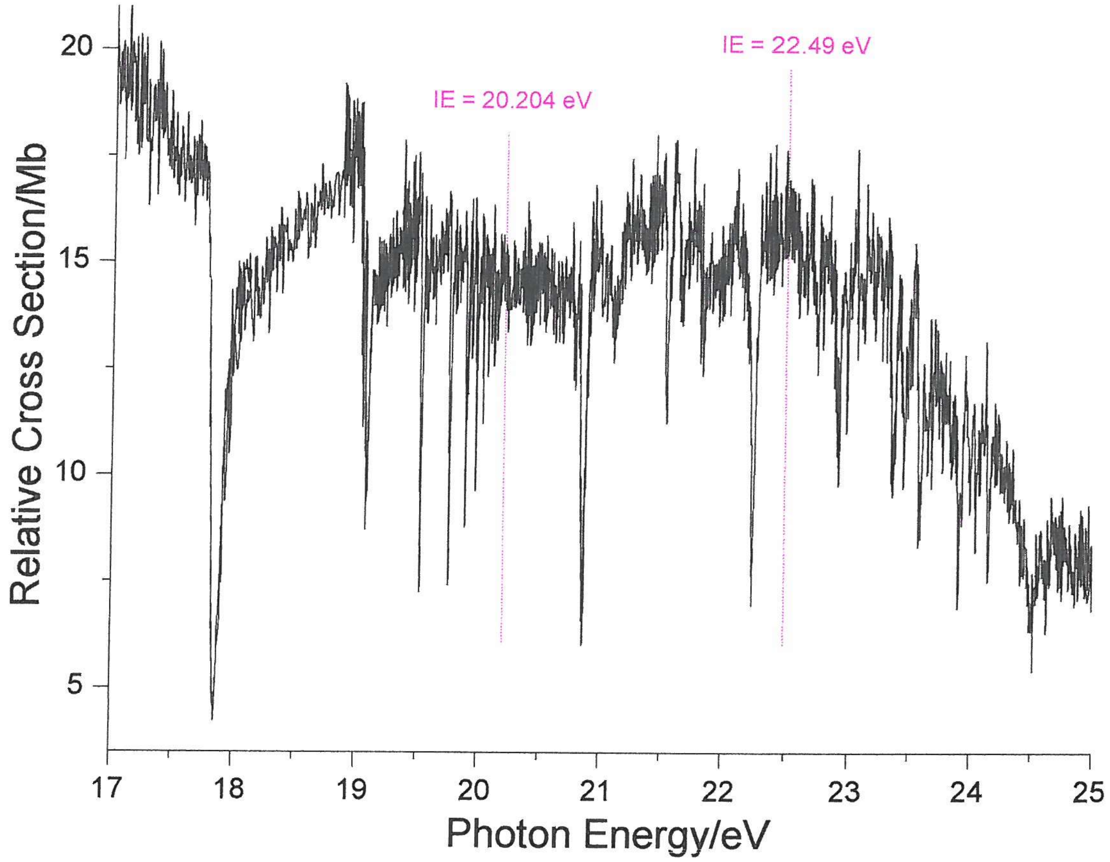

Figure 8.25: CIS spectrum recorded for the $S^+(^4S) \leftarrow S^* \leftarrow S(^3P)$ process in the 17.0-25.0 eV photon energy region, at $\theta = 54°44'$ with the fourth (IE =20.204 eV) and fifth (IE =22.49 eV) ionization limits marked (magenta trace)

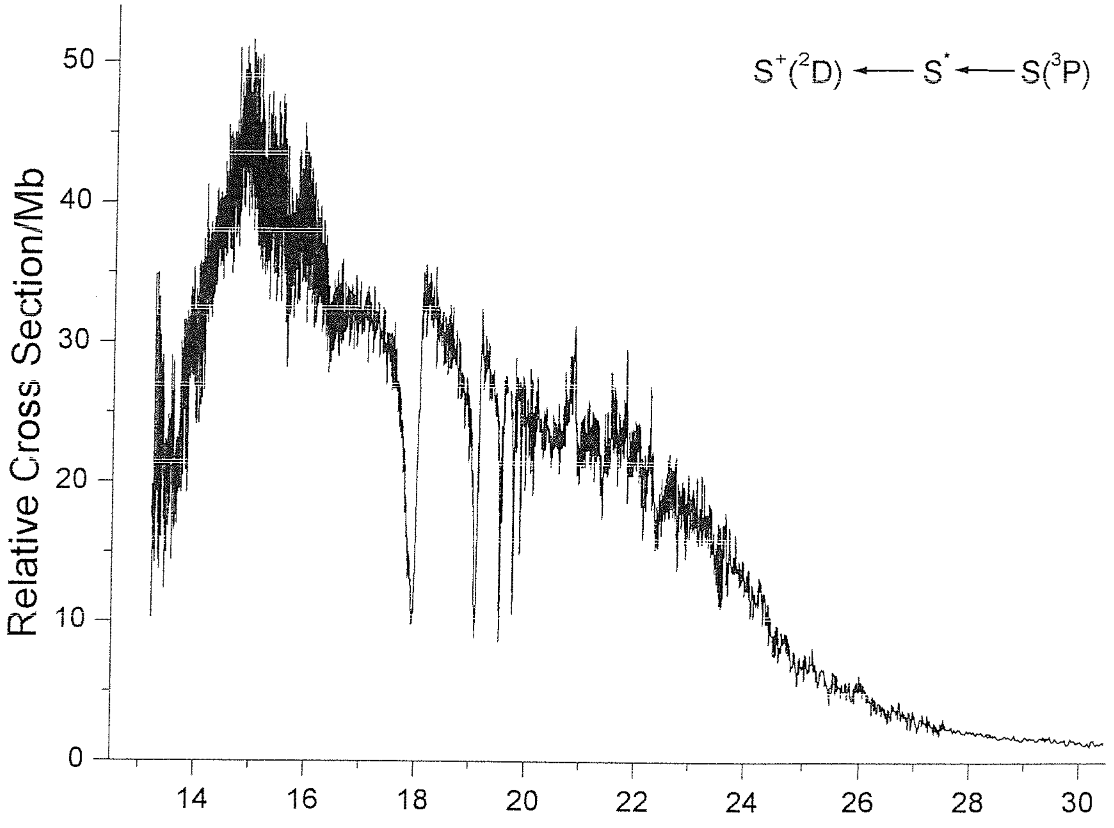

Figure 8.26: CIS spectrum recorded for the $S^+(^2D) \leftarrow S^* \leftarrow S(^3P)$ process in the 13.5-30.5 eV photon energy region, at $\theta = 54°44'$ detection angle

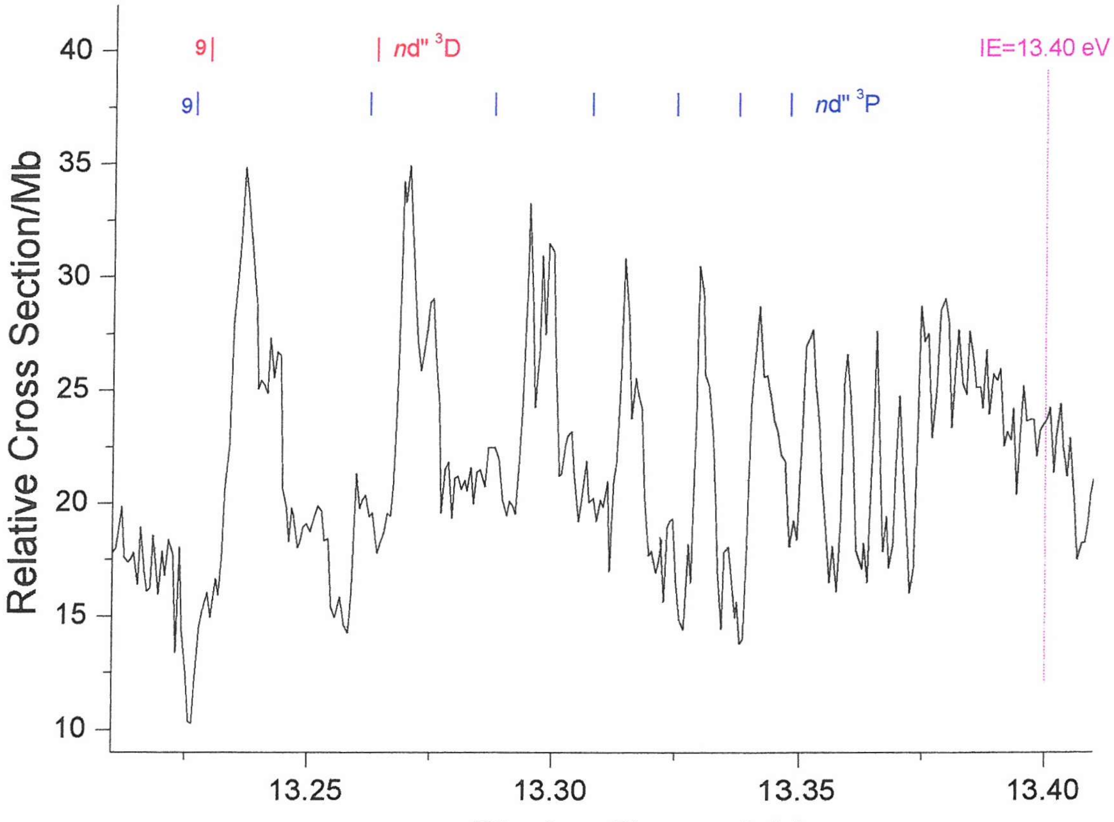

Figure 8.27: CIS spectrum recorded for the $S^+(^2D) \leftarrow S^* \leftarrow S(^3P)$ process in the 13.10-13.42 eV photon energy region, at $\theta = 54°44'$ detection angle with the third ionization limits marked (magenta trace) $S^* \leftarrow S$ transitions are indicated according with references (13) and (14), double prime on the Rydberg electron in the excited state designates terms converging to the third ionization limit

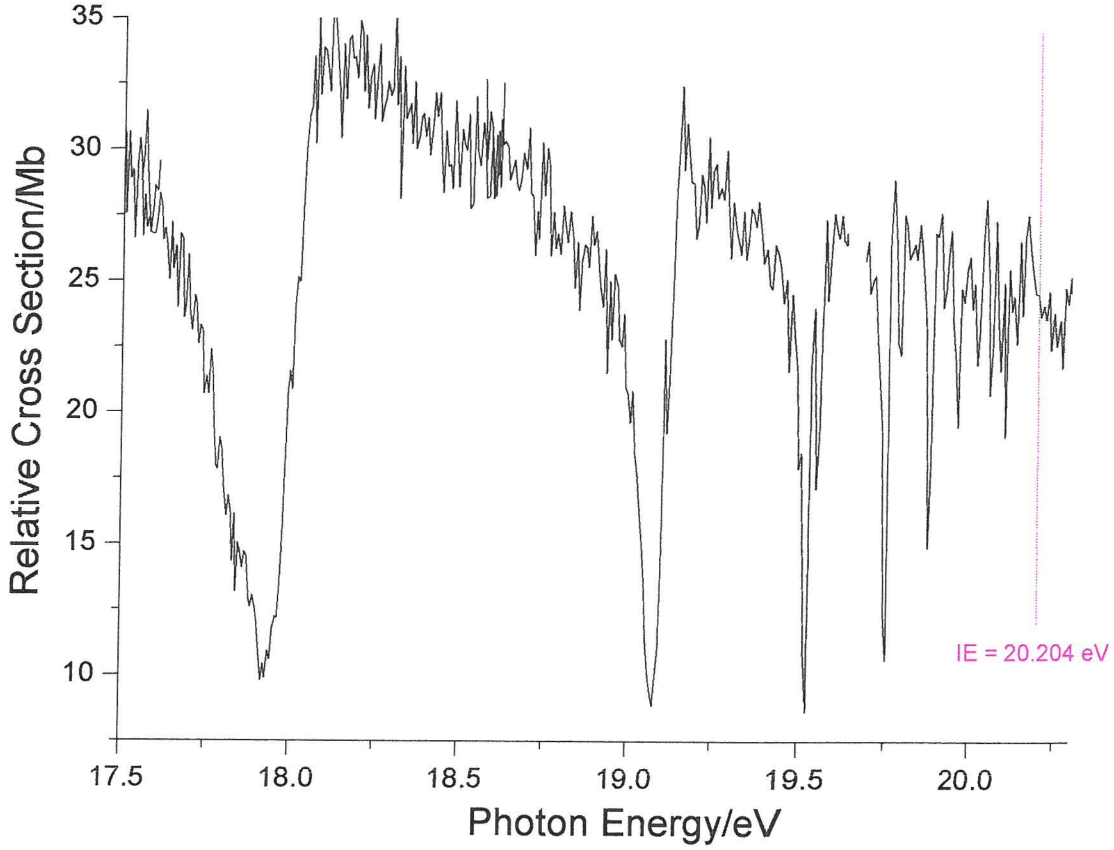

Figure 8.28: CIS spectrum recorded for the $S^+(^2D)\leftarrow S^*\leftarrow S(^3P)$ process in the 17.5-20.3 eV photon energy region, at $\theta = 54°44'$ detection angle with the fourth ionization limit marked (magenta trace)

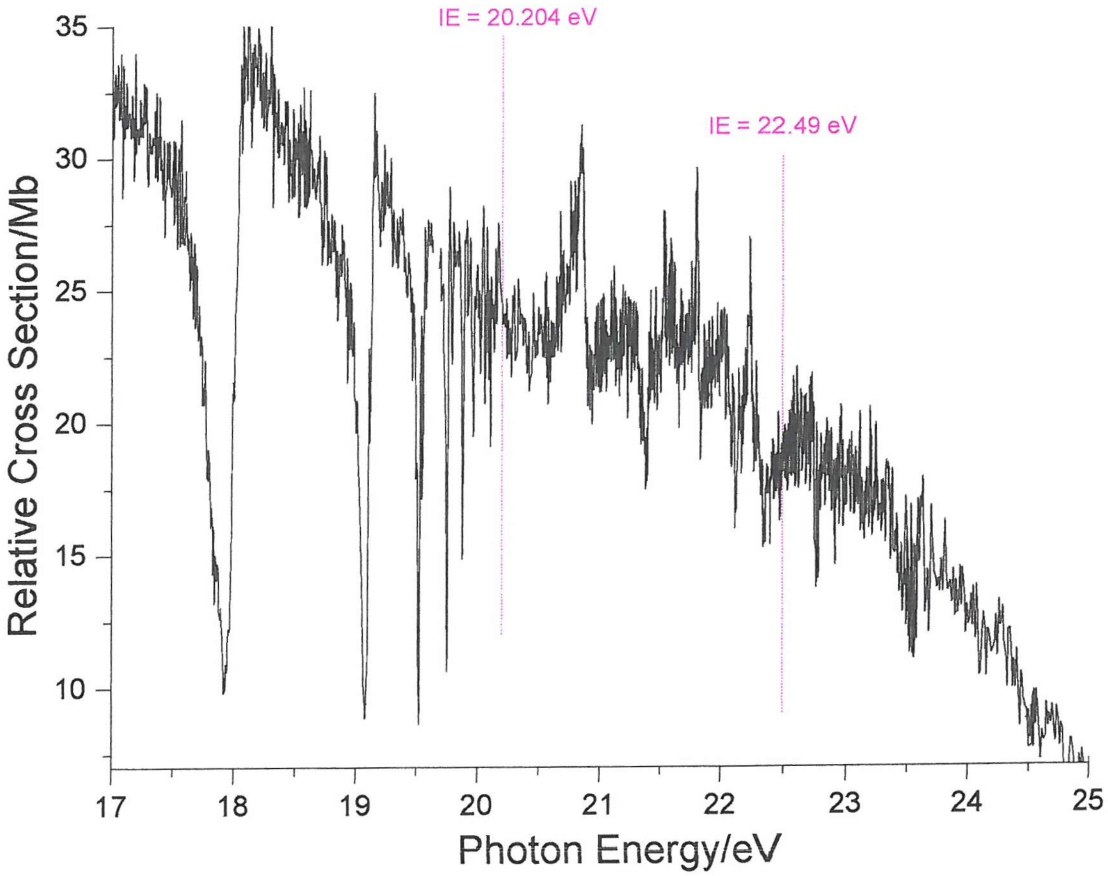

Figure 8.29: CIS spectrum recorded for the $S^+(^2D) \leftarrow S^* \leftarrow S(^3P)$ *process in the 17-25 eV photon energy region, at* $\theta = 54°44'$ *with the fourth (IE = 20.204 eV) and fifth (IE = 22.49 eV) ionization limits marked (magenta trace)*

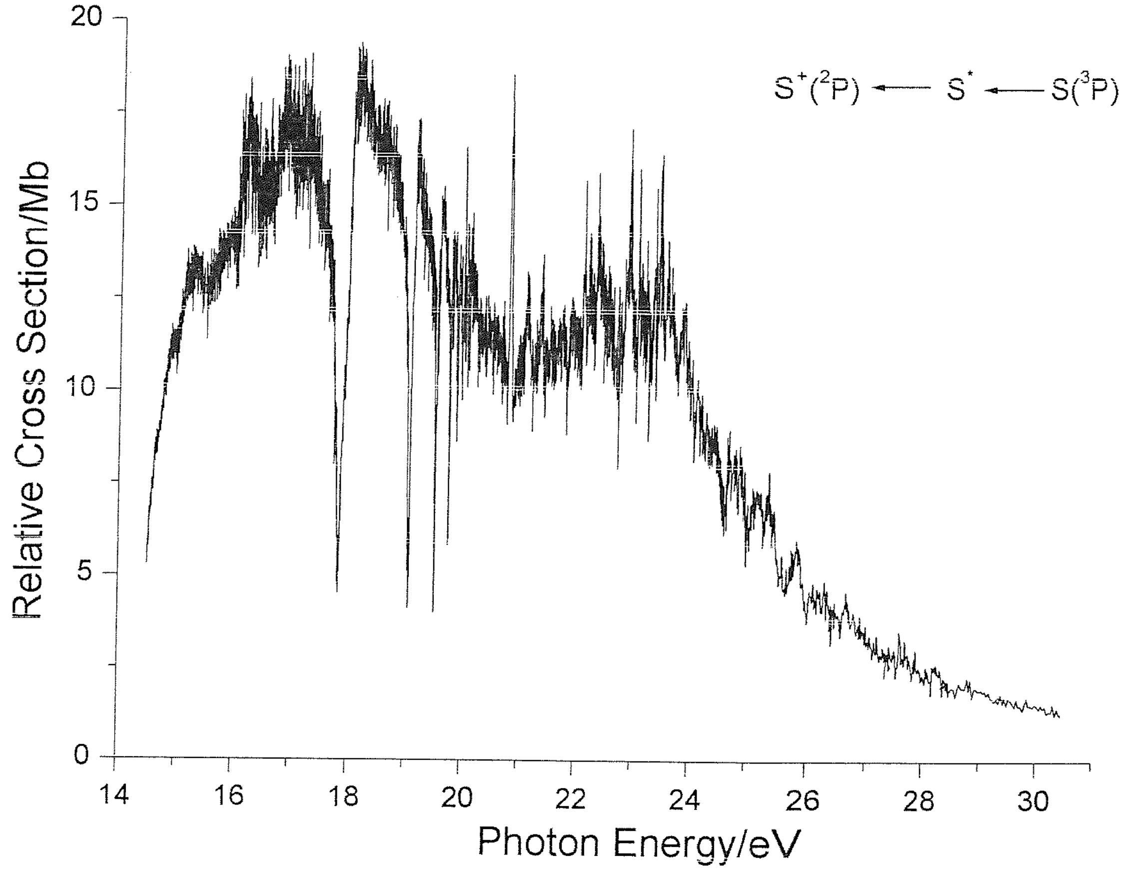

Figure 8.30: CIS spectrum recorded for the $S^+(^2P) \leftarrow S^* \leftarrow S(^3P)$ *process in the 14-31 eV photon energy region, at* $\theta = 54°44'$ *detection angle*

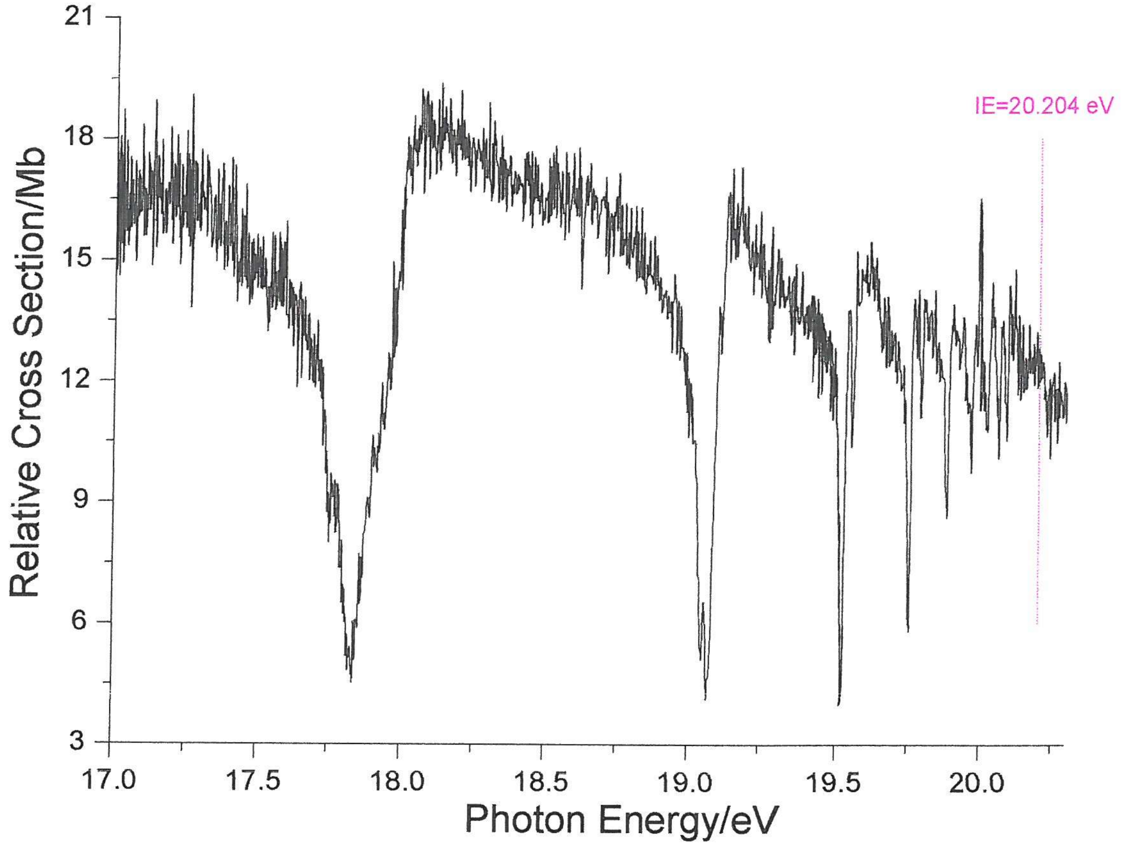

Figure 8.31: CIS spectrum recorded for the $S^+(^2P) \leftarrow S^* \leftarrow S(^3P)$ *process in the 17.0-20.3 eV photon energy region, at* $\theta = 54°44'$ *detection angle with the fourth ionization limit marked (magenta trace)*

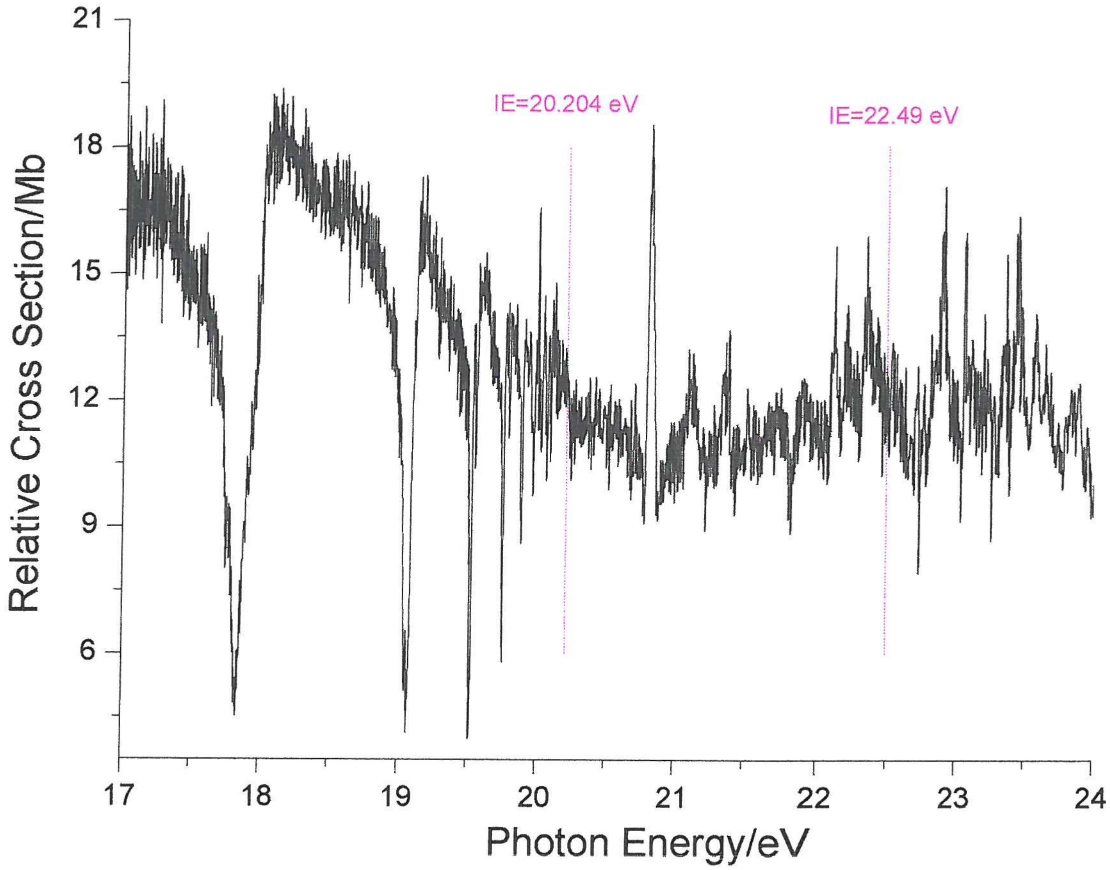

Figure 8.32: CIS spectrum recorded for the $S^+(^2P) \leftarrow S^* \leftarrow S(^3P)$ process in the 17-24 eV photon energy region, at $\theta = 54° 44'$ with the fourth (IE = 20.204 eV) and fifth (IE = 22.49 eV) ionization limits marked (magenta trace)

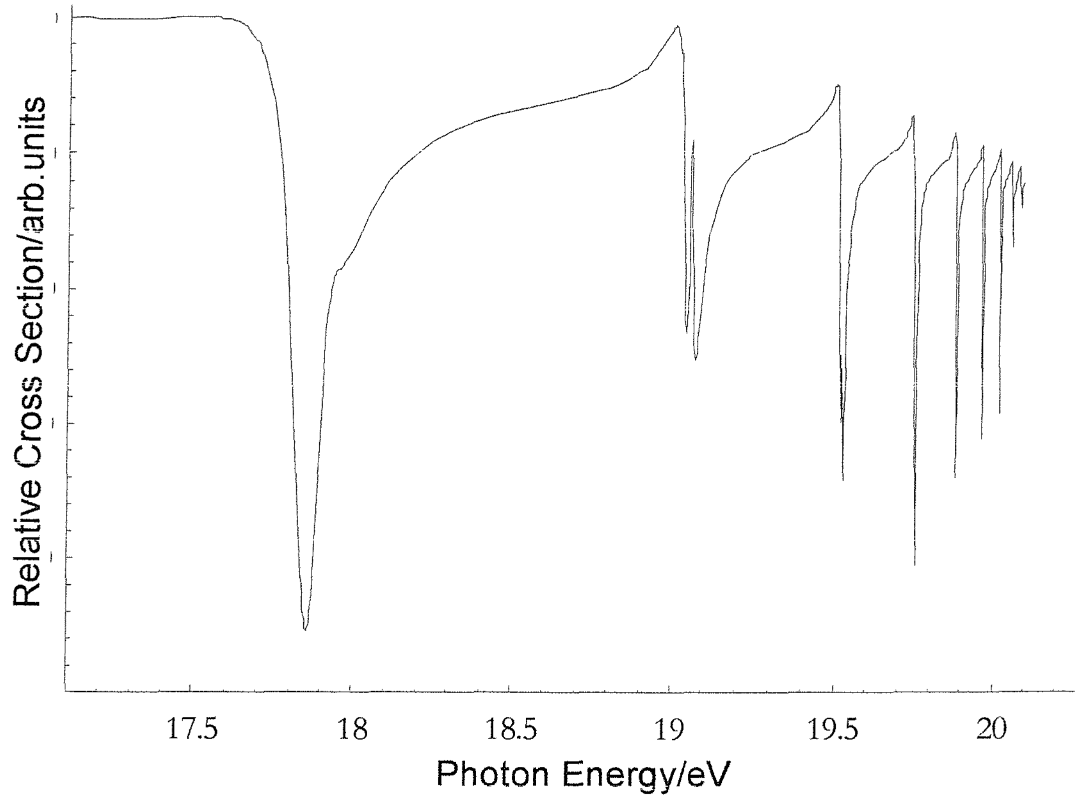

Figure 8.33: Fit of the data recorded for the $S^+(^4S) \leftarrow S^* \leftarrow S(^3P)$ *process in the 17.0-20.3 eV photon energy region, at* $\theta = 54^\circ 44'$ *detection angle This should be compared with the experimental spectrum in Figure 8.24*

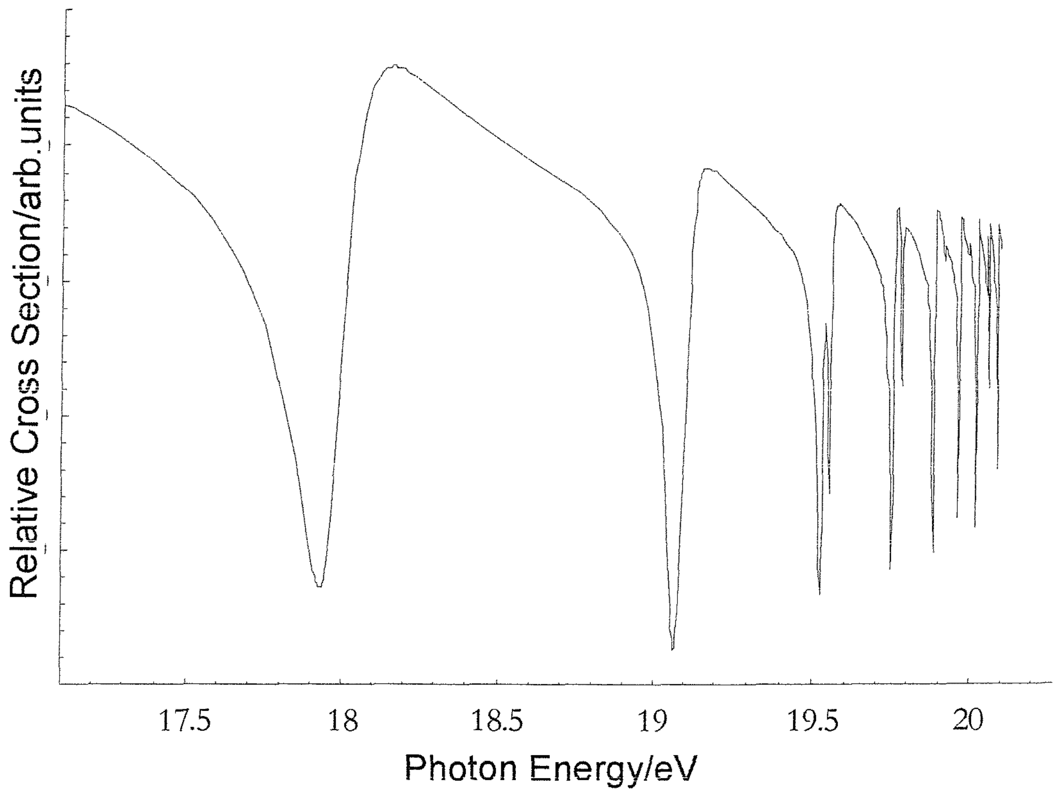

Figure 8.34: Fit of the data recorded for the $S^+(^2D) \leftarrow S^* \leftarrow S(^3P)$ *process in the 17.5-20.3 eV photon energy region, at* θ*=54° 44' detection angle This should be compared with the experimental spectrum in Figure 8.28*

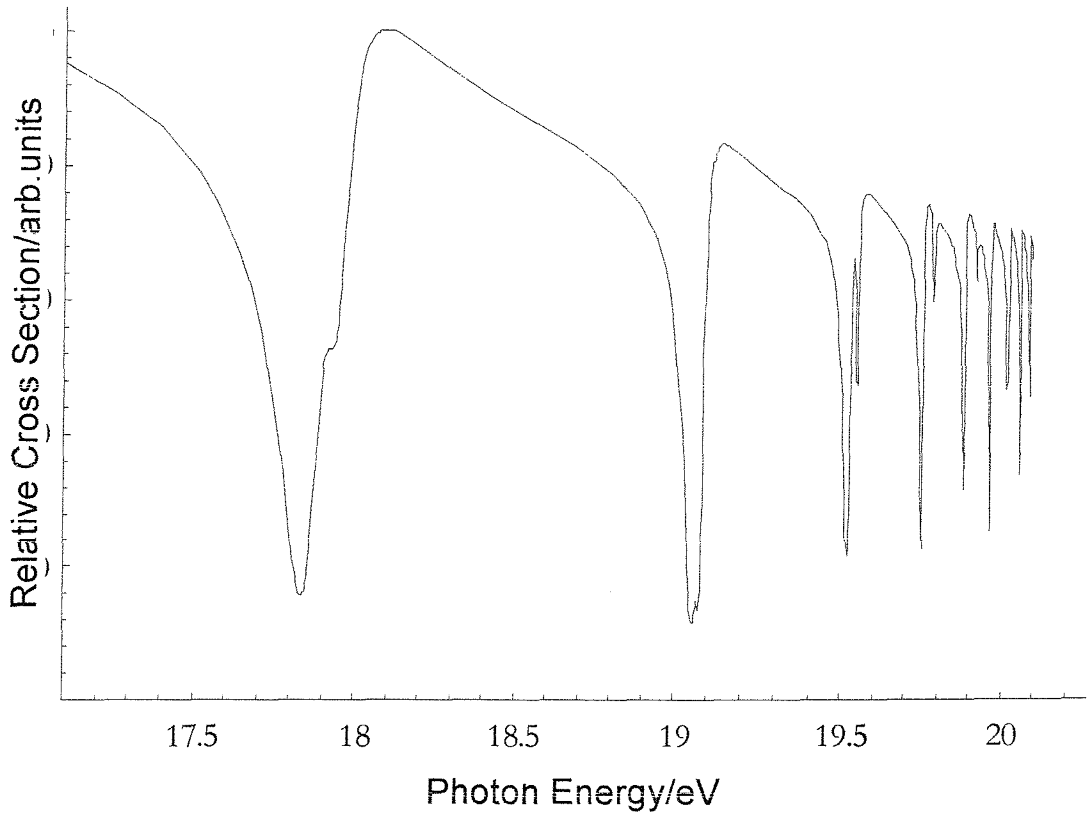

Figure 8.35: Fit of the data recorded for the $S^+(^2P) \leftarrow S^* \leftarrow S(^3P)$ *process in the 17.0-20.3 eV photon energy region, at* θ*=54° 44' detection*
This should be compared with the experimental spectrum in Figure 8.31

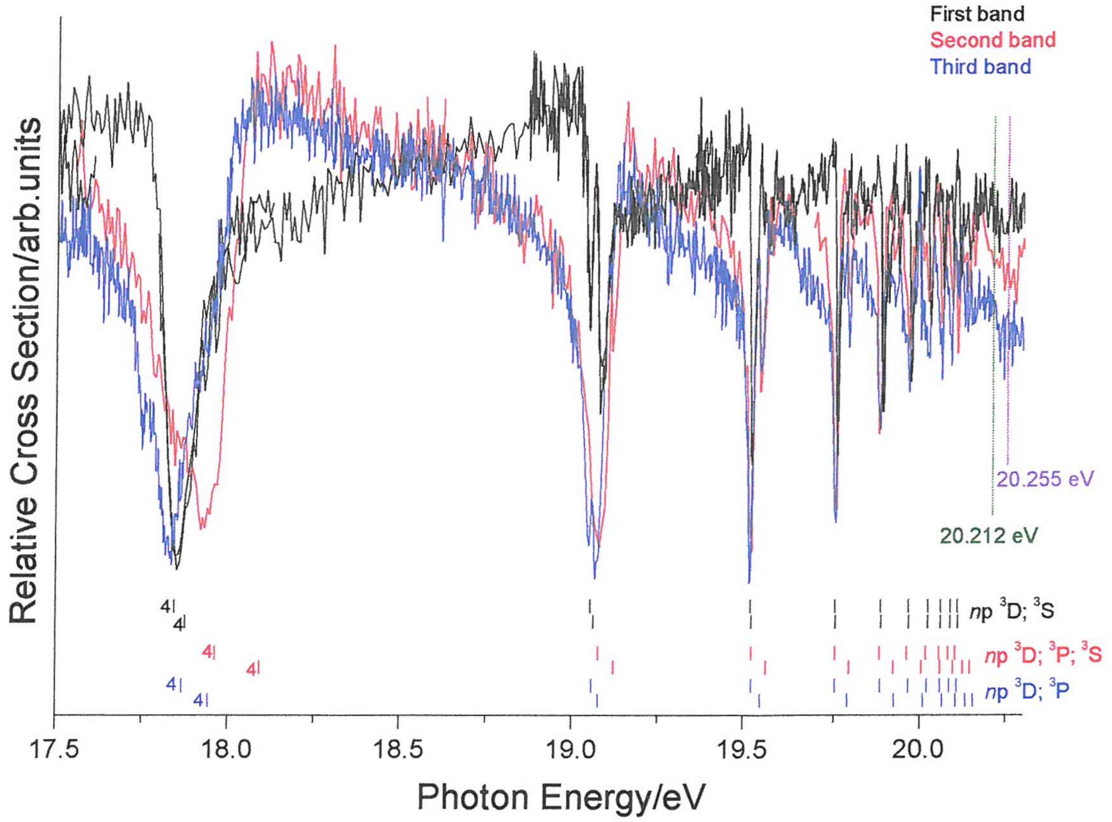

Figure 8.36: CIS spectra recorded for the $S^+(^4S) \leftarrow S^* \leftarrow S(^3P)$, $S^+(^2D) \leftarrow S^* \leftarrow S(^3P)$ *and* $S^+(^2P) \leftarrow S^* \leftarrow S(^3P)$ *processes in the 17.5-20.3 eV photon energy region, at* $\theta = 54°44'$ *detection angle, with the fourth ionization limit at 20.204 eV marked (magenta trace)*
The tentative assignment of the Rydberg series is presented according to the Russell-Saunders selection rules[52,53]
(see text for further details)

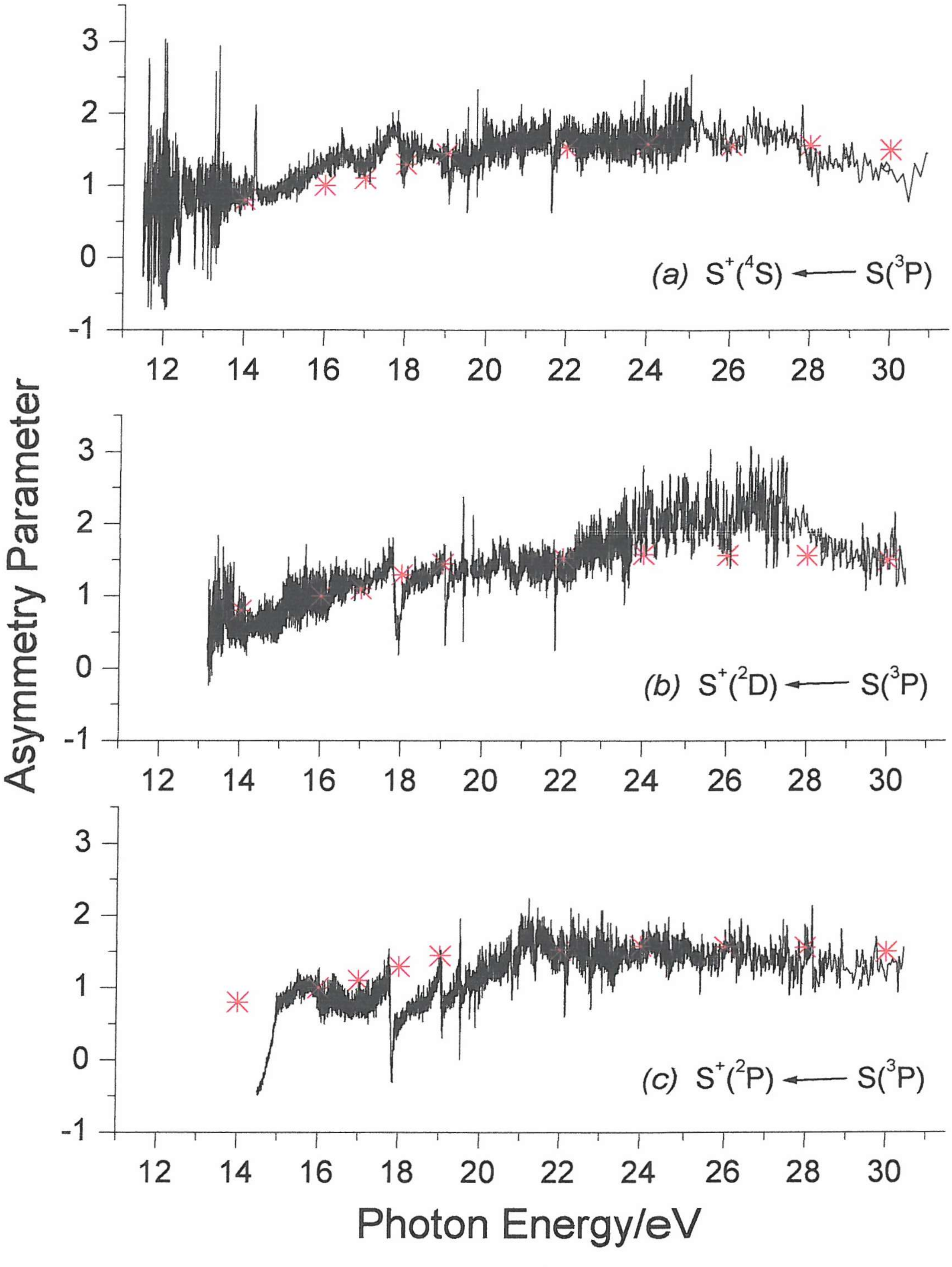

Figure 8.37: Plots of the asymmetry parameter (β) as a function of photon energy over the range $h\nu$ =10.0–30.0 eV, for the first three photoelectron bands of S atoms

All the plots includes β values for the first band of H_2S measured at different photon energies in Ref.(34), denoted with the symbol (*)

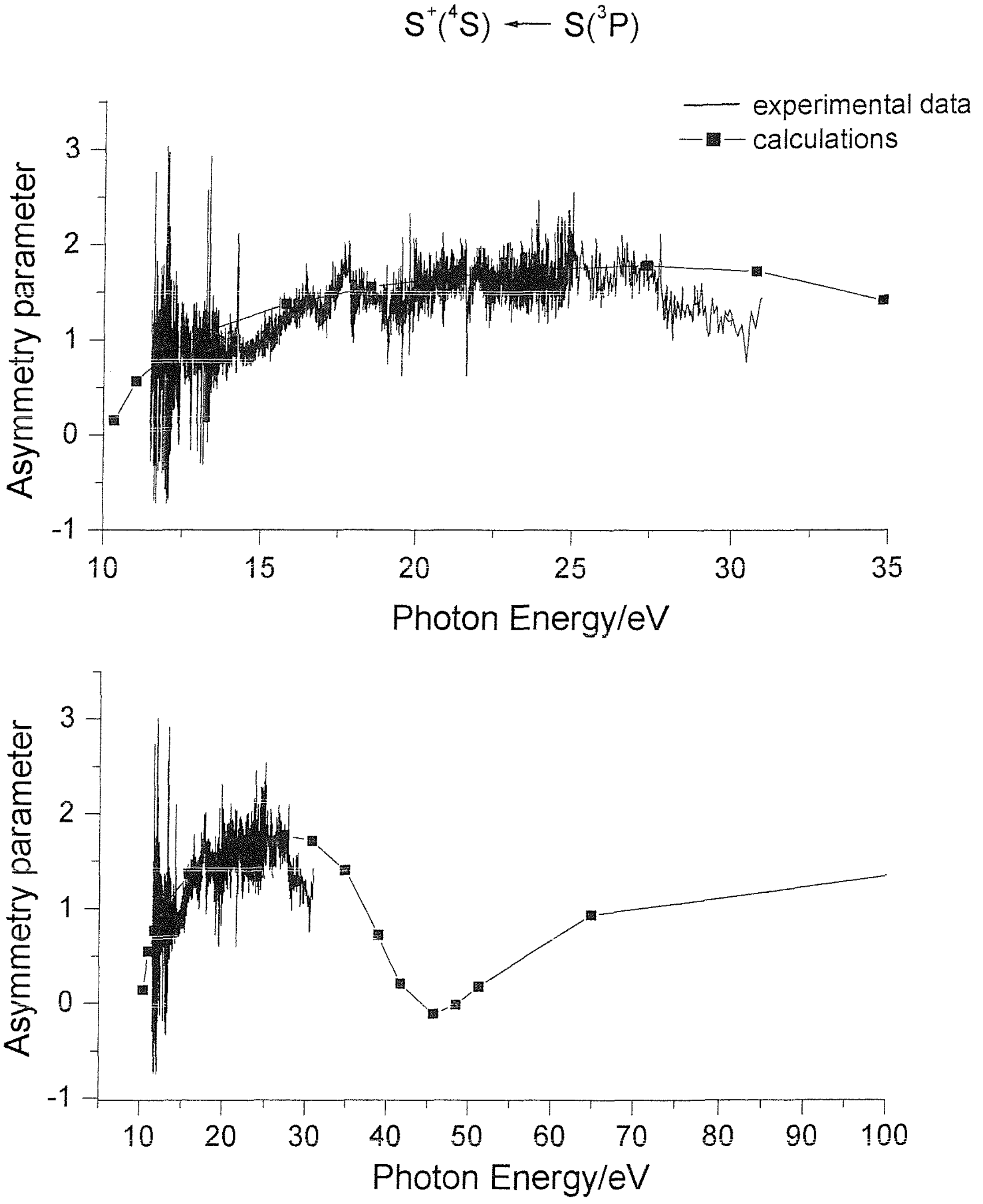

Figure 8.38: Asymmetry parameters for S atoms plotted as a function of photon energy and compared with the results of Dill et al.[7]*, for the first S atom band* $S^+(^4S) \leftarrow S(^3P)$

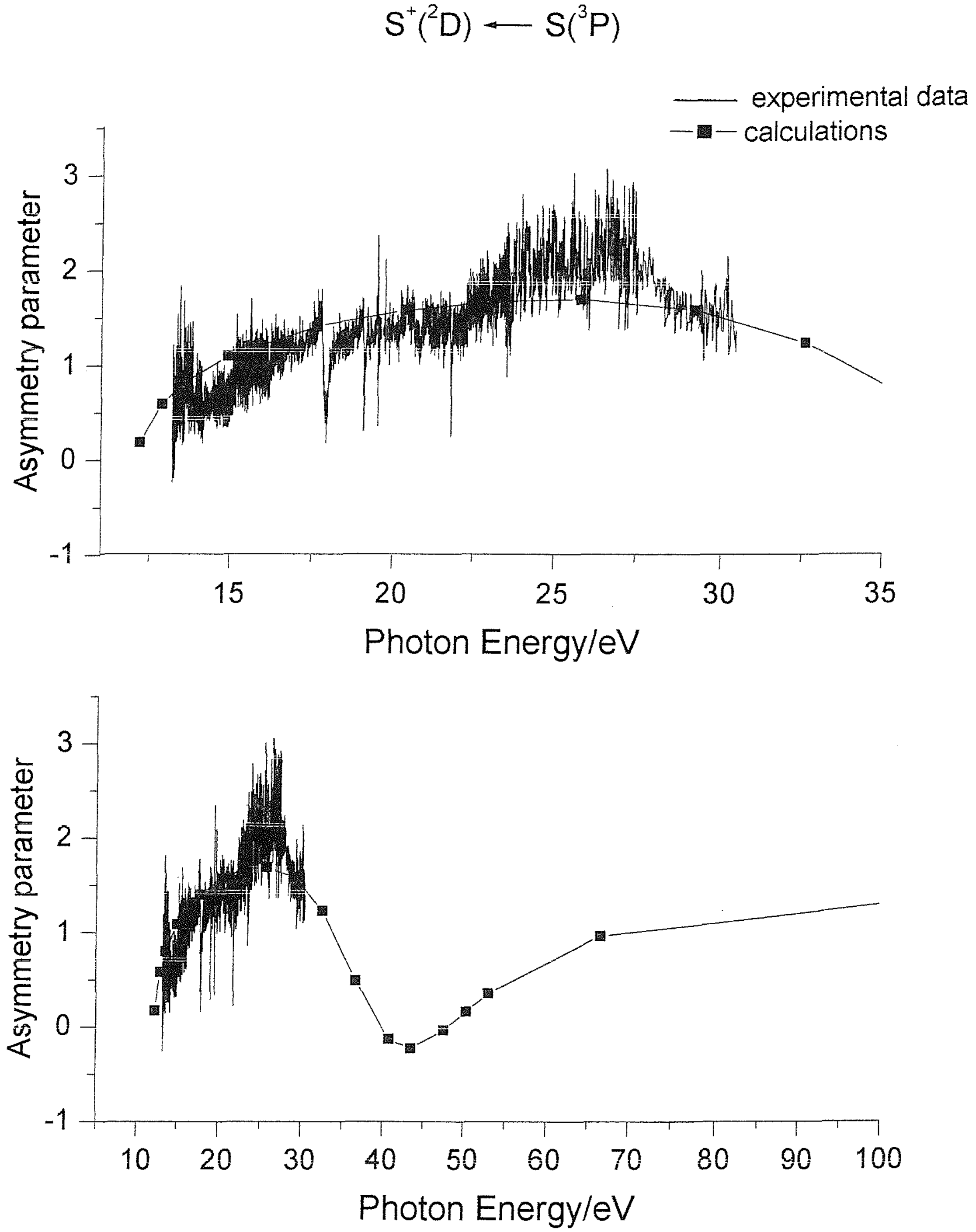

Figure 8.39: Asymmetry parameters for S atoms plotted as a function of photon energy and compared with the results of Dill et al.[7]*, for the second S atom band $S^+(^2D) \leftarrow S(^3P)$*

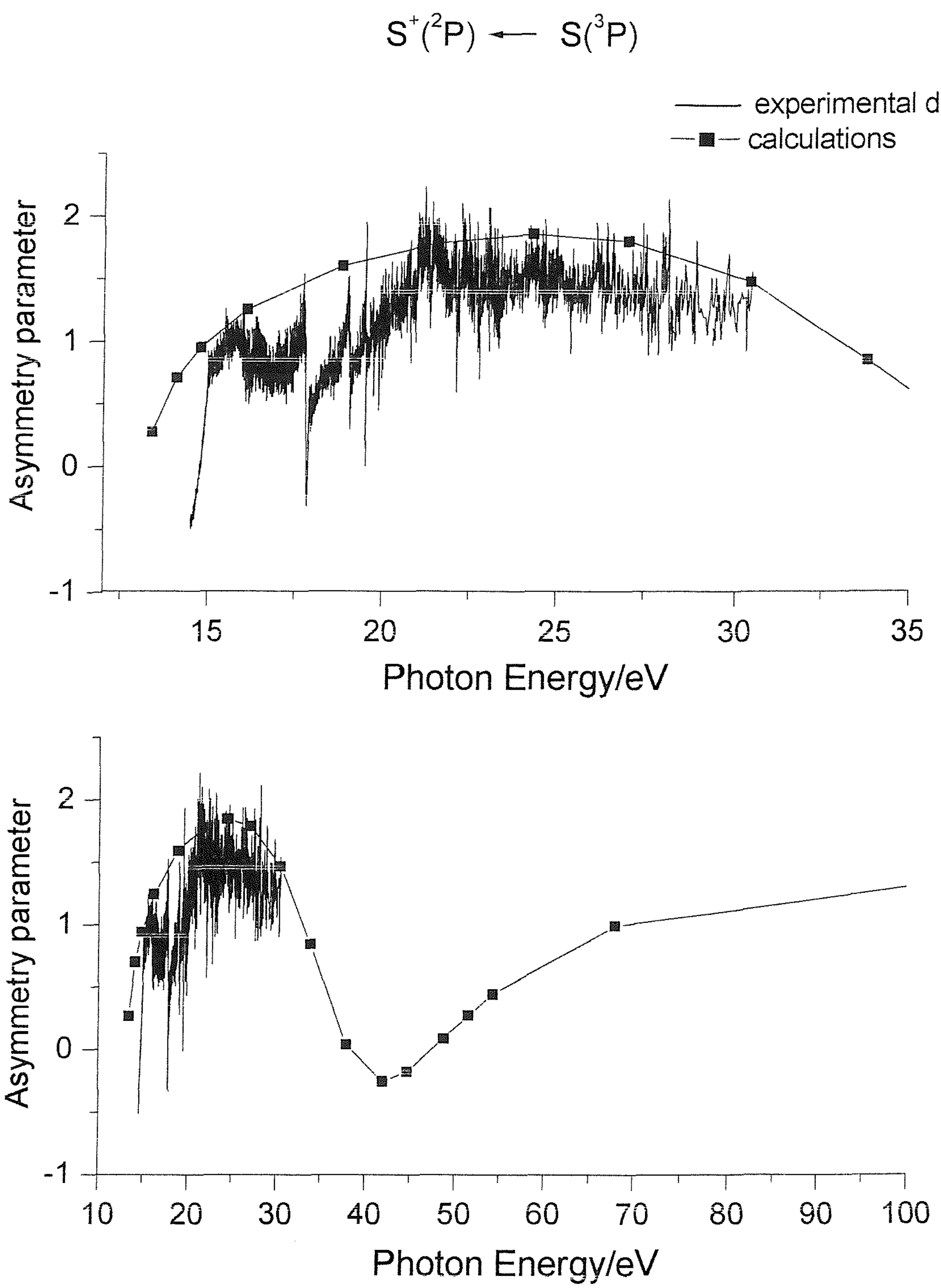

Figure 8.40: Asymmetry parameters for S atoms plotted as a function of photon energy and compared with the results of Dill et al.[7] *for the third S atom band $S^+(^2P) \leftarrow S(^3P)$*

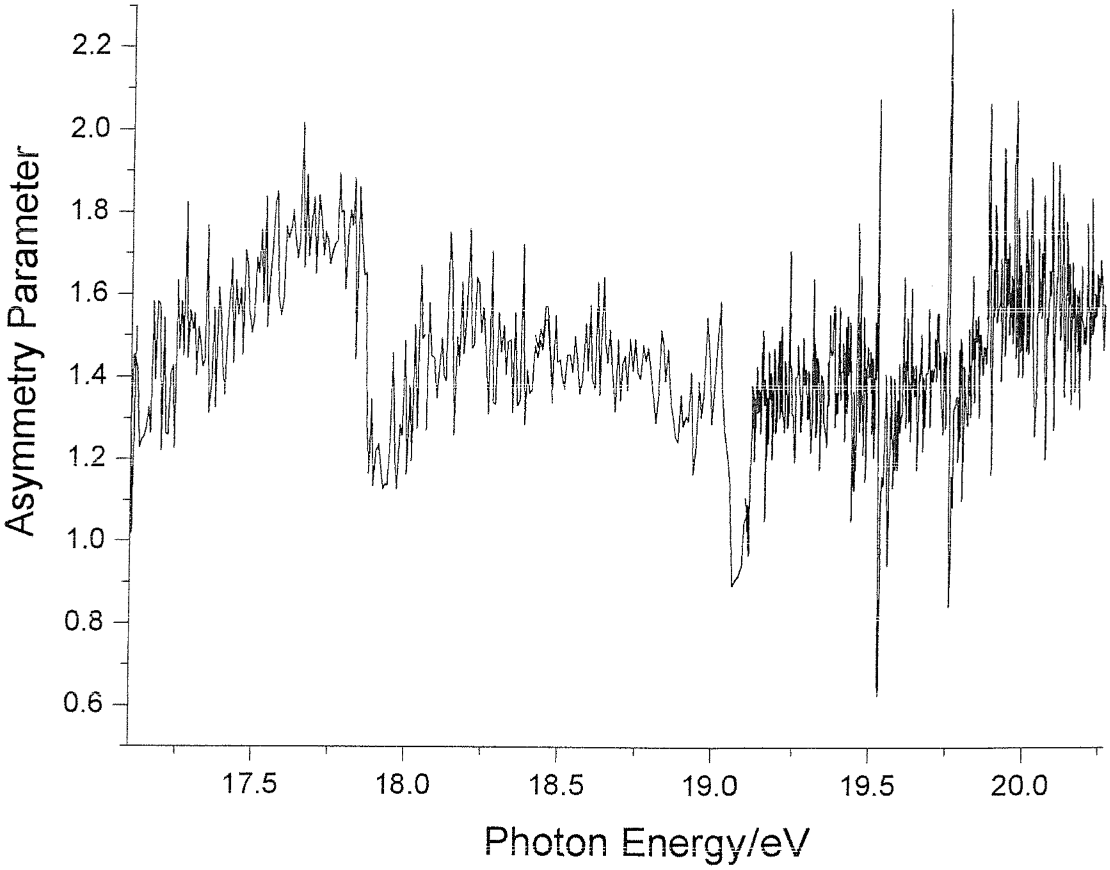

Figure 8.41: Spectrum of the experimental asymmetry parameter (β) *for the* $S^+(^4S) \leftarrow S^* \leftarrow S(^3P)$ *ionization process as a function of the photon energy over the range* $h\nu = 16.5\text{–}20.5$ *eV*

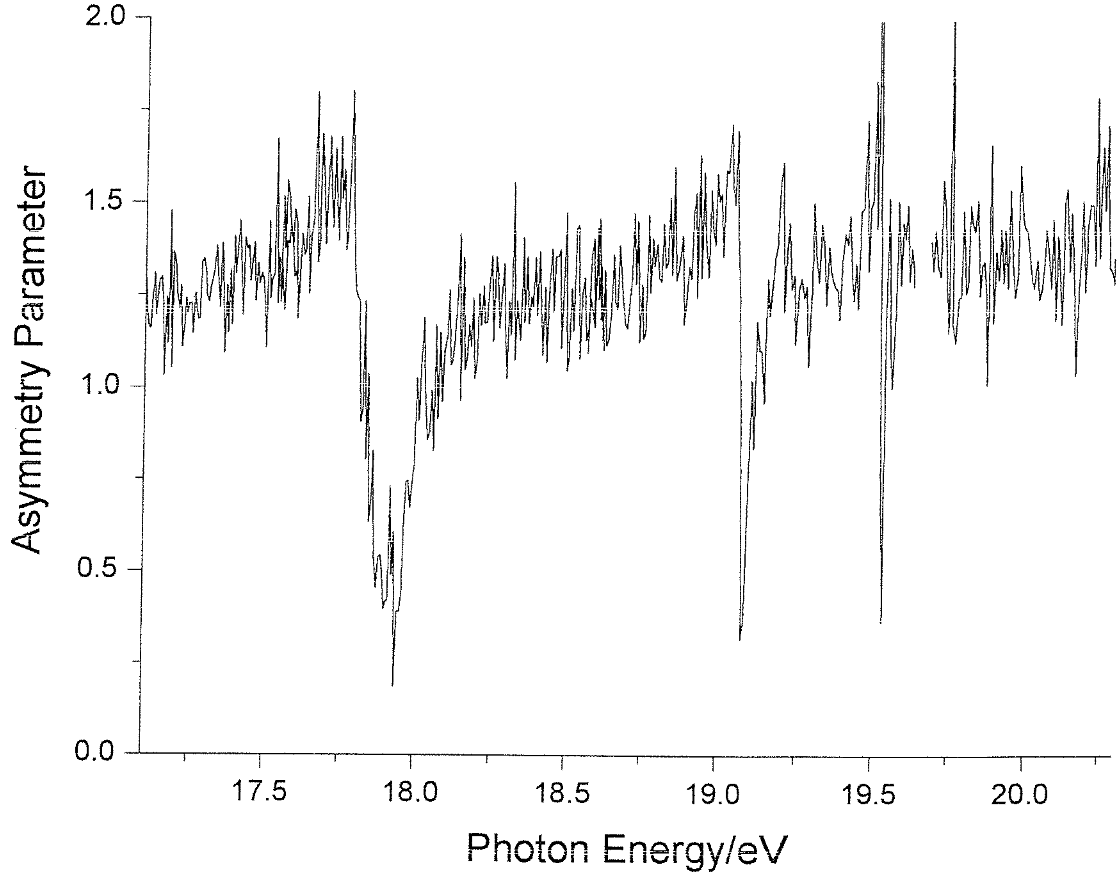

Figure 8.42: Spectrum of the experimental asymmetry parameter (β) for the $S^+(^2D) \leftarrow S^* \leftarrow S(^3P)$ ionization process as a function of photon energy over the range hν =16.5–20.5 eV

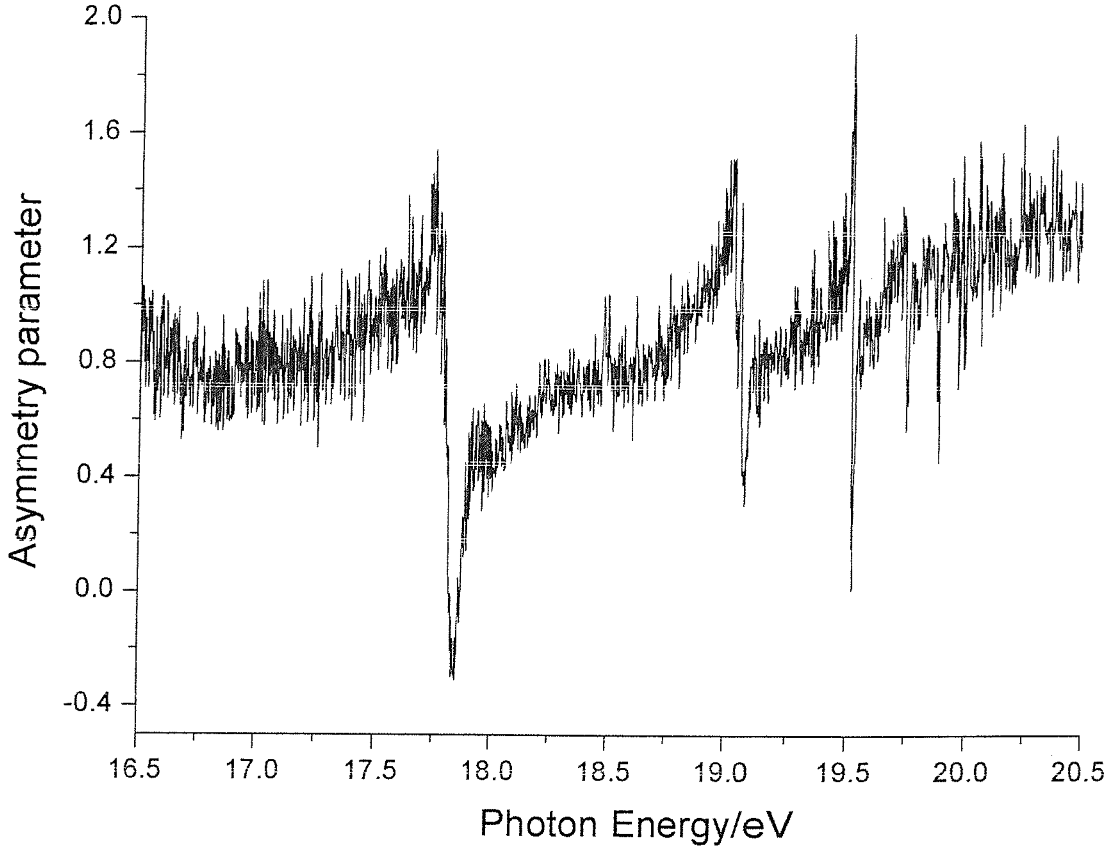

Figure 8.43: Spectrum of the experimental asymmetry parameter (β) for the $S^+(^2P) \leftarrow S^* \leftarrow S(^3P)$ ionization process as a function of photon energy over the range hν =16.5–20.5 eV

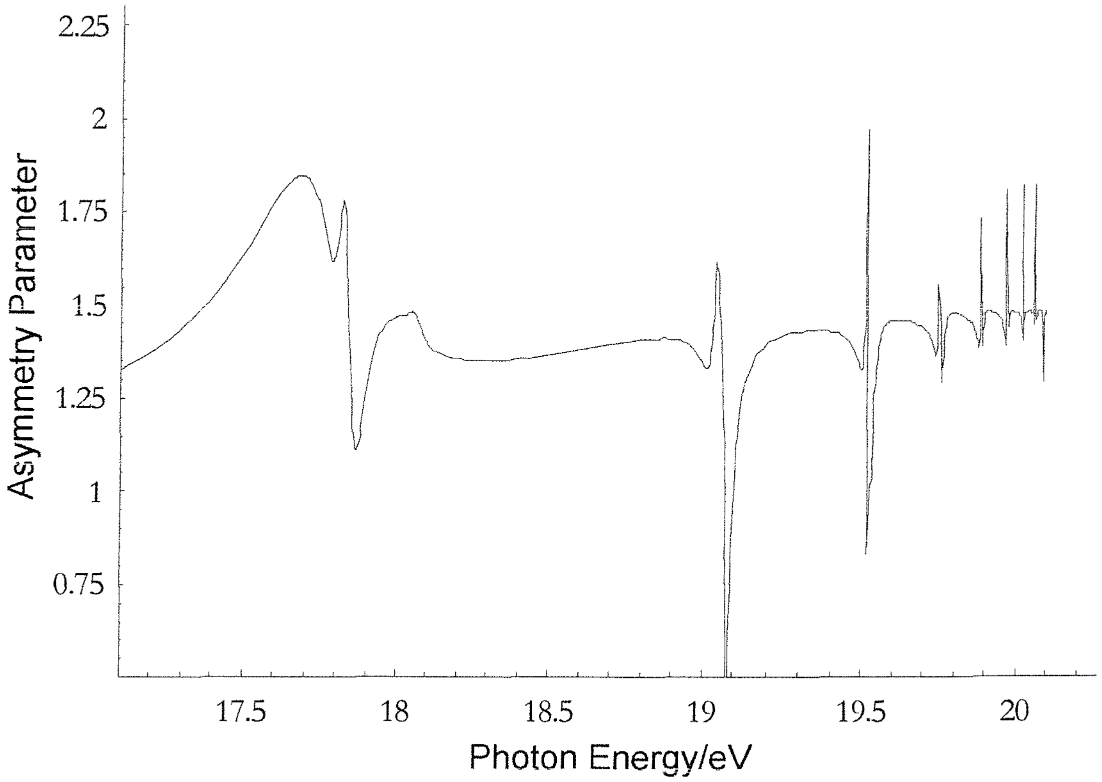

Figure 8.44: Spectrum of the calculated asymmetry parameter (β) for the $S^+(^4S) \leftarrow S^* \leftarrow S(^3P)$ *ionization process as a function of photon energy over the range* $h\nu = 17\text{–}20.5$ *eV*

This should be compared with the experimental spectrum in Figure 8.41

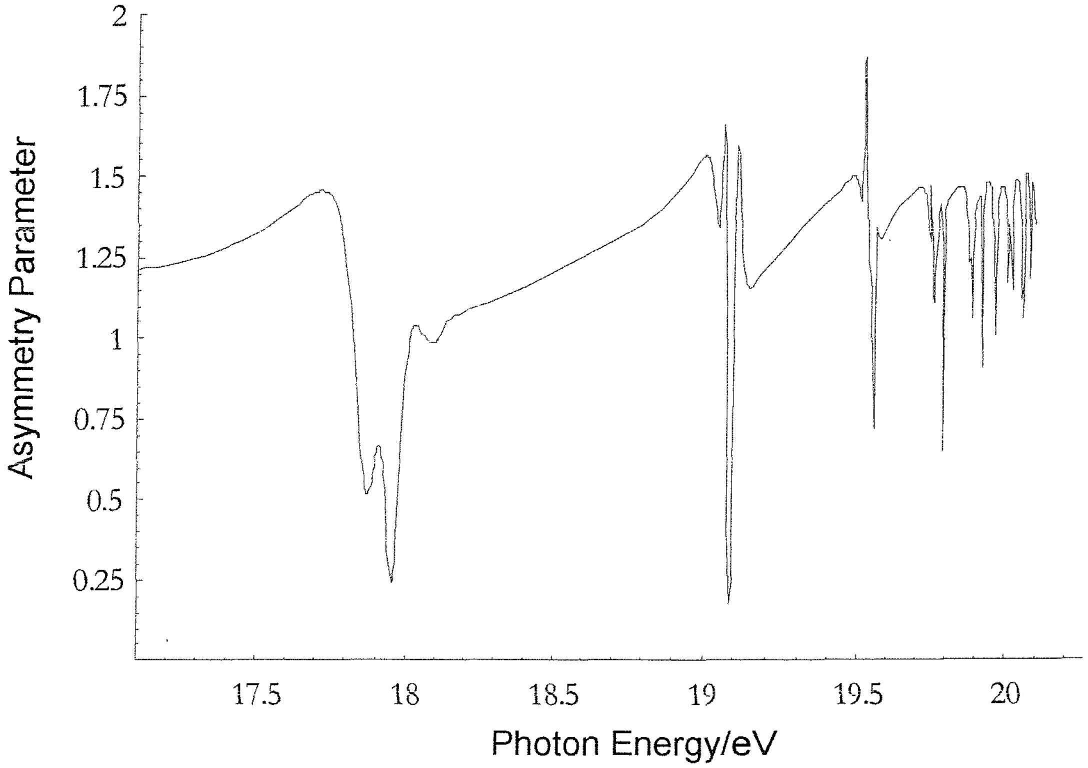

Figure 8.45: Spectrum of the calculated asymmetry parameter (β) for the $S^+(^2D) \leftarrow S^* \leftarrow S(^3P)$ *ionization process as a function of photon energy over the range* $h\nu = 17\text{–}20.5$ *eV*

This should be compared with the experimental spectrum in Figure 8.42

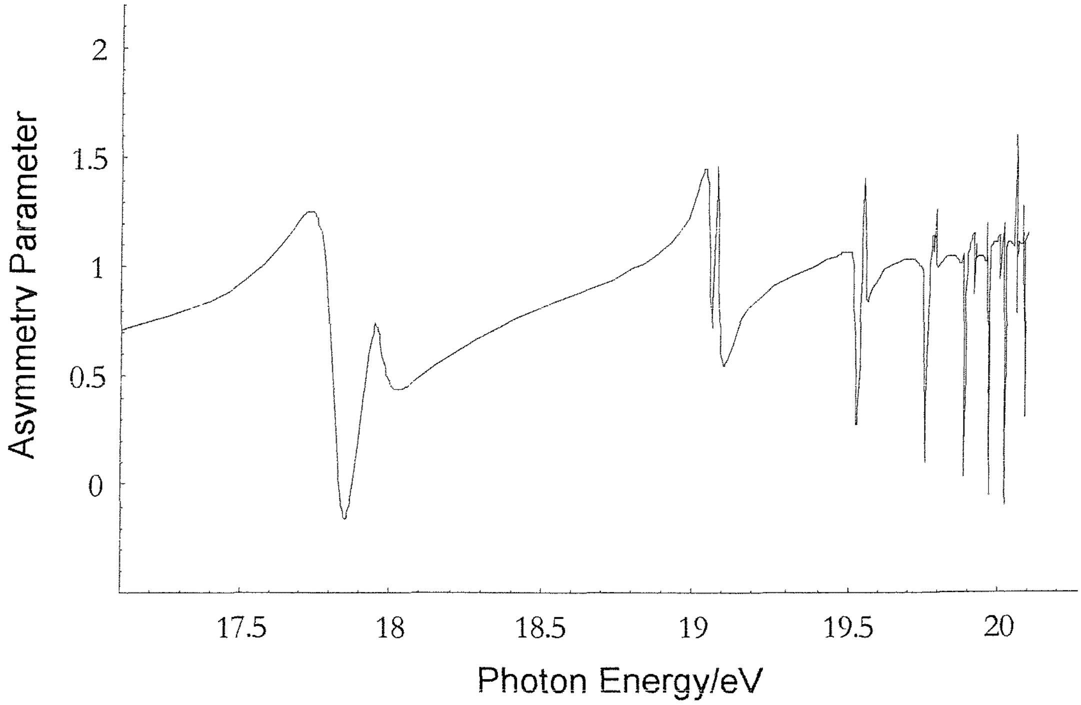

Figure 8.46: Spectrum of the calculated asymmetry parameter (β) for the $S^{+}(^2P) \leftarrow S^* \leftarrow S(^3P)$ ionization process as a function of photon energy over the range $h\nu = 17$–20.5 eV

This should be compared with the experimental spectrum in Figure 8.43

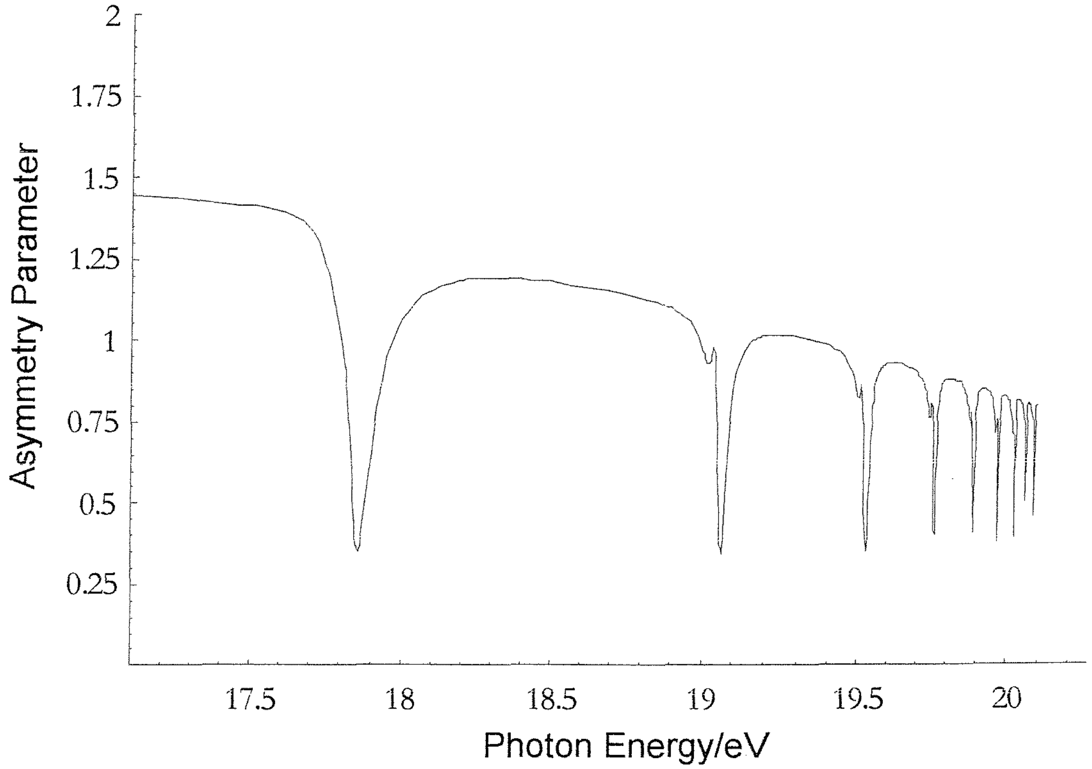

Figure 8.47: Spectrum of the calculated asymmetry parameter (β) for the Rydberg Series 1 of the $S^+(^4S) \leftarrow S^* \leftarrow S(^3P)$ *ionization process as a function of the photon energy over the range* $h\nu = 17\text{–}20.5$ *eV*

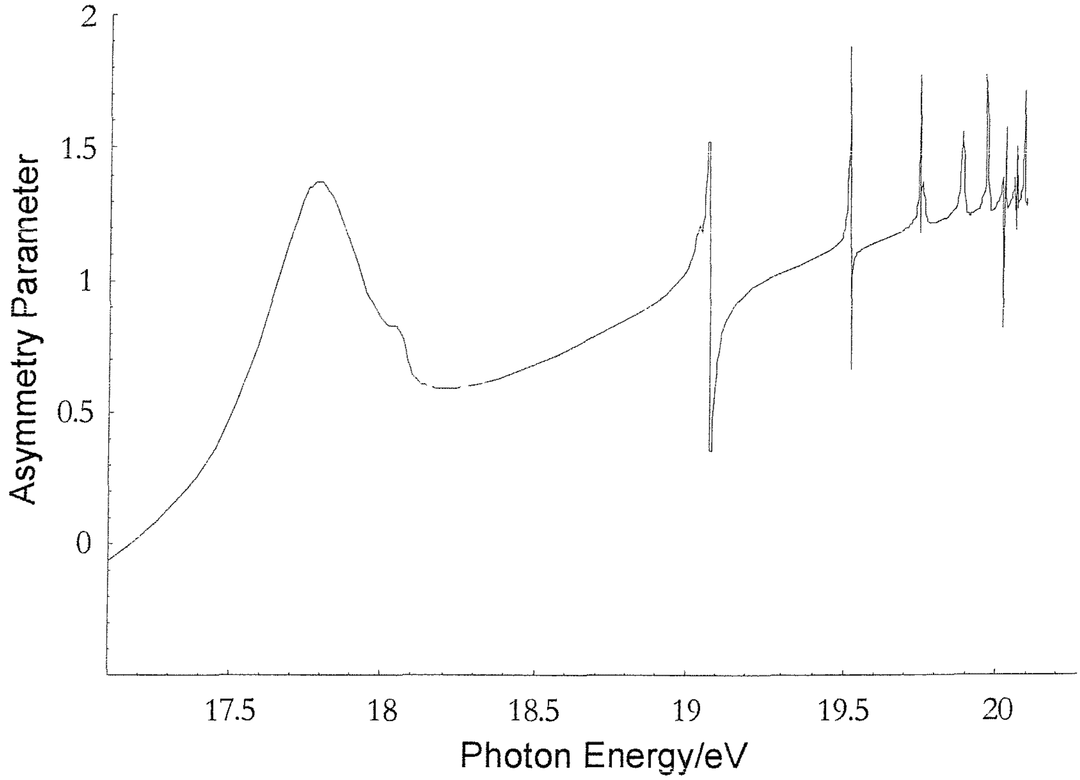

Figure 8.48: Spectrum of the calculated asymmetry parameter (β) for the Rydberg Series 2 of the $S^+(^4S) \leftarrow S^* \leftarrow S(^3P)$ *ionization process as a function of the photon energy over the range* $h\nu = 17\text{–}20.5$ *eV*

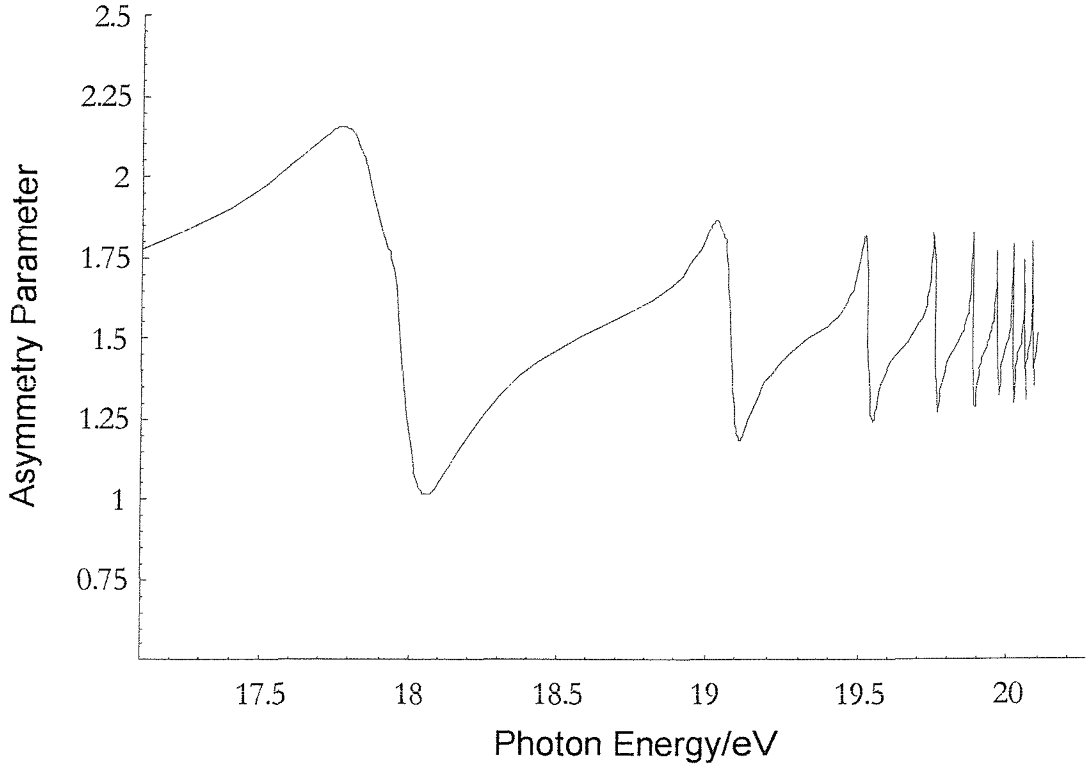

Figure 8.49: Spectrum of the calculated asymmetry parameter (β) for the Rydberg Series 1 (^3P) of the $S^+(^2D) \leftarrow S^* \leftarrow S(^3P)$ ionization process as a function of the photon energy over the range $h\nu = 17–20.5$ eV

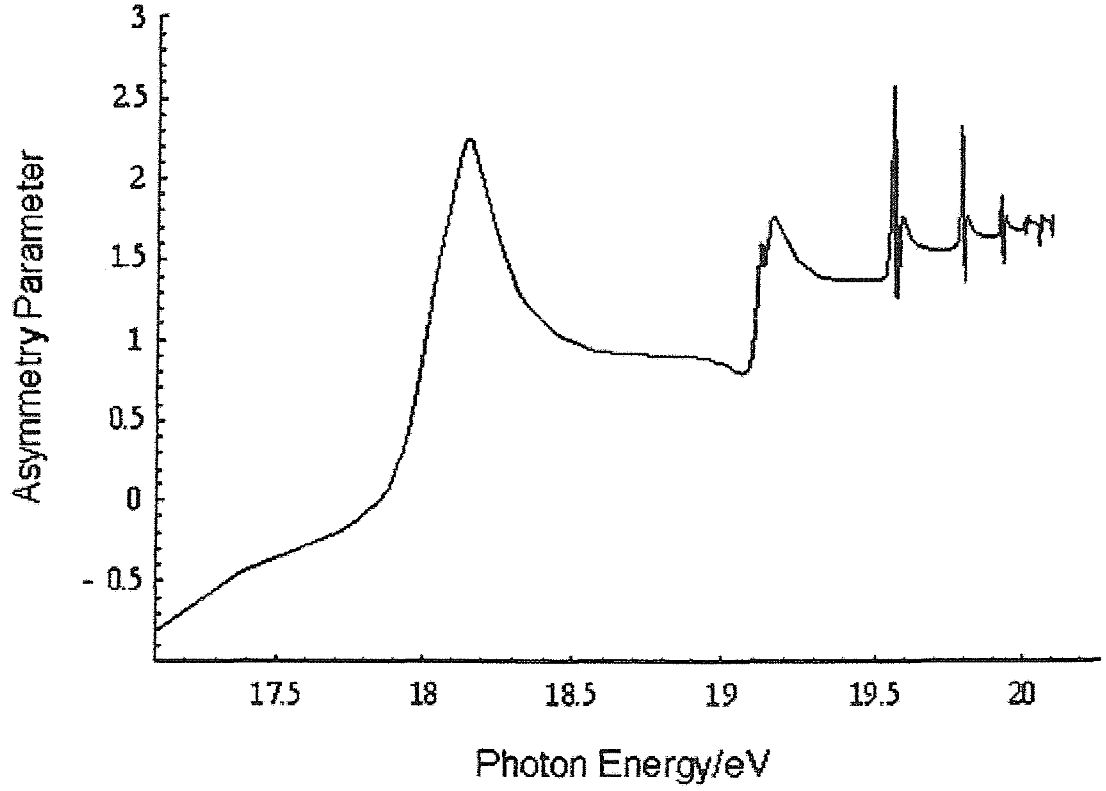

Figure 8.50: Spectrum of the calculated asymmetry parameter (β) for the Rydberg Series 2 (^2P) of the $S^+(^2D) \leftarrow S^* \leftarrow S(^3P)$ ionization process as a function of the photon energy over the range $h\nu = 17–20.5$ eV

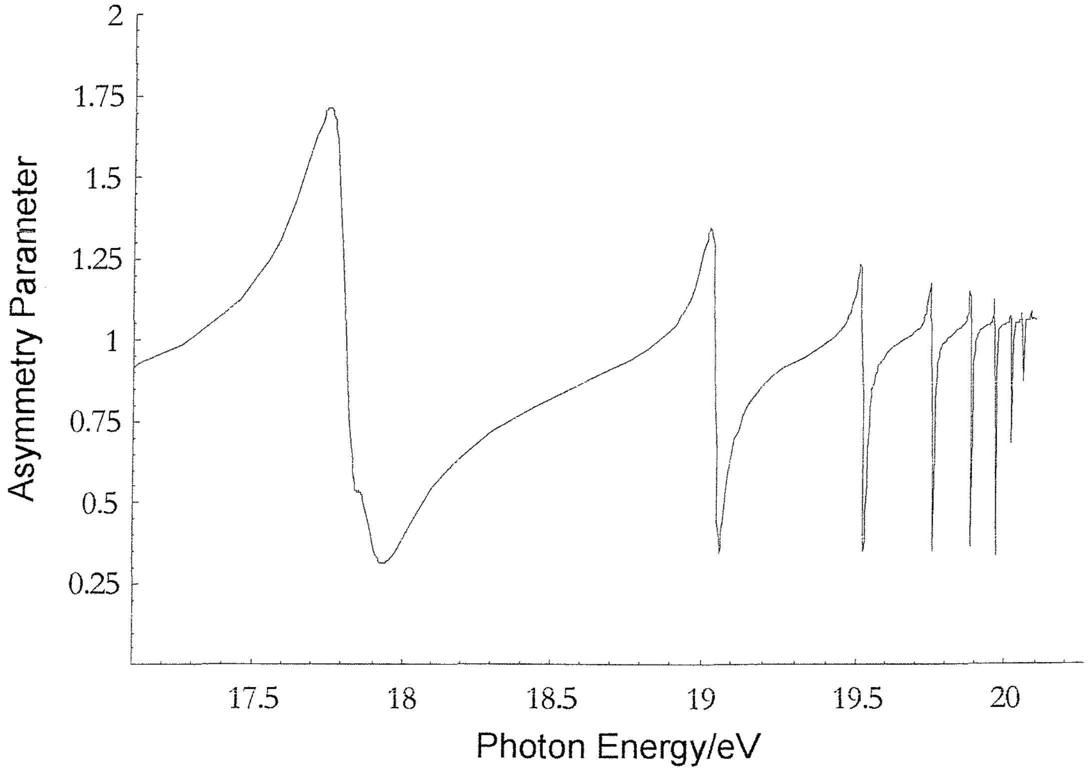

Figure 8.51: Spectrum of the calculated asymmetry parameter (β) for the Rydberg Series 1 (^3D) of the $S^+(^2P) \leftarrow S^* \leftarrow S(^3P)$ ionization process as a function of the photon energy over the range $h\nu = 17$–20.5 eV

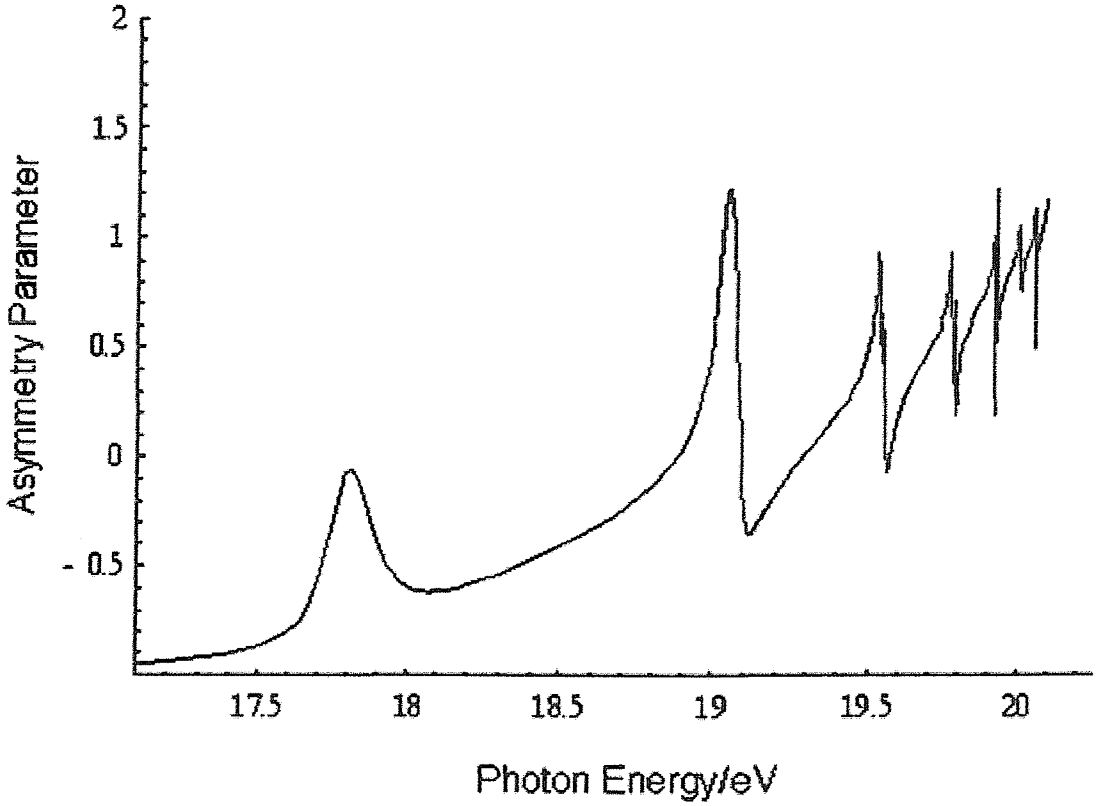

Figure 8.52: Spectrum of the calculated asymmetry parameter (β) for the Rydberg Series 2 (^3D) of the $S^+(^2P) \leftarrow S^* \leftarrow S(^3P)$ ionization process as a function of the photon energy over the range $h\nu$ =17–20.5 eV

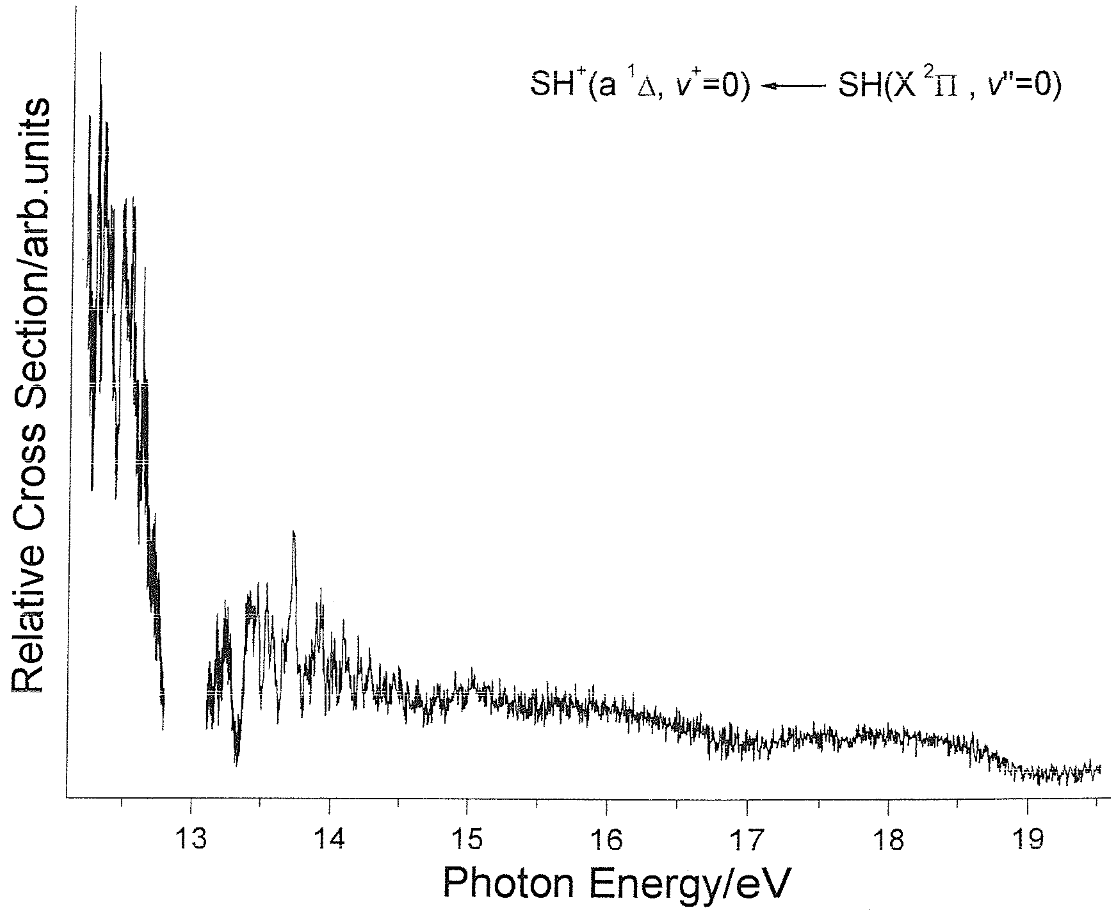

Figure 8.53: : CIS spectra recorded for the $SH^+(a\,^1\Delta)\leftarrow SH(X\,^2\Pi)$ *process in the 12.1-19.6 eV photon energy region, at* $\theta = 54°44'$ *detection angle*

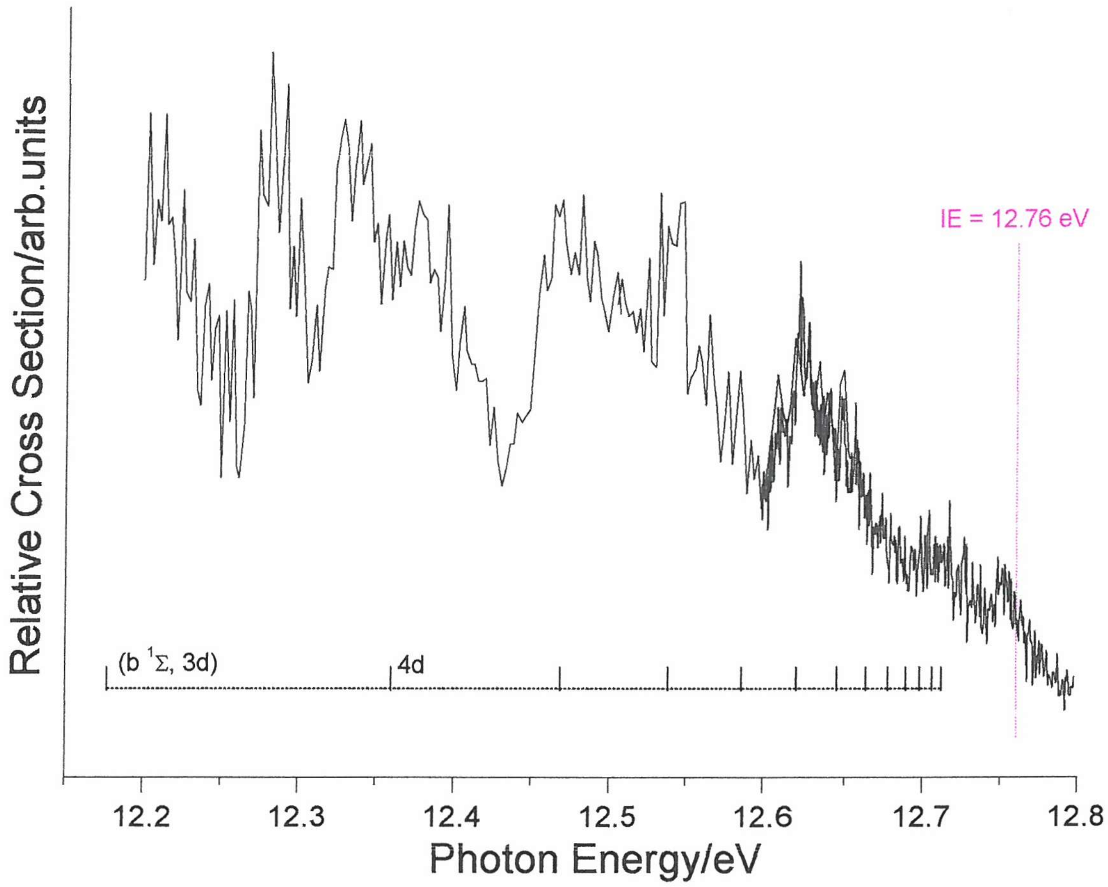

Figure 8.54: CIS spectra recorded for the $SH^+(a\ ^1\Delta) \leftarrow SH(X\ ^2\Pi)$ process in the 12.2-12.8 eV photon energy region, at $\theta = 54°44'$ detection angle, with the third ionization limit marked (magenta trace) Expected positions of $SH^*(b\ ^1\Sigma,\ nd)$ Rydberg states are indicated

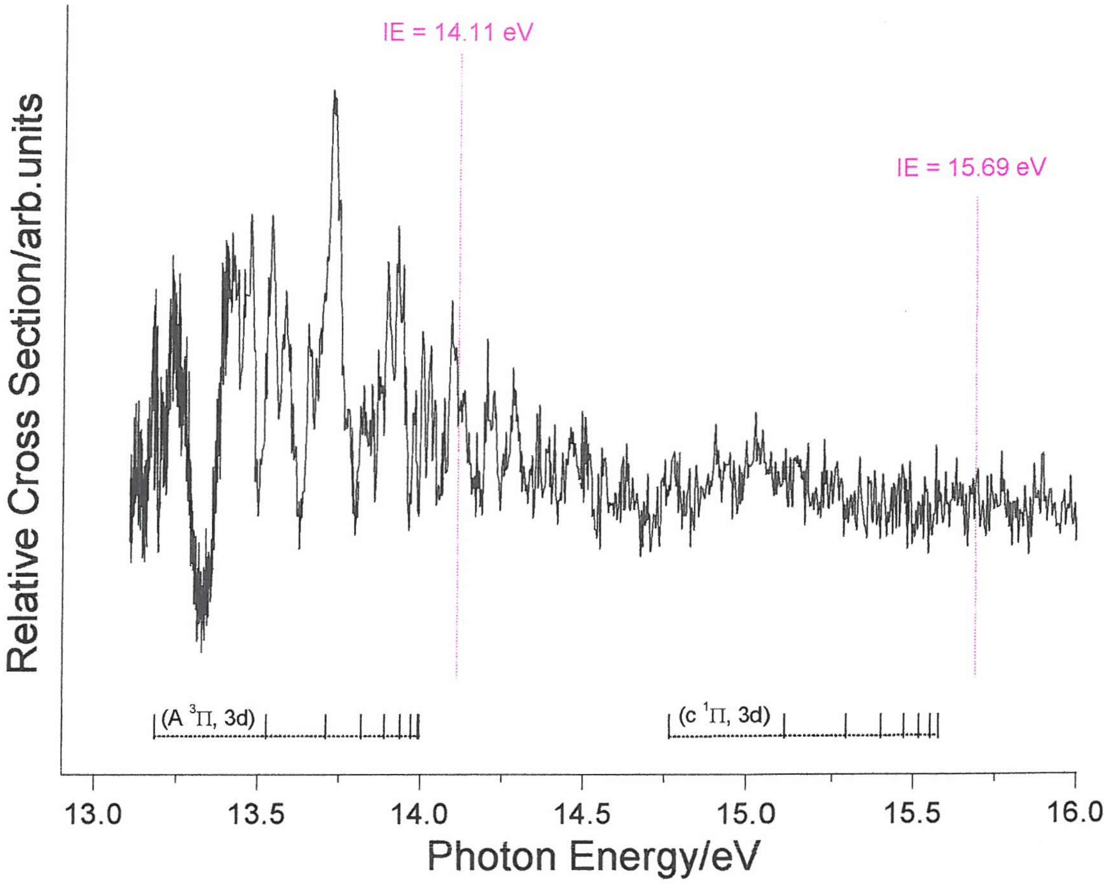

Figure 8.55: CIS spectra recorded for the $SH^+(a\ ^1\Delta) \leftarrow SH(X\ ^2\Pi)$ *process in the 13-16 eV photon energy region, at* $\theta = 54°44'$ *detection angle, with the fourth (IE =14.11 eV) and fifth (IE =15.69 eV) ionization limits marked (magenta trace)*

Expected positions of $SH^*(A\ ^3\Pi,\ nd)$ *Rydberg states and* $SH^*(c\ ^1\Pi,\ nd)$ *Rydberg states are indicated*

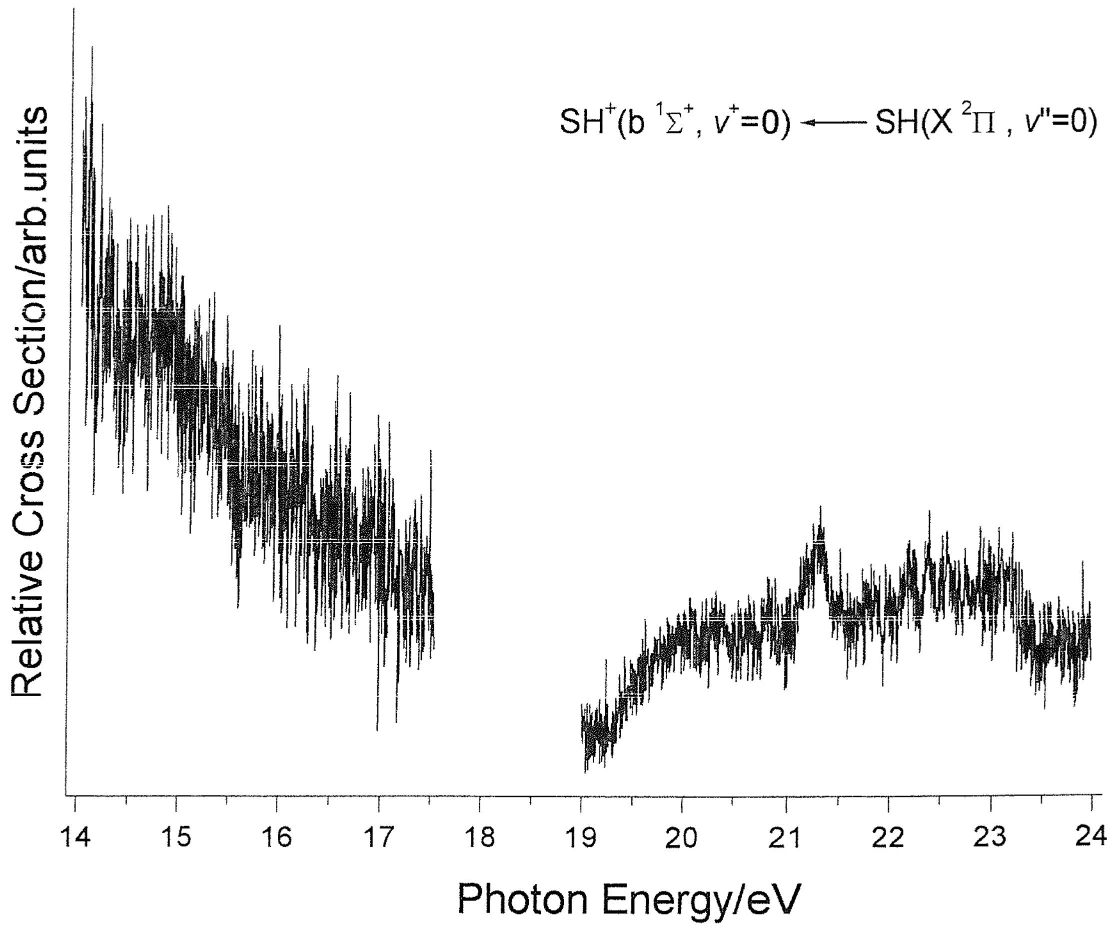

Figure 8.56: CIS spectra recorded for the $SH^+(b\ ^1\Sigma^+) \leftarrow SH(X\ ^2\Pi)$ *process in the 14-24 eV photon energy region, at* $\theta = 54°44'$ *detection angle*

8.4 References

[1] http://www.elettra.trieste.it

[2] G. G. Lombardi, B. L. Cardon and R. L. Kurucz
Astrophysical Journal **248**, 1208 (1981)

[3] J. E. Vernazza, E. H. Averett and R. Loeset
Astrophysical Journal Supplement **45**, 635 (1981)

[4] M. L. Meeks, M. A. Gordon and M. M. Litvak
Science **163**, 173 (1969)

[5] K. Sinha
Proceedings of the Astronomical Society of Australia **9**, 32 (1991)

[6] S. J. Dunlavey, J. M. Dyke, N. K. Fayad, N. Jonathan and A. Morris
Molecular Physics **38**, 729 (1979)

[7] M. J. Conneelly, K. Smith and L. Lipsky
Journal of Physics B **3**, 493 (1970)

[8] D. Dill, A. F. Starace and S. T. Manson
Physical Review A **11**, 1596 (1975)

[9] S. T. Manson, A. Msezane, A. F. Starace and S. Shahabi
Physical Review A **20**, 1005 (1979)

[10] J. J. Yeh and I. Lindau
Atomic Data and Nuclear Data Tables **32**, 1 (1985)

[11] G. Tondello
Astrophysical Journal **172**, 771 (1972)

[12] V. N. Sarma and Y. N. Joshi
Physica **123 C**, 349 (1984)

[13] Y. N. Joshi, M. Mazzoni, A. Nencioni, W. H. Parkinson and A. Cantu
Journal of Physics B **20**, 1203 (1987)

[14] S. T. Gibson, J. P. Green, B. Ruscic and J. Berkowitz
Journal of Physics B **19**, 2825 (1986)

[15] G. W. vanLoon and S. J. Duffy
Enviromental Chemistry a global perspective
University Press, Oxford, 2000

[16] M. N. R. Ashfold, B. Tutcher and C. M. Western
Molecular Physics **66**, 981 (1989)

[17] G. Herzberg and K. P. Huber
Molecular Spectra and Molecular Structure
D. VAN NOSTRAND COMPANY Inc., 1966, Vol. IV

[18] B. A. Morrow
Canadian Journal of Physics **44**, 2447 (1966)

[19] J. Brzozowski, N. Elander, P. Erman and M. Lyyra
Physica Scripta **10**, 241 (1974)

[20] P. E. Cade and W. M. Huo
Journal of Chemical Physics **47**, 649 (1967)

[21] M. Horani, J. Rostas and H. Lefebvre-Brion
Canadian Journal of Physics **45**, 3319 (1967)

[22] J. B. Milan, W. J. Buma and C. A. deLange
Journal of Chemical Physics **105**, 6688 (1996)

[23] C. W. Hsu, D. P. Baldwin, C. L. Liao and C. Y. Ng
Journal of Chemical Physics **100**, 8047 (1994)

[24] J. B. Milan, W. J. Buma and C. A. deLange
Journal of Chemical Physics **104**, 521 (1996)

[25] http://kinetics.nist.gov/index.php

[26] M. C. R. Cockett, J. M. Dyke and H. Zamanpour
Vacuum Ultraviolet Photoionization and Photodissociation of Molecules and Clusters
edited by C.Y. Ng, World Scientific, 1991, Chapter 2

[27] J. B. West and G. V. Marr
Atomic Data and Nuclear Data Tables **18**, 497 (1976)

[28] A. Derossi, F. Lama, M. Piacentini, T. Prosperi and N. Zema
Review of Scientific Instrumentation **66**, 1718 (1995)

[29] D. Desiderio, S. DiFonzo, B. Diviacco, W. Jark, J. Krempasky, R. Krempaska, F. Lama, M. Luce, H. C. Mertins, M. Piacentini, T. Prosperi, S. Rinaldi, F. Schefers, F. Schmolla, G. Soulle, L. Stichauer, S. Turchini, R. P. Walker and N. Zema
Synchrotron Radiation News **12**, 34 (1999)

[30] A. B. Cornford, D. C. Frost, C. A. McDowell, J. L. Ragle and I. A. Stenhouse
Journal of Chemical Physics **54**, 2651 (1971)

[31] P. M. Guyon, R. Spohr, W. A. Chupka and J. Berkowitz
Journal of Chemical Physics **65**, 1650 (1976)

[32] D. M. deLeeuw, R. Mooyman and C. A. deLange
Chemical Physics **34**, 287 (1978)

[33] C. E. Moore
Atomic Energy Levels
U.S. Government Printing Office, Washington DC, 1952, Vol. 1

[34] P. Baltzer, L. Karlsson, M. Lundqvist, B. Wannberg, D. M. P. Holland and M. A. MacDonald
Chemical Physics **195**, 403 (1995)

[35] M. Y. Adam, P. Morin, C. Cauletti and M. N. Piancastelli
Journal of Electron Spectroscopy and Related Phenomena **36**, 377 (1985)

[36] K. Watanabe and A. S. Jursa
Journal of Chemical Physics **41**, 1650 (1964)

[37] G. Fronzoni, M. Stener and P. Decleva
Journal of Chemical Physics **118**, 10051 (2003)

[38] J. Cooper
Physical Review **128**, 681 (1962)

[39] J. Cooper and R. N. Zare
Lectures in Theoretical Physics
edited by S. Geltman, K.T. Mahanthappa and W.E. Brittin, New York, 1967, Vol. XI-C

[40] R. Feng, G. Cooper and C. E. Brion
Chemical Physics **249**, 223 (1999)

[41] K. Kimura, S. Katsumata, Y. Achiba, T. Yamazaki and S. Iwata
Handbook of HeI photoelectron spectra of fundamental organic molecules
Japan Scientific Societies Press, Tokyo, 1981

[42] D. Muller
Zeitschrift fur Naturforschung **23 A**, 1707 (1968)

[43] U. Fano
Physics Review **124**, 1866 (1961)

[44] U. Fano and J. W. Cooper
Physics Review **137**, 1364 (1965)

[45] M. J. Seaton
Proceedings of the Physical Society **88**, 801 (1966)

[46] M. J. Seaton
Reports on Progress in Physics **46**, 167 (1983)

[47] A. Giusti-Suzor and U. Fano
Journal of Physics B **17**, 215 (1984)

[48] J. P. Connerade
Journal of Physics B **16**, 329 (1983)

[49] W. E. Cooke and C. L. Cromer
Physical Review A **32**, 2725 (1985)

[50] J. Dubau and M. J. Seaton
Journal of Physics B **17**, 381 (1984)

[51] K. Ueda
Physical Review A **35**, 2484 (1987)

[52] H. G. Kuhn
Atomic Spectra
Longmans, London, 1964

[53] J. M. Hollas
Modern Spectroscopy
Wiley & Sons, Chichester, 1996

[54] K. Maeda, K. Ueda and K. Ito
Journal of Physics B **26**, 1541 (1993)

[55] T. K. Fang and T. N. Chang
Physical Review A **57**, 4407 (1998)

Chapter 9

9 EXPERIMENTS TO STUDY THE PHOTODISSOCIATION OF ETHYLENE AT VUV PHOTON ENERGIES USING SYNCHROTRON RADIATION

As part of a collaboration between the Southampton and Orsay groups within the EC "Reactive Intermediates" Network, work has been undertaken in Orsay, in the group of Prof. Dolores Gauyacq[1]. This involved using the Super-ACO Synchrotron Radiation Source[2] to study photodissociation of hydrocarbons of importance in atmospheric and astrophysical chemistry and combustion. In these experiments, the photodissociation mechanisms of ethylene are probed through the detection of visible fluorescence emitted by the fragments, using an optical device designed by the Orsay group. In this Chapter an extensive description of the apparatus utilized is given and some results obtained during a visit to the French group of the EC Network are also presented.

The Chapter is organized as follows. In section 9.1 the experimental apparatus used for the photodissociation studies of hydrocarbons is described. In section 9.2 previous investigations on ethylene that are considered important for the present work are briefly reviewed. Section 9.3 summarizes the results obtained on ethylene photodissociation by means of this original apparatus and section 9.4 summarizes the conclusions.

9.1 Introduction

In the present work, the visible fluorescence of electronically excited fragments formed from the VUV photodissociation of ethylene in the 11.7-21.4 eV energy region has been studied in a gas-flow system, using Synchrotron Radiation as the photon source and an original light collection device used to detect the fluorescence. The isotropic visible fluorescence of the fragments was efficiently collected by a silver coated ellipsoidal mirror system coupled to a bundle of silica optical fibres which guided the fluorescence signal towards the measurement system (a photomultiplier or monochromator/photomultiplier combination).

9.1.1 The ellipsoidal mirror-optical fibre bundle photon collector system: EGG

The collection and subsequently the analysis of the light emitted on de-excitation of molecules is the main goal of one of the most common spectroscopic techniques. In the case when the number of photons emitted during the process is relatively small, it is important to optimize their collection in order to obtain as much information as possible on the event under investigation. In this particular study, where Rydberg states of the parent molecule are excited via absorption of UV radiation from a synchrotron source, dissociation or predissociation leads to the production of excited fragments that subsequently loose their excitation energy. Generally, dissociation or predissociation of electronically excited parent molecules leads to the production of electronically and/or vibrationally excited fragments that may fluoresce; often this fluorescence occurs in the visible energy region. A design for a fluorescence collection system coupled with optical fibres was made and the apparatus was built[3] in the Orsay group. This device is based on the optical properties of a revolution ellipsoid.

In a perfect ellipsoidal mirror, all the light-rays coming out from a point light source located at one of the two focal points converge on the second focal point after only one reflection on the mirror surface. The second focal point is a perfect image of the point source, as it can be seen in Figure 9.1 *(a)*. A possible plan for a light collection optical system using this property would be to detect photons by placing the detector, or in this case the optical fibre bundle, nearer the second focal point. However, the use of an optical fibre bundle with a fixed aperture to guide the light from the collector to the detector (photomultiplier or spectrometer) reduces the number of collected photons when this geometry is adopted. If the path of a light-ray originating from the same point light source which undergoes additional reflections is considered as illustrated in Figure 9.1 *(b)*, it is clear that after each reflection, there is a parallelisation of the light-ray towards the main axis of the ellipsoid. Moreover, there are two regions on the mirror surface where the light-rays are converging: the two ellipsoidal caps at the extremities of the main axis.

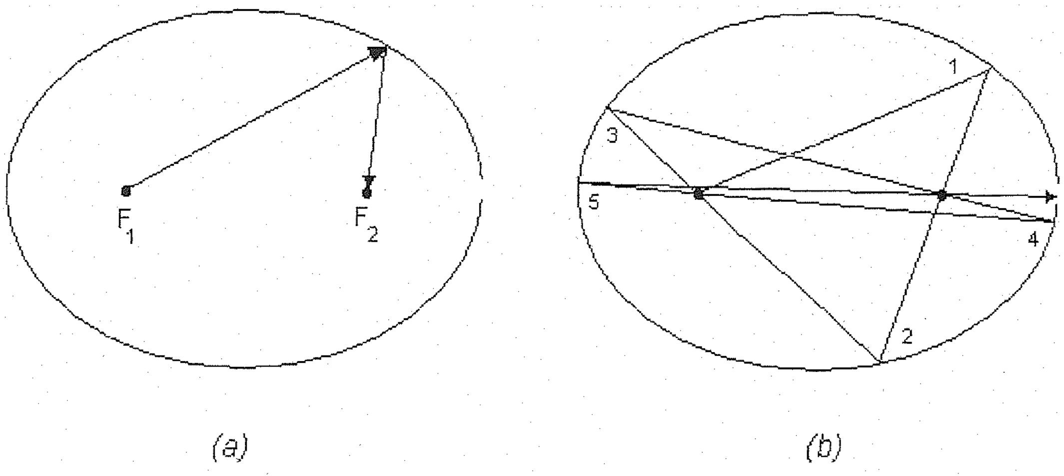

Figure 9.1: Trajectory of a light-ray coming from a point light source located at the focal point F_1 of the ellipsoidal mirror
(a) after one reflection
(b) after several (5) reflections

These two main properties, parallelization of the light-rays and convergence toward a surface point, occur without distinction of the initial direction of the light-ray for a point light source located at one of the focus points of the ellipsoidal mirror. Hence, an aperture located on the main axis at one extremity of the ellipsoidal mirror would provide the ideal position for the optical fibre bundle. In this ideal case 100% of the emitted photons would be guided to the optical fibre bundle; in reality losses occur caused by the fact that the source has a spatial distribution, the bundle entrance covers a small part of the reflecting surface and the surface of the mirror is not 100% reflective. Several numerical ray tracing simulations have been carried out by the Orsay group to estimate the percentage of photons emitted by a finite source (about 1 mm^3) that can be guided to an optical fibre bundle of fixed geometry aperture[3]. From these simulations it appeared that the percentage of the out-going light-rays for a typical 1 mm^3 wide source is maximized when the source is located about 2 mm away from the focal point towards the end of the mirror, instead of being placed at one of the two focal points. This surprising finding has been verified experimentally during beamtime sessions dedicated to the full characterisation and testing of the system.

From the results of the simulations, two half-ellipsoidal mirrors with specified dimensions have been built in stainless steel[3]. In Figure 9.2 a detailed diagram of the mirror, the so-called the EGG, is presented. From Figure 9.2 the dimensions of the holes in the mirror necessary for gas evacuation (ϕ=30 mm) and for the excitation synchrotron beam to reach the focal point (ϕ=10 mm) can be seen. Both holes are drilled perpendicularly to the main revolution axis of the mirror. Furthermore, to evacuate the gas more efficiently from inside the EGG, a free space of 14 mm between the two halves has been left. This gap between the two halves has some consequences on the collection efficiency of this system, but they can be considered negligible with respect to the total percentage of collection. The internal mirror surface is coated with a SiO_2 protected silver layer with an optimum reflection coefficient in all the visible range (from 700 nm to 400 nm) of 99%.

The EGG has been fixed on a metallic frame designed to be positioned in the existing vacuum chamber SAPHIRS of the beamline SA63, at the Synchrotron Radiation Facility Super-ACO in Orsay (France)[2].

In Figure 9.3 a picture of the EGG inside the vacuum chamber is presented.

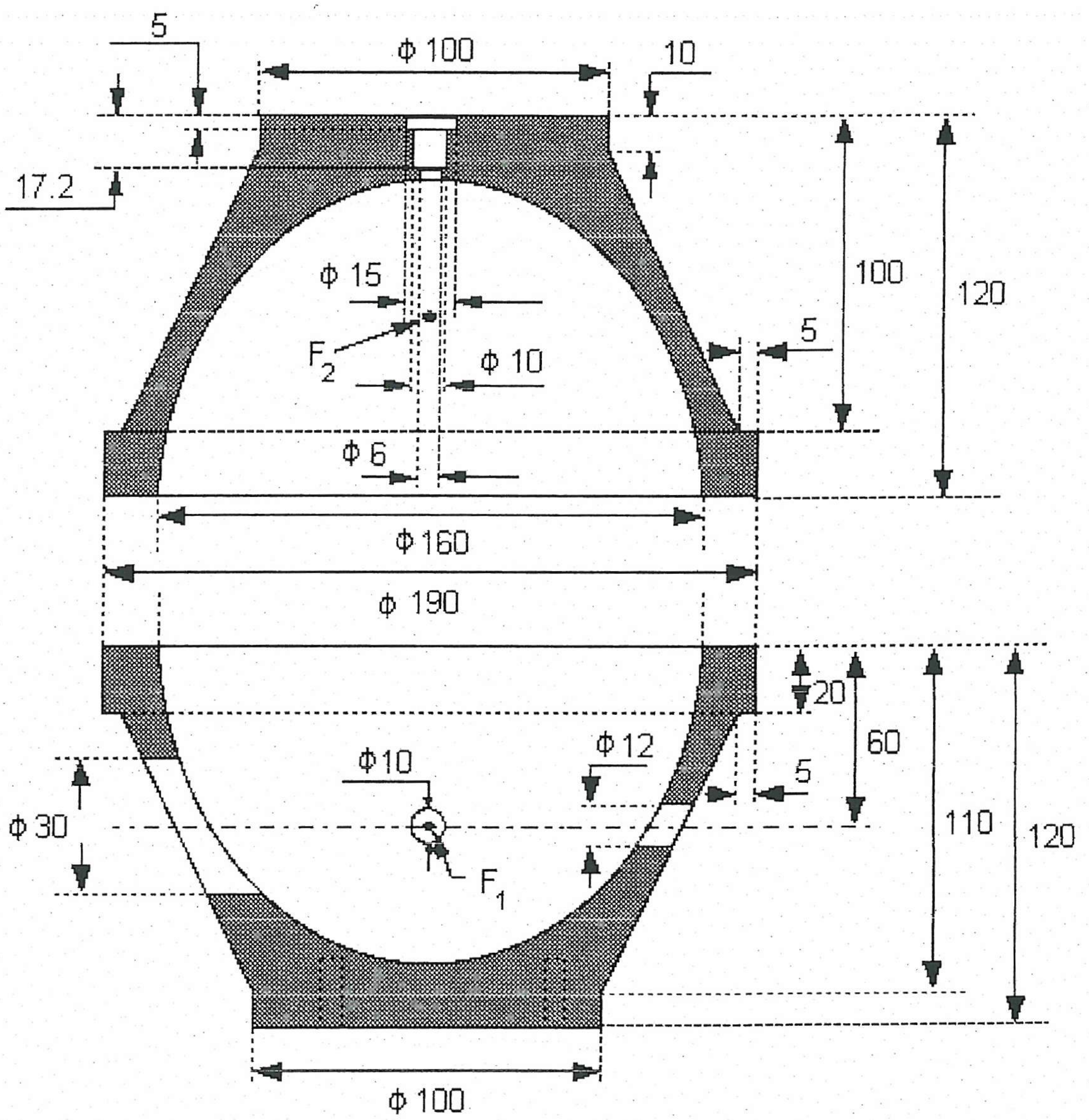

Figure 9.2: Detailed diagram of the EGG mirror system composed of two half ellipsoidal mirrors with the dimensions indicated (expressed in mm)

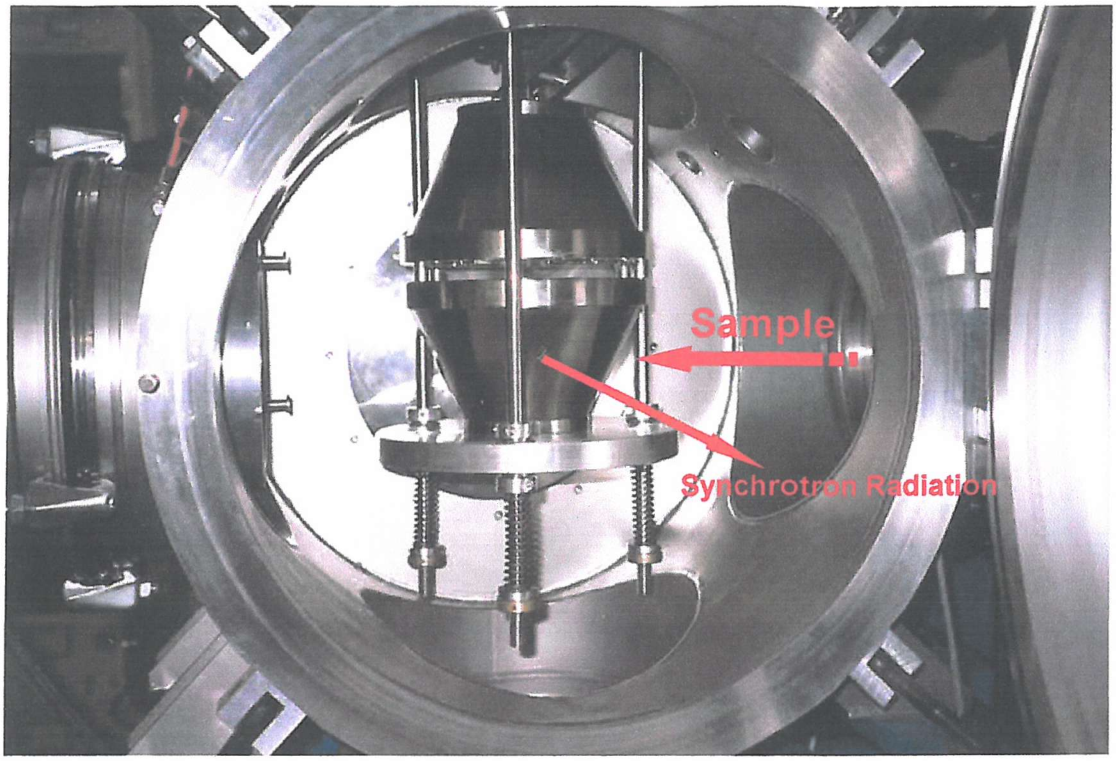

Figure 9.3: Picture of the EGG inside the SAPHIRS chamber. The vertical position of the ellipsoidal mirror can be finely adjusted from the outside in relation to the position of the synchrotron beam. The optical fibre bundle can easily follow the change in position of the EGG

9.1.2 Experimental set-up

The experiment was performed at the Synchrotron Radiation Facility Super-ACO in Orsay (France)[2] by using the beamline SA63.

This beamline is equipped with a 3-m Eagle normal incidence monochromator and a 1800 grooves/mm grating operating in the 10-22 eV energy region, with 8 meV average resolution when using 1 mm slit width.

The sample was introduced into the vacuum chamber by a stainless steel needle with a 100 μm nozzle at right angles to the VUV beam. A background pressure of about 10^{-4} mbar was maintained in the vacuum chamber under operating conditions by two Seiko H1000C and two Leybold TURBOVAC 1000 turbopumps. Differential pumping was achieved by means of a VARIAN V70 turbopump installed on the line between the high-vacuum synchrotron line and the vacuum chamber. With this arrangement, it was possible to work without any window up to a pressure of 10^{-3} mbar in the main chamber. Collisional effects were negligible, as confirmed by earlier experiments carried at the same conditions on acetylene[4].

The isotropic visible fluorescence of photodissociation fragments was efficiently collected by the original silver-coated ellipsoidal mirror system, the EGG, coupled to a bundle of silica optical fibres (about 3000 fibres 1.25 m long) which guided the fluorescence signal towards the measurements systems. The advantage of this set-up is that it permits the measurement of both the transmitted VUV photon intensity (and hence allows absorption data to be obtained) and the fluorescence signal.

The output of the fibre bundle (7×4 mm^2) was coupled either to a photomultiplier tube, Hamamatsu R928 (spectral range 950-185 nm), or to the entrance slit of a 0.27 m, f/4, Jobin-Yvon monochromator 270 M (150 grooves/mm grating, 13 nm resolution at 546 nm, spectral range 900-250 nm) equipped with a liquid-nitrogen-cooled CCD matrix detector (256×1024 pixels), as can be seen in Figure 9.4.

With this set-up three types of spectrum could be recorded:

- Absorption spectra, obtained by deriving the absorbance from the classical Beer-Lambert law[5]

  $$\sigma_{abs} \propto \ln\left[\frac{I_0(\nu)}{I(\nu)}\right] \qquad \text{Eq. 9.1}$$

  where $I_0(\nu)$ represents the transmitted intensity from the synchrotron beam line monochromator and $I(\nu)$ the transmitted intensity when the sample is present.

- Fluorescence excitation spectra, obtained while scanning the synchrotron beamline monochromator wavelength from 10 to 22 eV, and detecting any visible emission in the range 900 to 330nm.

- Dispersed fluorescence spectra, in the 840-350 nm range, could be recorded at fixed excitation wavelengths.

The photon flux was estimated by measuring the photocurrent emitted from an Au grid and the fluorescence signal monitored by a sodium salicylate layer positioned in front of the photomultiplier.

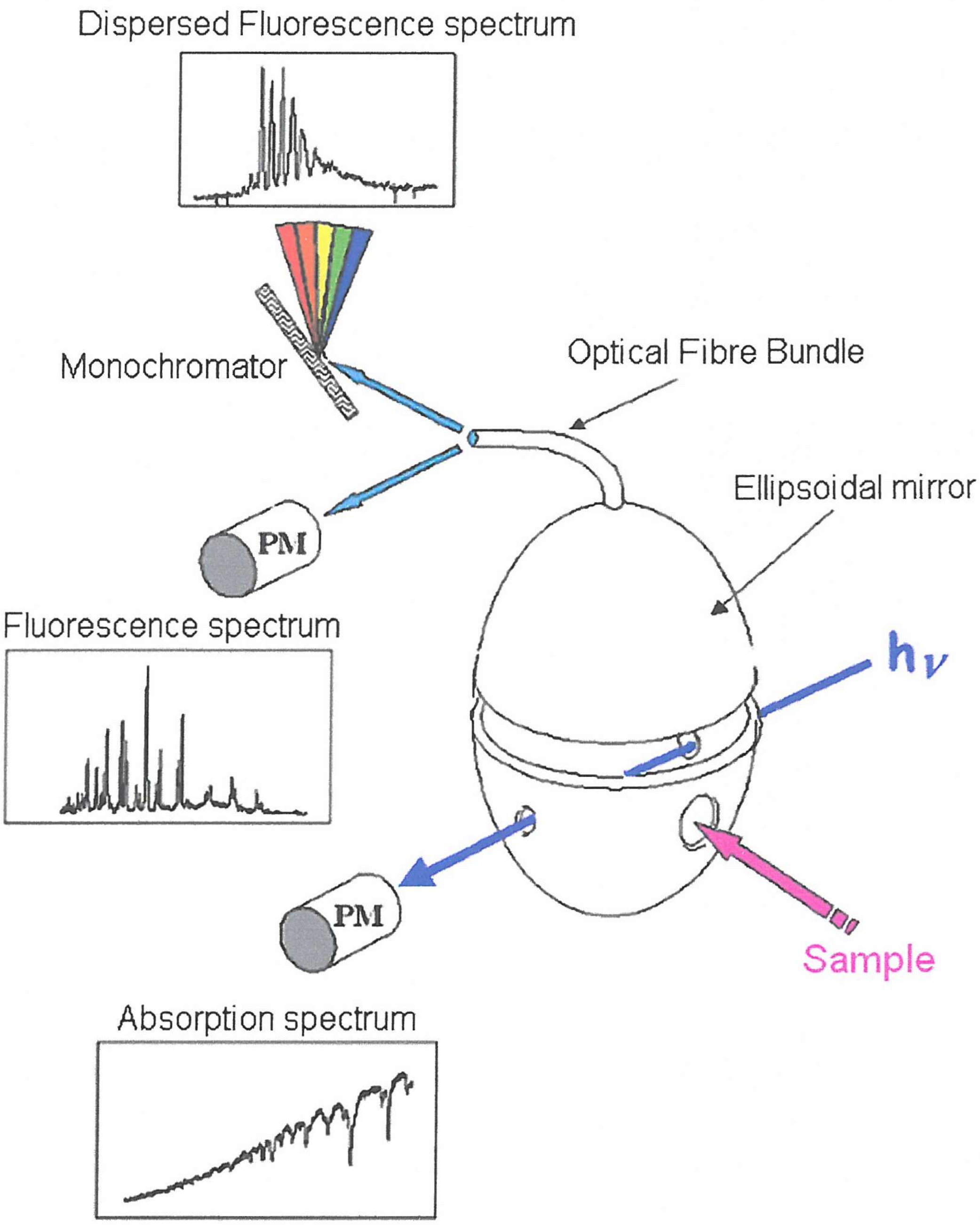

Figure 9.4: Experimental set-up in which the EGG ellipsoidal mirror is used in three possible configurations, to measure:
the transmitted VUV light intensity and hence allows the absorption spectrum to be obtained;
the total fluorescence signal, coupling the optical fibre bundle with the photomultiplier tube Hamamatsu;
the dispersed fluorescence signal, coupling the optical fibre bundle with the Jobin-Yvon monochromator

After exposure to Synchrotron Radiation for a known time (typical accumulation times of 10 min), the CCD image of the whole emission spectrum was transferred to a computer. Further data treatment was needed in order to remove contributions from cosmic rays. Finally, the data were numerically deconvoluted from the apparatus function, which allows for the contribution to resolution and sensitivity as a function of energy from the detector, monochromator and CCD spectral response.

9.2 Previous investigations on ethylene

Ethylene is an important molecule in astrophysics[6,7], combustion[8] and atmospheric science[9]. The UV absorption spectroscopy of ethylene has been extensively investigated[10,11]. Experimental[12] and theoretical[13-15] work has also focused on elucidating the decomposition of ethylene at the laser excimer wavelengths of 193 nm (6.4 eV) and 157 nm (7.9 eV). As a result of these investigations, the observed dissociation processes at these energies have been established as:

$$C_2H_4 + h\nu \rightarrow C_2H_3 + H \rightarrow C_2H_2 + 2H \qquad \text{Eq. 9.2}$$

$$C_2H_4 + h\nu \rightarrow acetylene + H_2 \qquad \text{Eq. 9.3}$$

$$C_2H_4 + h\nu \rightarrow vinylidene + H_2 \qquad \text{Eq. 9.4}$$

At the wavelengths employed in previous investigations, there is sufficient energy for a secondary step in the dissociation process as shown in Eq. 9.2.

In an attempt to describe molecular hydrogen elimination from ethylene, Evleth *et al.*[16] presented two elimination pathways to give acetylene (HCCH), Eq. 9.3, and vinylidene (H_2CC), Eq. 9.4. In the work of reference (16), the elimination process in Eq. 9.3 was proposed to occur via the formation of the ethylidene intermediate ($HCCH_3$), the isomer of ethylene. A considerable interest in the ethylidene isomer arose in the study of hydrocarbon molecules, which undergo isomerisation via H-atom migration[17,18].

The most recent *ab initio* theoretical treatment of this system has been performed on the ground state potential energy surface by Chang *et* al.[13,14]. It was determined that ethylidene is a local minimum on the reaction coordinate leading to acetylene formation. Unfortunately, similar calculations on the excited state potential energy surfaces do not exist.

The present work focused on the analysis of the dispersed visible fluorescence from fragment following photolysis of ethylene by Synchrotron Radiation between 106 and 58 nm (11.7-21.4 eV). Only excited state fragments are selectively detected and such fragments are therefore generated on an excited potential energy surface. Whether dissociation occurs through various steps from a highly excited potential energy surface to a less excited potential energy surface cannot be addressed here.

However, it is the case that the observed fragments cannot arise from dissociation via the ground state surface, an important distinction between this and all previous studies.

The only previous experimental work related to the present investigation was performed by Kameta *et al.*[19] where undispersed emission in the UV-visible region, following excitation by Synchrotron Radiation between 100 and 30 nm, was detected. CH (A-X and B-X) emissions were observed but no firm interpretation for the fragment formation was offered.

However, in the work described in this Chapter the higher resolution data obtained has permitted the proposal of dissociation mechanisms. Two channels have been identified leading to the formation of excited $CH^*(A^2\Delta, B^2\Sigma^-)$. Emissions from additional fragments, such as C_2, C_2H and H atoms (4-2 and 3-2 Balmer transition), were also observed. Seven dissociation channels have been identified in this excitation range.

9.3 Results and discussion

A typical absorption spectrum of ethylene recorded in this work is shown in Figure 9.5. The absorption signal, above the first ionization energy at 118 nm, consists of prominent and very broad features on top of which weaker vibrational structures are observed. It is very similar to the one shown in Figure 9.6, previously reported by Holland *et al.*[11].

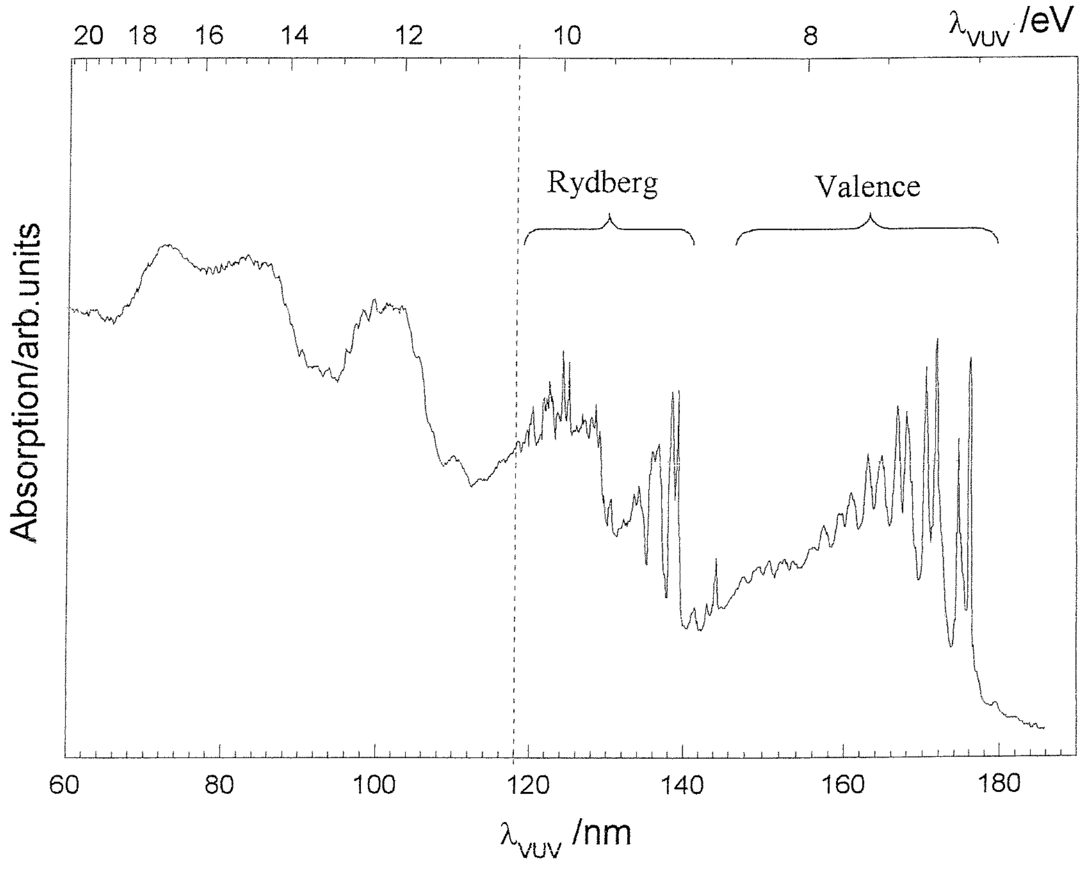

Figure 9.5: Absorption spectrum of ethylene in the 190-60 nm region (6.5-24.8 eV) The vertical dotted line at 118 nm indicates the position of the first ionization energy

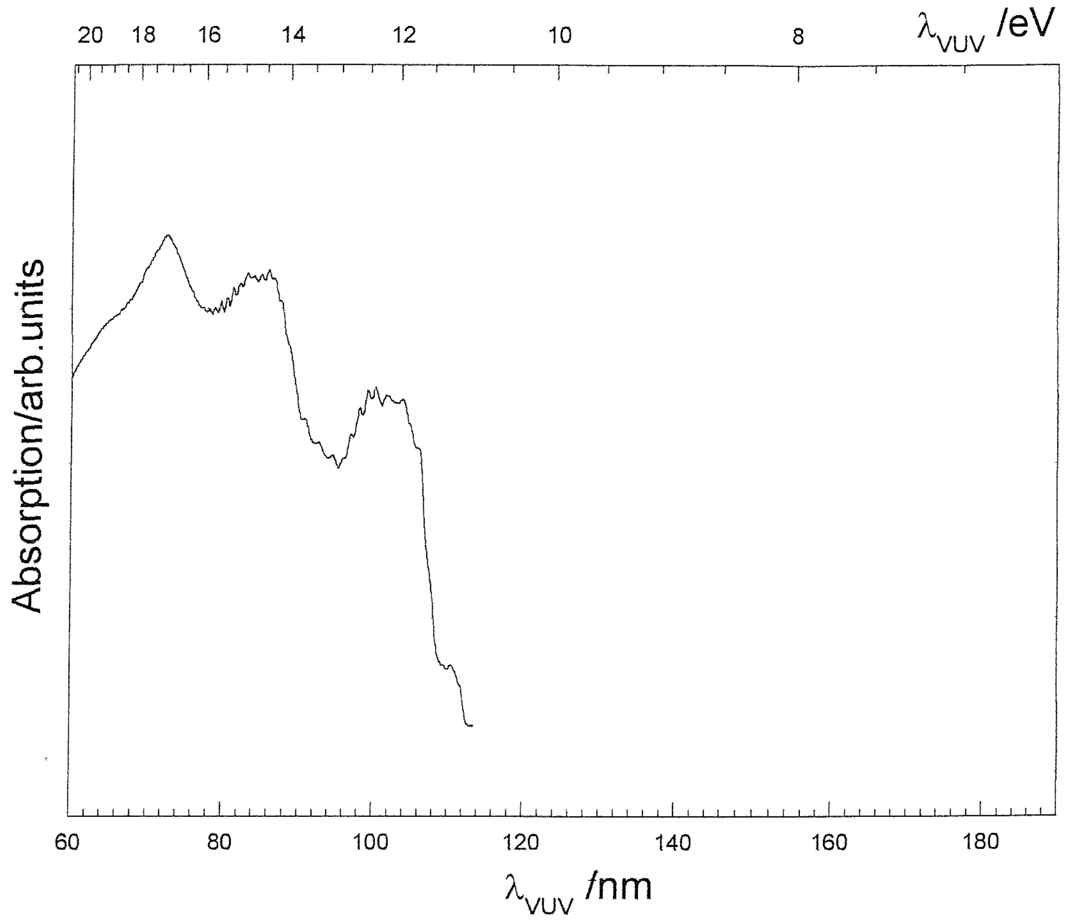

Figure 9.6: Absorption spectrum of ethylene recorded in the 190-60 nm region by Holland et al.[11]

According to Holland *et al.*[11], the broad features might be due to excitation to valence states and the weak overlapping structures due to excitation to autoionizing Rydberg states which form a series which converge to an excited state of ethylene cation. Nevertheless, very little information is known about the neutral excited states above the first ionization threshold of ethylene at 118 nm. Probably these high Rydberg states are predissociative states which lead to the neutral excited fragments from which emissions are observed.

Below the first ionization energy, between 140 nm and 118 nm, different Rydberg series are observed. They were assigned by McDiarmid[10] as transitions to the *n*s, 3p, *n*dσ and *n*dδ Rydberg states and their vibrational sub-bands. Between 177.4 nm and 140 nm the transition between the first excited singlet valence state and the ground state overlaps the transition from the ground state to the first 3s Rydberg state and some vibrational sub-bands.

In Figure 9.7 the total fluorescence in the visible from neutral fragments of C_2H_4, recorded in the region 180 to 40 nm excitation wavelength, is shown. This spectrum, although having much better statistics than that of reference (19), agrees very well with the one published by Kameta *et al.*[19], as can be seen in Figure 9.8.

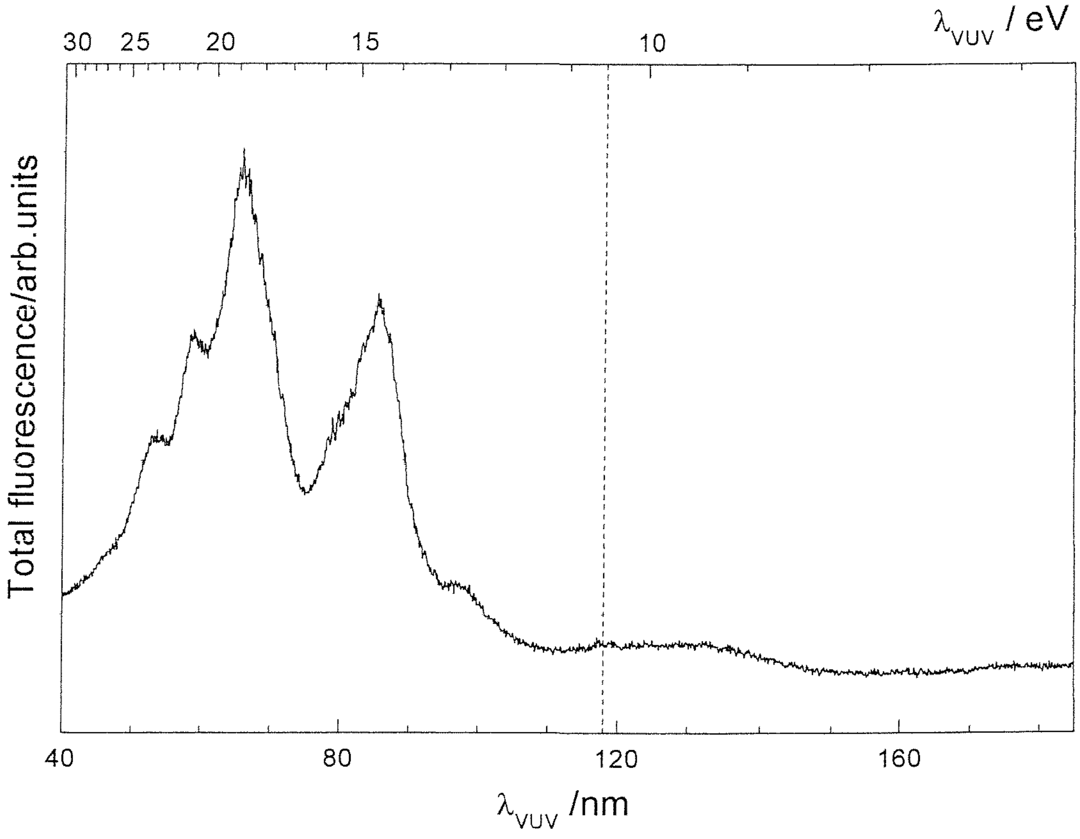

Figure 9.7: Total fluorescence spectrum in the visible of the neutral fragments of C_2H_4, obtained in the present work
The vertical dotted line at 118 nm indicates the position of the first ionization energy

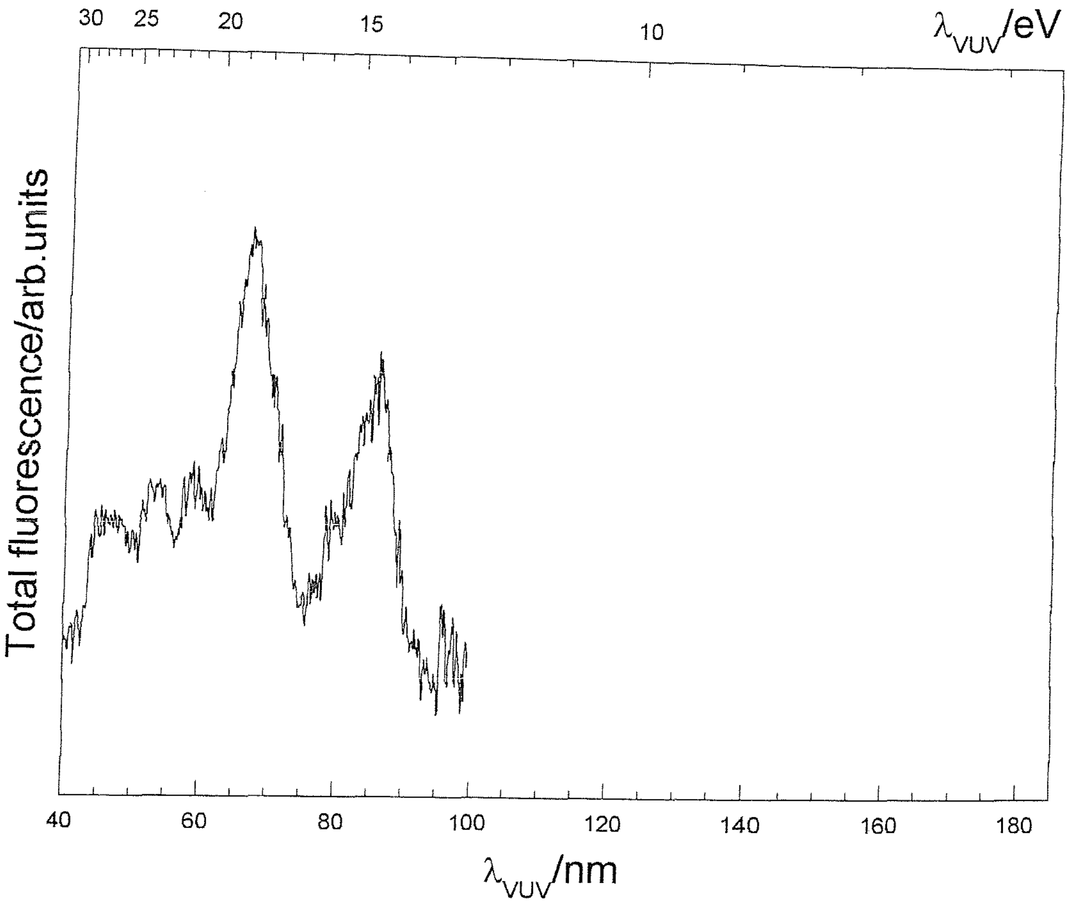

Figure 9.8: Total fluorescence spectrum of ethylene in the 180-40 nm region recorded by Kameta et al.[19]

As can be seen in Figure 9.9 where the total fluorescence spectrum in the visible region is compared with the absorption spectrum, the formation of fragments that emit in the visible represents only a small fraction of all possible decay mechanisms. The experimental technique discussed in this Chapter is "blind" to ionization and to fragments that are formed in their ground electronic states. Also fragments that emit in the infrared or in the UV are not observed.

As can be observed in Figure 9.9, the visible fluorescence signal increases between 100 and 40 nm and forms three broad bands: a weak one at 97.9 nm, an intense one at 86.0 nm and the last one at 66.5 nm. No significant visible fluorescence signal was observed at higher wavelengths than 100 nm. Since the fluorescence excitation spectrum does not reproduce the structures observed in the absorption spectrum below 118 nm, as no visible emission is observed below the first IE, it can be deduced that none of the dissociation processes are able to yield fragments with enough excitation energy to fluoresce in the visible below the first ionization energy. Indeed for ethylene the first dissociation channels thermodynamically accessible involve production of acetylene, vinylidene or the vinyl radical through H or H_2 elimination (or CH_2 from dissociation). Apart from C_2H in the A state, these fragments do not have emissions in the visible region[10-12,16] ‡.

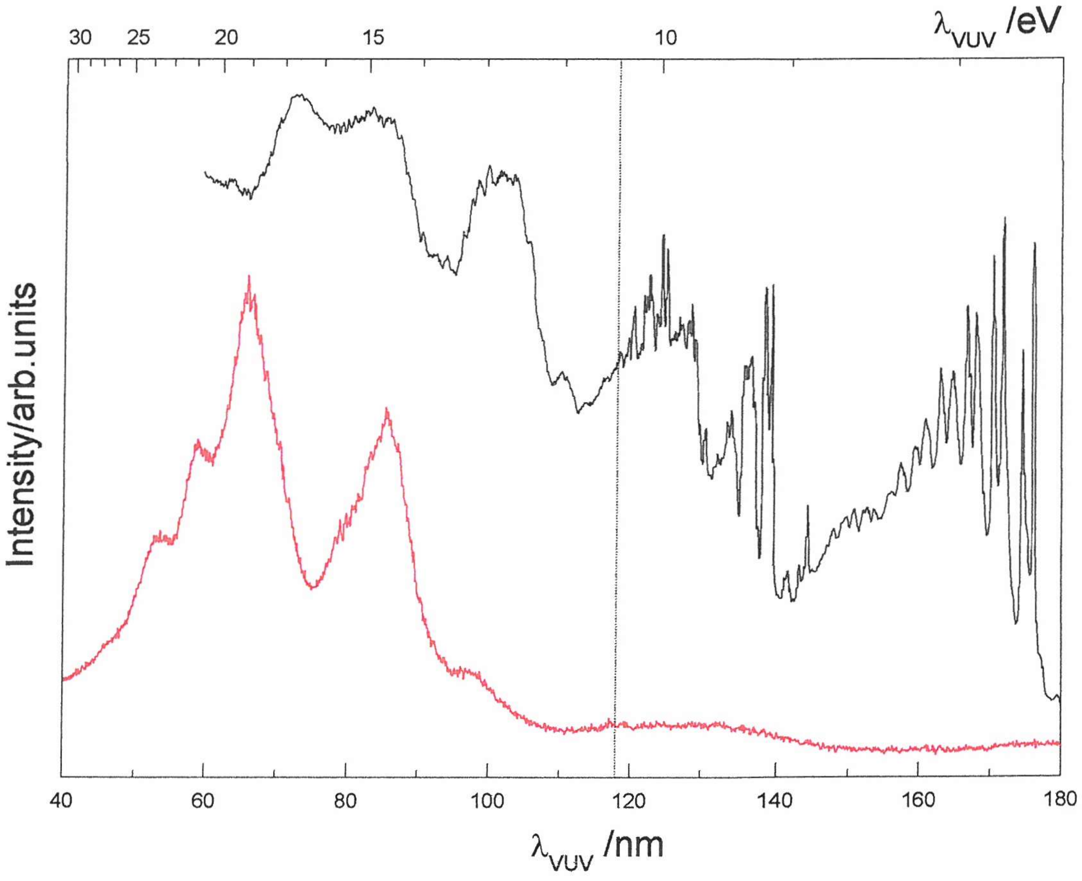

Figure 9.9: Total fluorescence spectrum (red line) compared with the absorption spectrum (black line) of the ethylene molecule
The vertical dotted line at 118 nm indicates the position of the first ionization energy

---

‡ After this work was completed, emission in the visible region was observed from C_2H (A) with a threshold of 8.6 eV (144 nm).

Figure 9.10 shows a three dimensional representation of the dispersed fluorescence spectra in the 350-840 nm wavelength region as a function of the photon energy from 10 to 22 eV.

Several well known visible transitions are observed, such as the CH(A $^2\Delta$-X $^2\Pi$) transition[20] centred at 431 nm, the CH(B $^2\Sigma^-$-X $^2\Pi$) transition[20] at 390 nm, the C_2(d $^3\Pi_g$-a $^3\Pi_u$) Swan bands[21] between 500 nm and 610 nm, and the H_β and H_α hydrogen atomic lines[22] at 486 nm and 656 nm respectively. Moreover, a quasi-continuum between 450 and 850 nm has been detected and assigned to emission from vibrationally excited states of C_2H in the (A $^2\Pi$) state to the ground state (X $^2\Sigma^+$)[23].

The prominent peak in Figure 9.10 centred at ~ 431 nm arises from the CH(A $^2\Delta$-X $^2\Pi$) transition[20] and that at ~390 nm arises from the CH(B $^2\Sigma^-$-X $^2\Pi$) transition[20]. For both transitions, the fluorescence intensity increases from 11.7 eV to a local maximum at 14.5 eV and subsequently diminishes to rise again to a second local maximum at approximately 18.5 eV after which the intensity again diminishes. The evolution of the fragments' fluorescence bands as a function of the photon energy is better displayed when integrating the fluorescence intensities as a function of the synchrotron photon energy, as shown in Figure 9.11. The signal is proportional to the probability of formation of excited CH at a given excitation photon energy. The similar general form of both the A-X and B-X transitions argues that they are both formed in similar overall dissociation mechanisms. This suggests that at a given excitation energy, the ethylene molecule relaxes through a dominant mechanism through an intermediate species. This species will in turn decay to give CH(A $^2\Delta$) and CH(B $^2\Sigma^-$). The only difference in Figure 9.10 between the (A-X) and (B-X) emissions is a relative intensity factor, suggesting a branching ratio significantly lower for the CH(B $^2\Sigma^-$) channel than for the CH(A $^2\Delta$) channel.

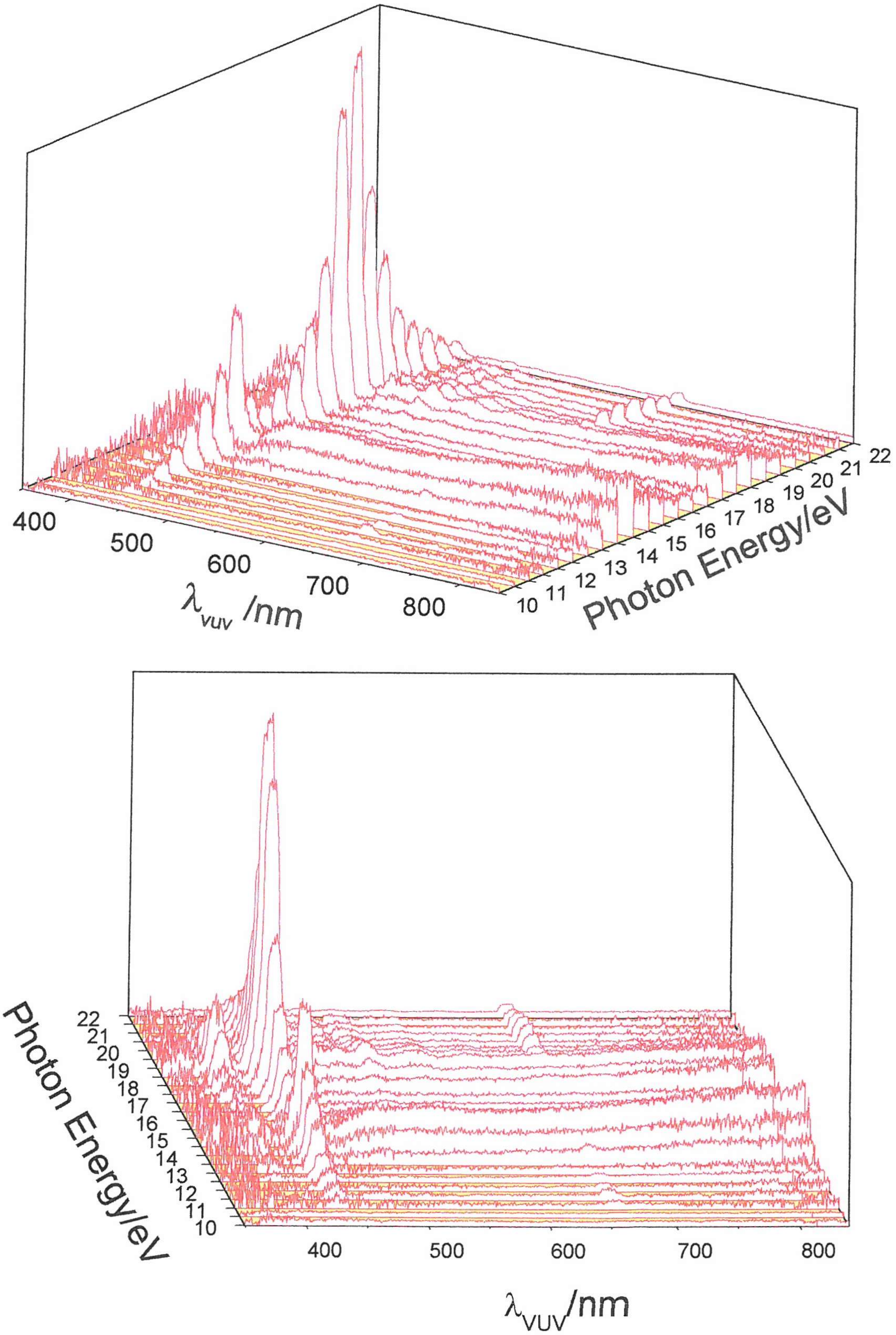

Figure 9.10: Dispersed fluorescence spectra in a three dimensional representation in the 350-840 nm wavelength region as a function of the photon energy from 10 to 22 eV

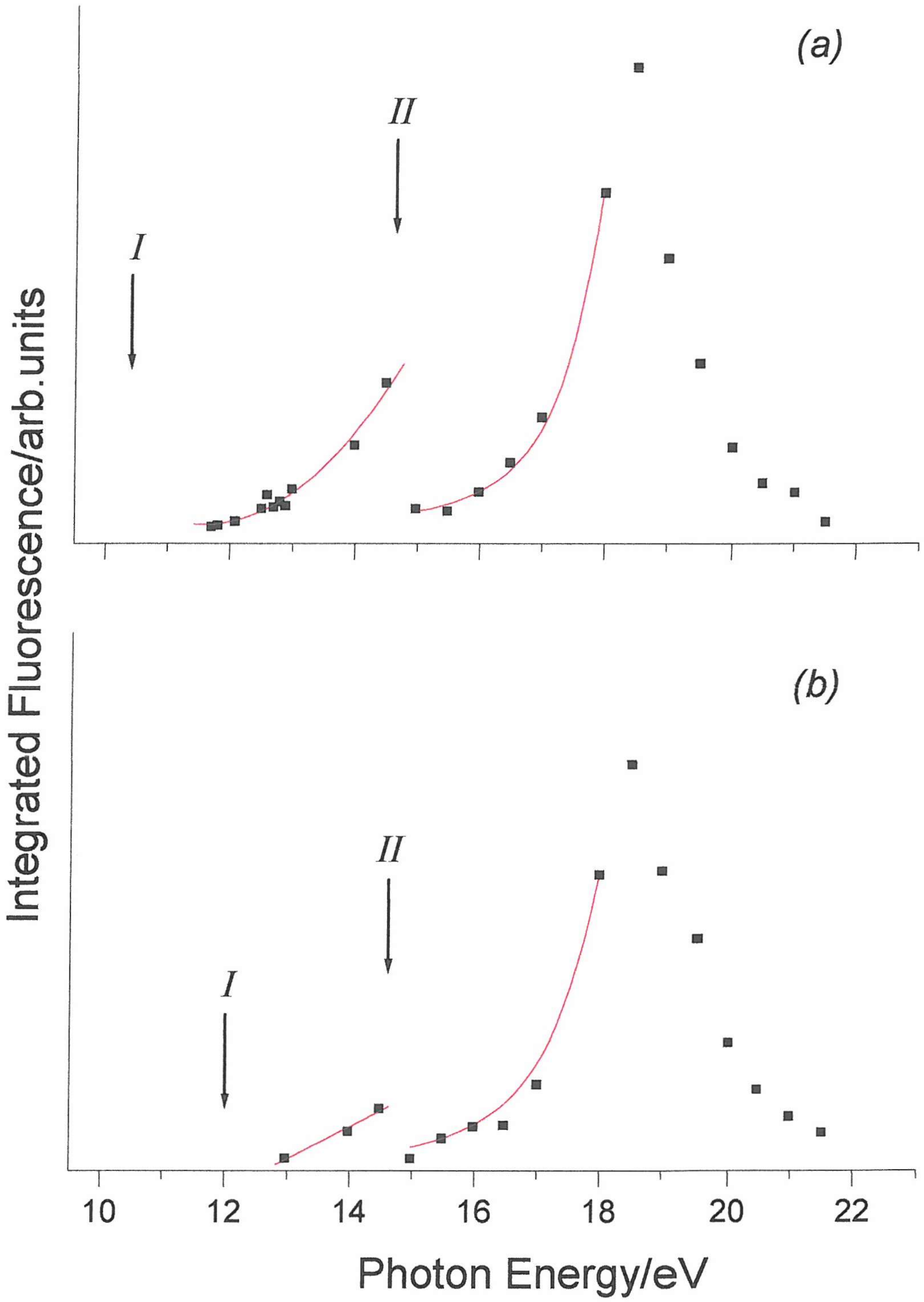

Figure 9.11: Integrated fluorescence as function of the photon energy for:
(a) CH(A $^2\Delta$*-X* $^2\Pi$*) emission*
(b) CH(B $^2\Sigma$*-X* $^2\Pi$*) emission*
The thresholds are indicated by the labels (I) and (II) for the lower and higher energy bands, respectively

In Figure 9.11 the integrated fluorescence for the CH(A $^2\Delta$-X $^2\Pi$) transition and the CH(B $^2\Sigma^-$-X $^2\Pi$) transition are plotted as function of the photon energy. The thresholds for these transitions have been extracted by extrapolating the fluorescence intensity to zero, as indicated by a red line in Figure 9.11. The thresholds are indicated by the labels *(I)* and *(II)* for the lower and higher energies, respectively, and summarized in Table 9.1 with the corresponding calculated thermodynamic values.

Table 9.1: Experimental and theoretical[14,24] *thresholds determined for the two channels (I) and (II) indicated in Figure 9.11*

Channel	CH($A^2\Delta$-$X^2\Pi$) Thermodynamic threshold calc. in refs. (14,24)	CH($A^2\Delta$-$X^2\Pi$) Observed threshold	CH($B^2\Sigma^-$-$X^2\Pi$) Thermodynamic threshold calc. in refs. (14,24)	CH($B^2\Sigma^-$-$X^2\Pi$) Observed threshold
(I) CH^*+CH_3	10.0	10.4±0.5	10.3	<12
(II) CH+CH^*+H_2	14.69	14.6±0.8	14.9	14.6±0.8

For the CH(B $^2\Sigma^-$-X $^2\Pi$) emission, threshold *(I)* only an upper limit can be given because of the poor number of data points in this region.

The heat of formation (or enthalpy of formation) of a species in the gas phase can, in principle, be obtained through a straightforward treatment of the thermochemistry of the dissociation process. For example, the threshold of the CH^*+CH_3 channel from the C_2H_4 in its groud state can be obtained by adding the enthalpy of formation of CH to the enthalpy of formation of CH_3 and the adiabatic (ν_{00}) transition energy for the CH transition under investigation and subtracting the enthalpy of formation of the parent molecule (C_2H_4).

In this section, the threshold values have been recalculated with the above-mentioned method to compare with the values calculated in refs. (14,24) and observed in Orsay. The calculated values of the thresholds for the two channels have been summarized in Table 9.2 with the corresponding thermodynamic values taken from the literature[14,24].

Table 9.2: Calculated and theoretical[14,24] thresholds determined for the two channels (I) and (II) indicated in Figure 9.11

	Channel	$CH^{*}+CH_3$	$CH+CH^{*}+H_2$
$CH(A^2\Delta\text{-}X^2\Pi)$	$\Delta_fH(CH)$[25]	6.14 eV	6.14 eV
	$\Delta_fH(CH_3)$[25]	1.51 eV	-
	v_{00}[26]	2.88 eV	2.88 eV
	$\Delta_fH(C_2H_4)$[25]	0.54 eV	0.54 eV
Calculated threshold, this work		9.99 eV	14.62 eV
Threshold calc. in refs. (14,24)		10.0 eV	14.69 eV
$CH(B^2\Sigma^-\text{-}X^2\Pi)$	$\Delta_fH(CH)$[25]	6.14 eV	6.14 eV
	$\Delta_fH(CH_3)$[25]	1.51 eV	-
	v_{00}[26]	3.17 eV	3.17 eV
	$\Delta_fH(C_2H_4)$[25]	0.54 eV	0.54 eV
Calculated threshold, this work		10.28 eV	14.91 eV
Threshold calc. in refs. (14,24)		10.3 eV	14.9 eV

As can be seen from Table 9.2, good agreement is obtained between the two calculated thresholds.

In summary, it is clear that the visible fluorescence observed from photodissociation of ethylene in the VUV region can be explained in this way, although the routes by which $C_2H_4^*$ decomposes into CH^*+CH_3 and $CH+CH^*+H_2$ are not known.
Hence, detailed studies of the potential energy surfaces of $C_2H_4^*$ in the 10.0-20.0 eV excitation energy region would be very useful. Also, although Super-ACO is being closed and the experimental work on this project is being discontinued, a possible extension of this work would be to redesign the apparatus to study fluorescence over a much wider wavelength region, e.g. extend the measurements into the ultraviolet and infrared regions.

9.4 Conclusion

An extensive description of the experimental apparatus used for the photodissociation studies of small hydrocarbons has been described in this Chapter. The visible fluorescence of electronically excited fragments obtained via VUV photodissociation of ethylene in the 11.7-21.4 eV energy region has been studied in a gas-flow system, using Synchrotron Radiation as the photon source and an original light collection device. Some previous investigations on ethylene that are considered important for the present work have been briefly reviewed and the results obtained on the ethylene photodissociation have been summarized.

9.5 References

[1] http://www.chem.uva.nl/imc/reactive_intermediates.html

[2] http:www.lure.u-psud.fr

[3] S. Douin, A. Campos, S. Boyé and P. Bréchignac
to be published

[4] A. Campos, S. Boyé, P. Bréchignac, S. Douin, C. Fellows, N. Shafizadeh and D. Gauyacq
Chemical Physics Letters **314**, 91 (1999)

[5] P. W. Atkins
Physical Chemistry
Oxford University Press, Oxford, 1978

[6] J. Lequeux and E. Roueff
Physics Review **200**, 241 (1991)

[7] J. Crovisier
Faraday Discussions **109**, 437 (1998)

[8] H. Wang and M. Fenklach
Combustion and Flame **110**, 173 (1997)

[9] R. Atkinson
Journal of Physical and Chemical Reference Data **26**, 215 (1997)

[10] R. Mc Diarmid
Journal of Physical Chemistry **84**, 64 (1980)

[11] D. M. P. Holland, D. A. Shaw, M. A. Hayes, L. G. Shpinkova, E. E. Rennie, L. Karlsson, P. Baltzer and B. Wannberg
Chemical Physics **219**, 91 (1997)

[12] J. J. Lin, C. C. Wang, Y. T. Lee and X. Yang
Journal of Chemical Physics **113**, 9668 (2000)

[13] A. H. H. Chang, A. M. Mebel, X. M. Yang, S. H. Lin and Y. T. Lee
Journal of Chemical Physics **109**, 2748 (1998)

[14] A. H. H. Chang, A. M. Mebel, X. M. Yang, S. H. Lin and Y. T. Lee
Chemical Physics Letters **287**, 301 (1998)

[15] A. H. H. Chang, D. W. Hwang, X. M. Yang, A. M. Mebel, S. H. Lin and Y. T. Lee
Journal of Chemical Physics **110**, 10810 (1999)

[16] E. M. Evleth and A. Sevin
Journal of American Chemical Society **103**, 7414 (1981)

[17] O. S. Tee and K. Yates
Journal of American Chemical Society **94**, 3074 (1972)

[18] D. T. T. Su and E. R. Thornton
Journal of American Chemical Society **100**, 1872 (1978)

[19] K. Kameta, S. Tsutomu, M. Watanabe, N. Kouchi and Y. Hatano
Journal of Electron Spectroscopy and Related Phenomena **101**, 65 (1999)

[20] J. O'Reilly, S. Douin, S. Boye, N. Shafizadeh and D. Gauyacq
Journal of Chemical Physics **119**, 820 (2003)

[21] A. Tanabashi and T. Amano
Journal of Molecular Spectroscopy **215**, 285 (2002)

[22] http://physics.nist.gov/PhysRefData/

[23] S. Boye, A. Campos, S. Douin, C. Fellows, N. Shafizadeh, D. Gauyacq, P. Halvick and M. Boggio-Pasqua
Journal of Chemical Physics **116**, 8843 (2002)

[24] M. W. Chase
Journal of Physical and Chemical Reference Data Monograph **9**, 1 (1998)

[25] http://webbook.nist.gov/chemistry

[26] H. Herzberg
Molecular Spectra and Molecular Structure
D. van Nostrand Company Inc., New York, 1966, Vol. I

Chapter 10

10 CONCLUSIONS AND FURTHER WORK

The aim of the work presented in this thesis was to use photoelectron spectroscopy, to investigate the electronic structure and the photoionization dynamics of atmospherically important species. This work covers Synchrotron Radiation spectroscopic studies of O, N and S atoms and OH, OD, and SH molecular radicals, and a study of photodissociation of ethylene undertaken in Orsay, in the group of Prof. Dolores Gauyacq[1]. An overview of what has been achieved, suggestions for further studies, and possible improvements for the spectrometer used are given in the following sections of this Chapter.

10.1 Advancement of the spectrometer

The basic design of the synchrotron spectrometer enables it to be used to study short-lived atoms and molecules. Its performance could be readily enhanced to produce extra spectral information, by increasing the efficiency of electron collection, improving the resolution or utilizing the ions produced from photoionization.

10.1.1 Multichannel detector

At present the spectrometer utilizes a single channel electron multiplier as a detector. It is proposed to replace the single channel detector, with a position-sensitive, multichannel device[2]. This will increase the rate of acquisition of spectra by at least an order of magnitude and will decrease the acquisition time needed. For these reasons this type of detector is especially advantageous for synchrotron studies, as synchrotron time is limited in availability. Moreover, the use of chemically aggressive species can rapidly contaminate the spectrometer, decreasing its performance. Hence, spectra of reactive intermediates must be acquired as quickly as possible, while achieving acceptable signal-to-noise ratios.

10.1.2 Threshold spectroscopy

The resolution of a UV photoelectron spectrometer is routinely 30 meV and, at best, 20 meV. This is only adequate to resolve vibrational structure in most molecules, and often gives rise to difficulties in assignment when several bands are overlapped. Overlapping bands is a common problem in studying radicals as they are often produced in an experiment at small relative partial pressures in the presence of more stable species. This can lead to weak bands of the radical of interest being overlapped with a stronger band of a reagent or product.

A large improvement in resolution (3 meV) and sensitivity can be achieved in PES if threshold techniques are employed. Threshold photoelectron spectroscopy (TPES) is complementary to conventional PES as threshold techniques are more sensitive to indirect processes (e.g. autoionization). TPES requires a continuously tuneable photon source (e.g. Synchrotron Radiation) and in TPES the photoelectron yield of nominally zero kinetic energy electrons is recorded as a function of photon energy[3,4]. Photoelectrons are collected over a solid angle of 4π (using the penetrating field technique[3,4]), which greatly increases sensitivity, but means total loss of any angular information. The work of King[4] has demonstrated the usefulness of TPES with Synchrotron Radiation for a number of small molecules including HF[5], DF[5], ICl[6], SF_6[7], HBr[8], DBr[8], HCl[9] and DCl[9]. An alternative to the penetrating field technique is pulsed field ionization (PFI). In PFI a field is applied to the ionization region shortly after the sample has been illuminated with UV radiation. This applied field causes field ionization of long-lived Rydberg states, producing low kinetic energy electrons which are subsequently detected. This requires the timing of the detection system of the spectrometer to be coupled with the temporal structure of the photon source. For example it is possible to apply an electric field and collect electrons produced by pulsed field ionization during the dark gap of a Synchrotron Radiation Source[10-12].

10.1.3 Coincidence Studies

A common problem when studying the photoelectron spectra of short-lived intermediates is that of overlapping photoelectron bands produced by different species present in the ionization region. If the electrons and the ions produced in a photoionization event can be correlated, then the signal attributed to each species present in the mixture may be separated and the overlapping band problem is avoided.

Photoelectron-photoion-coincidence (PEPICO) has been widely used in laser spectroscopy[13] and similar experiments can be performed in UV-PES. If PFI (see section 10.1.2) is employed along with a time-of-flight ion and electron detection system, coupled to a time-structured light source, then photoelectrons and photoions may be measured in coincidence (PFI-PEPICO)[14,15]. Typicallyn a resolution smaller than 1 meV is possible. Several experiments of PFI-PEPICO measurements using Synchrotron Radiation have proved successful[10-12,14,15]. It should be possible to perform ion-electron coincidence measurements of reactive intermediates in a UV photoelectron spectroscopy experiment using a synchrotron as a radiation source.

10.2 Photoelectron spectroscopy of short-lived species using Synchrotron Radiation

In this work, Synchrotron Radiation was successfully used for angle resolved studies. CIS spectra taken at two angles enabled the assignment of Rydberg series to autoionizing resonances and enabled the calculation of the asymmetry parameter (β) as function of incident photon energy. This study established the viability of angle resolved studies of short-lived species using Synchrotron Radiation with the spectrometer used.

Photoelectron spectroscopy of O atoms (see Chapter 5) using a third generation Synchrotron Radiation Source (ELETTRA) have shown that the increased photon flux and improved spectral resolution obtained with this photon source can be used to obtain CIS spectra of short-lived species that contain much more information than was previously possible with a second generation source[16]. In the study of OH and OD radicals (see Chapter 6) rotational resolution of the bands corresponding to transitions to Rydberg states was observed in the CIS spectra and the spectra obtained compared favourably with earlier UV absorption and PIMS studies.

The studies presented in this thesis have shown that with the high photon flux, high degree of polarization and good spectral resolution, photoelectron spectroscopy can be used to obtain information on photoionization dynamics, asymmetry parameters as function of photon energy, and highly excited Rydberg states.

The success of the studies made on short-lived species means that these methods can be successfully applied to other short-lived radicals. In the future it is planned to undertake analogous studies on NO, CF, NH, and NH_2.

10.3 Conclusions

In conclusion, the initial objective of this project on photoelectron spectroscopic studies of selected reactive intermediates, O atoms, OH and OD radicals, N atoms, S atoms and SH radicals have been successfully performed. These studies have highlighted the improvement in resolution achieved using a synchrotron of third generation, especially when constant ionic state measurements are performed. Measurements of angular distribution asymmetry parameters and relative cross sections have also been made. The existing experimental apparatus can allow further measurements on atmospherically important reactive intermediates to be obtained, a selection of these are planned for the near future.

10.4 References

[1] http://www.chem.uva.nl/imc/reactive_intermediates.html

[2] J. V. Hatfield, P. J. Hicks, D. G. Lomas and J. Comer
Review of Scientific Instruments **63**, 792 (1992)

[3] G. C. King, A. J. Yencha, M. Cristina and A. Lopes
Journal of Electron Spectroscopy and Related Phenomena **114**, 33 (2001)

[4] G. C. King
Radiation Physics and Chemistry **68**, 15 (2003)

[5] A. J. Yencha, A. J. Cormack, R. J. Donovan, A. Hopkirk and G. C. King
Journal of Physics B **32**, 2539 (1999)

[6] A. J. Yencha, M. Cristina, A. Lopes and G. C. King
Chemical Physics Letters **325**, 559 (2000)

[7] A. J. Yencha, A. Lopes, D. B. Thompson and G. C. King
Journal of Physics B **33**, 945 (2000)

[8] A. J. Yencha, A. J. Cormack, R. J. Donovan, K. P. Lawley, A. Hopkirk and G. C. King
Chemical Physics **238**, 133 (1998)

[9] A. J. Yencha, A. J. Cormack, R. J. Donovan, A. Hopkirk and G. C. King
Chemical Physics **238**, 109 (1998)

[10] C. W. Hsu, M. Evans, P. A. Heimann and C. Y. Ng
Review of Scientific Instrumens **68**, 1694 (1997)

[11] G. K. Jarvis, Y. Song and C. Y. Ng
Review of Scientific Instrumens **70**, 2615 (1999)

[12] W. Chen, J. Liu and C. Y. Ng
Journal of Physical Chemistry A **107**, 8086 (2003)

[13] T. Baer, J. Booze and K. M. Weitzel
Vacuum Ultraviolet Photoionization and Photodissociation of Molecules and Clusters
edited by C.Y. Ng, World Scientific, London, 1991, Chapter 5

[14] C. Y. Ng
Annual Review of Physical Chemistry **53**, 101 (2002)

[15] X. M. Qian, T. Zhang, C. Chang, P. Wang, C. Y. Ng, Y. Chiu, D. J. Levandier, J. S. Miller, R. A. Dressler, T. Baer and D. S. Peterka
Review of Scientific Instruments **74**, 4096 (2003)

[16] L. J. Beeching, A. A. Dias, J. M. Dyke, A. Morris, S. Stranges, J. B. West, N. Zema and L. Zuin
Molecular Physics **101**, 575 (2003)

Appendix A

11 MEASUREMENT OF THE ASYMMETRY PARAMETERS (*β*) FOR THE FIRST AND SECOND BANDS OF DIMETHYLSULPHIDE (DMS) USING LINEARLY POLARIZED SYNCHROTRON RADIATION

Dimethylsulphide (DMS) is an important sulphur-carrying gas in the Earth's atmosphere that arises from natural sources[1]. The dominant sulphur compound released from the oceans is DMS, which is produced by metabolic processes in certain algae. Oceanic surface waters are super-saturated with DMS with respect to atmospheric concentrations and thus supply a net flux to the atmosphere[2].

Atmospheric oxidation of DMS can be initiated by attack either of OH, during the day, or NO_3 at night. The products that result from the atmospheric oxidation of DMS are of considerable importance. It has been proposed that DMS may be a link in an ecosystem regulation of cloud formation over the Earth[3]. If oxidation of DMS leads to sulfuric acid, which serves as cloud condensation nuclei and contributes to the natural acidity of precipitation, DMS could contribute as much as 25% to total acid deposition, at least over Europe[3].

Recent experiments at Southampton University with photoelectron spectroscopy using HeI (21.22 eV) radiation have provided interesting results on the mechanisms and pathways of DMS reactions of atmospheric importance. Although these experiments are still in progress, it is clear that measurement of the asymmetry parameter for the first two photoelectron bands of DMS, at 21.22 eV, will provide valuable supporting information.

11.1 Results

The photoelectron (PE) spectra recorded at a photon energy of $h\nu$=21.22 eV and at two different angles with respect to the major polarization axis of the photon source (θ=0° and θ=60°) of DMS+N_2 are shown in Figures 12.1 with the assignment of the major features indicated. These spectra were recorded at the ELETTRA Synchrotron Radiation Source using the spectrometer described in Chapter 4.

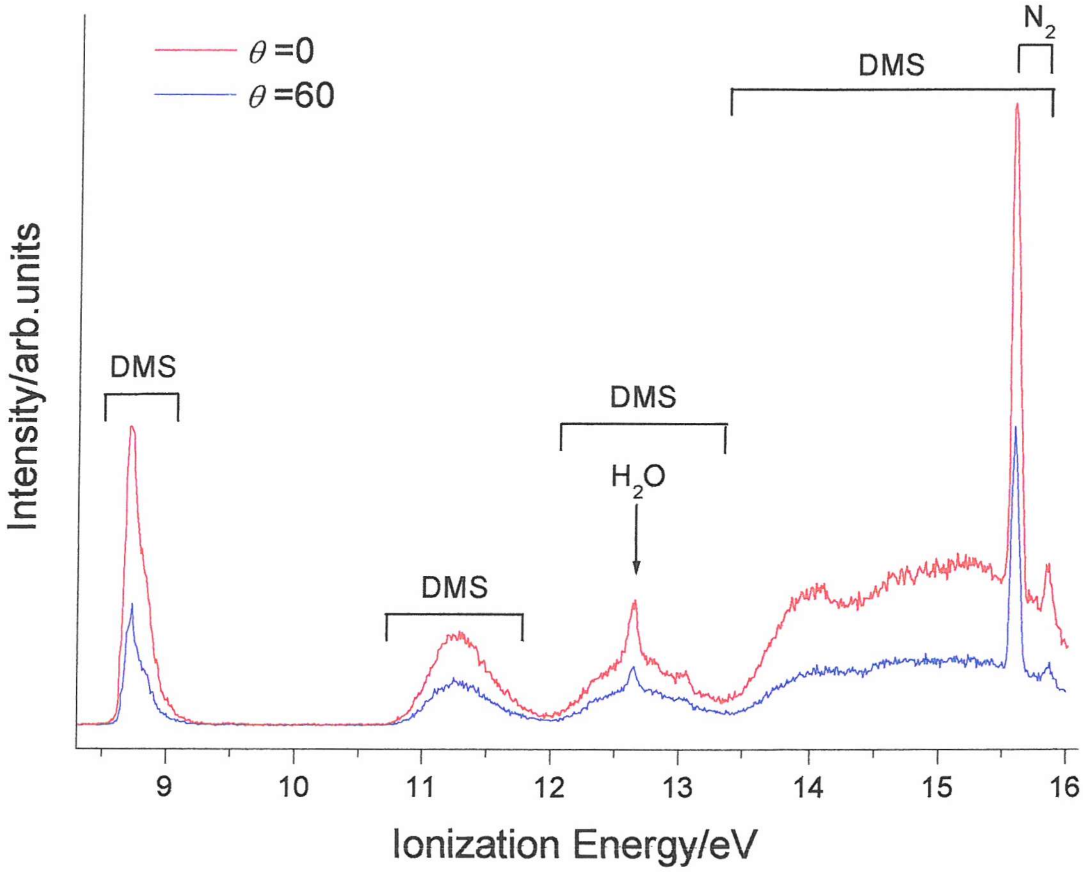

Figure 11.1: Photoelectron spectra at $h\nu$=21.22 eV of DMS+N_2 measured at two different angles θ=0° (red trace) and θ=60° (blue trace) with respect to the major polarization axis of the photon source

The $N_2^+(X\ ^2\Sigma_g^+, v=0) \leftarrow N_2(X\ ^1\Sigma_g)$ photoelectron band of molecular nitrogen, at 15.6 eV ionization energy, was used as internal check for the correction factor applied for the evaluation of the asymmetry parameter for the first two bands of DMS.

Indeed, for the measurements of angular distribution it is important to make sure that the efficiency of the analyser does not change when the spectrometer is rotated. The biggest contribution to the change of the efficiency of the analyser comes from small misalignments between the axis of rotation and the direction of the photon beam. This contribution is minimised by adjusting, after each rotation of the spectrometer, the direction of the photon beam in such a way as to maximise the signal coming from the detector and the current measured by the photodiode on the far side of the ionization chamber of the spectrometer, opposite the photon source, as described in Chapter 4. However, to quantify this contribution for all the experiments related to angle resolved studies, a correction factor is evaluated at each set of experiments at ELETTRA by measuring the intensity of peaks at $\theta=0°$ and at $\theta=60°$, usually at 21.22 eV photon energy, of samples where the asymmetry parameter is well established (e.g. Ar).

The value of the asymmetry parameter, β, for the $N_2^+(X\ ^2\Sigma_g^+, v=0) \leftarrow N_2(X\ ^1\Sigma_g)$ band of is known to be equal to 0.68±0.05 at photon energy 21.22 eV[4]. From the comparisons between the calculated asymmetry parameter and the known asymmetry parameter the correction factor is determined.

At 21.22 eV photon energy, the asymmetry parameter could be calculated from the expression (see Chapter 2.2.6):

$$\beta = \frac{8(R-1)}{R+8} \qquad \text{Eq. 11.1}$$

where $R = \frac{I_0}{I_{60}}$ is the ratio of the experimental intensities at the two angles.

In the following table, the estimations of the asymmetry parameters for the first band (VIE 8.72 eV[5]) and the second band (VIE 11.30 eV[5]) of DMS are tabulated with the relative errors.

Table 11.1: Values of the asymmetry parameters for the first and second bands of DMS determined in this work

State	Asymmetry parameter
1st band	1.05±0.35
2nd band	0.70±0.12

The asymmetry parameter value for the first band of DMS can been compared with the beta value of the first band of H_2S determined at photon energy 21.22 eV (β=1.60±0.03)[6,7].

Both these first bands correspond to ionization from a 3p "lone pair" on the sulphur atom. In H_2S, the outermost occupied orbital consist entirely of the S 3p "lone pair" orbital. In DMS, however the 2p orbital interacts to some extent with C 2p orbitals perpendicular to the C-S-C plane. For this reason, it is not surprising that only moderate agreement is obtained. Also β is expected to change with vibrational component but the measurements made here were not vibrationally resolved.

11.2 References

[1] R. P. Wayne
Chemistry of Atmospheres
Claredon Press, Oxford, 1991

[2] M. O. Andreae and H. Raemdonck
Science **211**, 744 (1983)

[3] J. P. Friend
Chemistry of lower atmosphere
Plenum Press, New York, 1973

[4] W. H. Hancock and J. A. R. Samson
Journal of Electron Spectroscopy and Related Phenomena **9**, 211 (1976)

[5] K. Kimura, S. Katsumata, Y. Achiba, T. Yamazaki and S. Iwata
Handbook of HeI photoelectron spectra of fundamental organic molecules
Japan Scientific Societies Press, Tokyo, 1981

[6] T. A. Carlson and G. E. McGuire
Journal of Electron Spectroscopy and Related Phenomena **1**, 209 (1972)

[7] S. Katsumata, K. Mitani and H. Shiromaru
Chemical Physics Letters **75**, 196 (1980)